2-13-2020 1:30 PM

Advanced hardware and software approach to seismic site response investigations

Aleksandar Dimitrov Mihaylov
The University of Western Ontario

Supervisor
El Naggar, M. H.
The University of Western Ontario

Graduate Program in Civil and Environmental Engineering
A thesis submitted in partial fulfillment of the requirements for the degree in Doctor of Philosophy
© Aleksandar Dimitrov Mihaylov 2020

Recommended Citation

Abstract

Vibration measurement is an essential aspect of modern geotechnical engineering. It is particularly vital task for measuring the dynamic soil parameters, estimating seismic hazards and evaluating influence of industrial, traffic and construction vibrations on the surrounding buildings, structures and their elements. Meanwhile, commercial exploration seismic stations and data acquisition systems require significant professional knowledge and training in geophysics or vibration measurement, as well as practical skills and experience in adjusting data acquisition parameters. Furthermore, available seismological investigation and vibrometry sensors are not universally suitable for field applications in geophysical studies, soil-structure interaction investigations or structural vibrations. The frequency range suitable for seismic studies and industrial vibration measurement vary from 1 Hz to 300 Hz with sensitivity corresponding to the expected vibration level. To address these challenges, the first part of this thesis was focused on developing an innovative data acquisition system and sensors that are easy to use in a wide range of field applications.

Geophysical techniques, including the Multichannel Analysis of Surface Waves (MASW) and Horizontal to Vertical Spectral Ratio (HVSR) methods, are gaining popularity in site investigations and seismic hazard characterization applications. The second part of this thesis involved conducting field studies using MASW and HVSR methods to evaluate the influence of challenging site conditions such as sloping surface topography, complicated soil stratigraphy and sloping bedrock boundaries on the results of the applied methods.

The application of theoretical or numerical models of site amplification often poses a challenge under real field conditions. In the third part of the thesis, an analytical model was developed to allow for the removal of site effects from strong motion records and proposed a method for HVSR curve parameterization that resulted in an analytical expression for the amplification factor based on HVSR results.

Keywords

Summary for Lay Audience

Accurate evaluation of dynamic soil parameters is important for many engineering applications such as proper design of industrial and civil buildings and infrastructure and urban planning for resilient and sustainable communities. Estimation of these parameters often requires extensive field studies and specialized equipment or laboratory testing.

Vibration measurement is an essential part of these undertakings. It is particularly vital task for estimating seismic hazards and evaluating influence of industrial, traffic and construction vibrations on the surrounding buildings, structures and their elements. Currently available commercial exploration seismic stations and vibration measurement systems are expensive and very difficult to use because they require significant professional knowledge and training in geophysics or vibration measurement. To address these challenges, this thesis is subdivided into three parts. The first part was focused on developing an innovative data acquisition system and sensors that are easy to use in a wide range of field applications. The second part of this thesis involved conducting field studies for Multichannel Analysis of Surface Waves (MASW) and Horizontal to Vertical Spectral Ratio (HVSR) studies to evaluate the influence of challenging site conditions such as sloping surface topography, complicated soil stratigraphy and sloping bedrock boundaries on the results of the applied methods. In the third part, a theoretical study was conducted to evaluate seismic amplification factors that resulted in an analytical expression for the amplification factor based on HVSR results.

Co-Authorship Statement

This thesis has been prepared in accordance with the specifications and regulations of the manuscript format stipulated by the Society of Graduate and Post Graduate Students (SGPS) at Western University, Ontario, CA.

All the experimental work was conducted under the supervision of Prof. M. Hesham El Naggar. The author carried out all experimental work, data analysis, interpretation, and writing of the initial draft of the thesis. The contribution of his research advisor consisted of providing guidance and supervision and helping in the development of the final versions of the thesis. Assistance with the logistics of the field work performed was provided by Lucas Capretz and Jamal Assaf.

Chapter 5 is published in the journal of Soil Dynamics and Earthquake Engineering and is co-authored by Hesham El Naggar, Dimitar Mihaylov and Savka Dineva. Prof. M. Hesham El Naggar provided valuable review and feedback on the developments of the paper. Dr. Dimitar Mihaylov proposed the smoothing function used in the paper and suggested the development of the analytical HVSR curves. Dr. Savka Dineva assisted with data procurement and source spectral estimation

Section 3.4 Software based sensor frequency range expansion is under consideration for publication in Acta Geophysica and is co-authored by Prof. M. Hesham El Naggar who provided valuable feedback and review of the paper.

Acknowledgments

First and foremost, I would like to thank my supervisor Hesham El Naggar for providing me with the opportunity to do this work. I appreciate his excellent supervision, patient help, crucial guidance and support very much. I have learned a lot from him.

Dr Dimitar Mihaylov provided invaluable support and encouragement during the work done on this thesis. I would like to thank him for his persistence and guidance that contributed to the completion of this thesis. I also appreciate his help with data processing techniques, filed measurement guidance as well as editorial involvement

I would also like to thank Dr. Savka Dineva for much appreciated guidance in the field of seismology and the review of the work in this thesis.

Special thanks to my wife Maggie Sazio for her endless patience and belief in my abilities. I appreciate everything she has done to make this thesis possible and the review of some of the aspects of this work.

I very much appreciated the help of Lucas Capretz and Jamal Assaf for their assistance with field measurements and would like to thank them for their involvement.

Table of Contents

List of Tables

List of Figures

Nomenclature

$\mathcal{F}^{-1}$	Inverse Fourier Transform
$\mathcal{F}$	Forward Fourier Transform
G_a	Accelerometer generator constant
G_d	Seismometer generator constant
G_v	Geophone generator constant
$H_a(f)$	Accelerometer transfer function
$H_d(f)$	Seismometer transfer function
$H_v(f)$	Velocimeter/Geophone transfer function
R_{eq}	Equivalent resistance
R_{shunt}	Damping resistor for a geophone element
T_s	Sample Period
F_s	Sampling Frequency
V_P	Compressional Wave Velocity
V_R	Rayleigh Wave Velocity
V_s	Shear Wave Velocity
β_{hyst}	Hysteretic Damping
β_{visc}	Viscous Damping
ADC	Analog to digital Convertor
D	Damping Ratio
DAC	Digital to analog convertor
DEM	Digital Elevation Model
DFT	Discrete Fourier transform
E	Elastic/Young's modulus
EMI	Electromagnetic Interference
f_0	Fundamental frequency
f_d	Damped natural frequency
FFT	Fast-Fourier Transform
f_n	Natural frequency
G	Shear Modulus

G_{MAX}	Maximum shear modulus
GSC	Geological Survey of Canada
GUI	Graphical user Interface
h	Damping constant
h_e	Electrical damping of sensor element
h_m	Mechanical damping of sensor element
HVSR	Horizontal to Vertical Spectral Ratio
IRC	Instrument response correction
k	Spring constant
MAM	Microtremor Array Measurement
MASW	Multi-channel analysis of surface waves
MSPAC	Modified SPAC
N	Number of samples in processing window
NHNM	New High Noise Model
NLNM	New Low Noise Model
PGA/PGV	Peak Ground Velocity/Acceleration
QTS	Quasi transfer function spectrum
SAR	Successive Approximation ADC
SASW	Spectral analysis of surface waves
SDADC	Sigma-Delta ADC
SNR	Signal to Noise Ratio
SOSN	Southern Ontario Strong Motion Network
SPAC	Spatial Autocorrelation
t	Time
γ	Shear strain
ε	Compressional Strain
λ	Wavelength
v	Poisson's Ratio
ρ	Density
σ	Stress
ω	Angular frequency

Chapter 1. Introduction

Earthquakes are rare and devastating events that can result in major destruction and loss of lives. Only in the last 10 years, several earthquakes resulted in more than 100,000 fatalities (e.g. Pakistan (2005), Indonesia (2004, 2018, 2019), Haiti (2010), Tohuku (2011), Nepal (2015)) with many more earthquakes killing more than 1000 people each. To minimize the vulnerability to earthquakes and the resulting economic and human losses, it is necessary to properly characterize the seismic hazard. Naturally, the need is higher in high risk areas, as well as for construction projects of significant importance and sensitivity (i.e. power generation stations, hospitals and densely populated areas). Damages caused by earthquakes in some locations are exacerbated as a direct result of ground motion amplification due to local geological conditions. Amplified motions have a much stronger effect on structures when the soil resonances and the resonant frequencies of seismic waves are in the range of the dominant periods of structures. New urban development should not be undertaken without improving our understanding of and using new methods for better characterization of the shallow subsurface geological conditions.

The evaluation of the site response is important when assessing building behavior during an earthquake. Both soil and building resonances change if a strong dynamic load is experienced. Evaluation of static and dynamic soil properties is an important part of the design process for new constructions or refurbishment of existing infrastructure. For urban areas, the site response evaluation is also complicated by the influence of building loads, soil improvement, pile foundations, densification, etc. Other complicating factors are surficial topography, complicated stratigraphy, and sloping of underlying bedrock. In such areas, the soil resonances can be found using Horizontal-to-Vertical Spectral Ratio (HVSR) (Nakamura, 2009, 1989) or other geophysical methods only on the free surface between buildings or on sections of the topography that allow for the studies requirements. In such conditions, boreholes may be undesirable or infeasible, and space limitations could eliminate other methods of investigation, such as large Multi-channel Analysis of Surface waves (MASW) studies, refraction and reflection studies, as well as passive or active array-

based measurements such as Spatial Auto-Correlation (SPAC) or Microtremor Array Measurements (MAM).

As seismic waves propagate through the uppermost layers of soil and rock at a given site, the characteristics of the wave will change according to the soil and geological properties of the site. Shallow geological structures of the site, as well as past and present loads (both static and dynamic) influence these properties, and consequently the site transfer function. The term "transfer function" is used to relate the soil layers effects on an incoming seismic wave to a filter that can increase the duration and amplitude of earthquake shaking within a narrow frequency band (Molnar et al., 2014). The amplification of these waves is largely controlled by the mechanical properties of these layers, or more precisely, the variation in their impedance. The densities and shear-wave velocities (V_S) of the near-surface soil layers are smaller than those of the bedrock below. Considering the energy conservation principle and recognizing that denser bedrock has a much higher Young's modulus than near surface layers, it can be observed that in most cases the seismic wave at the surface is amplified. This is due to the larger strain experienced by less dense top-layers as the energy carrying wave passes through. Additionally, at the earth's surface, the half-space effect introduces additional amplification as there is no overlaying mass to resist the vibration. Where soil layers may alter the incoming seismic wave's amplitude or frequency composition, the particular shape of the bedrock at the site can introduce focusing, dispersion, reverberation and other effects (Davis et al., 2000; Gao et al., 1996; Hartzell et al., 2010). Recently many attempts were made to estimate static and dynamic soil properties using seismic techniques like HVSR, MASW and numerical modeling.

Measuring of vibration is used in geotechnical practice in two occasions: to estimate the soil parameters and site conditions from seismic data and to establish the influence of industrial, transportation, cultural, etc. vibrations on surrounding building, structures and their elements.

Many exploration seismic stations and data acquisition system require professional knowledge to be used and maintained properly. In many cases the field data must be recorded by personnel who are not professional geophysicists, specialists in vibration

measurements or familiar with the operation and requirements of the hardware and software required to perform reliable field studies. The proper use of the available specialized equipment on the market presume some training in geophysics or vibrometry as well as practical skills in the adjustment of many data acquisition parameters of the devices.

The available sensors for seismological investigation and vibrometry are not always suitable for field use in local geophysical study, soil-structure interaction, buildings and structures vibrations. The necessary frequency interval suitable for both field seismic study and industrial vibration measurement can be defined to be between 1 Hz and 300 Hz with sensitivity corresponding to expected level of vibration. Sensors need to be small enough to allow simple installation in difficult condition, especially in industrial or structural applications. Data acquisition system for vibration measurement and assessment exist in the market, however such systems are often designed for specific measurement purpose and their use outside the manufacturer's prescribed application can be limited, and in some cases require modification of the data acquisition system and its sensors.

Commonly utilized seismographs are heavy and require special conditions for installation and operation. There are small accelerometers available, but low sensitivity and higher noise at low frequency limit their use to relatively strong vibrations. Geophones are widely used for field seismic study and for artificial vibration measurements. Their output signal is proportional to the shaking velocity, but the linear frequency range is limited to frequencies above the natural frequency, typically at 4-14 Hz. There exist geophones with extended frequency range, but they are expensive and their use in risky environment is not recommended. These requirements and constraints limit the applicability of ordinary sensors. The demands for portability, simplicity of installation and use, necessary frequency range and sensitivity require some hardware solutions and software improvements both for sensors and data recording systems. All the above necessitates the development and prototyping of a data acquisition system including hardware, sensors and software, which are easy to use for field seismic investigation as well as measurement of artificially produced vibration.

A new vibration assessment data acquisition (DAQ) system including two versions of geophone-based sensors were developed to fit the above criteria, combined they are referred to as the DYNAMate DAQ system. Three prototype iterations of the DAQ were developed, tested and used in different aspects of the field studies performed as part of this thesis. Geophone based 4.5 Hz 3-component sensors were developed, and methods for their calibration and instrument response correction (IRC) in both real-time and post-processing are presented herein. Additionally, a hardware solution to the IRC problem is proposed, prototyped and tested.

1.1 Goals of this Thesis

- Conduct comprehensive literature review and propose a method for considering amplification/attenuation of earthquake shaking in deep sedimentary basins and potential resonance effects.
- Developing and prototyping of robust, reliable and versatile test equipment suitable for vibration measurement in different conditions, and particularly suitable for seismic microzonation studies to collect data for various sites during earthquakes and from vibration measurement.
- Conduct field study in areas which have different geological conditions including locations with edge effects in deep sediment basins and slope topology.
- Methods and tools for predicting amplification/attenuation of earthquake shaking in deep sedimentary basins and potential resonance effects
- Investigate the discrepancy between the measured Nakmaura site amplification and the actual site performance for various geological and lithographic conditions
- Develop software for signal processing in real time during the data acquisition and for postprocessing of already recorded waveforms.

1.2 Organization of this Thesis

This thesis is divided into chapters describing the work done as part of the research effort to develop new seismic and industrial field equipment, as well the analysis of field data from field studies to characterize site effect for locations with complex subsurface geological conditions.

Chapter 1

The introduction includes the objectives and scope of this study, organization of the dissertation and some original contributions of the thesis.

Chapter 2

This chapter focuses on literature review of dynamic soil properties, seismic wave propagation, geophysical methods and ground motion prediction equations. The review aims to identify the limitations as well as recent developments in the application of geophysical methods to site characterization.

Chapter 3

This chapter introduces the development of a 3-component 4.5Hz field geophone sensor. As part of the development, a procedure for the characterization and calibration of geophone elements was implemented. Methods for IRC of already recorded vibration data are then introduced and implemented in both real-time and post-processing scenarios. Finally, a 0.5Hz expanded frequency range geophone hardware prototype is proposed, prototyped and tested.

Chapter 4

This this chapter describes the design and implementation of a DAQ system specifically designed for seismic, foundation and structural vibration measurements. Limiting the application areas allows developing a much simplified and reliable design, which only requires basic user experience.

Chapter 5

This chapter investigates the application of the HVSR method for both microtremor and strong motion (earthquake) applications. The importance of spectral smoothing and its effects on the HVSR spectra are discussed and a new smoothing function is proposed. The function is also used as a basis-function in the development of an analytical model of HVSR curves. This model is utilized to remove site effect amplification from strong motion recordings of the Southern Ontario Strong Motion Network (SOSN).

Chapter 6

This chapter describes some of the field studies performed as part of this thesis. It focuses on the effects of surficial as well as bedrock topology on geophysical methods. Results from both HVSR and MASW investigations are presented. Additionally, it compares the results obtained from the field measurements to the published predictions of numerical models regarding the effects of sloping topography on HVSR results.

Chapter 7

This chapter presents the summary and conclusions of this work, chapter by chapter, as well as recommendations for future research.

Chapter 2. Literature Review

2.1 Dynamic behaviour of soil

Strong seismic motion can result in localized damage to the soil/bedrock structure, especially in areas with large changes in the dynamic properties of the medium, i.e. shear modulus (G) (Ben-Zion and Sammis, 2003). This process affects the relatively shallow layers of the Earth crust and recovers after time as the increasing normal stress with depth restrains the generation of new cracks and contributes to the damage recovery (Peng and Ben-Zion, 2006).

The stress-strain behavior of soils under dynamic loads is commonly characterized based on the in-situ damping ratio (D) and shear modulus (G_{max}). These parameters are modified using empirical relationships (degradation curves) describing the increase in damping and decrease in the shear modulus with increasing in strain level of the medium. The recommended practice is to establish the dynamic soil properties using laboratory tests.

Dynamic material properties depend on a variety of parameters and site conditions such as: overburden pressure, strain amplitude and rate, water content, plasticity, particle shape and size as well as overconsolidation ratio. (Vucetic and Dobry, 1991) present a comprehensive study on the effect these parameters have on the dynamic behavior of soils (Table 2.1). Additionally, (Kishida, 2017) notes that the degradation curves are very sensitive to the choice of variables used to develop them.

Using laboratory testing, (Xenaki and Athanasopoulos, 2008) concluded that effect of water content on the values of shear modulus is more significant for low values of cyclic shear strain as well as for low values of confining pressure. Clarification of the effects of grain size distribution is offered by (Iwasaki and Tatsuoka, 1977) for different sands. In all cases an increase of shear modulus is observed with an increase of confining pressure, and a decrease with an increase of the void ratio of the sample. In general, it is observed that the shear modulus of clean sand samples decreases with an increase in uniformity coefficient and decreases with fines contents at equal confining pressures.

Shear modulus at any strain level can be related to the shear wave velocity (V_s) and density (ρ) by:

$$G = \rho V_S^2 \qquad (2.1)$$

Table 2.1:Effects of Various Factors on G, G_{max} and Damping ratio on clays
(Vucetic and Dobry, 1991)

Increasing factor	G_{max}	G/G_{max}	Damping ratio D
Confining Pressure	Increases	Constant to small change	Constant or small decrease
Void Ratio	Decreases	Increases	Decreases
Geologic age	Increases	May Increase	Decreases
Cementation	Increases	May Increase	May decrease
Overconsolidation Ratio	Increases	Not affected	Not affected
Plasticity Index	Increases for OCR>1, otherwise constant	Increases	Decreases
Cyclic strain amplitude	-	Decreases	Increases
Cyclic strain rate	Increases	Probably not affected	May increase
Duration of loading	Decreases for the duration, followed by recovery	Decreases	No significant change for moderate strain amplitude and duration

2.1.1 Effect of strain level on in-situ dynamic soil parameters

Based on the level of strain soil dynamic parameters change, and in general the soil behavior goes from linear-elastic to plastic behavior. (Yuliyanto et al., 2017) identified three categories that describe soil behavior and susceptibility during different ranges of strain:

- For strains ranging from 10^{-6} to 10^{-5} the soil structure responds with vibration propagation and it behaves elastically.

- For strains from 10^{-5} to 10^{-3} cracking and degradation of the soil is to be expected and the dynamic behaviour is changing from purely elastic to elastoplastic.
- For strains larger than 10^{-3} landslides, liquefaction and severe strength degradation will begin to occur, and dynamically the soil parameters are in the plastic region.

A simplified diagram showing the strain dependent reduction of shear modulus and increase in damping for these levels of strain is shown in Figure 2.1.
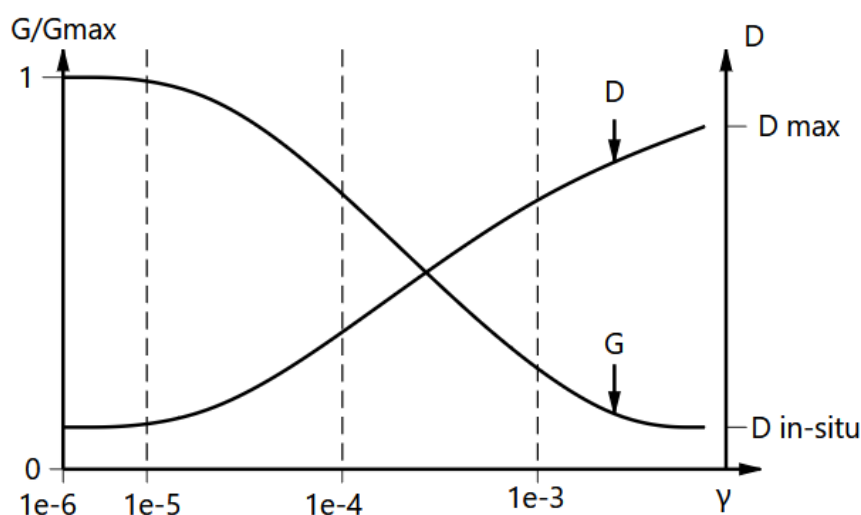
Figure 2.1: Simplified strain dependent reduction of shear modulus and damping increase

(Mancuso and Vassallo, 2002) show that for the small to medium strain range, soil dynamic behavior has non-uniform, differentiated sensitivity to strain rate. They conclude that for design purposes the design parameters should be obtained in a laboratory setup at strain rates and conditions comparable to the ones existing in-situ. Additionally, it is shown that soil stiffness is affected by the rate of strain such that at low strain levels the soil matrix has time to react and deform leading to lower stiffness, when compared to higher strain rates at which pore water and soil skeleton structure do not have time to react and the soil act like a rigid body, leading to higher stiffness.

The computational aspects related to large-deformation behavior in static and dynamic partially saturated soil analysis were presented by (Meroi et al., 1995). The authors introduced a variable permeability scheme depending both on saturation and on the current void ratio, which is particularly relevant when large strains are considered. This allows one to model more realistically soil behavior in all those situations where the applied load is large in comparison with the usual Young's modulus of the soil and when the initial void ratio is large. The developed models were used to estimate both horizontal and vertical displacements along with the changes in pore water pressure for both constant and simulated seismic loading.

Stiffnesses at intermediate strains can be assumed as a modified hyperbola. Many such relationships have been proposed in literature and the use of any one will depend on its applicability to the soil type and conditions, for example:

$$\frac{G}{G_{max}} = 1 - a \left(\frac{\tau}{\tau_{max}}\right)^b \tag{2.2}$$

Where a and b are empirically determined material parameters that control the the rate of the modulus decay, and $\frac{\tau}{\tau_{max}}$ is the mobilized shear strength.

2.1.2 Cyclic loading and changes in soil properties during dynamic loading

Damping forces oppose soil motion, and therefore wave propagation, and are out of phase with the displacement that caused them. Energy dissipated through damping is converted to heat or material transformation (sliding of particles, inelastic deformation, etc.) and is irrecoverable. Vibration energy is dissipated through two mechanisms:

- **Geometric or viscous damping** – due to energy dissipated with the propagation of the wave front away from the source, with increasing radius. Viscous damping is proportional to vibration velocity and for harmonic excitation its force magnitude is:

$$F = c \frac{d(\Delta x cos(\omega t))}{dt} = -c\Delta x \omega sin(\omega t) \tag{2.3}$$

Where Δx is the displacement of the harmonic motion, ω is the excitation frequency, and c is the viscous damping coefficient. The force peak amplitude is $\beta_{visc} = |F| = c\Delta x\omega$, and the damping is proportional to the excitation frequency.

- **Material or hysteretic damping** – Due to inelastic deformation, soil exhibits hysteretic loop under cyclic loading (see Figure 2.2). The dissipated energy is given by the total area of the hysteretic loop (**W** in Figure 2.2), it depends on strain and is unchanged by the excitation frequency. The magnitude of material damping can be experimentally estimated using the hysteretic loop:

$$\beta_{hyst} = \frac{W}{2\pi(A1+A2)} \tag{2.4}$$
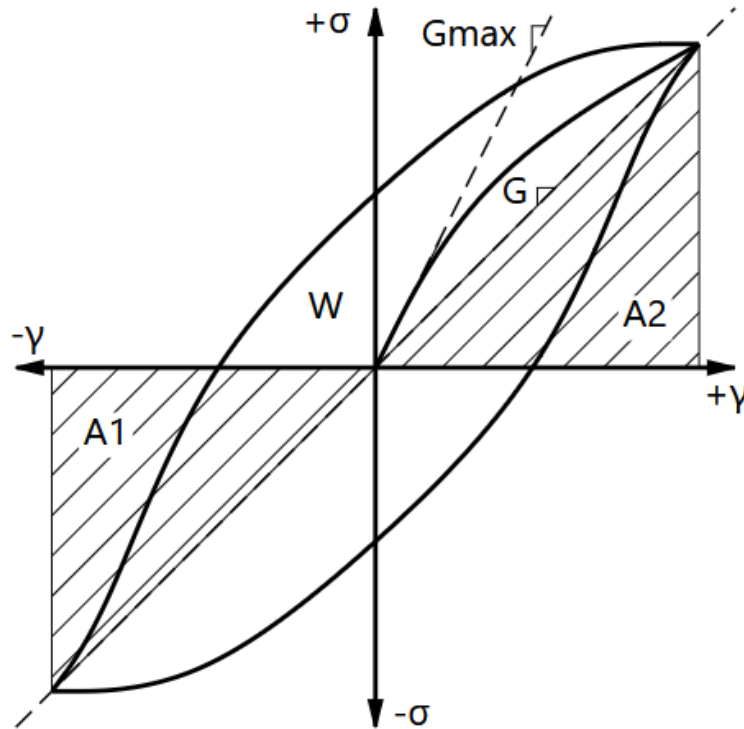
Figure 2.2: Simplified hysteresis stress-strain relationship. A1 and A2 are the areas of the two highlighted triangles (input strain energy), and W is the area under the loop.

During cyclic loading both the damping ratio and shear modulus experience changes. In drained triaxial test conditions the shear modulus increases with the number of cycles, whereas in undrained condition there is a reduction in shear modulus. The damping is reduced with the number of cycles in undrained conditons, and increased in drained conditons (Jafarzadeh and Sadeghi, 2012; Wichtmann and Triantafyllidis, 2004a, 2004b). Three ranges for the strain rate have been established (Mancuso and Vassallo, 2002):

- Low - creep generates increasing damping ratio with increasing frequency
- Intermediate - hysteretic damping dominates
- High - frequency dependant mechanisms are triggered (i.e. pore fluid viscosity) which increase both stiffness and damping.

2.1.3 Methods for dynamic soil properties measurement

Estimation of dynamic soil properties is complicated by large uncertaines in the measured parameters when in-situ methodologies are used. In most cases, the G/G_{max} relationship can be accurately modelled using laboratory experiments, however damping is less accurate. One of the methods encountered to accurately estimate the damping in literature for the determination of the in-situ damping ratio is to model it based on the better defined G/G_{max} degradation curve (Zhang et al., 2005).

In general, geophysical methods utilize very small strain excitation, and cannot be used to evelute the non-linear paramters of the soil. (Jafari et al., 2002) examine the dynamics of fine-grained soils using field investigations: seismic refraction, down-hole logging, Spectral Analysis of Surface Waves (SASW) and Standard Penetration Tests (SPT). Complementing the field studies, laboratory tests (stress controlled cyclic triaxial and resonant column tests) are performed on undisturbed samples of low to medium silty plastic materials. Based on field geo-seismic investigations, the authors develop a new V_S-N (SPT) correlations for the fine-grained soils considered. Also, laboratory test results reveal that effective confining pressure at stage of consolidation influences both strain dependent shear modulus and damping ratio of very low plastic soils.

2.2 Seismic Waves

2.2.1 Introduction

Seismic waves are elastic low-frequency waves generated as a result of earthquakes, volcanic activity, landslides, blasting and other strong artificial sources. Ambient seismic noise is composed of seismic waves generated by natural and anthropogenic sources such as wind, ocean tides, traffic, industrial vibration etc. The propagation velocity of seismic waves depends on the density, elastic parameters and structure of the geological formations. In general, the propagation velocity increases with depth

Different kinds of seismic waves are known, and they cause different particle motions depending on their type and polarization. The two main categories can be defined: body waves and surface waves.

Body waves have higher frequency than surface waves and travel through the bulk of geological formations. They usually arrive first at any distance from the source point. Two kinds are distinguished:

- P (primary) waves are compressional waves. They have the highest velocity and can propagate through solids and fluids. Particle motion is in the same direction as the propagation direction, with particles being pushed and pulled along the propagation vector.
- S (secondary) waves are shear waves. This type has a slower propagation velocity than the P wave and cannot propagate through media that cannot resist shear (i.e. liquids). Particle motion is perpendicular to the propagation vector, with SV moving up and down (vertically polarized) and SH moving side to side (horizontally polarized)

Surface waves propagate though the Earth's crust and upper soil layers and have lower velocity and lower frequency than the body waves. Unlike the body waves, surface waves are dispersive. They can be presented as groups consisting of many waves with different frequency and velocity of propagation. Because of this, group and phase velocity, and

different modes can be found out and used in practice. Two main types are widely used in geotechnical investigation:

- Love Waves - named after A.E.H. Love, who worked out the mathematical model for this kind of wave in 1911. It's the fastest surface wave and moves the ground from side-to-side and is characterized by entirely horizontal motion. Amplitude of displacement reduces with depth. Generating and propagating Love waves requires a shallow low velocity surface layer.
- Rayleigh Waves - named for John William Strutt, Lord Rayleigh, who mathematically predicted the existence of this kind of wave in 1885. A Rayleigh wave produces a rolling motion of the surface and is a result of coupling between P and SV body waves. The motion, in general is retrograde and particles move elliptically, opposite the propagation direction.

Very little information is available on the distribution of seismic energy between the different types of surface and body waves for microtremors. Some quantitative information is given in (Bonnefoy-Claudet et al., 2006b). The authors report that low frequency microseisms predominantly consist of fundamental mode Rayleigh waves, while there is no real consensus for higher frequencies (> 1 Hz). Different approaches were followed to reach these results, including analysis of seismic amplitude at depth and array analysis to measure the phase velocity. However, as demonstrated by (Miller and Pursey, 1955), for a vertically oscillating source positioned onto the surface of a homogenous, isotropic, elastic medium, the energy is distributed between the different wave types: 26% into S-wave and 7% into P-waves, and the rest into surface waves.

2.2.2 Attenuation of seismic waves

As the wave propagates through any given medium it will experience attenuation. The reduction of wave energy has two main mechanism that govern it: material and geometrical damping. (Kim and Lee, 2000) specify the attenuation for a homogenous medium as:

$$A_2 = A_1 \left(\frac{r_1}{r_2}\right)^n e^{-\frac{\pi \eta f}{c}(r_2 - r_1)} \tag{2.5}$$

where A_1 and A_2 are the wave amplitudes at distance r_1 and r_2 from the source, n is the geometric damping coefficient, f the frequency and c the propagation speed of the wave. The frequency dependent material damping is represented by the loss factor η. It is associated with energy lost due to friction. Geometrical damping is a result of energy spreading over the increasing area of the wave front.

2.2.3 Surface Waves

Surface waves exist in a horizontally bounded medium, such as the free surface of the earth. Two major types of surface waves are Love and Rayleigh waves. Their dispersive behavior is a function of the layering structure of geological formations.

Rayleigh and Love waves, in general are attributed to most of the destructive force encountered during earthquake motions, especially for sedimentary basins. This observation indicated, not only the existence of an additional solution to the wave equation, but also that it must be confined to the surface, where its energy is dispersed more slowly than the P and S-wave attenuation.

Rayleigh waves come from the coupling of SV and P waves by discontinuities in a medium. The particle motion is confined to a vertical plane parallel to the direction of propagation and with amplitudes vanishing with depth. The amplitude of both vertical and horizontal motion, as well as the coupling phase and ratio of the two components depends on several factors: frequency content of the wave, depth of propagation and the existence of higher order surface wave modes.

Unlike Rayleigh waves, which can exist on the surface of a homogenous (in terms of propagation velocity) semi-infinite medium, Love waves require layering of the medium to be present, in order for the seismic energy to be trapped between the free surface and the velocity discontinuity at depth. Love are comprised of SH-waves, trapped in the superficial layer. Multiple reflection from the lower layers of the layer facilitate wave propagation. Particle motion due to a Love wave is constrained within the horizontal plane and its transverse to the propagation direction.

The normal components of elastodynamic stress produced by wave motion must disappear at the Earth's surface. By forcing this boundary condition to the wave equation, the following expression involving the Rayleigh wave velocity (V_R) results (Beker, 2013):

$$\mathbf{0.125} \left(\frac{V_R^2}{V_S^2}\right)^3 - \left(\frac{V_R^2}{V_S^2}\right)^2 + \left(\frac{2-v}{1-v}\right)\left(\frac{V_R^2}{V_S^2}\right) - \frac{1}{1-v} = \mathbf{0} \qquad (2.6)$$

The above solution can have three roots; however, the Rayleigh wave velocity must correspond to the real root in the range $0 < \frac{V_R^2}{V_S^2} < 1$. The other two roots are related to physically impossible conditions, such as surface wave amplitude that increases with depth. Therefore, in conditions such as wave propagation through soils the velocity of Rayleigh waves is lower than the velocity of the shear wave.

With depth, due to the difference in velocity of the P and SV component, the P and SV-wave amplitudes decay exponentially with different decay factors, given by q and p respectively:

$$q = \sqrt{1 - \frac{V_R^2}{V_P^2}}, for\ the\ P-wave\ component \qquad (2.7)$$

$$\mathbf{p} = \sqrt{1 - \frac{V_R^2}{V_S^2}}, \textbf{for the SV} - \textbf{wave component} \qquad (2.8)$$

(Rayleigh, 1885) gives the horizontal and vertical displacements based on the solution of the wave equation and the above decay factors. The amplitudes of both components vary with time, depth and horizontal distance from the source. The variation of horizontal and vertical displacement with depth are given in Figure 2.3
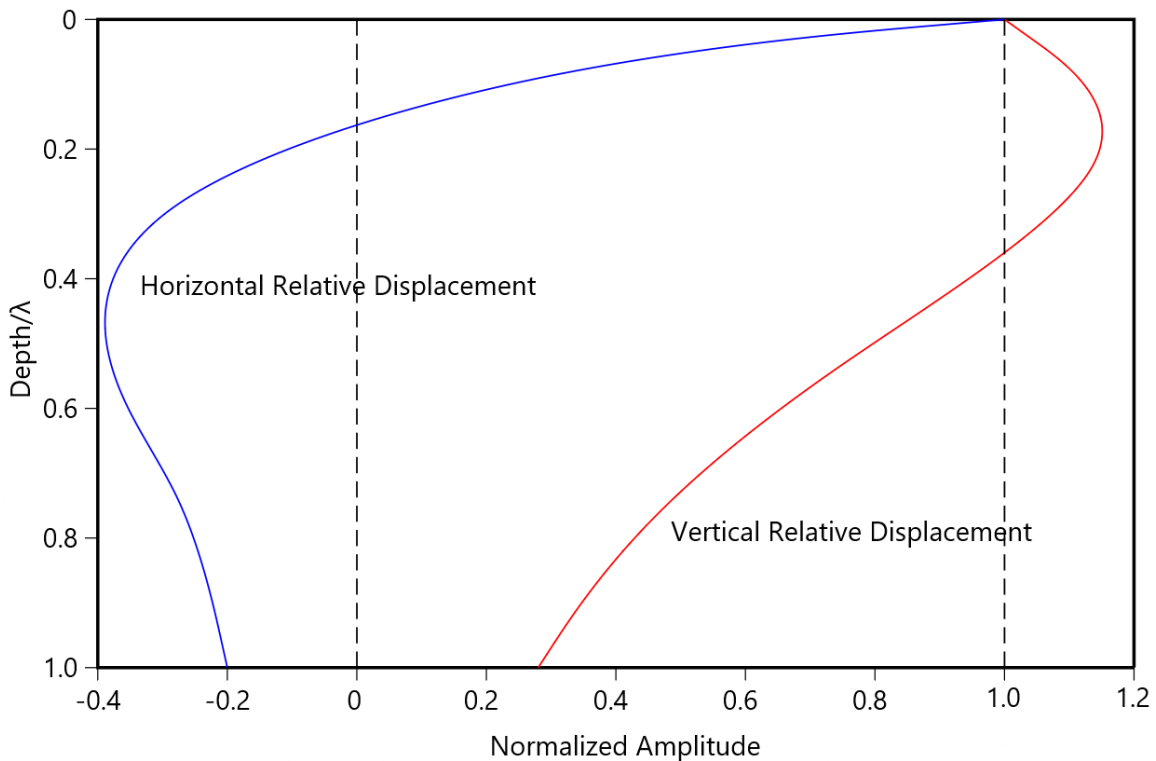
Figure 2.3: Vertical and horizontal displacements of a Rayleigh wave in homogeneous half-space. λ is the Rayleigh wave wavelength. After (Yoon, 2005)

The particle motion of a Rayleigh wave on the surface traces an ellipsoid that is in a plane parallel to the propagation direction. The particle motion, for a wave travelling left to right, is counterclockwise, a motion that is referred to as retrograde (clockwise rotation is prograde). With depth the amplitude of the horizontal motion decays faster and at a depth of around $0.2\lambda_R$ the sign changes, and the motion becomes prograde. This change in ellipticity has a frequency dependence, that is due to a phase lag in either the vertical or horizontal components of the motion at a distance from the source. If no lag is present, the particle motion is described by a diagonal, linear displacement, whereas at 90° lag between horizontal and vertical components the equation for displacement describes circular motion.

Based on (Foti, 2000), who investigated Rayleigh wave propagation and generation using numerical simulations for a homogenous medium the following general conclusion are important to note:

- Rayleigh waves are present within a given depth of the free surface and their travel is confined to a limited depth nearly equal to one wavelength (Figure 2.4)
- The ratio between the velocities of Rayleigh waves and shear waves is a function of the Poisson ratio within a small range (0.87 to 0.96).
- Particles undergo retrograde elliptical motion at the surface with possible change in ellipticity of the motion with depth
- For a source on a surface source circular footing 60% of the input energy goes into surface waves and the rest into body waves

Rayleigh surface waves for most seismic surveys are generated using vertical seismic sources (Park et al., 2007)
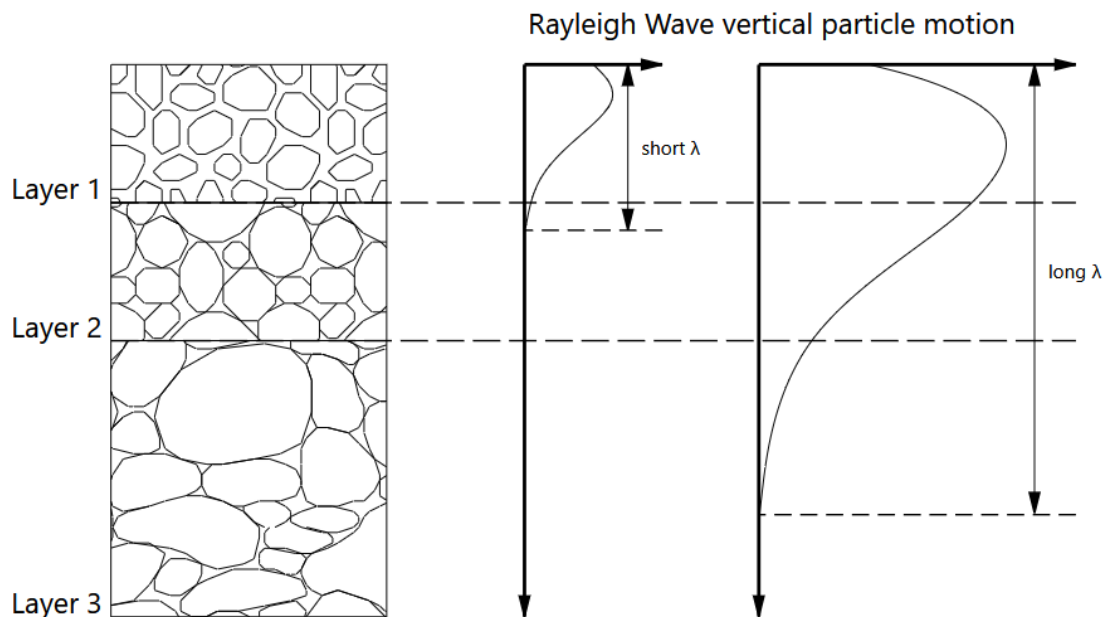
Figure 2.4 Illustrative vertical particle motion due to Rayleigh wave with different wavelengths

2.2.3.1 Dispersion of Rayleigh waves

For a homogenous half-space, the Rayleigh wave has propagation velocity slightly lower than the shear wave. However, for a homogeneous half-space, it is non-dispersive, unlike Love waves which are dispersive, provided they can exist, which is not the case for a homogeneous half-space, as Love waves require a large contrast boundary. For layered soil structure Rayleigh waves are dispersive. Each wavelength of a dispersive wave has a different propagation velocity called the phase velocity and it mainly depends on the P and S wave velocities, density and Poisson's ratio (Yoon, 2005). Lower frequency components penetrate deeper, have greater phase velocity, and higher frequencies have lower phase velocity and are more sensitive to the physical properties of the near-surface layers. The Rayleigh wave propagates in several discrete modes. The phase velocity c, and the group velocity V_g for each mode depends on frequency and are related:

$$c = V_g \left[1 - \frac{f}{c}\frac{dc}{df}\right] \tag{2.9}$$

If no dispersion is present, then the phase and the group velocities are equal. If the phase velocity is decreasing when the frequency increases, then the phase velocity is greater than the group velocity, and that is called normal dispersion (Al-Husseini et al., 1981).

For layered, gradient or generally inhomogeneous media the phase velocities of the Rayleigh wave modes (fundamental and higher) are frequency dependent. (Harkrider, 1970, 1964) developed the analytical models for the generation and propagation of Rayleigh and Love waves in more complicated multilayer elastic strata and the higher modes that exist in these cases. Each wave mode, characterized by a wavenumber, has a specific phase velocity. Therefore, the effective measured phase velocity is a combination of the different modes. Since each mode involves a different distribution of displacement with depth, the phase velocity has a spatial dependence and there exists mode separation as the wave propagates further from the source. The conditions for multiple surface wave modes propagation has been investigated by (Angel and Achenbach, 1984) leading to the conclusion that multiple modes of propagation are due to constructive interference between transmitted and reflected waves.

For soil stratigraphy with increasing shear wave velocity with depth, the dispersion profile exhibits a strong fundamental mode. In all other cases, multiple modes can be present. In general, it is very difficult to estimate which mode will dominate the dispersion, and over the measured frequency range the transition from one dominant mode to another is often observed (Gucunski and Woods, 1992)

Based on synthetically generated Rayleigh waves (Gribler et al., 2016) proposed a technique to determine the instantaneous particle motion on the Rayleigh wave front. The technique is based on polarity muting, a process of modifying the recorded traces, by selectively nulling sections where prograde or retrograde motion is recorded. This technique was shown to achieve better isolation between fundamental and higher modes, resulting a more coherent dispersion curves and more accurate shear wave velocity estimation.

2.2.3.2 Effects of Surface Topography and Sloping Bedrock

As it is claimed by (Ohtsuki and Harumi, 1983), Rayleigh waves are generated by incident SV waves near the toe of the slope and then propagate along the surface towards the crest of the slope. It has also been stated that the generated Rayleigh waves behind the slope crest can have an amplitude of up to 35%-40% compared to that of the incident waves. The patterns of topographic effects rely upon the geometry of the irregularity and upon the types, frequencies, and angles of incident waves (Sánchez-Sesma et al., 2011)

A homogenous soil, sloped surface numerical model was developed by (Zhang et al., 2018). The slope topography model was subjected to wavelets with different frequencies and the acceleration amplification along the surface was evaluated. They showed significant changes in the acceleration amplification factor due to variations in the slope angle, slope height, signal frequency and signal cycling. The ratio between the slope height and the wavelength can significantly affect not only the amplification amplitude but also the location where the largest amplification is observed. With an increasing number of cycles, the amplification values increased and secondary peaks of the curve of acceleration amplification were produced, which also increased with an increase in the number of cycles of input motion.

(Messaoudi et al., 2012) used 2D finite element modelling to establish the relationship between three parameters: slope angle, ratio between slope height and wavelength and the relative depth to bedrock and site amplification. Their conclusion is that in most cases topographic amplification is much lower than site amplification, i.e. the shape of the low velocity basin surface has a much smaller effect as compared to the depth characteristics of the layer. Additionally, they noted:

- The topographic effects are affected by the slope angle
- For steep slopes the horizontal motion at the crest of the slope and along the upper surface varies greatly
- An amplification-deamplification of the response is observed on short distance (comparable to the dimension of structures) from the crest.

2.3 Geophysical methods for field investigations

2.3.1 Introduction

Direct observations (drilling, trenching, excavations, CPT, SPT, etc.) are a very reliable source of subsurface information; however, are limited to sampling a small volume of the site under investigation and often are very difficult to use in highly urbanized areas. Additionally, even in rural areas, these methods can be very expensive and time consuming. Indirect measurements are in contrast, cheaper and much faster to perform. The advantage of geophysical methods is that they can discover hidden structures and features inaccessible to direct observation and inspection. Near-surface investigations using geophysical methods can be a challenging task, particularly in urban and industrial environments. Such environments, however, are prone to high levels of natural seismic noise and anthropogenic vibrations. In urban areas, traffic movement, and transportation infrastructure often imposes a limitation on the ability to perform geophysical tests. Moreover, subsurface geological strata may have a complex structure (inclined layering, voids, weak layers overlaid by stronger layers and sand lenses), it can be disturbed by infilling materials or covered by asphalt and paved surfaces. This can make sensor installation and data interpretation challenging. Despite these difficulties, if correctly

designed and implemented, geophysical methods can provide essential information and detailed images of subsurface structures for infrastructure planning, site characterizations, mine development and exploration, among others.

2.3.2 Active source methods

These are a set of in-situ tests/methodologies that are used to evaluate soil stratigraphy and composition. The common requirement for all of them is that an active source (sledge hammer, weight drop, air gun, etc.) is used to excite the soil at a test site and the response to the excitation is recorded by either one sensor, a spread of sensors or an array. Recording can be done on the surface, or in a borehole. In all cases these methods take advantage of Snell's law, and use modelling to infer the soil structure for the test site.

Spectral analysis of surface wave (SASW) and multichannel analysis of surface wave (MASW) are both very common, quick and inexpensive techniques for soil characterization. Both generate the dispersive profile by measuring the propagating surface waves at different points along the ground surface, using a different number of receivers. In either case, once the dispersion profile is acquired, an inversion procedure is required to establish a corresponding soil layering profile.

The inversion process iteratively estimates a dispersion curve based on an assumed initial V_s profile. Two different approaches are generally used for the inversion: forward modeling and least-squares estimation. The forward modeling assumes a profile, computes the theoretical dispersion curve and then compares it with the empirical (Stokoe et al., 1994). The assumed profile is then perturbed until there is a good match between the theoretical and empirical dispersion curves, this is the approach used in the KGS software package SurfSeis (KGS, 2019). In the case of the implementation in Geopsy (SESAME Geopsy Team, 2019), multiple models are evaluated at once, and at each iteration step, one or a few of the models are chosen to be refined further in the next step of the process. In the least-squares inversion the algorithm tries to optimize the difference between the theoretical and empirical curves in least-squares sense, using the model parameters (Vs, thickness, density and Poisson) to adjust the model (Nazarian et al., 1983; Nazarian and Stokoe, 1983; Rix and Leipski, 1991).

2.3.2.1 Spectral Analysis of Surface Waves (SASW)

This method was first developed by (Heisey et al., 1982; Nazarian and Stokoe, 1983).The SASW method utilizes an active source: sledgehammer, explosive charge, etc. and two receivers to record the generated seismic waves. Many studies were undertaken to improve the experiment requirements and data processing techniques (Al-Hunaidi, 1993; Gucunski, 1992; Heisey et al., 1982; Hiltunen and Woods, 1990; Stokoe et al., 1994).

Figure 2.5 shows the general setup for a SASW test. By using only two receivers to measure Rayleigh wave dispersion several problems arise in the use of this technique (Chen et al., 2004; Zywicki, 1999):

- To acquire data relevant to different depth, multiple tests with different spacing need to be performed.
- Separation of surface waves modes is very difficult
- In the presence of near-field interference, noise removal is less reliable, when only using two receivers.
- Attenuation characteristics are harder to obtain, as multiple points are measured at different times.
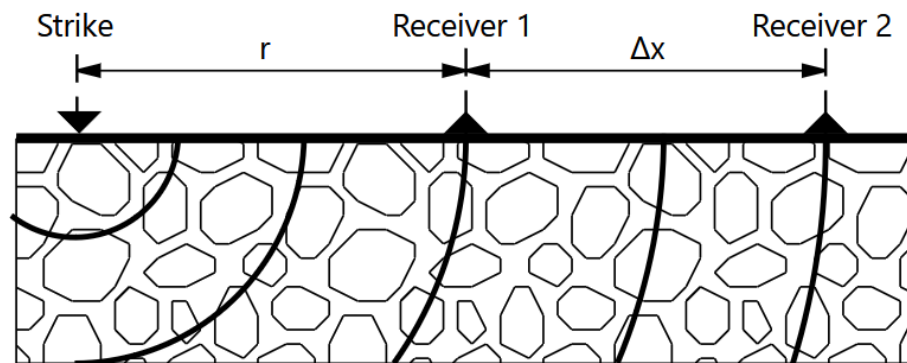
Figure 2.5: Simplified diagram of the SASW test setup

The method relies on the interpretation of the phase characteristic of Rayleigh waves at both receivers. The difference in phases between the two receivers is related to the wavelength of the Rayleigh wave, $\lambda_R(f)$ by:

$$\lambda_R(f) = \frac{2\pi\Delta x}{\Delta\phi(f)} \tag{2.10}$$

Where Δx and $\Delta\phi$ are the receiver spacing and phase difference between the receivers, respectively. To obtain the Rayleigh wave velocity for a given mode (f_k) the following equation can be used:

$$V_R|_{f=f_k} = f_0\lambda_R(f_k) \tag{2.11}$$

One of the main limiting factors of a SASW investigation is the source-receiver and inter receiver distances. Depending on the desired investigation depth the spacings between the receivers and the distance to the source may need to be changed several times. Thus, requiring multiple and repeated tests prolonging the investigation. The tests will also require that the source be placed on either side of the receivers to cover any phase shifts due to receivers and instrumentation and layer sloping (Nazarian et al., 1983).

Spatial aliasing can occur depending on the inter-receiver spacing and theoretical studies (Hunt, 2005) suggest that the source distance should be equal to the receiver spacing:

$$\lambda_{R,min} = 2\Delta x \tag{2.12}$$

$$r = \Delta x \tag{2.13}$$

This only applies in the case of ideal plane wave propagation, however that is not achievable in most realistic scenarios. (Chen et al., 2004) demonstrated that the receiver separation, for a given wavelength, depends on Poisson ratio, and saturation state of the soil.

A study by (Brown, 2002) demonstrates that in many situations the SASW method can provide subsurface information suitable for site response predictions, confirming the results and predications using borehole investigations, with the SASW models showing higher velocities in the surficial layers.

2.3.2.2 Multichannel Analysis of Surface Waves (MASW)

The MASW method, is an extension to the SASW, utilizing, in the general case, a linear array of receivers. It was popularized by (Park et al., 1999). The method utilizes frequency-wavelength transformation to extract the phase information of the multi-channel record. The phase velocities obtained this way are then used as the target of an iterative inversion algorithm that adjust a soil model to match the output (see Figure 2.6). The soil model consists of number of layers, each with its own shear wave velocity, Poison's ratio, density and thickness. Two MASW techniques have been proposed by (Park et al., 1997) The first one uses a vibratory source to excite Rayleigh waves and the second utilizes an impact or impulse source. Recently, the inversion of passive recordings (MAM), where the Rayleigh wave is due to microseismic noise has been proposed (Park et al., 2007). Each technique uses different type of source and data processing technique to generate the dispersion curve. The main difference between the passive and active mode of MASW, is that passive experiments show clear dispersion at frequencies lower than the impact or vibratory MASW for the same site. In terms of depth, MAM could penetrate deeper (more than 30 m) compared with the MASW, as demonstrated by (Nazri et al., 2016).

MASW surface wave method was used by (Miller et al., 1999) along with precision drilling to establish high-resolution bedrock and surficial profiles. Roll-out was used to acquire multiple profiles 4ft apart and it additionally demonstrated insensitivity to cultural noise.

The one dimensional shear wave velocity model resulting from the inversion process is an average of the soil structure beneath the geophone spread, and it is reasonable to assign the model to below the middle of the geophone spread (Khaheshi Banab and Motazedian, 2010)
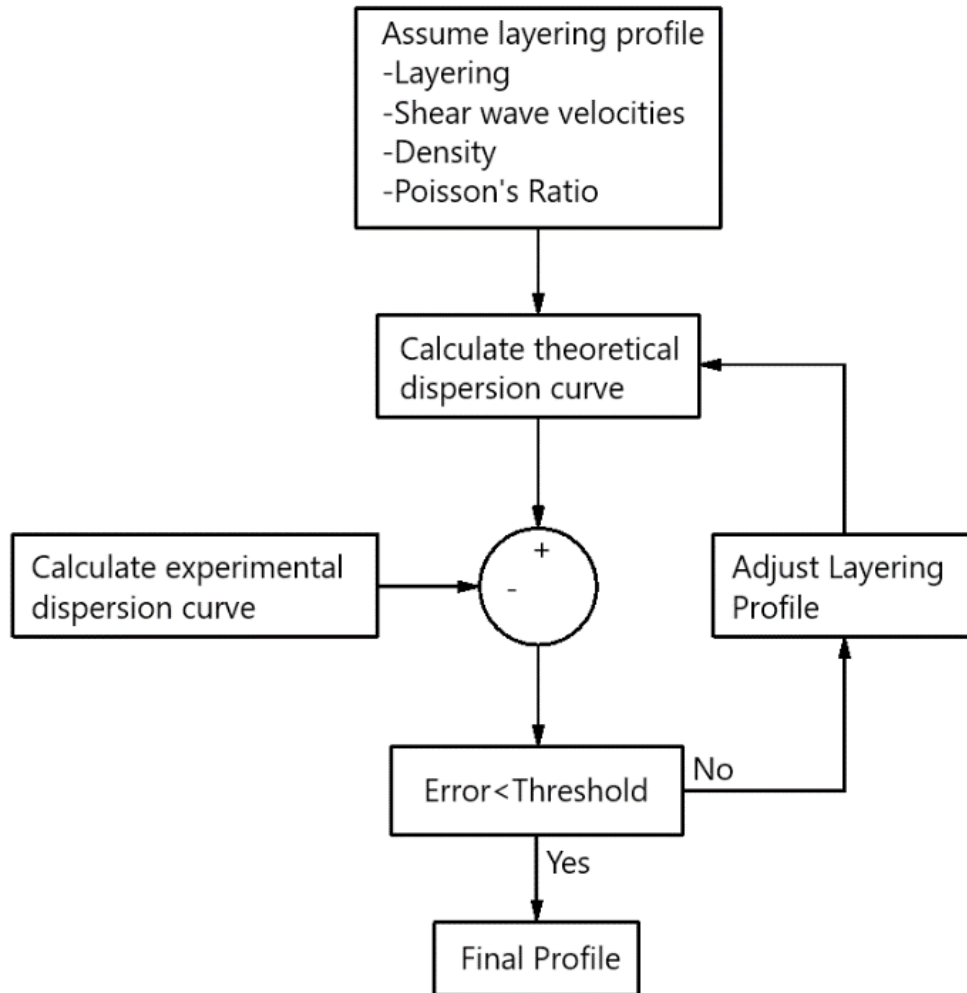
Figure 2.6: Simplified diagram of the MASW inversion algorithm

The typical setup of the MASW test is shown in Figure 2.7. The distance between the source and the first receiver, generally determines the affected depth, as the generated wave can propagate to deeper layers. The inter-receiver distance determines the overall resolution of the resulting dispersion and soil profile. The shortest wavelength surface wave that can be extracted from a MASW data set is equal to the geophone spacing. Similarly, to SASW the possible spatial aliasing should be considered.
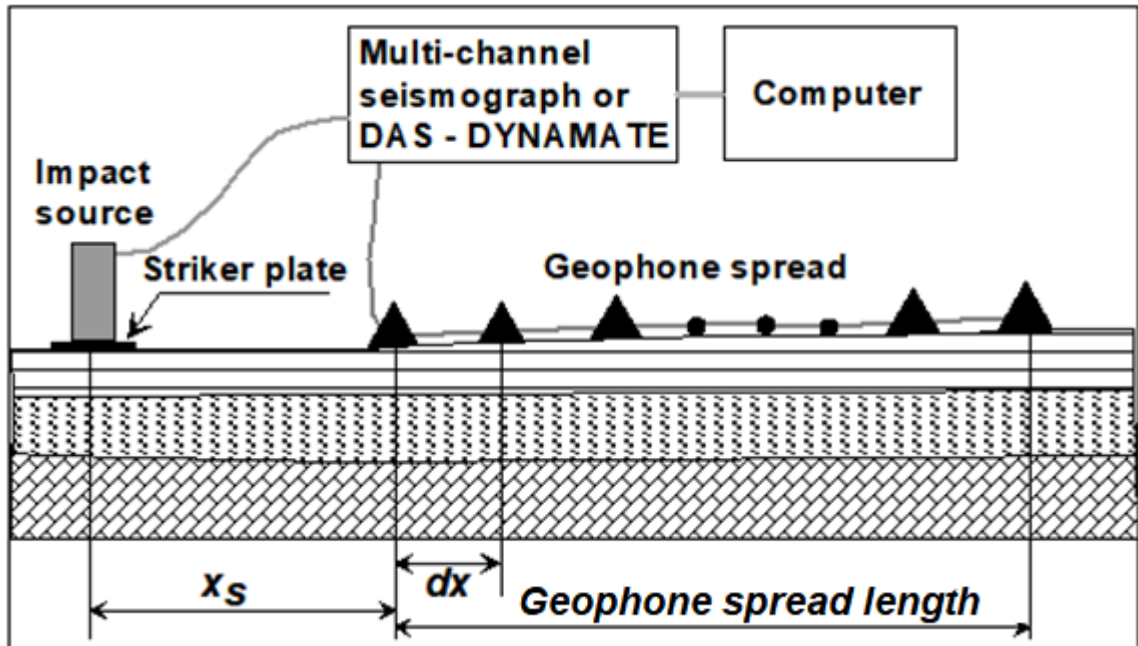
Figure 2.7: Geneal MASW experimental setup

The volume of bedrock engaged in transmission of incoming incident waves depends on the wavelength, thus at greater depths the amount of bedrock mobilization is large, as the depth of engagement of Rayleigh waves is directly proportional to the period of motion (*Vs/4H*). The result is a horizontal averaging of the soil mass, which will smooth the acquired profile in relation to the theoretically expected.

To analyze the influence of the inclined soil layers (Evangelista and Santucci de Magistris, 2015) used a finite elements model for normally dispersive two layer soil profile with slope interface between 5% and 25%. They proposed a correction procedure to correct for a known slope and obtain a more reliable shear wave velocity from MASW studies.

Since the SASW method requires a smaller source-receiver offset range to evaluate *Vs* to a given depth it is better suited for experiments where there is limited space available, or lateral heterogeneity can be expected. However, the MASW method can evaluate soil profiles based on higher modes of Rayleigh waves, unlike the SASW method, where multiple modes can result in ambiguous interpretations of the results. (Roesset et al., 1991) proposed mode inversion technique that allows the SASW method to compensate for multi-modal content in some cases.

2.3.2.3 Estimation of the dispersion curve

The wavefield transform method is used to generate the dispersion curve based on the data recorded by MASW. The shot-gather, $U(x, t)$, is composed of the stacked records from all receivers where x is the receiver offset and t is time. Fast Fourier transform is applied to the shot gather and the result is express in terms of amplitude and phase (Khaheshi Banab and Motazedian, 2010; Park et al., 1997):

$$U(x, \omega) = \int U(x, t) \, e^{i\omega t} dt = A(x, \omega) P(x, \omega) \qquad (2.14)$$

Where $A(x, \omega)$ is the amplitude spectrum and $P(x, \omega)$ is the phase spectrum. If $P(x, \omega)$ contains the phase dispersion and can be expressed in terms of phase velocity c:

$$P(x, \omega) = e^{-\frac{\omega}{c} x} \qquad (2.15)$$

$U(x, \omega)$ is then normalized by its amplitude and the following transformation is applied:

$$V(x, \varphi) = \int e^{-i\varphi x} \left[\frac{U(x, \omega)}{|U(x, \omega)|} \right] dx = \int e^{-i\left(\frac{\omega}{c} - \varphi\right)x} \left[\frac{A(x, \omega)}{|A(x, \omega)|} \right] dx \qquad (2.16)$$

Where φ is the transform parameter, equivalent to an offset specific phase shift. The resulting function $V(x, \varphi)$, which is the summation over all offsets, has its maxima at points where $\frac{\omega}{c} - \varphi = 0$, therefore the locus of all peaks for different values of the angular frequency ω forms the dispersion curve.

Another method, the frequency-wave number (F-K) method, is based on the imaging of the stacked seismic energy in FK space. Detailed description and methodology for the FK transformation and processing is given by (Capon, 1969; Gal et al., 2014), where the implementation performs the slowness estimations individually for each frequency bin and sums the resulting slowness spectra over a specific frequency range. (Zhang et al., 2003) demonstrated that the FK method provides estimation of the apparent velocity rather than fundamental mode velocity, which will introduce an error in the inversion process results, and thus an inaccurate soil profile.

2.3.3 Passive methods

Passive surface-wave methods can be divided into multi-sensor measurements and single station measurements. With multiple sensors, methods like beamforming (Lacoss et al., 1969), spatial autocorrelation using a circular array (SPAC) (Capon, 1969), which has seen a lot of development recently, most notably (Ohori, 2002) allowing the use of non-circular arrays and (Bettig et al., 2001), which improved the method to include arbitrary shape arrays. The array methods are generally used along with inversion procedures to establish shear wave velocity profiles.

The most common single station method is the Horizontal to Vertical Spectral Ratio (HVSR) and is based on the ratio of the microtremor Fourier spectra in three component measurements.

Analysis of earthquake records or strong motion records is generally considered the more reliable and fruitful approach to study site effects (Borcherdt, 1970; Lermo and Chávez-García, 1994, 1993). However, in recent time due the significant difference in setup times and cost, seismic noise methods have been gaining popularity. (Bonnefoy-Claudet et al., 2006b; Cornou et al., 2004; Martin et al., 2017) give a detailed review of many studies employing these methods and provide guidelines for the analysis and data collection.

2.3.3.1 SSR

Site response is generally determined by the spectral ratio method using a reference station (Bard and Riepl-Thomas, 2000). Because it has provided consistent results (Field and Jacob, 1995; Frankel et al., 2002) the standard spectral ratio technique (Borcherdt, 1970) is most commonly used. The technique takes the ratio of the component spectra at the surface and spectra at bedrock or at the reference site. The ratio can be defined using all three components or just horizontal or vertical components. One important precondition for using the SSR technique is the availability of a reference (bedrock) site with negligible site response, close to the considered soil site. Without a reference rock station more recent techniques have been developed (Drouet et al., 2008; Lermo and Chávez-García, 1993), however these techniques are not universally applicable. In some studies seismometers

installed in boreholes are used instead of the rock reference station (Rong et al., 2019; Tsuboi, 2001). The use of a borehole, can in some cases reduce the effect of P and S wave mode conversion at layer interfaces closer to the surface, however it is still less reliable than the standard SSR, and subject to the assumption that the recorded spectra and their ratio are only applicable to small strain conditions.

HVSR can be used for the assessment of possible reference sites for SSR. For rock sites with flat HVSR curves or no reliable and small HVSR peaks usually indicate good locations for reference sites.(Koller et al., 2004)

2.3.3.2 HVSR

The HVSR or Nakamura method makes use of the horizontal-to-vertical spectral ratios (HVSR) of seismic noise records to provide a reliable estimate of the dominant frequency of a layered subsoil structure. The method was based on developments in the 1950s and subsequently on techniques used to evaluate site dynamic characteristics using earthquake and other strong motion records (Nakamura and Samizo, 1989). The reliability of the fundamental (dominant) period estimation using HVSR has been very well established in literature and field studies, however the amplitude of the resulting spectral ratio remains a somewhat controversial point in the scientific community. This lead (Nakamura, 2000) to refer to the ratio as the quasi-transfer function of the site (QTS). In many cases, especially at sites showing large amplification, the maximum value of the HVSR spectral ratio may be considered as an estimate of ground motion amplification (Arai and Tokimatsu, Kohji, 2000; Mucciarelli et al., 2003) while in others it underestimates true site amplification (Bard, 2004; Haghshenas et al., 2008)

The HVSR ratio is defined based on single three component station recordings: S_Z, S_{NS}, S_{EW}, the vertical and two horizontal components, respectively. The total horizontal component is calculated using the vector average:

$$\boldsymbol{HVSR} = \boldsymbol{QTS}(\boldsymbol{\omega}) = \frac{\sqrt{S_{NS}(\omega)^2 + S_{EW}(\omega)^2}}{S_Z(\omega)} \qquad (2.17)$$

When there is a strong impedance contrast in the soil stratigraphy, seismic noise HVSR gives very reliable estimates of the fundamental frequency, especially when the site has large amplification (Horike, 2001). Where these conditions are not met, HVSR results may be unreliable and sometimes misleading, multiple peaks and broadening of the peaks are often encountered. For the cases with a simple singular spectral peak (Tsuboi, 2001) conclude that the HVSR can be used for the estimation of the site response, implying that for simple structures the vertical component will not be affected. For more complex peak structures, thicker deposits should be expected.

In general, having a good estimate of the shear wave velocity (V_s) at the site is a major requirement for obtaining an accurate estimation of the depth to bedrock (H) using the fundamental frequency (f_0) obtained by HVSR (Kramer, 1996):

$$H = \frac{(2n+1)V_s}{4f_0} \qquad (2.18)$$

Where the n denotes the resonant mode, with $n=0$ giving the fundamental. The HVSR method used in the multi-modal investigation of (Martin et al., 2017) was found to be useful for identifying shallow-rock sites and for evaluating the relative variability of the depth-to-rock. Rock and shallow sediment sites are generally more challenging to characterize than deep sediment sites. Especially in cases where weather bedrock outcrops are encountered, mode conversion at the interface between the intact and weather rock leads to non-flat HVSR curves. (Bonilla, 2002) studied this effect and concluded that the vertical component has significant site responses associated with it due to S-to-P mode conversions at the weathered granite boundary.

(Mucciarelli and Gallipoli, 2001) suggest that during any field measurement the wavefield composition is uncertain and it is unknown exactly which kind of waves are used in the HVSR technique, nevertheless a good estimate of elastic soil behavior can be obtained when strong direct S-waves are present.

The purpose of trying to use microtremor HVSR as a technique for evaluating amplification caused by soft soil is utilitarian: Microtremors are always present and single-station

techniques are easy to implement. However, several major problems exist in terms of interpretation of HVSR results:

- Large proportion of the wavefield of microtremors is surface waves, specifically Rayleigh waves, and the HVSR will be affected by the change of particle motion with frequency. When the vertical motion of the Rayleigh wave disappears for a given frequency the theoretical HVSR will have an infinite peak at that frequency, and a trough (minimum) will appear for the frequencies where the horizontal motion is zero.
- HVSR records near slopes, such as basin edges, and at the toe or crest of sloped surface topologies will reflect additional Rayleigh wave scattering and generation from discontinuities in the topography, affecting the measured HVSR amplification factor.
- In many studies, the benchmark that is used for the verification of the HVSR results is the SSR or the HVSRe (HVSR applied to earthquake data). Both have issues, i.e. for earthquake data it is important to note the window of time used to calculate the ratio, and special care should be taken in terms of which waves are captured in the analysis. In the case of SSR it is often difficult to find suitable reference sites, without detailed geological knowledge of the area and previous in-situ studies. Moreover, for both reference methods, large nearby events (especially ones resulting in surface ruptures) could produce a much different distribution of wave energy for the different components of the wavefield, and thus result in a very different excitation pattern at the site.
- If the seismic event is large enough, it is reasonable to expect that soil will act in a nonlinear fashion, making it impossible to apply any linear response-based reasoning. And since the HVSR method relies on ambient noise, which can only be associated with very small strain in the linear range of the soil. Soil dynamics predicted using the method are only suitable for evaluation of low-magnitude motion.

2.3.3.2.1 Assumptions and interpretation of HVSR curves

Uncertainty in the scientific community is present in the interpretation of the source of the peak with the literature being split between statements that the HVSR is due to Rayleigh ellipticity present on the studied site's surface or that the estimated amplification factor is

caused by multiply refracted/reflected incident SH waves. The assumptions behind either of these descriptions of the HVSR are:

- If the HVSR peak is due to Rayleigh waves, the microtremor must consist of purely fundamental mode waves (Bonnefoy-Claudet et al., 2006b).
- If the peak is due to multiple SH reflections, the vertical motion does not undergo a similar process, thus the ratio describes the SH fundamental frequency of the site (Nakamura, 2009, 2000).

(Rong et al., 2019) Show that one of the principle assumptions behind Nakamura's method: that the H/V ratio at the bedrock is equal to unity does not always hold true. The difference between borehole ratios and surface HVSR is closely related to the level of P-wave amplification, which is frequency dependent. Therefore, equality should exist in cases where P amplification is negligible. Moreover, (Tsuboi, 2001) used borehole recorded seismograms of several earthquakes and indicate that the vertical component of the S wave at the surface is unaffected by the site response, and that the assumption may be true only for simple surficial velocity structures. In general, it is found that the spectral peaks of HVSR and surface-to-borehole ratios at around 3 Hz agree well, and the agreement becomes worse at higher frequencies.

By using numerically generated synthetic waveforms for SH, SV, and P waves with non-vertical incidence (Kawase et al., 2011) have shown that HVSR of observed earthquake strong motion records should agree with the predictions from 1D diffuse wave field theory. Differences in the observed HVSR and the theoretically predicted ratios can be due to incomplete constraints on the analytical model. However, this means that the inversion can be used to obtain the velocity structure, if the HVSR of either the S wave portion or the coda of strong motions is used. This in effect confirms (Nakamura, 2000) assumption that S wave interference is the cause for the HVSR peak, with surface waves acting to alter the amplitude and Q factor of the peak, depending on the energy and frequency distribution of the motion. Additionally, (Nakamura, 2000) demonstrated that Rayleigh wave energy is small for the observed peak frequency, and it is therefore unlikely that the HVSR peak is due to the Rayleigh component of microtremors.

The interpretation of the HVSR peaks is dependent on the distribution and composition of the seismic ambient noise. This composition is in turn dependent on the type, source and direction of the wave as well as the subsurface structure between the recording site and the source. Finally, different wave types will have different effects on the HVSR (Acerra et al., 2004).

Based on numerical modelling and data from the Ottawa area (Motazedian et al., 2011) demonstrated that the fundamental frequency obtained from the HVSR microtremor measurements represents a linear soil response. A higher level of motion causes a significant shift the fundamental frequency to lower frequencies. This can be explained by a reduction in the shear modulus due to the large strain, and corresponding decrease in the shear wave velocity.

2.3.3.2.2 Amplification factor and site effects

In some studies, the amplification factor of the site effect is estimated as the equal to the amplification factor obtained from HVSR (Arai and Tokimatsu, Kohji, 2000; Mucciarelli et al., 2003). However, a detailed study into the relationship between the HVSR peak and site amplification done by (Bonnefoy-Claudet et al., 2006b) based on a large set of HVSR, SSR and borehole data determined that in general the HVSR peak underestimates site amplification, More recent studies have confirmed that finding (Chávez-García and Raptakis, 2017; Pilz et al., 2009).

(Kawase et al., 2018) calculated the horizontal-to-vertical spectral ratios from observed microtremors as well as those of observed weak earthquake ground motions and compared predominant peak frequencies and amplitudes at these peak frequencies of the microtremor and earthquake HVSR with those calculated theoretically from S-wave velocity models based on the diffuse wave concept. Comparing them it was found that they share similarities but have significant differences in their shapes. Using logarithmic spectral smoothing (Konno and Ohmachi, 1998) demonstrated that HVSR peak of microtremors can be directly related to the site amplification factor, and for the case where the proportion of Rayleigh waves in the microtremor is 40%, the two are equal.

HVSR has been used with earthquake records (Field and Jacob, 1995; Lermo and Chávez-García, 1993) or with seismic noise records (Bard, 1998; Jamroni et al., 2017; López Casado et al., 2017). Reviews of these techniques have been presented in (Chávez-García and Raptakis, 2017). No difference was observed between HVSR obtained from strong motion records and HVSR from ambient microtremor noise in the study by (López Casado et al., 2017).

(Nakamura, 2009) The presence of strong Rayleigh wavefield, the peak of HVSR is altered/reduced. This may explain why in most studies HVSR amplification gives a lower bound of the amplification factor for the site.

Based on simulations and literature review (Bonnefoy-Claudet et al., 2006a) concluded the following regarding the shape and composition of the HVSR curve based on the location of the microtremor sources:

- If ambient noise sources are in the bedrock, HVSR peaks are due to multiple S wave reflections and refractions
- If ambient noise sources are far from the recording station and inside the low-velocity overlying layer the HVSR can present with up to two peaks. In the latter case, one peak is most likely due to the fundamental Rayleigh mode and the second to S wave resonance.
- If ambient noise sources are close to the recording station and inside the low velocity overlying layer the HVSR presents a single peak due to horizontal ellipticity of the fundamental mode of Rayleigh waves.

The effect of distance of the source on the HVSR peak depends on the relative distance as compared to the depth to bedrock. In general, for cases where the source is closer than twice the depth to bedrock, refraction of the wave fronts will prevent them from affecting deeper layers before being received. In this case only shallower impedance contrast will be represented in the HVSR. For further distances, wave propagation can involve deeper layers. This will result in a better defined HVSR peak at the fundamental frequency, associated with the bedrock interface. Additionally, the amplitude of the H/V peak was

shown to be very sensitive not only to the velocity contrast, but also to parameters such as Poisson's ratio in the sedimentary structure (Lachetl and Bard, 1994).

If surface wave effects are to be included in the HVSR generation, then in general a peak trough structure is to be expected. The location of both the peak and the trough are governed by the surface wave ellipticity (Love wave and higher modes Rayleigh waves). (Stephenson, 2003) suggests that the presence of a peak/trough structure in a microtremor-derived HVSR is an indicator of extreme site amplification. (Fäh et al., 2001) using theoretical models concludes that the first trough in the HVSR signaled a predominance of Rayleigh waves in the noise records and is preceded by a peak at lower frequencies.

2.3.3.2.3 HVSR slope effects

The effects and interaction between slope topography and input seismic motion for sloped surfaces is investigated by (Zhang et al., 2018). The authors use an elastic, homogeneous soil model combined with a Gabor pulse type source applied vertically to the surface of the model. By varying model parameters, the effects of slope angle, height and curvature are analyzed for the single layer homogenous model. Additionally, the properties of the source pulse, i.e. frequency, number of cycles and pulse shape, are varied to observe the resulting amplification. The results demonstrate that amplification tends to 1 at long distances after the crest of the slope, however significant differences are observed for the different parameter combinations of the slope and pulse shape. The major contributing factor is the relation between slope size and input wavelength. The other significant result is where the peak of the amplification function occurs after the crest of the slope. This location is determined by the value of the critical reflection angle from the slope. Past this angle, reflected waves from the slope can reach the upper ground surface, rather than be parallel or sub-parallel to it. This wave front introduction results in a shift of the maximum value of amplification further away from the crest. The exact location depends on the wavelength, slope height and crest/toe curvature, however these only come into effect once the critical angle is exceeded. The maximum amplification factor increases substantially with the number of cycles of input motion.

(Guéguen et al., 2007) found that the fundamental peak frequency of the microtremor HVSR curve does not agree with the peak of the fundamental-mode Rayleigh wave H/V spectrum in areas, where irregular subsurface structures occur. The microtremor HVSR peak shape broadens in areas with irregular subsurface structures (Uebayashi, 2003).

Numerical simulation done by (Cornou et al., 2004) of noise in 1D and 3D structures is used to investigate the possibilities and limits of the HVSR technique, under the assumption that the HVSR is generated from fundamental mode Rayleigh wave. For HVSR ratios obtained over slopes in the model it is found that HVSR peaks are less pronounced and broader as compared to the flat sections of the model; and that the amplitude is significantly different than the theoretical 1D local value.

2.3.3.2.4 Data Processing for HVSR

Most common issues encountered during acquisitions and processing of the HVSR spectral ratio are due to spurious peaks present in the spectrums of either the vertical or horizontal or both raw spectra. To this end many researchers have utilized the smoothing functions given by (Konno and Ohmachi, 1998). Others however approach the problem differently, i.e. using a boxcar smoothing filter or in general a fixed width window that is convolved with the spectrum to achieve smoothing. Doing this results in good reduction of spurious peaks at lower frequencies, however higher frequencies tend to be more variable and contain more spurious peaks. This can sometimes lead to erroneous conclusions and peak determinations.

Depending on the location used for HVSR data collection, near sources may dominate the record. Such sources, i.e. traffic, wind on structures, etc., contribute to the resulting shape of the HVSR curve, by adding more energy from near surface impedance contrasts, and may mask the fundamental peak or alter its amplitude. (Mihaylov et al., 2016) proposed a method for signal separation due to nearby strong sources, such as traffic wind, etc. and microtremors. The technique is based on a threshold of the time-domain energy envelope of the signal.

One of the major problems surrounding the HVSR technique is that there is not a general agreement about a standard for data collection and processing. This makes comparing the

HVSR technique with other methodologies or with models difficult. Most publications do not go into the details of which equipment was used, or any specifics of the methodology applied during the data processing stage. There are multiple views about which seismic phases we are dealing with and interested in, nevertheless we can obtain a satisfactory estimate of elastic soil behavior in the presence of direct S waves.

The most widely accepted guideline for HVSR data acquisition and analysis are the specifications given by the SESAME team (Acerra et al., 2004; Koller et al., 2004) which outlines some general requirements for reliable HVSR data acquisition and analysis:

- Data Acquisition System configuration needs to reflect the frequency range of interest at the expected amplitudes, clipping of channels should be avoided but the gain needs to be as large as possible to reduce the effects of electronic noise on the measurements.

- Sensor Installation – sensor coupling and leveling at the site can have a large effect on the obtained HVSR curves.

- Optimum window length, which is a function of the lowest expected fundamental peak and is recommended to contain at least 10 periods at the lowest frequency of interest.

- Number of windows used in the analysis to obtain statistically significant results - usually 100-200 windows.

- Spectral smoothing – most commonly the (Konno and Ohmachi, 1998) logarithmic smoothing function.

- Combination of the two recorded horizontal components into one horizontal vector – geometric mean is the most common approach.

- Averaging should be applied on both H spectra and the V spectrum, not on the resulting H/V spectral ratio.

Data collection may require very long recordings (>30min), or at least several recordings at the same site with combined duration enough to cover a large number of cycles of the lowest expected peak frequency. Since weather conditions and time of day have significant

effects on HVSR data collection (Acerra et al., 2004; Koller et al., 2004) measurements need to be designed to accommodate for these effects.

2.3.3.3 Microtremor array methods for subsurface evaluation

For the analysis of surface waves from ambient vibrations, a planar sensor array is typically deployed, and array processing techniques are employed. Most of the array processing techniques in use assume planar wave fronts. Two main categories off methods for estimation of soil velocity profiles are found in literature: Spatial Auto-Correlation Analysis (SPAC) (Claprood, 2012; Vidal et al., 2016) and frequency wavenumber analysis/decomposition (FK) (Capon, 1969; Huang and Wu, 2008; Satoh et al., 2001). Both methods are shown to be effective, with FK analysis in general applicable to vertical and both horizontal wavefield components. (Horike, 2001) analytically demonstrated that if the velocity structure can be adequately evaluated based on the vertical microtremor dispersion curves, then the recorded microtremor must mainly consist of S waves.

A method that uses maximum likelihood estimation to account for all three components of microseismic recordings is presented by (Maranò et al., 2012) and includes Rayleigh and Love velocities and directions as well as polarization in the analysis resulting a method for extraction of Rayleigh and Love waves from array measurements of ambient noise. This allows for the establishment of dispersion curves and ellipticity vs frequency relationships for both Rayleigh and Love and their various modes present in the recordings and is an improvement to the standard FK method.

An extension of the modified spatial autocorrelation method (MSPAC) is described by (Köhler et al., 2007) describes on three-component array analysis and its application to seismic ambient vibrations. Using both synthetic and field measured data the dispersion curves for both Rayleigh and Love wave fundamental modes are obtained to within a frequency band comparable to the array size and reliably used for the estimation of subsurface structure. Forward computation of fundamental and higher mode Rayleigh wave dispersion curves then allows for identifying correctly the dispersion curve branches of Rayleigh waves. This is crucial for using advanced inversion scheme that include fundamental and higher modes.

In an effort to determine landslide susceptibility of study area (Yuliyanto et al., 2017), used HVSR ellipticity inversion to obtain a Vs profile with depth. They used a modified neighborhood search algorithm for the ellipticity inversion. This is similar to other recent studies that have demonstrated the evaluation of S-wave velocity profiles from the inversion of HVSR only (Arai and Tokimatsu, 2004; Fäh et al., 2003) or joint inversion of the HVSR spectra with dispersion curves obtained at the site (Arai and Tokimatsu, Kohji, 2005; Picozzi, 2005)

2.4 Site Effect and Ground Motion Prediction Equations

The empirical prediction of ground motion from future earthquakes is based on an assumed seismic source model, propagation parameters and site conditions. Ground Motion Prediction Equations (GMPEs), i.e. (Bozorgnia et al., 2014) are used to establish expected peak ground velocities (PGV) and peak ground accelerations (PGA) at a site for a given earthquake size and epicentral distance. The independent variables in the GMPE invariably include magnitude, source-to-site distance and some parameterization of local site conditions, and often the fault mechanism that initiated the event. Commonly, GMPEs are empirically derived from the regression of recorded strong motion data. Typical GMPE expression without the error term is given as (Boore and Atkinson, 2008):

$$lnY = F_M(M) + F_D(R_{JB}, M) + F_S(V_{S30}, T_0) + \varepsilon\sigma_e(V_{S30}, R_{JB}, M) \quad \textbf{(2.19)}$$

where Y is the response variable, F_M, F_D, and F_S are respectively: the magnitude scaling, distance function, and site amplification function. M is moment magnitude, R_{JB} is the Joyner-Boore distance (closest distance to the surface projection of the fault plane), V_{S30} is the average shear-wave velocity to a depth of 30 m and T_0 is the period. σ_e represents the aleatory uncertainty, which is due to random, natural variability in earthquake processes and by (Atkinson and Adams, 2013) is approximated by a single frequency-dependent model. ε is the standard deviation of the predicted value around the mean of lnY.

The distance function F_D given by:

$$F_D(R_{JB}, M) = [c_1 + c_2(M - M_{ref})] ln\left(\frac{R}{R_{ref}}\right) + c_3(R - R_{ref}) \quad \textbf{(2.20)}$$

$$R = \sqrt{R_{JB}^2 + h^2} \qquad (2.21)$$

Where c_i, h, M_{ref} and R_{ref} are coefficients determined empirically by a regression.

The magnitude scaling function depends on the fault geometry as well the hinge magnitude M_h, which is used as a shaping parameter:

$$F_M(M) = \begin{cases} e_0U + e_1SS + e_2NS + e_3RS + e_4(M - M_h) + e_1(M - M_h)^2, for\ M \leq M_h \\ e_0U + e_1SS + e_2NS + e_3RS + e_6(M - M_h), for\ M > M_h \end{cases}$$

$$(2.22)$$

Where *U, SS, NS,* and *RS* are used to specify unspecified, strike-slip, normal-slip, and reverse-slip fault types, respectively. Parameters e_i are regression coefficients.

The site amplification function is given as a sum of the non-linear and linear amplification functions scaled to the reference site condition ($V_{ref} = 760\ m/s$) and it depends on the period T_0:

$$F_S(V_{S30}, T_0) = b_{linear}(V_{S30}, T_0)\ ln\frac{V_{S30}}{V_{ref}} + b_{non-linear}(V_{S30}, T_0)\ ln\frac{PGA_{760m/s} + 0.1g}{0.1g}$$

$$(2.23)$$

Where b_{linear} and $b_{non-linear}$ are amplification coefficients as determined by (Seyhan and Stewart, 2014).

GMPEs for eastern North America were initially developed by (Atkinson and Boore, 1995) using a stochastic point source model with the source and attenuation parameters empirically determined from small to moderate earthquake data. There have been several modifications of these GMPEs resulting in the set proposed as addition of the NBCC 2015 (Atkinson and Adams, 2013). They were defined for a reference site condition of B/C boundary ($V_{S30} = 760$ m/sec) with nonlinear amplification factors to convert from reference site condition to softer site conditions (Atkinson and Boore, 2006). It is accepted that a significant source of uncertainty comes from the conversion of GMPEs from hard-rock to B/C boundary (Atkinson, 2008). (Tremblay et al., 2015) describes the (National Research

Council of Canada. Canadian Commission on Building and Fire Codes, 2015) guidelines for the selection and scaling of ground motion time histories for both linear and nonlinear structural dynamic response analysis.

GMPEs have significant effect on the result of probabilistic seismic hazard analysis (PSHA), and particularly the site effect term and uncertainties associated with it are the reason for large uncertainties in the resulting uniform hazard spectra (UHS). V_{S30} is used as both the simplified classification of the site in terms of its seismic response in the building codes (National Research Council of Canada. Canadian Commission on Building and Fire Codes, 2015) and as variable for the site amplification term in the GMPEs (Atkinson and Adams, 2013; Bozorgnia et al., 2014). A significant amount of variation of ground motion remains after removing site effects predicted solely by V_{S30} . (Stewart et al., 2012, 2012) performed a review of site parameters used in GMPEs for all major tectonic domains and found that single-value site parameters generally have shown to better performance than V_{S30}.

Currently, data for V_{S30} is much more widely available for various sites, however one alternative parameter that has been considered is the site period. Site classification and empirical relationships have been developed suggesting that it could be used as a replacement (Ghofrani and Atkinson, 2014). Another alternative for the site response if HVSR. It was found that HVSR is comparable to V_{S30} and that it is more descriptive for sites with deep deposits. Additionally, HVSR is usually easier to obtain than V_{S30}.

With pushing towards including longer periods in the building code, and HVSR as a replacement predictor in place of V_{S30}, the need for accurate and reliable analysis of HVSR curves at lower frequencies becomes more important.

2.5 Conclusions

Dynamic soil parameters are important during the design and retrofit phases of any infrastructure project. In many cases, these parameters are difficult to obtain, and where precise parameters values are required, laboratory tests need to be used. As in-situ and

laboratory obtained parameters may differ greatly, field measurements are an important part of site characterization and soil parameter estimation.

Recently, using a single-station microtremor measurement, many site investigation studies are published about horizontal-to-vertical (H/V) spectral ratio as a method for characterization of shallow subsurface (Bard, 1998; Bonnefoy-Claudet et al., 2006a; Fäh et al., 2001; Lermo and Chávez-García, 1993; Lontsi et al., 2015). Another widely used method is the multi-channel analysis of surface waves (MASW), which utilizes inversion of the Raleigh wave's dispersion curve (Park et al., 1997). A common problem in research activity is related to the application of theoretical or numerical models to processes under real field conditions. In many cases unevenly distributed soil layers (slope in surface or bedrock topography etc.) produce effects difficult to explain with existing numerical and theoretical models. Similar problems appear in soil-structure interaction and behavior of the structure or buildings which are not properly build or damaged from previous vibration or earthquake shaking.

New approaches to site characterization, for example (Ghofrani and Atkinson, 2014) demonstrate that simple field tests, like the HVSR method can be applied to the problem of site characterization. The implication of this will be an increased interest in research and application of such methods, due to their simplicity and quick turnaround. Evaluation of the applicably of these methods for difficult or complicated sites is therefore required.

Chapter 3. Seismic Sensors

3.1 Introduction

Vibration measurement is an essential aspect of modern geotechnical engineering. It is particularly vital task for estimating dynamic soil parameters, estimating seismic hazards and evaluating influence of industrial, traffic and construction vibrations on the surrounding buildings, structures and their elements. Meanwhile, commercial exploration seismic stations and data acquisition systems require significant professional knowledge and training in geophysics or vibration measurement, as well as practical skills and experience in adjusting data acquisition parameters. Furthermore, available seismological investigation and vibrometry sensors are not universally suitable for field applications in geophysical studies, soil-structure interaction investigations or structural vibrations. The frequency range suitable for seismic studies and industrial vibration measurement vary from 1 Hz to 300 Hz with sensitivity corresponding to the expected vibration level. Therefore, the first part of this thesis was focused on developing an innovative data acquisition system and sensors that are easy to use in a wide range of field applications.

The design and development of geophone-based 3-component field sensors for the DYNAMate DAQ System is presented here. Detailed description of the design and development of the DAQ system itself is given in Chapter 4. A method for sensor element characterization, including the estimation of sensor parameters, such as the natural frequency, mechanical damping and generator constant using the impulse response of the sensor element is presented. Additionally, calibration procedures using shake-table a reference accelerometer and a linear variable displacement transducer (LVDT) are also implemented and discussed.

In many cases, geophones do not have a sufficiently large frequency response range to cover the needs of certain geophysical studies, such as HVSR. Instrument response correction, that extends the frequency range is required in such cases. The inverse filtering method is the most employed (Havskov and Alguacil, 2004), and this chapter presents an extension to the method, as well as its application in both the real-time and post-processing

applications. Based on the theory behind the software-based instrument response correction, a new 1 Hz geophone using 4.5 Hz elements is prototyped and tested.

3.2 Sensor types and applicability

The most common types of seismic sensors are seismometers, velocimeters and accelerometers. All three seismic sensor types measure ground motion and convert it into a voltage signal. The output voltage can be proportional to either displacement, velocity or acceleration. The measurement is done on an inertial mass suspended in a frame of reference.

Figure 3.1 shows a schematic of simplified seismometer that will detect vertical displacement of ground motion. A mass is suspended by a spring, which is attached to a fixed stiff frame, and the vertical movement is damped using a dashpot. The displacement measurement is shown as a ruler, which can be implemented using a linear variable displacement transducer (LVDT) or a capacitive transducer.
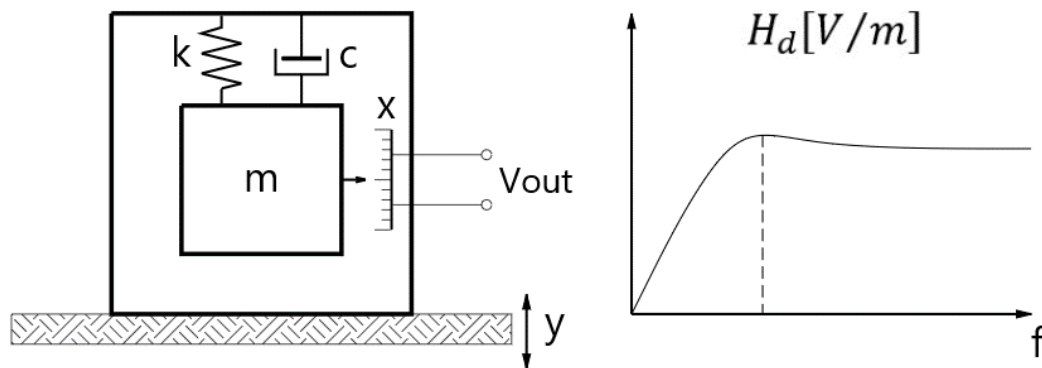
Figure 3.1: Simplified seismometer diagram and corresponding frequency response function

For sudden motions, i.e. high-frequency impulse, the mass will remain nearly stationary while the frame is displaced. Therefore, the frame displacement can be estimated as the reading on the ruler, which is related to the relative displacement between the mass and the frame. At high frequency vibration, a phase shift of 180° exists, since the base/frame moves up the measured relative displacement is negative. Thus, the seismometer measures relative displacement directly at high frequencies with a phase shift. At low frequencies, the mass

can follow the motion of the frame and the relative displacement no longer matches the ground motion, and the amplitude response decreases as the frequency decreases. At resonance, the mass will progressively move with larger amplitude, and therefore will have increasing displacement response. The maximum amplitude in this condition is limited by the amount of damping in the system.

Figure 3.2 presents a schematic of a geophone. It is similar to the seismometer with a few important differences. Instead of measuring the relative displacement, a geophone measures the velocity of the inertial mass utilizing a copper coil moving in a magnetic field. The inertial mass can be either a permanent magnet or a movable copper coil as shown in Figure 3.2. The motion of the coil with respect to the magnetic field induces a voltage proportional to the velocity of motion. Therefore, geophone produces voltage proportional to the first derivative of the relative motion. Performance is limited to the allowable travel distance of the inertial mass, i.e. the coil needs to be within the homogeneous part of the magnetic field to avoid non-linear output.
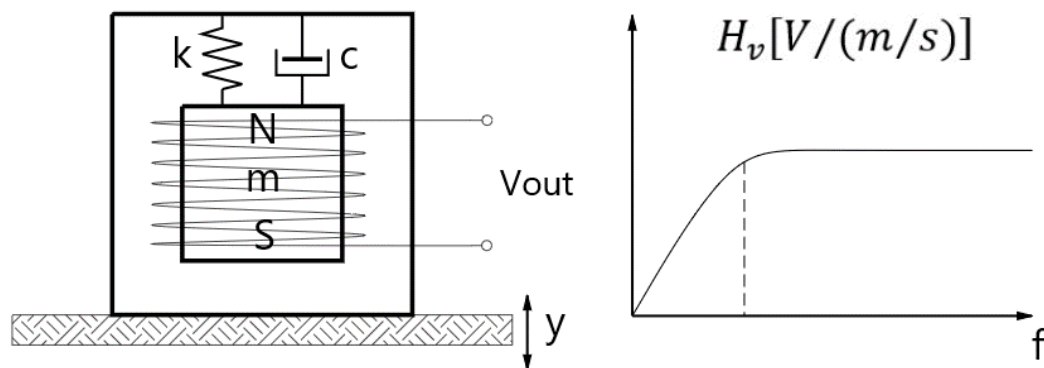
Figure 3.2: Simplified geophone diagram and corresponding frequency response function

Accelerometers, shown schematically in Figure 3.3, utilize passive piezo-electric transducers that give output voltage proportional to the applied force. The mass presses on the piezo-electric element which converts the reaction force into a voltage signal proportional to acceleration. The stiffness of the mass suspension is much higher than in a geophone or a seismometer. This allows such devices to measure motion down to 0 Hz; however, it introduces a sharp resonance peak at high frequencies.
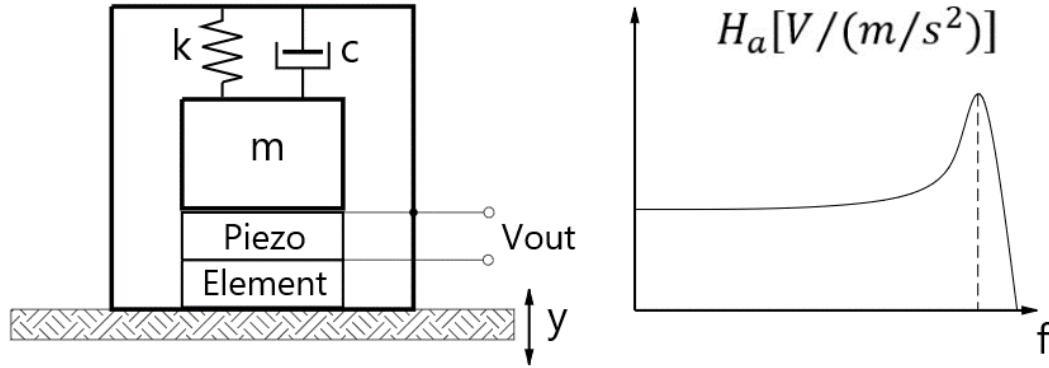
Figure 3.3: Simplified accelerometer diagram and corresponding frequency response function

Owing to the stiff mounting of the inertial mass, an accelerometer has a high natural frequency. For low frequencies, the amplitude of acceleration would generally be very small and high sensitivity devices are required. For example, studies by (Chatelain et al., 2008; Chávez-García and Tejeda-Jácome, 2010) show that seismic noise HVSR fails to identify amplification peaks below a frequency of around 1 Hz, due to the small amplitude of the input signal at such frequencies.

All three types of seismic sensors are single degree of freedom systems (SDOFs), and the motion of the inertial mass is defined by following general governing differential equation:

$$m\ddot{x} + c\dot{x} + kx = -m\ddot{y} \qquad\qquad (3.1)$$

Where x is the displacement of the mass with respect to the frame and y is the displacement of the frame as defined in Figure 3.1 with respect to an external stationary point. The parameters c and k are the damping and spring constants of the system and m is the mass of the inertial element.

For high frequency, the sensors linear responses are limited by spurious resonances and by their natural frequency. Due to the very stiff suspension of an accelerometer, it has linear response at very low frequency, theoretically down to 0 Hz. The amplitude of the transfer functions of each sensor type is given by:

For seismometers: $\quad |H_d(f)| = G_d \dfrac{\left(f/f_n\right)^2}{\sqrt{\left(1-\left(f/f_n\right)^2\right)^2+4h^2\left(f/f_n\right)^2}} \, [V/m]$ (3.2)

For velocimeters: $\quad |H_v(f)| = G_v \dfrac{\left(f/f_n\right)}{\sqrt{\left(1-\left(f/f_n\right)^2\right)^2+4h^2\left(f/f_n\right)^2}} \, [V/(m/s)]$ (3.3)

For accelerometer: $\quad |H_a(f)| = G_a \dfrac{1}{\sqrt{\left(1-\left(f/f_n\right)^2\right)^2+4h^2\left(f/f_n\right)^2}} \, [V/(m/s^2)]$ (3.4)

with natural frequency: $\quad f_n = \dfrac{1}{2\pi}\sqrt{k/m}$ (3.5)

and damping ratio: $\quad h = \dfrac{c}{4\pi m f_n}$ (3.6)

The generator constants G_d, G_v and G_a relate the output in Volts [V] and have the following units respectively: V/m, $V/(m/s)$ and $V/(m/s^2)$ The damped natural frequency is given by:

$$f_d = f_n\sqrt{1-h^2}$$ (3.7)

Existing low frequency seismometers are heavy and expensive. Most of them use a capacitive sensor or LVDT to measure the relative displacement between the inertial mass and the support. For field and industrial applications, this gives geophone type sensor several advantages over seismometers:

- Simple construction, well established manufacturing processes resulting in a cheap and reliable sensor element.
- Passive geophones do not require an external power supply, and therefore it is possible to connect them with long cables as well as wireless connections for farther reach.
- Outstanding noise properties – due to the minimum number of components the actual sensor has an inherent noise floor specified by vendors around $0.1 \, nm/\sqrt{Hz}$ (Collette et al., 2011).

For HVSR measurements, (Koller et al., 2004) suggests that accelerometers are too insensitive at low frequencies, and broadband instruments with periods larger than 20 sec take too long to stabilize after power-up and do not offer significant advantages to the standard 1 to 4.5 Hz velocimeter/geophones. However, if the HVSR peak is below the sensor natural frequency additional processing is required to verify its reliability.

The rest of this chapter is solely concerned with the characteristics of geophone elements and improvement of their original transfer functions for both seismic and industrial applications.

3.3 4.5 Hz Sensor design and Calibration

A compact 3 component seismic sensor was designed for the DYNAMate DAQ system (see Appendix A). The requirements for this sensor are as follows:

- Applicability of the sensor in both industrial and seismic studies
- Sufficiently wide frequency range for considered applications
- Ability to adjust and match the frequency characteristics of all 3 sensor elements
- Portability and ease of installation and calibration
- Low-power consumption
- Electromagnetic Interference (EMI) shielding in industrial applications

To satisfy these criteria, standard geophone elements were chosen. Available geophones have natural frequencies of 4.5 Hz, 10 Hz or 14 Hz for either the vertical or horizontal type elements. For this design, the 4.5 Hz option was selected. The generator constants, which is the coefficient that gives the voltage output to velocity input ratio, for this natural frequency range geophone vary between $20\ V/(m/s)$ and $35\ V/(m/s)$. The open-loop (mechanical) damping is between 0.45 and 0.65 and the inertial mass is around 11 g.

3.3.1 Sensor Element Characterization

It is important to obtain reliable parameters of the sensor element including internal resistance R_S, natural frequency f_n, open loop damping h_m, equivalent critical damping resistance *CDR* and generator constant *G*. Due to manufacturing variability, some differences can exist between sensor elements even from the same production run. Geophones are especially suitable for timing (kinematic) applications, such as seismic prospecting or MASW. The differences in performance parameters can be ignored in such studies. External circuitry is required to equalize the performance of the elements for precise dynamic measurement.

In most cases, shake-tables are used to establish these sensor parameters, however in some cases this testing method may not be applicable, i.e. lack of a shake table or a large number of sensors that need to be fully characterized. Here, a method for the estimation of these parameters based on the impulse response of the sensor element is described.

In the process of sensor characterization, several external damping resistors are used in order to establish different damping ratios for each element. The damping of a geophone element is controlled by an external resistor connected in parallel to the sensor element. The function of this resistor is to dissipate energy produced due to the motion of the inertial mass (usually coil) within magnetic field. The relationship between the resulting damping and the damping resistor is given by (Havskov and Ottemoller, 2010):

$$h = \frac{G^2}{4\pi(R_s + R_{shunt})f_n m} + h_m \qquad (3.8)$$

Figure 3.4 presents the circuit used for sensor characterization, which comprises the sensor element connected to 4 resisters R1, R2, R3 or R4, impulse resister R_IMPULSE connected to ground (GND) and analog-to-digital converter (ADC).
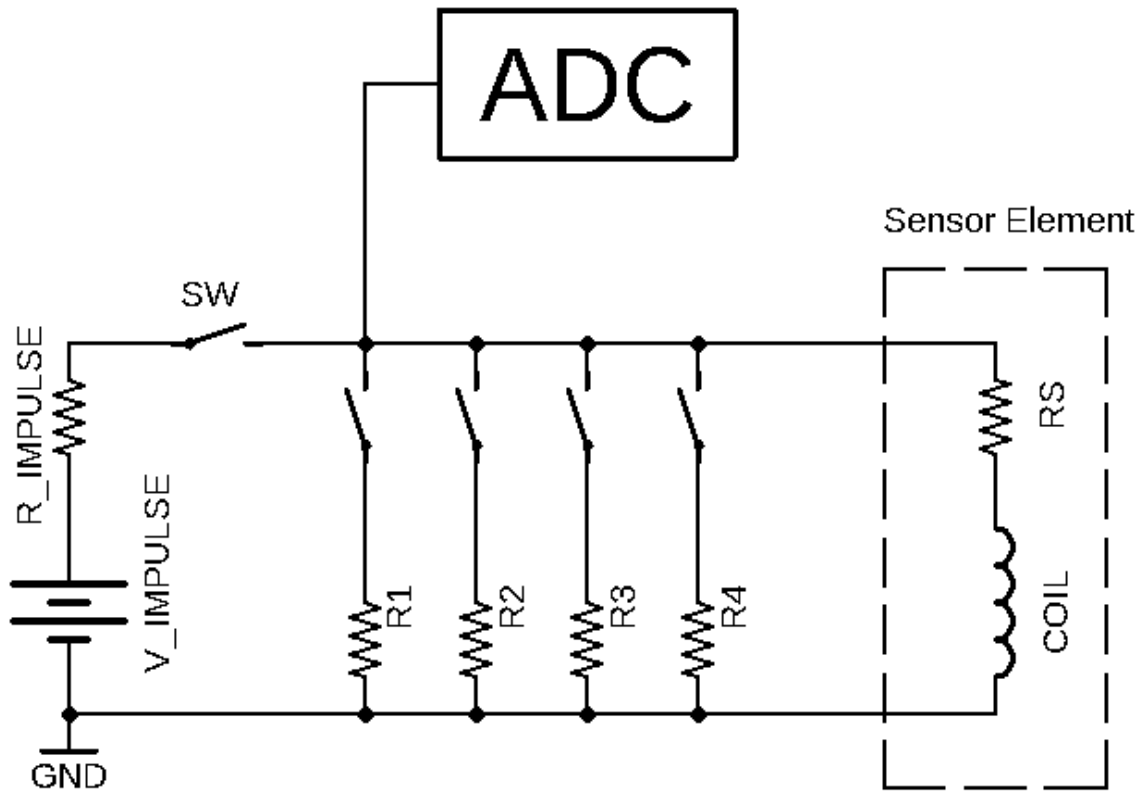
Figure 3.4: Sensor characterization schematic

The sensor characterization procedure can be described by the following steps:

Step 1 - generate the impulse response of a sensor element for different values of the damping resistor (R_{shunt}) using the circuit given in Figure 3.4. Only one or none (for open-loop parameters) of the resistors R1, R2, R3 or R4 is connected at a time to the sensor element (represented by a coil with internal resistance R_S). The connected resistor served as R_{shunt}, and in the case when all switches were open, only the ADC input resistance (~2MΩ) was damping the geophone element.

Step 2 - Using an external fixed voltage source and calibration resistor $R_{IMPULSE}$ a current pulse is sent through the copper coil; this induces a force on the geophone's mass resulting in a displacement. This current induced in the sensor coil depended on the value of $R_{IMPULSE}$ and generated a displacement of the inertial mass to a new position away from its equilibrium. $R_{IMPULSE}$ was adjusted for element type to eliminate the possibility of the

inertial mass exceeding its travel allowance (usually ~2mm). Once the external voltage source is disconnected the mass returns to equilibrium following the impulse response of a SDOF system, and the sensor output is recorded by the ADC. This transient voltage output is referred to as the 'off' impulse response. This process was repeated for an inverted voltage source to generate displacement in the opposite direction.

Ten impulses were recorded for each shunt resistor and polarity of the forcing impulse. Each impulse was generated by closing switch SW for long enough time that the element had enough time to settle and then opened to avoid acting as an additional damping resistor.

Step 3 – the impulse response records were filtered using a 32 Hz 8th order digital Butterworth low pass filter. Each 'off' impulse was identified and separated from the full record. Peaks recorded using inverted voltage source were flipped to match the positive configuration. A catalogue was formed with all recorded response peaks and the conditions for which they were recorded.

Step 4 – each recorded impulse response was fitted with the equation describing the impulse response of a SDOF system using non-linear least squares estimation. The parameters of the fitting operation (Figure 3.5) are the amplitude (*A)*, which depends on the value of the forcing voltage, phase lag (*φ*), to compensate for peak detection time misalignment, *B* is an offset value, the natural frequency of the sensor element f_n and the overall damping coefficient of the sensor/damping resistor combination (*h*). The SDOF impulse response equation given below:

$$|Response| = A \frac{2\pi f_n}{\sqrt{1-h^2}} e^{-h2\pi f_n t} sin\left(2\pi f_n t \sqrt{1-h^2} - \varphi\right) + B \quad \textbf{(3.9)}$$
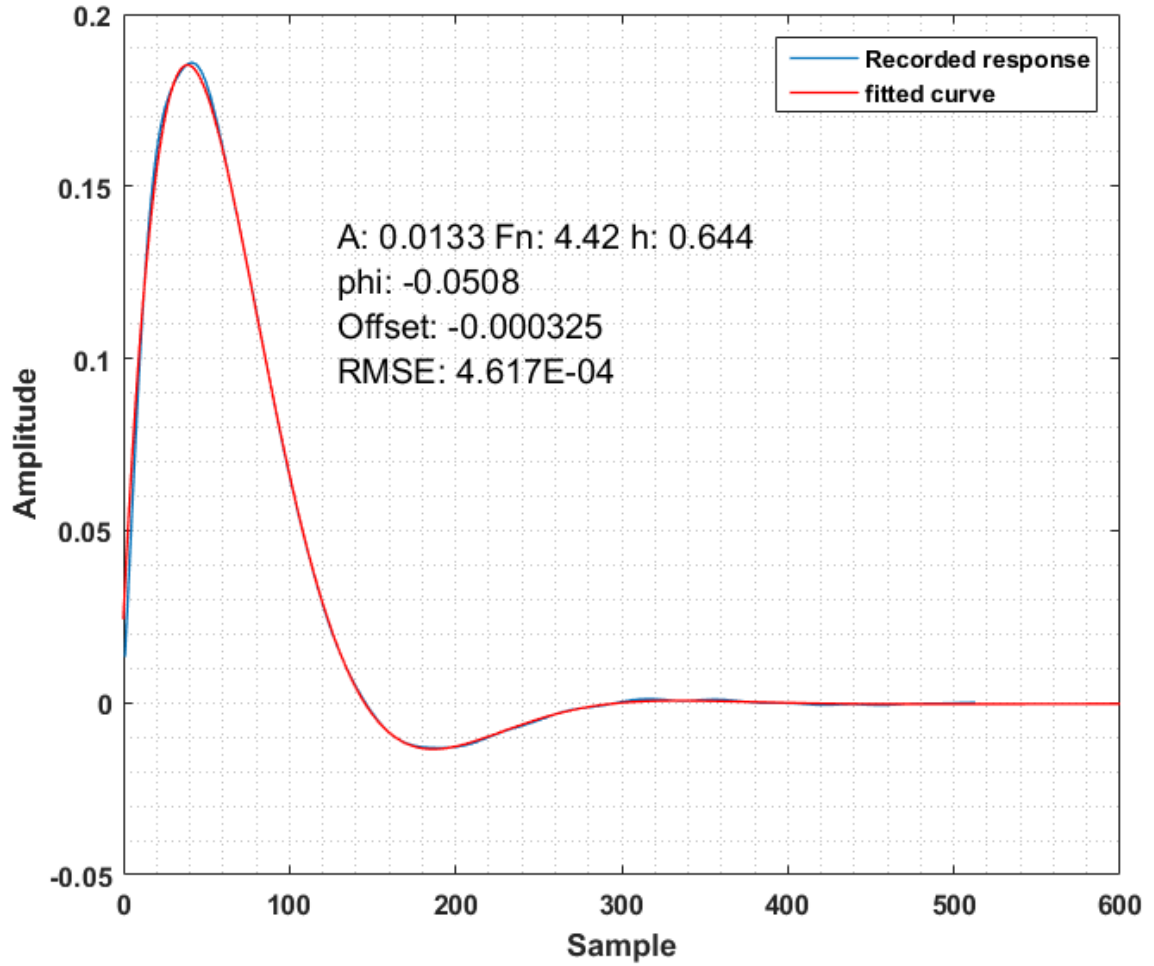
Figure 3.5: Impulse response estimation of a sensor element for a given value of the damping resistor

Step 5 –the parameters acquired for each value of damping resistor were combined and their variation was plotted vs the equivalent conductance given by:

$$\frac{1}{R_{eq}} = \frac{1}{R_s + R_{shunt}}$$

(3.10)

Where R_{shunt} is the connected damping resistor and R_s is the element's internal resistance as measured using a multimeter. Only the natural frequency and damping of

the resulting sensor/resistor combination is important here and for each impulse polarity (positive and negative) the resulting values are plotted in Figure 3.6.

Applying a linear regression to the combined results, using Linear Least Squares, results in the equations given in Figure 3.6. The equations relate the natural frequency and damping of each element to the applied shunt resistor value. These relationships are valid only for the geophone element used to produce the impulse responses, with large variations possible between different geophone elements. The values for damping coefficient for any given R_{shunt} can be estimated. In this case the required value for R_{shunt} for damping of 0.707 was calculated for each sensor element.
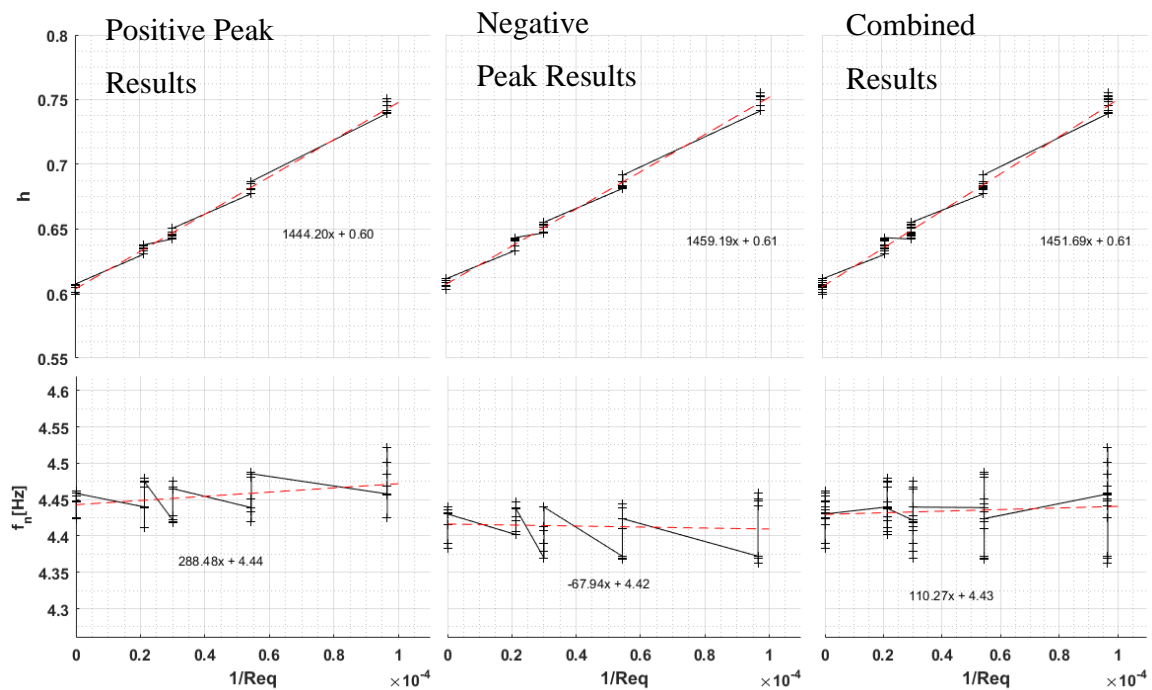
Figure 3.6: Example evaluation of sensor parameters from the sensor characterization procedure.

The natural frequency should remain constant for any value of R_{shunt}, and its value is estimated as the intercept of the linear fit of the total result, ignoring the slope present in the regression fit. This slope is most likely due to non-linearities in the sensor magnetic field as well as misalignment of the equilibrium position of the mass with respect to the magnetic field. The intercept of the damping line represents the mechanical damping of the sensor element (h_m) The critical damping resistance, CDR (i.e. R_{shunt} for which $h = 1.0$) is used to estimate the generator constant G_V (Havskov and Alguacil, 2004). It is defined as $CDR = R_{eq}\left(h_{R_{eq}} - h_m\right)/(1 - h_m)$.

This constant also depends on the inertial mass of the suspended coil; however, no non-destructive method is available to estimate its value, and therefore estimations rely on values published in the sensor elements data sheet. Generator constant also depends on the mechanical damping of the sensor (h_m):

$$G_V^2 = 4\pi(1 - h_m)CDRf_n m \tag{3.11}$$

This process allows the estimation of the natural frequency, damping and generator constant of any geophone element.

3.3.2 Sensor Element Conditioning

Figure 3.7 presents the passive 3-component geophone conditioning circuit, which was used to adjust the outputs of all three geophones that formed one 3-component DM 4.5 Hz sensor. The sensor elements were attached between X+/X-, Y+/Y- and Z+/Z-, and the outputs are taken differentially between OS1+/X-, OS2+/Y- and OS3+/Z-, for the three components, X, Y and Z respectively. Using the data obtained during sensor characterization, the available sensor elements were grouped together in sets with matching natural frequency. The damping was adjusted by resistor group Rx31, Rx32 and Rx33 combined in series with the potentiometer Rx21 according to the value of R_{shunt} required for total damping of 0.707. Potentiometer Rx21 was then used to match the overall generator constant between the elements and set its value to 20 V/(m/s).
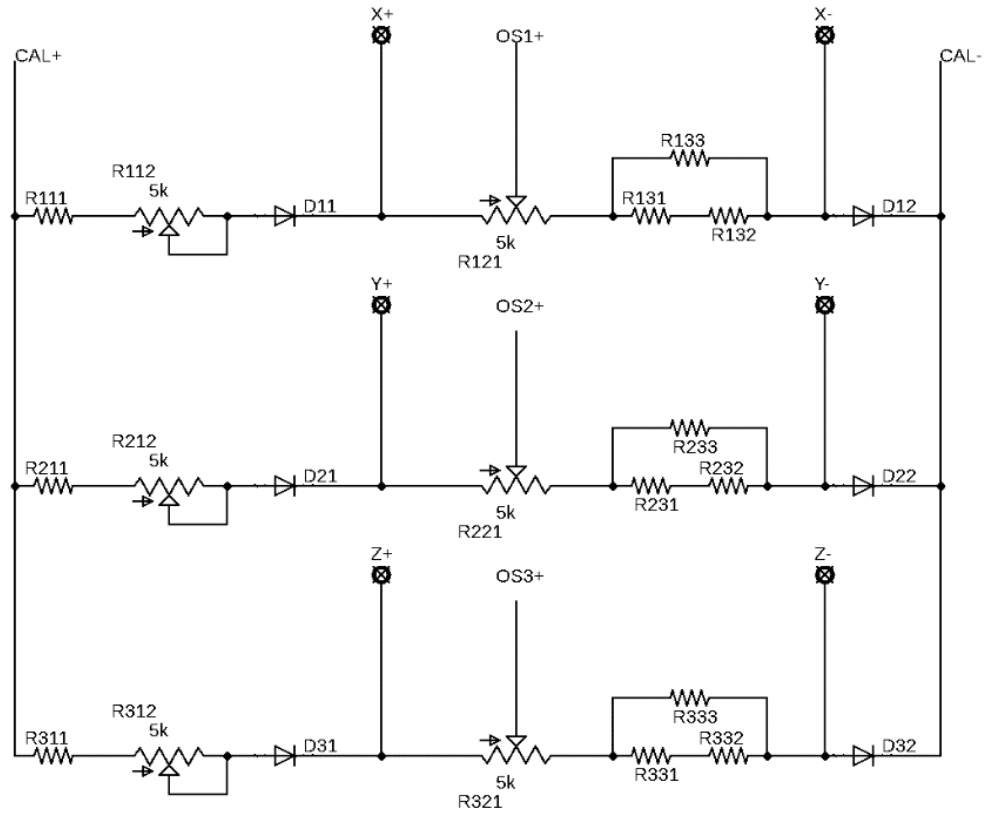
Figure 3.7: Passive 3 component geophone conditioning circuit

For verification and confirmation of calibration status, the lines CAL+/CAL- were used to apply a voltage across the geophone elements similar to the characterization process. The current that triggers the mass displacement is controlled by resistor Rx11 and trimmer Rx12. During normal operation both CAL+ and CAL- are left floating, i.e. not attached to a voltage source or any external resistance. The diodes in the schematic ensure proper current flow during calibration and prevent cross-connection between sensor elements.

3.3.3 Sensor Calibration

Each complete set of 3 geophones (2 horizontal and 1 vertical) had their resulting generator constants calibrated against a reference accelerometer on a shake table at a frequency of 10 Hz similar to the approach proposed by (Brincker et al., 2011). The velocity was calculated based on the amplitude of acceleration and calibration frequency and potentiometer Rx21 was adjusted until the overall generator constant of each sensor element was set to 20 V/(m/s).

LabVIEW based application was developed to accommodate the process of calibration. The software takes as an input both the sensor element output and the reference accelerometer output along with the known generator constant of the accelerometer.

A sine wave input voltage was applied to the shake table at a frequency of 10 Hz. The software acquired the frequency and voltages of both geophone element and accelerometer outputs and calculated the current generator constant for the geophone element. This value was used to adjust the output of the sensor in real-time and to achieve the generator constant 20 V/(m/s). This software is available on GitHub (Mihaylov, 2019a).

3.3.4 Three-component Sensor implementation

Based on the schematic given in Figure 3.7, field-ready three component, geophone-based sensors were constructed, referred to as DM 4.5 Hz (see Figure 3.10). An aluminum enclosure was designed and machined to specifications. The sensor elements were secured on an alignment platform, which was inserted into the aluminum body of the sensor and secured in place with casting silicone. Outputs of the elements were connected to the conditioning circuit PCB, designed as an integral part of the front lid of the sensor (Figure 3.8). A leveling bubble was installed in the sensor body to complete the assembly. The connector pinout is given in Figure 3.9.

Pin	Signal
A	Z-
B	X+
C	X-
D	Y+
E	Y-
F	N\C
G	CAL+
H	Cal-
J	N\C
K	Z+
L	N\C
M	N\C
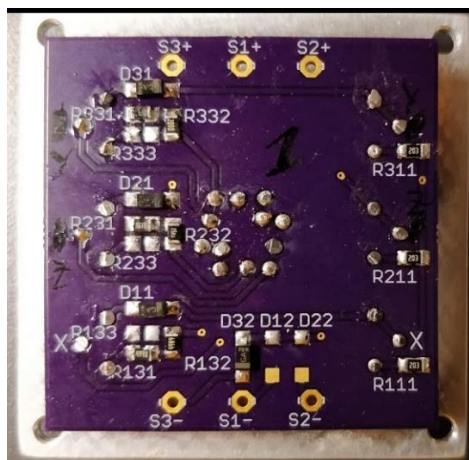
Figure 3.8: Sensor cap with condition circuit
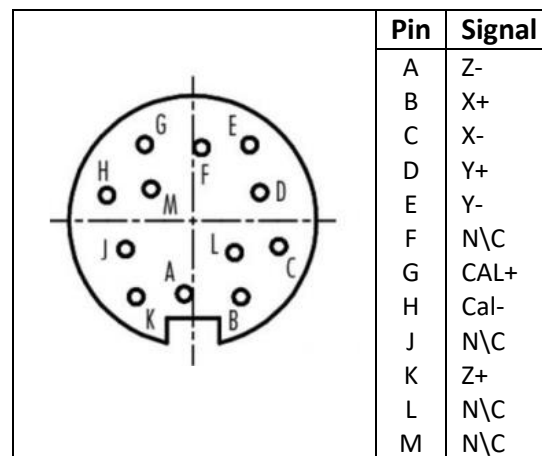
Figure 3.9: Sensor plug pinout
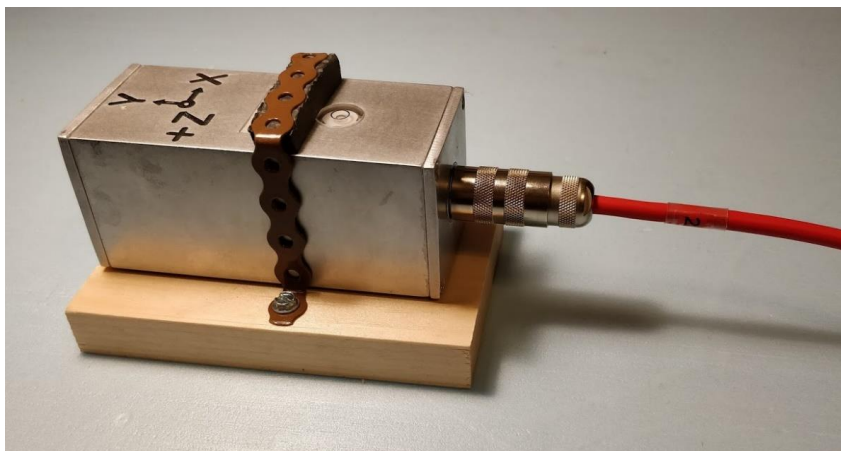
Figure 3.10: Completed sensor DM 4.5 Hz on a mounting platform

3.4 Software based sensor frequency range expansion

Waveforms recorded using geophones provide the vibration velocity limited by the working frequency range of sensor elements. Their voltage output is linearly proportional to vibration velocity for frequencies above the instruments' natural frequency. Below this frequency, there is no such simple relationship. The quantity of interest can be vibration velocity or displacement below the natural frequency of the sensor elements, and conversion of the recorded waveforms to cover the low frequency ranges of interest may be required. This procedure is referred to as instrument response correction (IRC).

The goal of IRC is the extension of the sensor element response towards longer periods. The simplest and most common way of extending the frequency response is to use the inverse filtering method (Scherbaum, 2013). This method utilizes the inverse sensor characteristic to selectively amplify the low frequency part of the signal such that the flat part of the response curve is extended towards the desired new corner frequency. The corrected sensor characteristic has a flat response in the desired frequency range resembling a sensor element with lower natural frequency.

The resulting characteristic depends on the specific application requirements; however, the method always employs the inverse characteristic of the geophone used for the measurement (Havskov and Alguacil, 2004). Without accurate estimation of the initial sensor parameters of the specific geophones (natural frequency and damping), the IRC will

produce ambiguous results. These parameters need to be accurately obtained either by using shake table testing or by approximation of the impulse response of the sensor element (Bowden, 2005).

IRC allows substituting one sensor for another in a simple way for a specific application, i.e. use of smaller sensors instead of short period seismographs for installation in tight space. For example, classic short period (1s) seismometers like the Sercel's L4 (Sercel, 2019), Geotech Instruments' S-13 (Teledyne Geotech, 2019) and Kinemetrics' SS-1 (Kinemetrics, 2019) offer low-frequency response and large generator constants but are heavy and expensive. In applications where the amplitude of vibration velocity is expected to be considerable, smaller devices with similar frequency range and in some cases lower sensitivity are preferable.

In general, IRC can be applied to all types of sensor element: seismometers (displacement), velocimeters or accelerometers, and can be used to change the frequency characteristic. This study focuses on the velocity response of a standard geophone element (with velocity transducer), which is given by the following equation (Havskov and Alguacil, 2004):

$$H_v(\omega) = G_V * SR(\omega) = G_V \frac{\omega^2}{\omega_0^2 - \omega^2 + 2j\omega\omega_0 h} \tag{3.12}$$

where $H_v(\omega)$ is the geophone response to vibration velocity in Volt/(m/s), G_V is the generator constant in Volts/(m/s), $SR(\omega)$ is the sensor dimensionless velocity transfer function with gain of 1 in the passband, ω is angular frequency, ω_0 is the sensor natural frequency and h is the damping. The equation describing SR is a second order high-pass filter, which is obtained utilizing the Laplace Transform (Proakis, 2001) and substituting $s = j\omega$, and is written in the s-domain as:

$$SR(s) = \frac{-s^2}{s^2 + 2s\omega_0 h + \omega_0^2} = \frac{s^2}{(s - p_1)(s - p_2)} \tag{3.13}$$

where p_1 and p_2 are the roots of the denominator. The above equation can also be obtained by solving the second order differential equation of a mass-spring-damper system, or a single degree of freedom system (SDOF). The denominator can be factored

to obtain the pole-zero representation of the linear time-invariant (LTI) system described by Equation (3.13). The frequency response for an accelerometer can be obtained from Equation (3.12) multiplying it by $j\omega$, and that for a displacement transducer can be obtained by dividing it by $j\omega$.

The following section describes two approaches used to generate and utilize IRCs and highlight the differences between them. To achieve sensor correction, the first technique uses spectral manipulation of pre-recorded waveforms. The second technique uses time-domain filtering in both post-processing and real-time applications. These procedures are applied here on synthetic and real data. The time-domain technique is demonstrated to be well suited for applications when the industrial vibrations need to be tracked and/or controlled in real-time.

3.4.1 IRC composition

The first step in creating an IRC for a specific sensor, or for sensor/DAQ combination is to obtain all relevant parameters for these systems. DAQ specification includes the pole-zero locations of all filters present in the acquisition hardware. Sensor specification consists of element type, natural frequency, damping, and generator constant. An electromechanical velocity transducer whose output voltage is proportional to the sensor velocity is used in this study. Since all operations described here are linear and time-invariant, the IRC curve can be normalized to have gain of 1 in the passband and the scaling between voltage and velocity can be performed last. The frequency extension of the velocity transducer and the correction for DAQ effects follow the same IRC procedure. Only sensor extension will be considered in the following discussion; however, the IRC can be generalized to include DAQ effects using the same principles.

Equation (3.13) can be used to derive the Laplace transform of the transfer function of a specific sensor *SR(s)* representing it as a second order linear time-invariant (LTI) system in pole-zero form. The polynomials of the numerator and denominator of Equation (3.13) are factored into their roots (real and imaginary) and the resulting representation is the pole-zero form of the transfer function:

$$SR(s) = \frac{-s^2}{(s-p_1)(s-p_2)} \tag{3.14}$$

The target response needs to be defined as a normalized transfer function. In most cases of IRC, a simple corner frequency shift needs to be introduced, and the target response uses the same equation as the sensor response with a lower natural frequency. The target response can be defined as:

$$TR(s) = \frac{-s^2}{(s-p_3)(s-p_4)} \tag{3.15}$$

Where p_3 and p_4 are the poles of the target transfer function.

If only these two transfer functions are used to define the IRC, the resulting response will have a gain of -3 dB at the desired corner frequency and the response amplitude decreases below the passband. By the addition of a second-order high-pass filter (HPF) with relatively smaller damping (< 0.5), the response gain at the desired corner frequency can be brought up to 1. The HPF is defined as:

$$HPF(s) = \frac{-s^2}{(s-p_5)(s-p_6)} \tag{3.16}$$

The HPF increases the resulting response slope below its corner frequency, suppressing by 12 dB/oct any lower frequency content, which results in a reduction of the offset and trend of the output signal if they exist in the input signal. The HPF's damping, its corner frequency and the target frequency need to be jointly adjusted to keep the gain close to unity for frequencies higher than the new corner frequencies. This step improves displacement estimation when integration of velocity records is used.

All three parts of the IRC have a gain of 1.0 in their respective passbands. The IRC is defined as the combination of these three transfer functions as follows:

$$IRC(s) = \frac{TR(s)*HPF(s)}{SR(s)} = \frac{-s^2(s-p_1)(s-p_2)}{(s-p_3)(s-p_4)(s-p_3)(s-p_4)} \tag{3.17}$$

Figure 3.11 shows an example transfer functions based on Equation (3.17) generated for a specific sensor element with a natural frequency 4.25 Hz and damping 0.707; the HPF has Fc = 0.5 Hz and damping = 0.4 and the target response is then calculated to have Fc = 0.826 Hz and damping = 0.707.
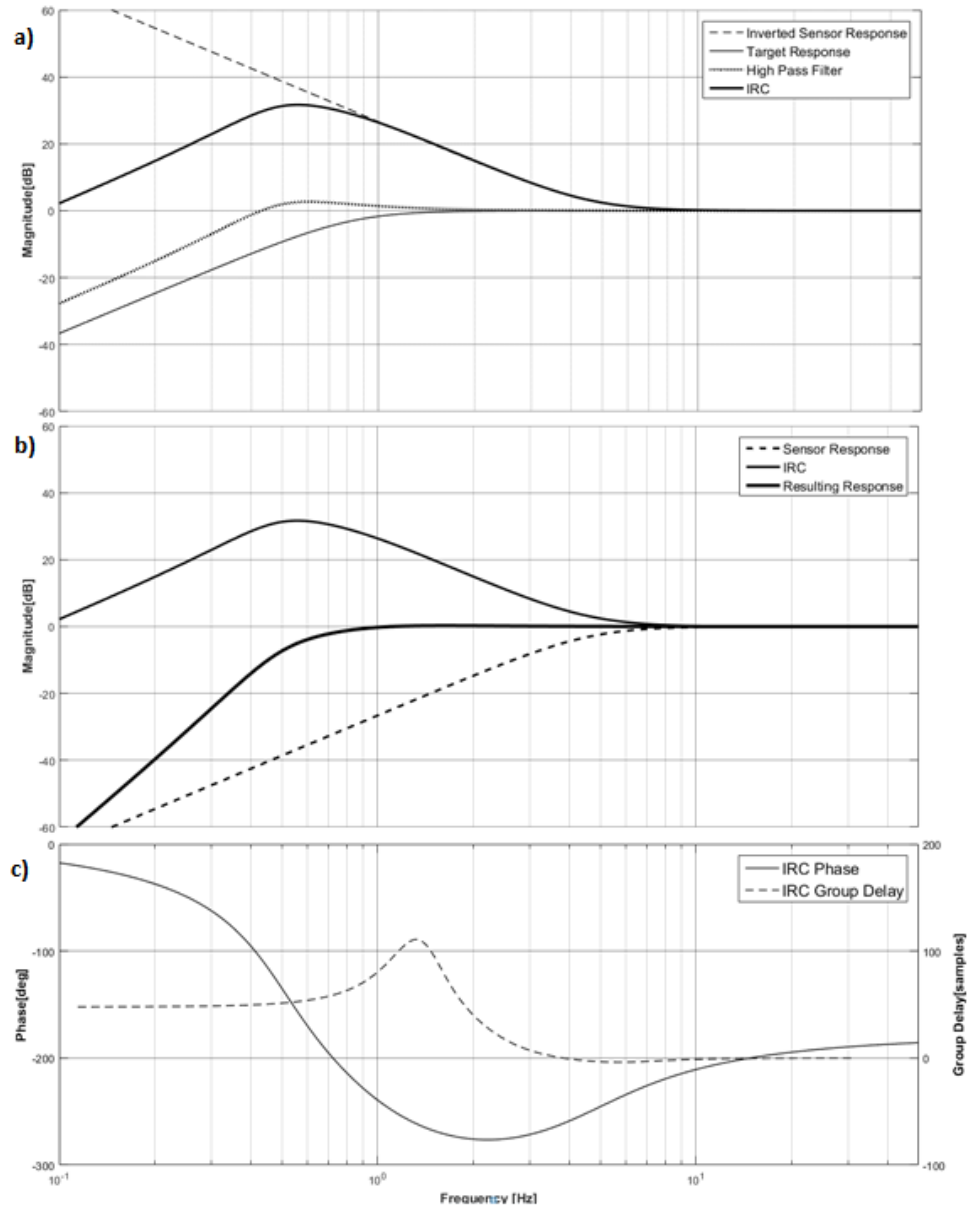
Figure 3.11: a) Components of the IRC; b) IRC Application; c) Phase characteristics and group delay of the IRC filter. The IRC is generated for a sensor element with 4.25 Hz, h = 0.707 damping, and the target has a corner frequency of 0.826 Hz, h = 0.707. The HPF has f_c = 0.5 Hz and h = 0.4.

Equation (3.17) describes a continuous time filter in the Laplace domain. It can be applied to a continuous time signal to perform the response correction. The signals from sensors are discretized (i.e. with a finite time step), requiring the IRC filter to be represented by its discrete Z-transform form. The bilinear transform (also known as Tustin's method) (Franklin et al., 1990) is used in digital signal processing and discrete-time control theory to transform continuous-time systems to discrete-time and vice versa. The transform preserves stability and maps every point of the frequency response of the continuous-time filter to a corresponding point in the frequency response of the discrete-time filter. However, a small shift in frequency is introduced for frequencies close to the Nyquist frequency (Franklin et al., 1990).

A continuous-time causal filter is stable if the poles of its transfer function fall in the left half of the complex s-plane. A discrete-time causal filter is stable if the poles of its transfer function fall inside the unit circle in the complex z-plane. The bilinear transform maps the left half of the complex s-plane to the interior of the unit circle in the z-plane. Thus, filters designed in the continuous-time domain that are stable are converted to filters in the discrete-time domain preserve that stability.

The conversion from continuous to discrete representation of the transfer function is based on the warping of the Laplace domain into the unit circle of the z-domain and it is achieved in either direction using the following substitution (Kester, 2004):

$$z = e^{sT_s} \Rightarrow s = F_s \ln z \tag{3.18}$$

where *Ts* and *Fs* represent the sampling period and frequency respectively. The natural logarithm in Equation (3.18) can be simplified by substituting it with the hyperbolic tangent function and its Maclaurin expansion (Proakis, 2001). Finally, the expression is further simplified by reducing it to the first term of the series:

$$ln(z) = 2 \tanh^{-1}\left(\frac{z-1}{z+1}\right) = 2 \sum_{k=0}^{\infty} \frac{1}{2k+1}\left(\frac{z-1}{z+1}\right)^{2k+1} \approx 2\frac{z-1}{z+1} \quad s = 2F_s\frac{z-1}{z+1} \tag{3.19}$$

Using this approximation, the IRC can be written in the following discrete filter form, which describes an Infinite Impulse Response (IIR) filter (Proakis, 2001):

$$IRC(z) = \frac{1+b_1z^{-1}+b_2z^{-2}+b_3z^{-3}+b_4z^{-4}}{1+a_1z^{-1}+a_2z^{-2}+a_3z^{-3}+a_4z^{-4}} \tag{3.20}$$

The parameters b_n and a_n are functions of the pole and zero locations of the continuous time transfer function for the IRC given in Equation (3.17). The resulting filter can now be used for instrument response correction.

For high sampling frequency (> 1000 Hz), this process may result in an unstable discrete filter representation. This effect is introduced by the relatively low (with respect to the sampling rate) frequency of the poles and zeros of the IRC transfer function. Poles and zeros are normalized on the unit circle to the Nyquist frequency and for low-frequency poles. Increasing the sampling rate moves the poles closer to the real axis of the unit circle, see Figure 3.12.

Discretization of filters that have poles very close to the unit circle can result in one or more poles being placed outside the circle and therefore makes the resulting filter unstable. This effect is due to the finite precision of discretized coefficient values. In these cases (Havskov and Alguacil, 2004), approximation using first-order hold conversion needs to be used instead of the bilinear transformation. Using first-order hold assumes that the input signal is piecewise linear in the time window of the record. This approach will provide an exact match of the impulse response in the time-domain without placing the resulting poles outside of the unit circle.
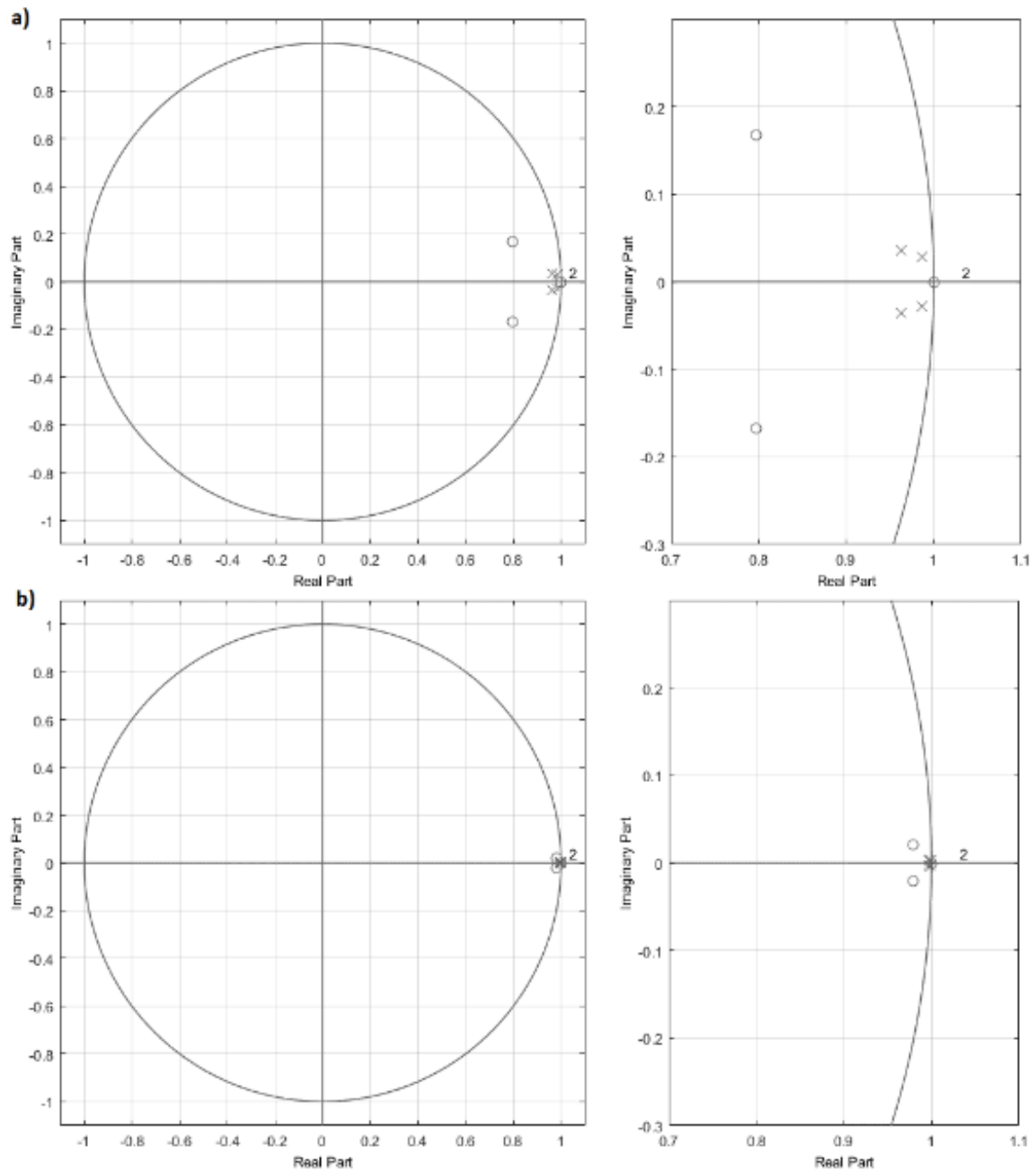
Figure 3.12: Pole-Zero Plots for the IRC. a) Sample frequency 100 Hz; b) Sample frequency 1000 Hz. Circles represent zeros, crosses represent poles

3.4.2 IRC Application

In general, recorded data can be corrected for instrument response either in the time or frequency domain. It is widely accepted to perform IRC correction in the frequency domain by modifying the spectra of the recorded data using the IRC's transfer function. Working with the data spectrum requires processing the entire time window of the record in order to obtain its Fourier transform, which limits the applicability of this technique to the post-processing of the collected data. Instead of processing the full data record at once, windowing can be employed to process sections taken from the entire record. In this case, the spectral approach could be applied in real-time applications; however, it introduces a significant delay as the window duration needs to be large enough to accommodate the lowest frequency of interest. This approach is excellent for post-processing of seismic data or data from long-term vibration monitoring when direct observation of the corrected signal is not required. However, if real-time feedback is required, this technique can be very computationally expensive with long lag introduced between acquisition and display/storage of the processed waveform. To avoid this problem the discretized version of the IRC, Equation (3.20) can be used to create an IIR filter.

Since a seismic sensor/DAQ can only record for a finite amount of time, this interval will inevitably have abrupt start and stop. Calculating the spectrum from signals with sharp onset and abrupt end, results in the introduction of high frequency noise. To mitigate this effect a tapering function can be used in post-processing. Reducing the effect of the start and tail of the signal also improves the estimate of the displacement, suppressing the spurious offset (transient) in the calculated displacement. The taper function used here is defined using the total signal duration (T) and the tapered time intervals at the beginning and end of the signal (τ):

$$taper(t, \tau) = \begin{cases} 1 & for\ t \in [\tau; T - \tau] \\ sin^2(\pi t) & for\ t < \tau \\ -sin\big(\pi(T - t)\big)^2 & for\ t > T - \tau \end{cases} \tag{3.21}$$

Verification and testing of the IRC is done using a synthetic test signal. It is defined as the sum of 9 logarithmically equally spaced sinusoids between 0.3 and 50 Hz with 10% white Gaussian noise added to the sum (Figure 3.13). To emulate the output of a standard velocimeter, the response curve (*SR*) is used to shape the spectral characteristic of the test signal. Both methods are then applied to this test data.

Field data recorded using a 4.4 Hz geophone element at a sample rate of 100 Hz, obtained from the study of structural vibrations of a frame was subjected to the same transformation, expanding the frequency range to 0.25 Hz. Total record duration was 120 seconds. The resulting waveforms and their spectra are given Figure 3.14 for velocity and Figure 3.15 for displacement.

3.4.3 Frequency domain correction, post-processing approach

In the frequency domain, IRC can be performed by the multiplication of the complex Fourier transform of the input signal and the complex transfer function characteristic of the IRC. The corrected signal is the inverse Fourier transform of the result of the multiplication:

$$signal_{corrected}(t) = \mathcal{F}^{-1}\big[IRC(f) * \mathcal{F}(signal_{input})\big] \tag{3.22}$$

Similar approach in frequency domain was proposed as an improvement to the time-domain deconvolution method (Dergach et al., 2019).

One important issue to discuss here is the length of the data record. IRC focuses on lower frequencies, and therefore recorded waveform should have enough periods of the target frequency. For post-processing tasks, this is important, and the length of the record should be set accordingly before data collection.

The first step in processing is to filter the input signal with a low-pass filter to eliminate high frequency noise. A 4th order low pass digital Butterworth filter with a corner frequency of 32 Hz was used. Next, the taper defined by Equation (3.21) with $\tau = 2$ was applied to the signal to remove sharp cut-offs.

The next step is to remove the offset, and then convert the signal to the frequency domain using FFT. The signal should have 2^n samples to avoid padding it with zeros. The tapering given by Equation (3.21) provides a smooth transition without distortion of the resulting spectrum.

3.4.4 Real-time correction, time domain correction

Sensor frequency response correction has been done in real time in the frequency domain by (Brincker et al., 2005) using the overlap-save method to process consecutive signal frames. The minimum length of the processing frames in samples is determined by the desired new corner frequency (f_{new}) and the sample frequency (F_s), and the use of overall-save with overlap parameter β results in total minimum delay of 2 frames:

$$N_{min} = \frac{F_s}{f_{new}}, \quad T_{delay,min} = N_{min}(1 + 2\beta)T_s = \frac{N_{min}(1+2\beta)}{f_{new}} \qquad (3.23)$$

In practice, the window length needs to be much larger than N_{min}, as to have sufficient FFT resolution for feature identification. This requirement makes this method better suited for post processing application, as the time delay becomes more significant as the desired corner frequency is decreased.

The main difference in this approach is that the IRC technique is performed in the time domain, where knowledge of the entire record of data is not required. Thus, this method can be applied using digital IIR filters during data collection in real-time. The filters used here are described by Equation (3.20).

Application of the IRC IIR filter in either real-time or post-processing results in a small transient response effect (approximately 3 periods of the HPF frequency) at the beginning of the signal, as the initial conditions are assumed to be zero. In real-time applications, this can be avoided by starting the record after the filter has had enough time to settle its transient response. In post-processing applications, the same time interval at the beginning of the output waveform would be affected.

In real-time applications, the filter output for any sample is based on the last 4 input and output samples. Their values are maintained in a circular buffer. There is no other

performance or qualitative difference between using this technique in post processing or real-time applications.
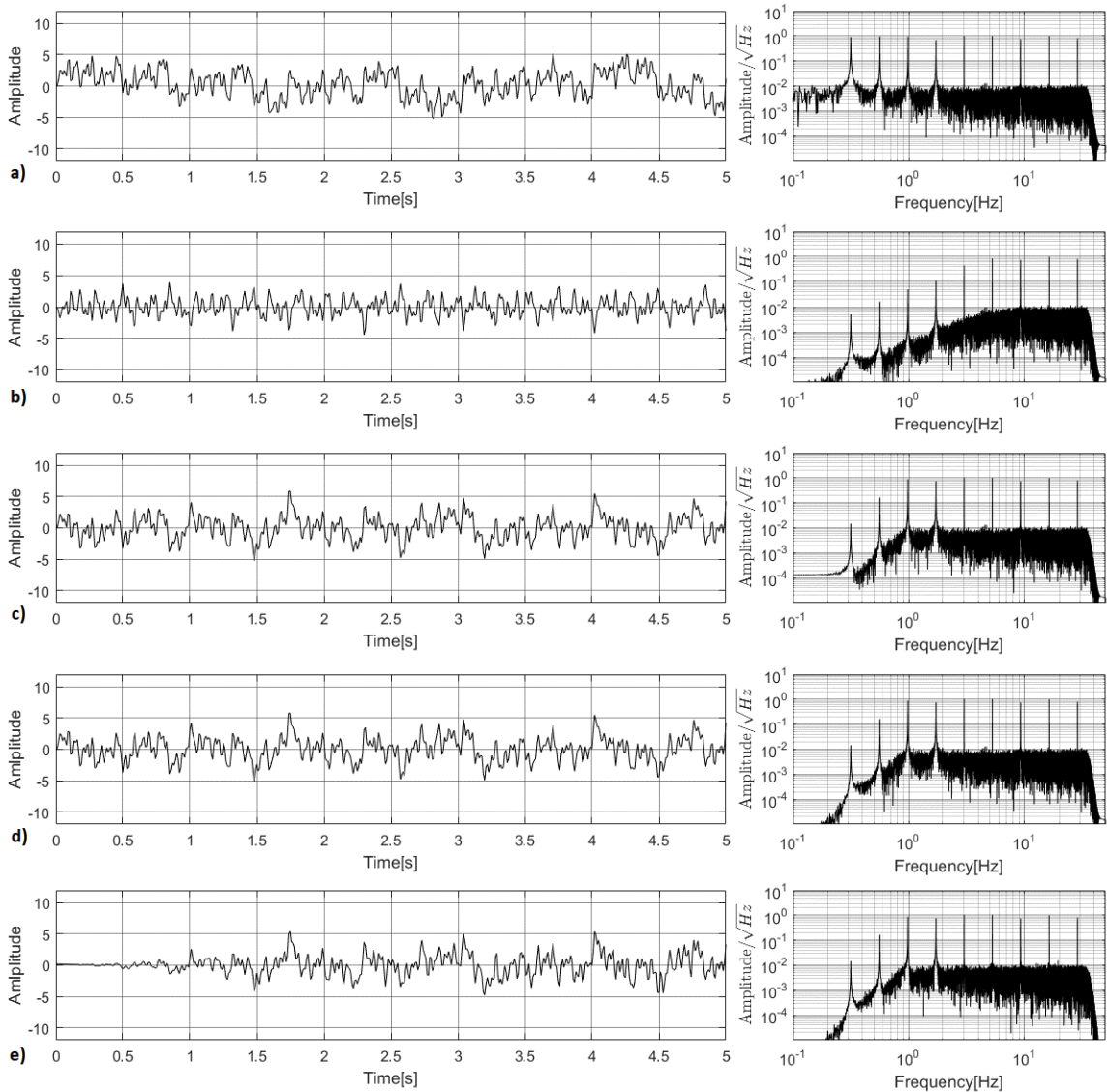
Figure 3.13:Result of IRC using both methods on synthetic signal with logarithmically distributed frequencies. Target response is set at 1Hz. a) Test Signal; b) Test signal shaped using 4.5 Hz sensor characteristic; c) IRC applied using IIR filtering; d) IRC applied using spectral multiplication; e) IRC applied using spectral multiplication on tapered input
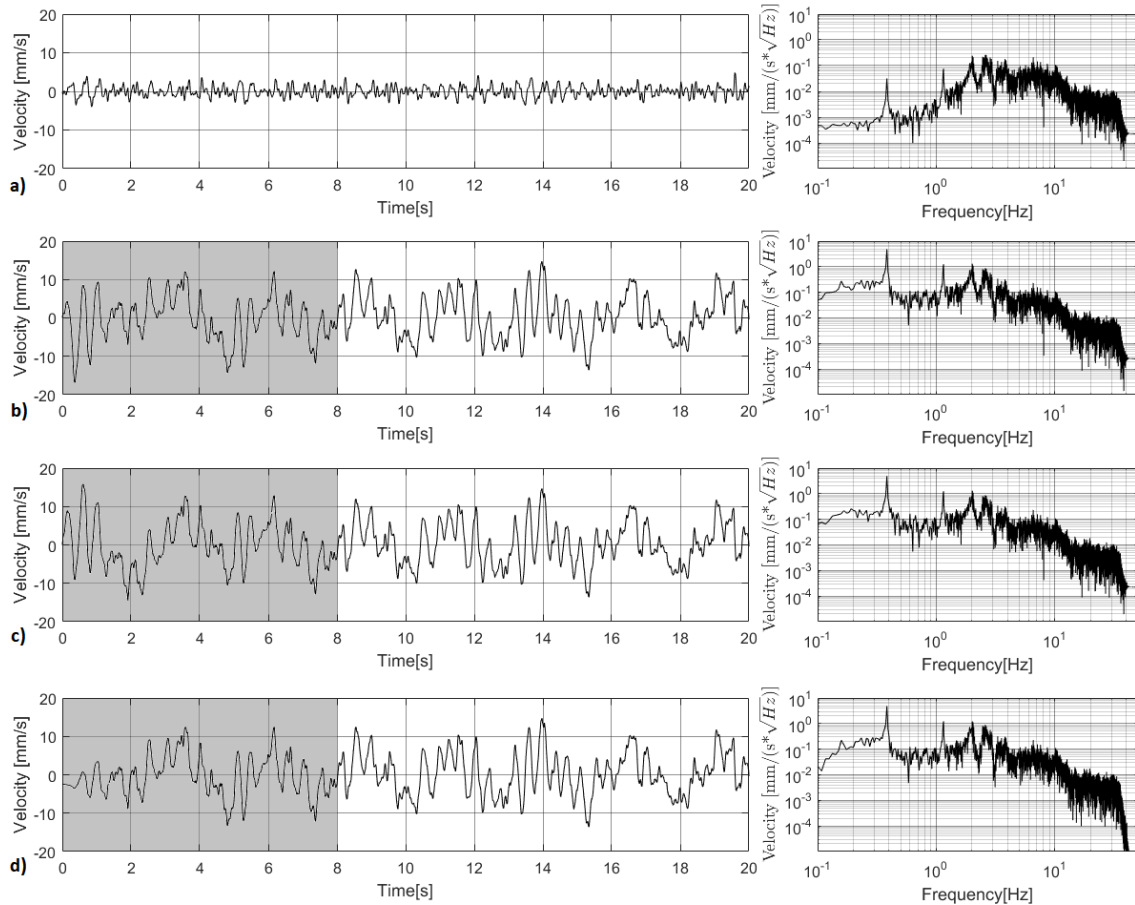
Figure 3.14: Result of IRC using both techniques on real-world velocity record. Target frequency is 0.25 Hz. Fs=100 Hz. a) Original Signal; b) IRC applied using IIR filtering first order hold approximation of the IRC; c) IRC applied using spectral multiplication; d) IRC applied using spectral multiplication and tapering of the input signal. Duration of the transient response is highlighted in grey.
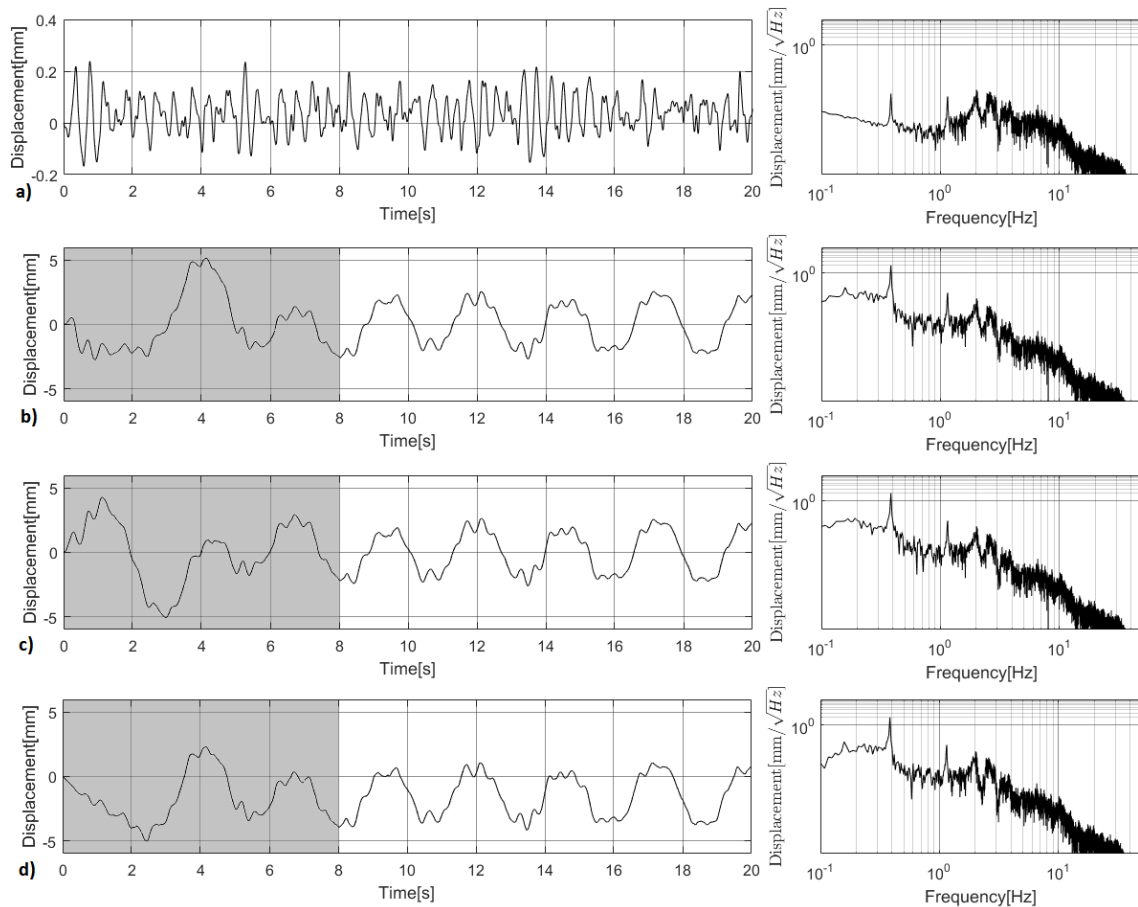
Figure 3.15: a) Displacement calculated form: a) Original Signal; b) IRC applied using IIR filtering and first order hold approximation of the IRC; c) IRC applied using spectral multiplication; d) IRC applied using spectral multiplication and tapering of the input signal. Duration of the transient response is highlighted in grey.

3.4.5 Discussion

Figure 3.13 shows the result from both techniques for IRC on the synthetic test signal described previously. The corrected spectra demonstrate that both approaches achieve the response expansion and have identical characteristics in the passband of the resulting waveforms. For the test signal, tapering does not give an observable benefit to the result. In the case of the IIR filter application the noise floor at frequencies below the new corner frequency is larger than the noise floor in the same range of the spectral manipulation method.

Figure 3.14 and Figure 3.15 demonstrate both techniques on real world data. The time intervals with transient response are highlighted in grey. The effect of the applying a taper to the input data is evident here as it limits the effect of the transient response; however, its duration remains the same. Additionally, adding the taper to the original velocity signal introduces a large transient in the displacement calculated from the corrected data. The benefit of calculating displacement after IRC application is clearly visible in Figure 3.15 that shows oscillations with 2.8 second period that were undetectable in the original record. Tapering effects, especially on the transient response are also much more significant in calculated displacement, as compared to IRC corrected velocity data.

3.4.6 Conclusions

Based on the results obtained from the frequency domain and time domain approaches presented herein, the following observations and conclusions are drawn. Both methods result in approximately the same IRC with a few important differences.

- In the absence of signal history before the start of data collection (i.e. initial conditions $t = 0$), the real-time approach introduces a transient response in the corrected signal. The IIR transient response quickly decays within the noise floor of the recording.

- High sample rates may result in an unstable IRC IIR filter when the Tustin approximation method is used. First-order hold approximation should be used instead.

- Double precision floating point quantization of filter parameters is required for filter stability, especially combined with high sample rates.

- Abrupt starts and ends in the signal introduce noise in the spectral amplitude. In post processing it is a good practice to use tapering to smooth the start and end of the digitized signal and mitigate this effect. In the time domain the abrupt start results in a transient response.

- Regardless of which IRC technique is used, the beginning of the signal is compromised with either filter transients or tapering effects.

- The IIR filtering method is prone to numerical instability when the continuous time IRC is transformed to the discrete time IIR IRC, especially when the sampling rates are high.

- Additional stability issue may arise due to round off errors in the quantization of filter tap parameters. The rounding-off error of the filter parameters can have a compounding effect resulting in signal drift as more samples are passed through the filter.

Noise present in the input data plays a critical role in the design of correction curves. At low frequencies the signal to noise ratio of recorded signals decreases, due to the reduced sensitivity of the sensor element at these frequencies. The target frequency of the IRC curve needs to be higher than the frequency at which the signal to noise ratio becomes less than three. If the recorded signal is not saturated the SNR remain constant throughout the frequency range before and after IRC application.

Saturation of the recorded data negatively impacts the results. Displacement calculated from such clipped data is not usable. Signal portions that are saturated should be cut-out from the record, and the signal tapered at the cut points.

3.5 Geophone with hardware expansion of the frequency range

3.5.1 Introduction

In many applications, the 4.5 Hz natural frequency limit of the DM 4.5 Hz (see section 3.3) sensor makes it inapplicable, or it requires further processing with the methods given in section 3.4. For measurements where frequency content lower than the sensor natural frequency (e.g. seismic investigations, industrial applications, and microtremor recordings for HVSR), the amplitude of the motion needs to be large enough to overcome the noise floor. The noise floor in this case includes the noise from the recording system as well as electro-magnetic interference (EMI) induced in the cabling and the sensor noise itself. If the vibration is not strong enough, post processing or real time correction strategies will

not work properly. For this reason, hardware expansion of the natural frequency of the sensor element is be necessary.

The most common approach for hardware correction of the frequency response of geophone elements is given in (Havskov and Alguacil, 2004; Havskov and Ottemoller, 2010). It utilizes a positive feedback circuit to increase the damping ratio to ~ 4-5, i.e. overdamped geophone element. A positive feedback is used by a negative impedance converter to keep the inertial mass nearly stationary with respect to the geophone housing during vibration, and therefore the geophone behaves more like an accelerometer. The electrical output of the overdamped geophone is proportional to acceleration in the linear response section around the natural frequency of the element. The negative impedance converter is followed by an integrator that is used to correct the resulting response characteristic and produce a modified high-pass filter with a linear velocity response in the passband (see Figure 3.18, blue line).

Other approaches are available in the literature, e.g. (Barzilai et al., 1998), who use the feedback from a separate displacement transducer to improve only the low frequency region of the response. (Song et al., 2016) used resistor/ capacitor networks along with the positive feedback for the same purpose(Havskov and Alguacil, 2004)(Havskov and Alguacil, 2004)(Havskov and Alguacil, 2004). Their impedance network is configured using genetic algorithm optimization to shift the natural frequency of geophones to lower values. This gives an ambiguous improvement of low-frequency response compared to the method with negative impedance convertor with integration.

3.5.2 Hardware expansion implementation

For this study, the hardware expansion of the frequency range is based on the general topology presented by (Havskov and Alguacil, 2004) with a few major modifications:

- Temperature compensation – the copper coil of the geophone has a significant temperature coefficient, which will compromise the effect of overdamping and the gain of the impedance converter.

- Output filtering – low and high pass filtering to shape the output of the sensor and to expand the linear band of the integrator output bellow 1 Hz.
- Differential output – EMI problems, especially in industrial settings, can cause significant influence over the recorded data. Differential signals are better suited for such situations, it can be received by the differential input of the DYNAMate system, cancelling common-mode EMI.

The complete schematic of the hardware-based expansion of the natural frequency of a 4.5 Hz geophone below 1Hz is given in Figure 3.16. The geophone is defined by a voltage source U_S and the internal resistance R_1. The output of the sensor is clamped by the diode circuit given by diode gropes D1 and D2. This clamping circuit limits the input voltage level to ~+/-2.5 V to prevent saturation in consequent steps of the circuit and limit the maximum output of the geophone to 100 mm/s (assuming a generator constant of 25 V/(m/s)). Additionally, without power applied to the rest of the circuit, the diodes shunt the geophone element and allow safer transportation by limiting the maximum voltage applied to the electronics during unintended drops or kicks to the sensor.
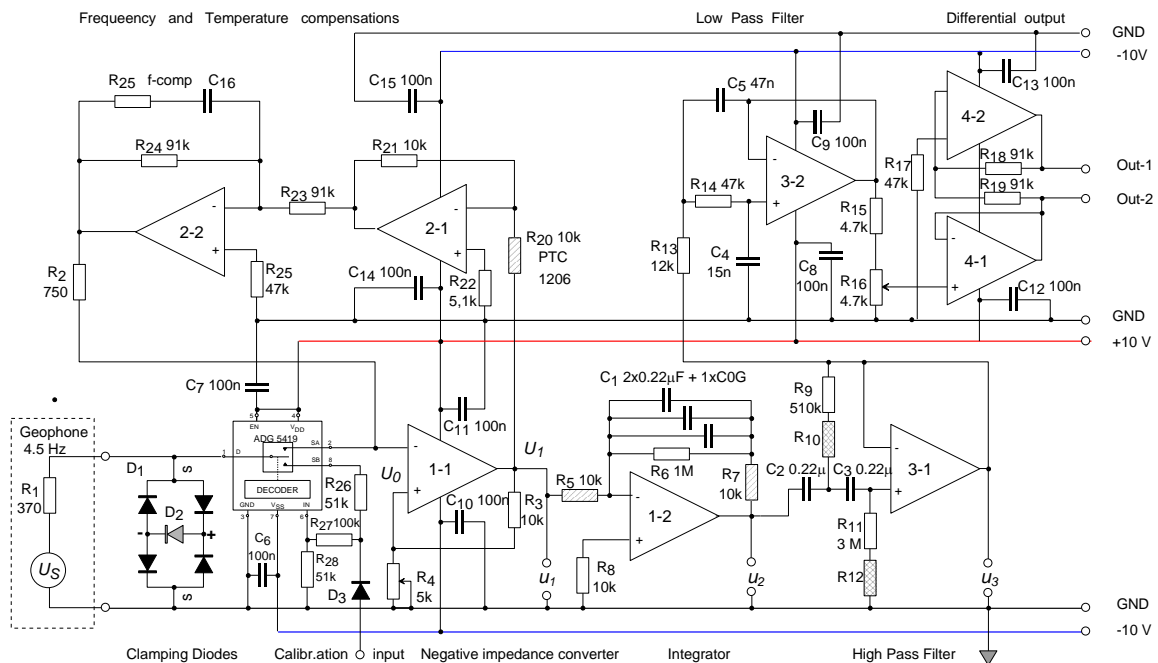
Figure 3.16: Schematic for the hardware based expansion of the frequency response of geophone elements

The digital switch (ADG5419) is used to apply a calibration pulse in the same manner as in the 4.5 Hz version of the sensor (see section 3.3.2), with resistors R26, R27 and R28 and diode D3 conditioning the calibration pulse. When the calibration pulse is applied the sensor is disconnected from the rest of the circuit, therefore the recording system will only record the return to equilibrium of the inertial mass.

The output of the switch is applied to the inverting input of operational amplifier (OA)1-1. OA1-1 has two loopback circuits. The positive feedback circuit forms a negative impedance converter applying the output voltage U_1 of OA1-1 to its noninverting input trough divider which produces voltage U_0 between R_3 and R_4.

This negative impedance (resistance), when connected to the geophone forces current through the element in a direction that opposes the motion of the inertial mass. This in effect decreases the equivalent shunt resistance and increases the damping of the geophone element.

The negative feedback circuit of OA1-1 is formed by R20, OA2-1, OA2-, R2. The output voltage U_1 of OA1-1 is applied to the temperature-controlled inverting amplifier OA2-1. The positive temperature coefficient resistor R_{20} reduces the gain of the inverting amplifier with increasing temperature. The voltage signal is inverted again by the band limited inverting amplifier OA2-2, and resistor R_2 sets the output impedance of the feedback circuit.

The differential voltage between the inverting and noninverting inputs of any OA is very small, and ideally zero. Therefore, the same voltage U_0 is present on both inputs of OA1-1. Miller's theorem and Kirchhoff's laws are used to calculate voltages at both inputs and output as well as the total amplification K and input resistance R_S of the impedance converter. All relevant equations are given below:

Common-mode input voltage	$U_0 = -U_1 \dfrac{R_4}{(R_3+R_4)}$	(3.24)

Gain calculation $\qquad U_S \dfrac{R_2}{R_1} = -U_1 \left[1 - \dfrac{R_4}{R_3+R_4}\left(1 + \dfrac{R_2}{R_1}\right)\right]$ $\qquad$ (3.25)

Double feedback gain $\qquad K = \dfrac{U_1}{U_S} = -\dfrac{R_2(R_3+R_4)}{R_1R_3 - R_2R_4}$ $\qquad$ (3.26)

Output voltage $\qquad U_1 = -KU_S$ $\qquad$ (3.27)

Common-mode input voltage vs. K $\qquad U_0 = U_S K \dfrac{R_4}{R_3+R_4}$ $\qquad$ (3.28)

Input resistance serving as a shunt resistor $\qquad R_S = \dfrac{R_3R_1 - R_2R_4}{R_3}$ $\qquad$ (3.29)

Electrical damping vs. R$_S$ $\qquad h_e = \dfrac{G_S^2}{2R_S m \omega_0}$ $\qquad$ (3.30)

Total damping including mechanical $\qquad h = h_m + \dfrac{G_S^2 R_3}{2(R_3R_1 - R_2R_4)m\omega_0}$ $\qquad$ (3.31)

Due to the overdamping the resonant frequency of the geophone is split into two corner frequencies values of the two frequencies can be obtained from the equation of a velocimeter without a differentiating electrical transducer:

$$|H_V(f)| = \frac{\left(f/f_n\right)}{\sqrt{\left(1-\left(f/f_n\right)^2\right)^2 + 4h^2\left(f/f_n\right)^2}}$$ (3.32)

After normalization using the maximum value of the response, the above equation becomes:

$$\frac{H_d(f)}{H_d(f)max} = \frac{2h\left(^f/_{f_n}\right)}{\sqrt{\left(1-\left(^f/_{f_n}\right)^2\right)^2 + 4h^2\left(^f/_{f_n}\right)^2}}$$

(3.33)

This function is shown in with a blue line in Figure 3.17. The -3 dB points (intercepts with the red line in the figure) for the curve are estimated as:

$$\frac{H_d(f)}{H_d(f)max} = \sqrt{0.5}$$

(3.34)

and the two corner frequencies (marked with black lines and corresponding values in Figure 3.17) are given by:

$$f_{1,2} = f_n\left(h \mp \sqrt{h^2 - 1}\right)$$

(3.35)
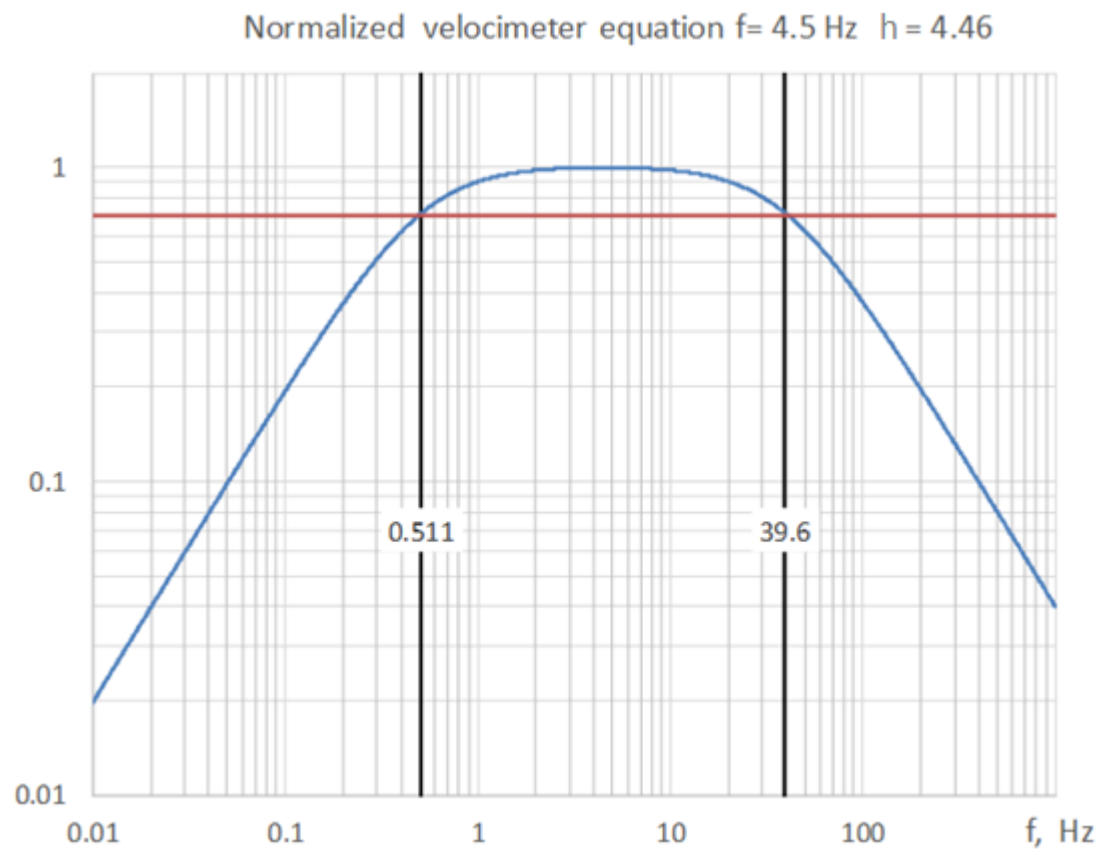
Figure 3.17: Normalized response after integration for $h = 4.46$ and $f_n = 4.5$ Hz

The sensor element's copper coil has a significant temperature coefficient, which will compromise the overdamping and the gain of the impedance converter. Here a temperature compensation schematic corrects the temperature influence over the impedance converter parameters using R_{20}, OA 2-1 and OA 2-2. This approach prevents potential overheating of the PTC R20 when intense industrial vibration is recorded.

The output voltage of the impedance converter from an overdamped geophone is described by Equation (3.3) for the given damping coefficient. This is shown by the red line in Figure 3.18.
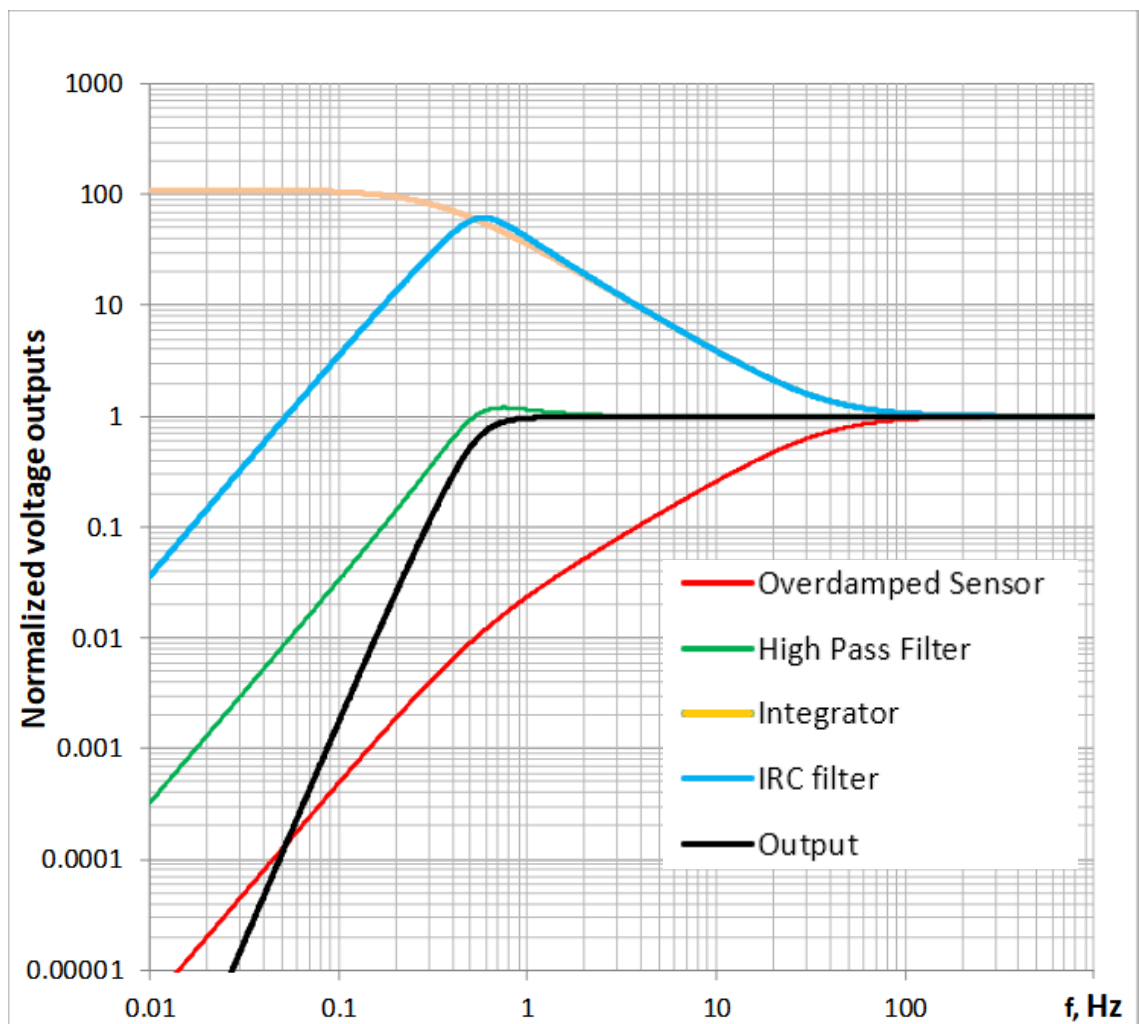
Figure 3.18: Voltage transfer functions normalized to their values at 1 kHz for each module in the expansion schematic. The overdamped sensor has a corner frequency of 4.5 Hz and damping of 4.22, the high pass filter has a corner frequency of 0.5 Hz

and damping of 0.474. The IRC filter represents the combined response of all stages, and the Output is the IRC applied to the overdamped sensor.

The output voltage U_1 from the impedance converter is integrated between f_1 and f_2 by partial integrator consisting of OA 1-2, R_5, R_6, R_7 and C_1. Here a new schematic for the partial integrator is used. R5 and R7 together with C1 are used in an inverting integrator with OA1-2 which allow integration in a limited frequency range between f_1 and f_2 and eliminate the common-mode voltage at the OA1-2 inputs. Its transfer function is shown Figure 3.18 by the orange line. An additional correction at low frequency is applied using a Sallen-Key second order high pass filter ($f_n = 0.553$, $h = 0.474$). This high-pass filter is formed by OA3-1 and its corresponding components and its response is given in Figure 3.18 by the green line. The integrator and high-pass filter are jointly presented as a modified high-pass filter shown by the blue line. The normalized output voltage is presented on the same figure with black line. A low pass second order Sallen-Key filter formed by OA3-1 and its corresponding components can be used to suppress the output signal after a desired frequency. The output stage consists of OA4-1 and OA4-2 that form a differential amplifier pair, with gain controlled by the voltage divider formed by resistor R_{15} and potentiometer R_{16}. The differential output allows using of long cables to the data recorder.

Based on this design a prototype was constructed and its performance verified using the procedure described in the next section.

3.5.3 Calibration and verification of the prototype of geophone with extended frequency response

Adjustment of component values and calibration of the resulting 0.5 Hz geophone was conducted in several steps:

Step 1 - Measurement and calculation of the internal resistance R_S, resonant frequency f_n, mechanical damping h_m and *CDR* of the geophone element chosen for the prototype. This was done using the procedures, hardware and software described in section 3.3.1.

Assuming definition for critical damping resistance (*CDR*), the generator constant *G* of a geophone element can be calculated as:

$$G = \sqrt{4\pi(1 - h_m)CDRf_n m}$$ (3.36)

Where all parameters can be measured or calculated precisely except for the mass of the moving coil *m* which must be taken from the manufacturer's specifications.

Step 2 - Calculation of the necessary values of resistors R_2, R_3 and R_4 for the negative impedance converter. The calculated values are then installed on the prototype PCB and measured with 2% precision

Step 3 – Install and measure capacitors C1 to C5 installed into integrator, high and low pass filters with accuracy better than 2%. Based on the measured value, calculate the exact values for resistors R_5 to R_{14}. Install and measurement the resistors and adjust the values to a precision better than 1%.

Step 4 – Apply a known input signal using a signal generator in place of the geophone element with a frequency above f_2. Adjust voltages U_0 and U_1 of the negative impedance converter.

Step 5 – Apply frequencies from 0.5 Hz to 500 Hz using a signal generator and construct the prototype's transfer function. The experimentally constructed transfer function values at several points is shown in the Figure 3.20.

Verification of the characteristics of the prototype was conducted using a shake-table with a reference accelerometer for high frequency inputs and LVDT for displacement reference for low frequency inputs (see Figure 3.19). The LVDT output is calibrated against a micrometer and used to establish an accurate estimate of the accelerometer's generator constant. The theoretically expected transfer functions of the prototype geophone with and without temperature compensation for several ambient temperatures are presented in Figure 3.20, and the experimentally obtained transfer function is given in Figure 3.21. The large resonant peak at 100 Hz is due to a resonance in the shake table and test platform setup and could not be damped any further.
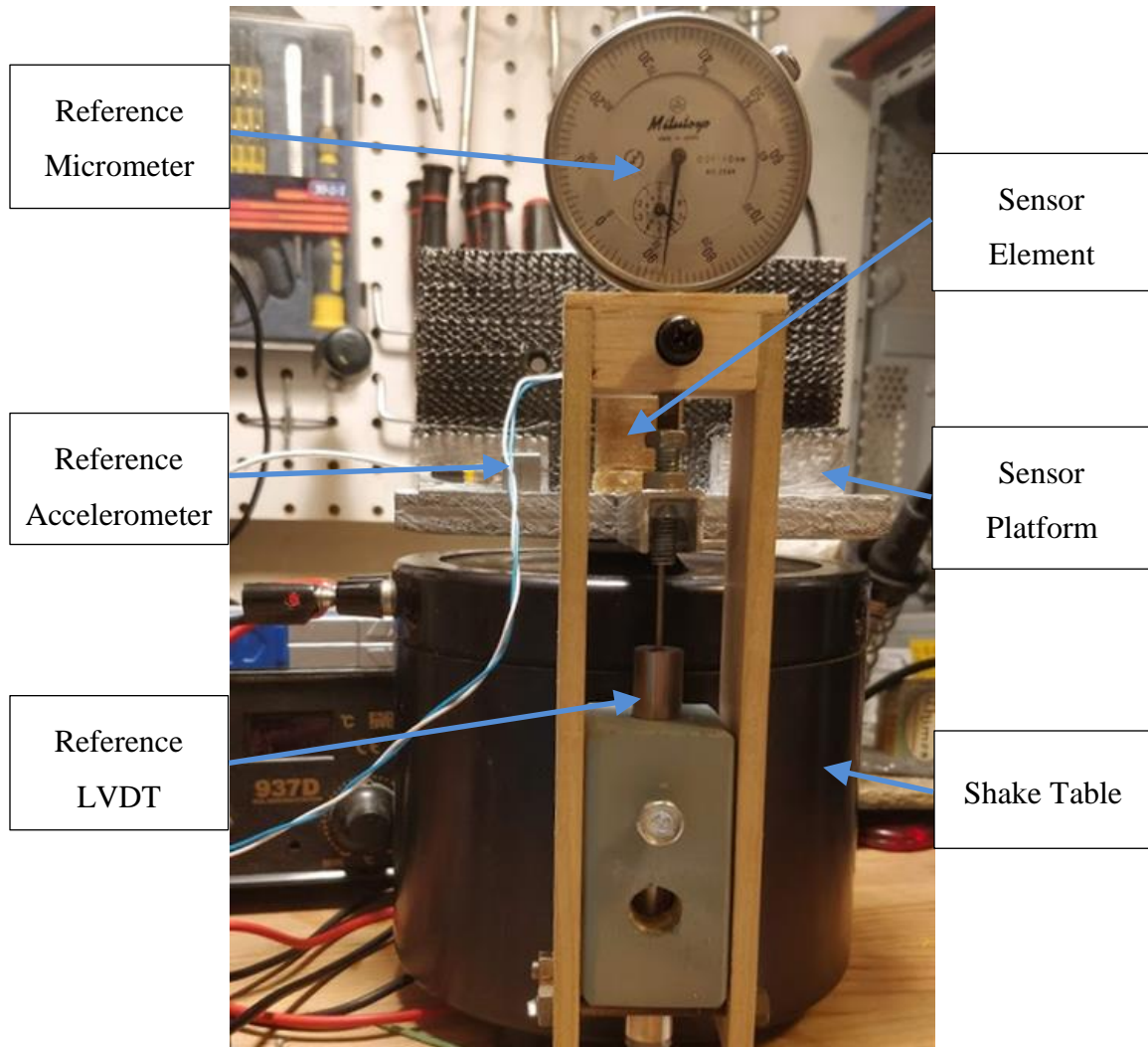
Figure 3.19: Calibration platform including 3 reference instruments: accelerometer, LVDT and a micrometer
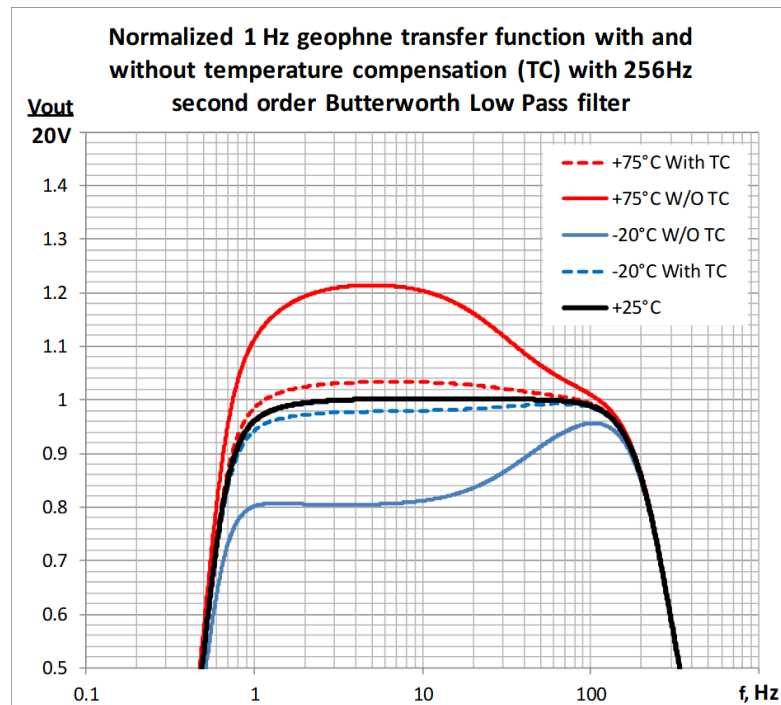
Figure 3.20: Prototype transfer function for different temperatures (theoretical)
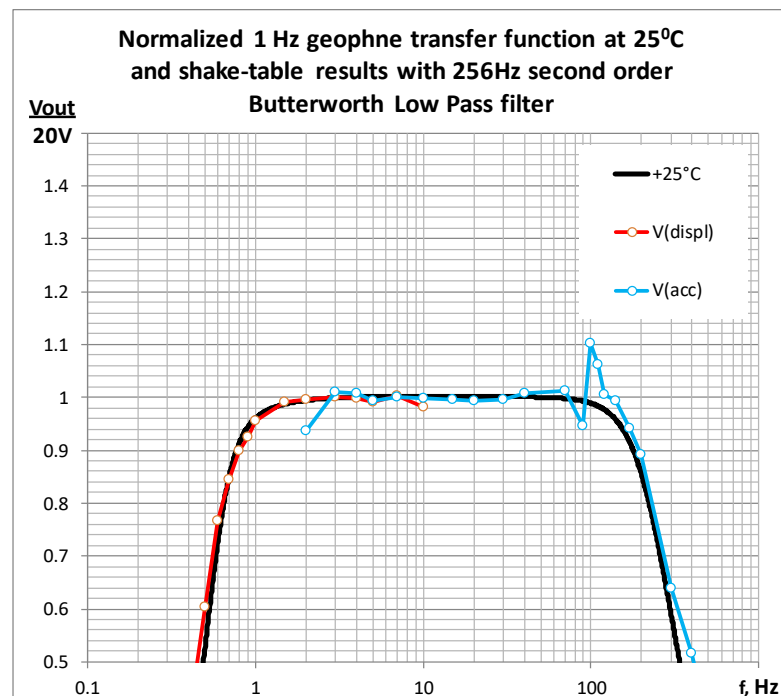
Figure 3.21 Transfer function obtained as a results of experimental verification of the prototype. Low frequency section (red) is obtained using LVDT reference, high freqeuency section (blue) is obtained using an acceleroemeter reference

3.5.4 Conclusions

This chapter discussed the general principles of seismic sensors like accelerometers, geophone and seismographs. Equation for the frequency response for each were provided, along with the typical sources of sensor noise

The design, calibration and verification of a 3-component geophone-based sensor was described. Additionally, a method for the characterization and calibration of such sensors was proposed based on the impulse response of a sensor element to external voltage stimulus.

Instrument response correction both in real time and post processing was described and algorithms were proposed for both. Based on the results obtained from numerical analysis, the following conclusion regarding the applicability and reliability of IRC techniques were drawn:

- Introduction of a transient response due to IRC processing in real-time and noise in the post-processing spectral approach.
- Regardless of which IRC technique is used, the beginning of the signal is compromised with either filter transients or tapering effects.
- Conditions for instability of the IIR based IRC – sampling rate and parameter quantization effects.
- Noise present in the input data plays a critical role in the design of correction curves.
- Saturation of the recorded data negatively impacts the results. Displacement calculated from such clipped data is not usable.

A geophone with electronically extended flat frequency range between 0.5 Hz and any desired frequency has been presented. A more precise shake table measurements are needed to characterize the response of the resulting sensor. However, the proposed design has several advantages over the standard Havskov (Havskov and Alguacil, 2004) negative impedance converter design, such as:

- A new solution for compensation in the temperature range from -10 °C to +75 °C.

- A novel solution for integration of an overdamped geophone without applying common-mode voltage to the integrator inputs.

- A set off equations which simplified calibration and verification of sensor parameters and transfer function.

- Easily adjustable sensitivity/generator constant.

- Differential output.

Chapter 4. DYNAMate vibration acquisition system

4.1 Introduction

Exploration seismic equipment is expensive and has complicated initial setup. Sometimes field measurements need to be performed by personnel with limited experience and knowledge in geophysical investigations or sensor installation and use of data acquisition systems. In addition, data acquisition systems (DAQs) and their corresponding software are generally intended to be used in different applications, varying from vibration measurement and sound recording to temperature and pressure measurements. Different types of sensors that can be interfaced to generic DAQs, forces the manufacturers of analog-to-digital converters (ADCs) to accommodate user defined adjustment of parameters such as sampling rate and scaling configurations, as well as different filter and amplifier setups.

The goal of this chapter is to describe the design and implementation of a DAQ system specifically designed for seismic, foundation and structural vibration measurements. Limiting the application areas allows developing a much simplified and reliable design, which only requires basic user experience. Minimal configuration is applicable for most measurement tasks, and the data is appropriately scaled to represent engineering units as opposed to a voltage output that usually requires further processing to convert it into absolute values corresponding to the measurement. The system has 24 channels (8 3-component channels) and is designed to operate with the DM 4.5 Hz sensors (Figure 4.1) or other geophones and short period seismometers. Despite the large number of channels, the system is designed to be portable for example see Figure 4.2.

Figure 4.1: DYNAMate system with 3 DM 4.5 Hz sensors

Figure 4.2: Using DYNAMate with one sensor in a vibration field study

4.2 Existing seismic stations and universal DAQ systems

Examples for specialized seismic stations and data acquisition equipment with their drawbacks are listed below:

- Geometrics Strataview, Geometrix GEODE – These two systems and a few of their variations are commonly used for seismic prospecting and near surface investigations such as MASW, shallow refraction and reflection techniques. The portable version of the devices is available with up to 72 channels. Data collection and preliminary analysis can be done directly on the device or on the attached computer. They are used with spread cables standard exploration geophones. Configuration of the systems can be difficult depending on the application. Utilizing these systems for vibration analysis of structures and foundations is difficult without some necessary modifications of the devices.

- National Instruments DAQs – National Instruments offers a wide variety of DAQ system; however, most are not specialized to a specific application area. This leads to complicated configuration of multichannel systems. Additionally, the hardware and software cost per channel are significant. Sensors need to match the application and chosen DAQ system, and must be carefully selected separately, sometimes with the help of NI representatives. Systems with high number of channels are often not very portable.

- PCE Vibration Meters – PCE manufactures hand-held vibration meters. The main disadvantage of this type of meter is lower accuracy as compared to systems where the sensors are securely mounted. Additionally, the number of available channels is limited.

- Tromino – this is a 3-component (XYZ) single channel vibration measurement system. It is primarily designed for HVSR microtremor measurements and is highly portable. It can operate alongside other Tromino devices with synchronization. To use Tromino for structural and foundation investigations, the time synchronisation between devices must be improved.

- OROS OR10 – is one of the best 8-channel mobile DAQ systems in the market for multiple applications and measurement needs. It can operate in standalone mode as well as connected to a PC or smartphone. Performs data analysis on-board based on additionally purchased modules. This is universal data acquisition system, which requires special operator training to take full advantage of its capabilities. All OROS DAQ systems are expensive and do not include software modules for geophysical field investigation.

In most cases, specialized equipment either has a limited number of channels per system or is not very portable, which is important for industrial applications when many sensors are deployed in many different points. Only seismic stations have geophysical software installed on the devices or on the attached to them computer. Cost is often high, especially for modular based systems such as the offerings from NI.

4.3 DAQ Hardware Description and Design

4.3.1 Introduction and Requirements

To manage simultaneous recording of noise and vibrations data at multiple test points in large areas, the equipment should be comparatively cheap and easy to use. Data must be collected and processed uniformly according to the specific test requirements. Multichannel configuration of the equipment must be useful in other geophysical studies, such as SASW/MASW, as well as for industrial vibration studies. The equipment needs to be straightforward to install, support and easy to use.

Overall specifications for the proposed equipment are:

- The equipment should be designed based on existing hardware modules and software packages.
- The final design should allow for mass-production of the proposed device.
- The technical solutions should be adapted based on general requirements for seismological and industrial equipment.

- It should be one piece of equipment which consists of sensors, signal condition modules, data acquisition module, timing module, recording module, communication modules and power supply.

- The device must handle different types and number of sensors using programmable configurations.

- It should be applicable for both seismological research and industrial vibration studies.

- The equipment must be feasible for both short- and long-term installations and data recording.

- The DAQ's hardware must work in different environmental conditions and must require minimum user interaction.

- Channels should be simultaneously sampled, or the waveforms corrected to adjust for the timing difference between channels.

- Provide programmable sensor natural frequency expansion in real time.

Based on these requirements, a specialized vibration measurement DAQ system was designed and prototyped. Three versions of the prototype have been constructed to this date, and this chapter outlines the design choices and accomplished system after the latest iteration in the design.

The system is characterized by 8, 3-component channels designed to be used with the DM 4.5 Hz sensor and it takes advantage of the already configured 20 V/(m/s) generator constant to provide recorded data directly in velocity units in the range 100 mm/s to 0.01 mm/s. Other sensors and senor types can be utilized as well. However, the output scaling needs to be adjusted to accommodate the difference.

Selectable hardware filtering is provided for 32 Hz, 64 Hz and 128 Hz cut-off frequencies. On-board calibration impulse generator that can be used to field test sensor installations as well as to obtain calibration parameters for attached sensors (see section 3.3.3)

The system is based on the NI9205 250 kSamples/s, 16-Bit, 32-Channel DAQ from National instruments (National Instruments, 2019), and incorporates additional hardware specifically designed to suit seismic investigation and industrial vibration measurements.

This includes different filters, amplifications and sampling configuration. The system uses a PC/Laptop to visualize and record field data. Connection to the recording computer can be done using either USB 2.0 or TCP/IP (over either ethernet or Wi-Fi).

A LabView-based driver and operation software was developed to facilitate real-time data visualization as well as data collection. The operator can configure which channels to record, provide notes for installation of each channel and select the sample rate for data logging. In cases where frequency range expansion is required specific sensor serial numbers can be associated with each channel, and a look-up-table is used to retrieve the corresponding instrument correction curves.

4.3.2 External System Overview
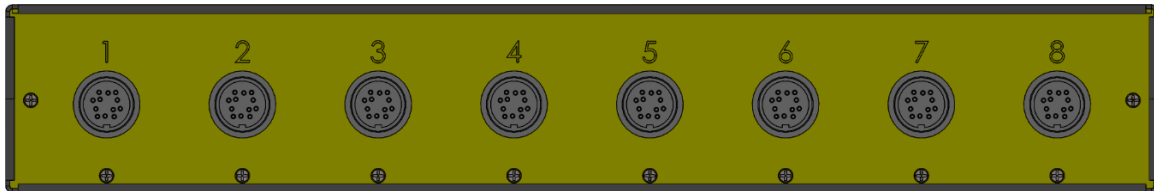
Figure 4.3: DYNAMate back panel

The back panel (Figure 4.3) contains the input ports for attaching the provided sensors. The ports are numbered form 1-8 and correspond to the channel numbers in the data logging software. All sensor ports, sensors and corresponding cables use polarized connectors to ensure proper mating. The DYNAMate connector is a Binder Female panel mount connector 09 0132 00 12 (Binder USA, 2019). Each input on every port has 20 kΩ input resistance and the port pinout is given in Figure 4.4.

Pin	Signal
A	Z-
B	X+
C	X-
D	Y+
E	Y-
F	N/C
G	CAL+/V_{Supply}+
H	CAL-/V_{Supply}-
J	N/C
K	Z+
L	N/C
M	N/C

Binder 09 0132 00 12
Connector Front View

Figure 4.4: DYNAMate sensor connector pinout.

Figure 4.5 shows the front panel, which contains a connector for data output, power supply connector and amplification and filter's cutoff selectors. The amplification controls the maximum recordable velocity before clipping occurs, and it supports 100, 10, 1, 0.1 and 0.01 mm/s with the DM 4.5 Hz sensors. The CAL position of the amplification knob enables connection between the internal calibration pulse generator and all sensors connected to the DAQ. The adjustable potentiometer to the right of the filter selector control the frequency of the calibration pulse. The selectable 4-th order low-pass filters have cutoff frequencies 32, 64 and 128 Hz. On the left side of the panel are the data and power interface ports. Computer connection is achieved using the USB 2.0 port, which also powers the internal ADC for the USB version. The TCP/IP version of DYNAMate has an Ethernet port in place of the USB connector and a coaxial connector for an external antenna for Wi-Fi connectivity.
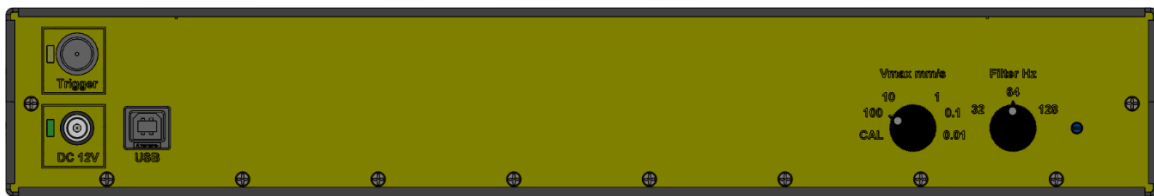
Figure 4.5: DYNAMate front panel

Internal electronics are powered by the DC 12 V plug (5.5/2.55 mm barrel connector). The nominal power supply voltage is 12 V; however, the system can support a supply voltage between 9 and 36 V. A red/green LED is provided beside the power supply port that monitors the polarity of the provided power supply, it will illuminate green when the power supply meets requirements, and red otherwise.

The trigger input is a 50 Ω coaxial BNC connector, and should be used with matching coaxial cable. It is internally isolated from the rest of the circuitry for up to 5 kV. The center pin of the coax is kept at 5 V DC through an internal pull up resistor. Triggering condition occurs when the BNC connector is shorted, and 0 V appears on the center pin of the connector (with respect to the connector sleeve).

In case of a short or overcurrent through the power supply unit, the internal protective fuse will blow to preserve the electronics. The fuse is MINI-ATO 2 A rated auto fuse and is located behind the power supply port. To replace the fuse the top lid should be opened by removing the 8 screws (4 on each side of the lid) and the fuse can be replaced.

4.3.3 System Modules Design

DYNAMate DAQ system utilizes a modular design. The block diagram of the system and its components can be seen in Figure 4.6. The system utilizes 24 channels of the NI9205 as data channels, with additional four channels that record the currently selected filter bank, amplification level, calibration line and trigger signal. Each of the 24 channels is processed using equivalent signal chains, one of which (Channel 1x) is highlighted in Figure 4.6. The processing chains are grouped in sets of three channels forming eight, 3-component data channels. The signal chain consists of:

- Input protection and calibration circuits.
- First preamplifier – provides a fixed a gain of approximately 5, this gain is adjustable to compensates for other stages along the signal chain.
- Second preamplifier or mixer amplifier – programmable gain of either 1 or 10. This module can be replaced by a mixing amplifier module to provide Galperin type sensor outputs (U-V-W).
- Filter bank – consisting of 9 filters: 32, 64 and 128Hz for each of the 3 components in each data channel.
- Post amplifier – Programable gain of x1, x10, x100 and x1000.
- Offset removal and Impedance buffer.
- NI9205 DAQ connected to a PC using either USB or TCP/IP (Wi-Fi or Ethernet).
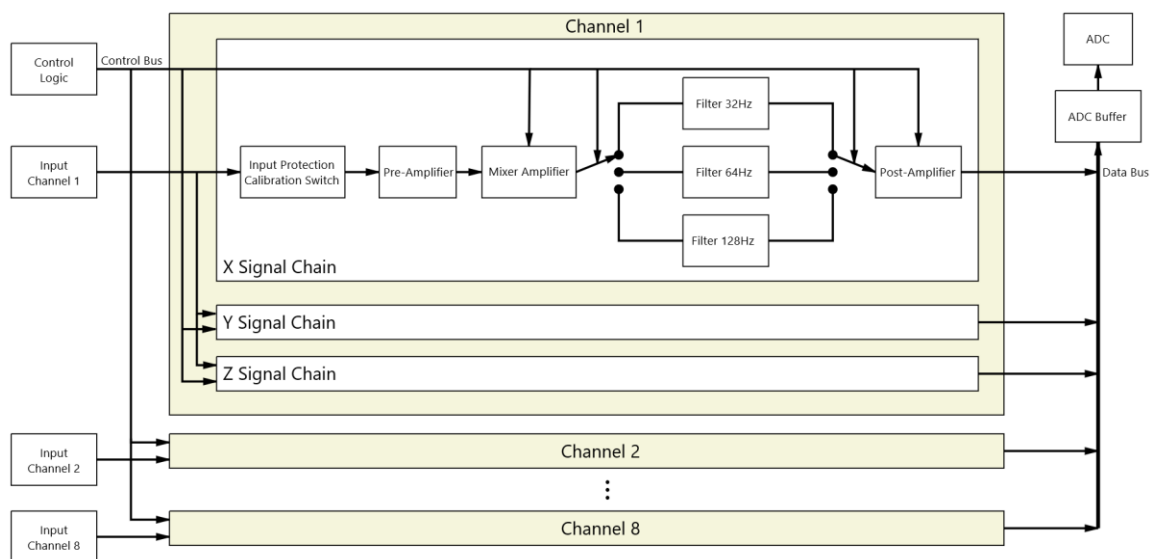
Figure 4.6: DYNAMate DAQ system functional block diagram

4.3.3.1 Power Supply and Isolated External Trigger

Power is provided to the DYNAMate system from an external 9-36 V DC connector. The minimum current rating of which is 1 A for the USB DYNAMate configuration and 2 A for the TCP/IP configuration. Figure 4.7 shows the power input stage of the system. The panel power connector is routed to the VIN+ and VIN- inputs and is protected with a Mini-ATO fuse before being distributed to the rest of the circuit.

Diode D2 detects the polarity of the input voltage and only opens the input relay if the polarity is correct. Output PS_OK is used to control an indicator dual-color LED, which is green for correct polarity or red when incorrect. A DH06S1205H 6 W DC to DC converter (Delta Electronics, 2019a) provides the 5 V power supply and 1.5 kV isolation for the trigger circuit.
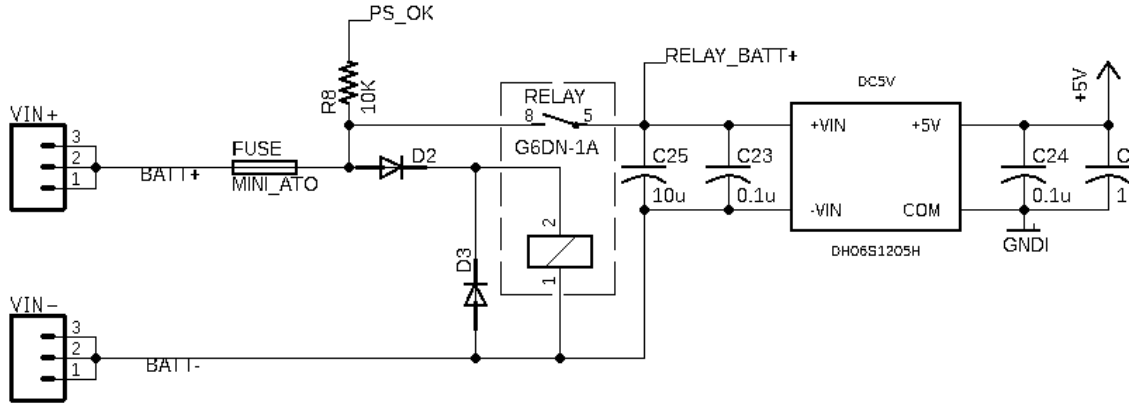
Figure 4.7: Power input stage of DYNAMate System

The +/-12 V power supply module of the DYNAMate system is based on the S24DE15 30W, Single/Dual Isolated outputs DC- DC Converter (Delta Electronics, 2019b). The schematic of the power supply is given in Figure 4.8. This device was chosen based on the low noise level introduced by the device compared to similar DC-DC converters. The schematic is based on the suggested implementation given in the data sheet for this device. The output of the DC to DC converter is +/-15 V which is reduced to +/-12 V using linear low-dropout voltage regulators: LM2940 and LM2990. All capacitors in the schematic and the input inductor serve to stabilize the +/15 V and +/12 V outputs and reduce the noise in the power lines.
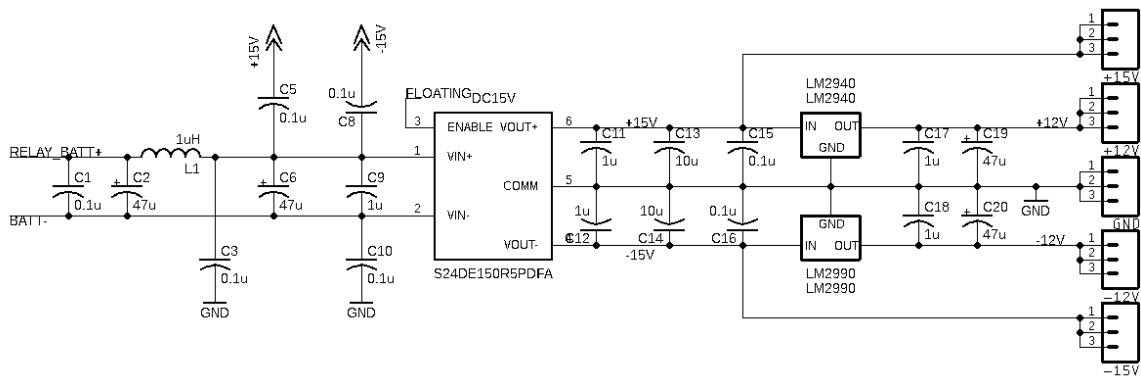
Figure 4.8: DYNAMate Power Supply schematic

Figure 4.9 presents the trigger circuit. It is isolated from the rest of the electronics in the DYNAMate system by the opto-coupler OK1, which has 1.5 kV isolation from the 5 V

power supply by the DH06S. The trigger port is internally protected to 70 V by the BAS70-04 diode and has an input impedance of 10 kΩ. R1 is an internal pull-up resistor that maintains 5 V on the trigger input. Triggering occurs when the input is brough down to 0 V (with respect to the isolated ground). The Schmidt-trigger NAND gates QC and QB (2 of 4 gates in a HD4093D device) are configured as a monostable multivibrator with an 'on' time constant determined by R3 and C21 and 'off' time-constant determined by R2 and C22. This generates a single impulse on the output trigger for every trigger input and ignores trigger inputs while the multi-vibrator is active. The final 2 gates of the HD4093D are used to invert the pulse. The output trigger line is isolated from the rest of the electronics by an opto-coupler, implemented using TLP291 from (Toshiba, 2019), which is followed by a voltage divider that generates 6 V on the TRIGGER_OUT line when no trigger is present and 0 V while the trigger pulse is active. The TRIGGER_OUT line connects to the NI9205 DAQ through the ADC buffer circuit. The trigger fire condition is processed in software (see Figure B.7).
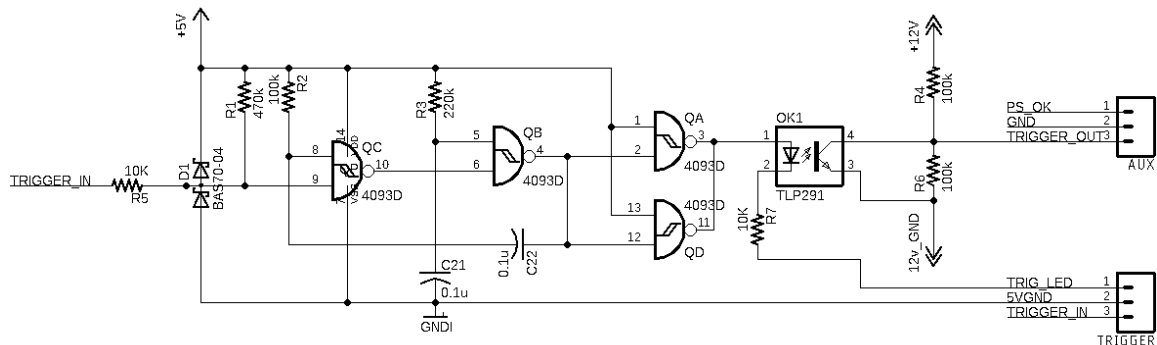
Figure 4.9: Isolated trigger circuit for DYNAMate

All three schematics given in Figure 4.7, Figure 4.8 and Figure 4.9 are implemented on a single PCB that is shown in Figure 4.10. Screw-terminal connectors with 3 positions are used to route power lines to and from the power supply PCB.
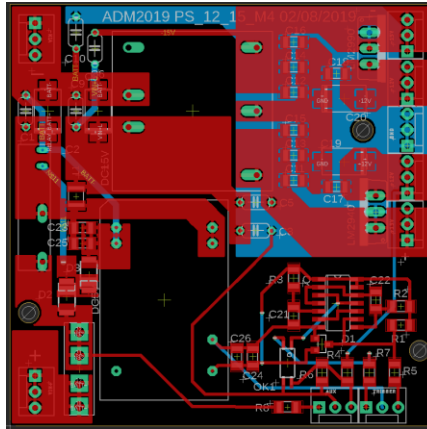
Figure 4.10: Power supply and trigger PCB for the DYNAMate System

4.3.3.2 Logic Control Unit

Filter selection and gain control for DYNAMate is achieved using rotary switches located on the front panel of the system (see Figure 4.5).

Filter selection uses a 3-position, 2-pole switch (see Figure 4.11). This switch selects the active filter bank and facilitates the output of a voltage signal that encodes the position of the switch. F1, F2 and F3 serve on-hot selection lines that active the filter banks. F1 activates the 32 Hz filter bank for all channels and components, with F2 and F3 activating the 64 Hz and 128 Hz filter banks respectively. The voltage divider that is formed by resistor RF4 and one of RF3, RF2 or RF1 encodes the selected filter with a specific voltage level on the output line FLT_ANA, which is recorded by the NI9205 ADC. The recorded value is used to update the DYNAMate user interface filter indicator. Voltage level of 1.7 V corresponds to 32 Hz filter selected, 3 V to 64 Hz and 4 V to 128 Hz.
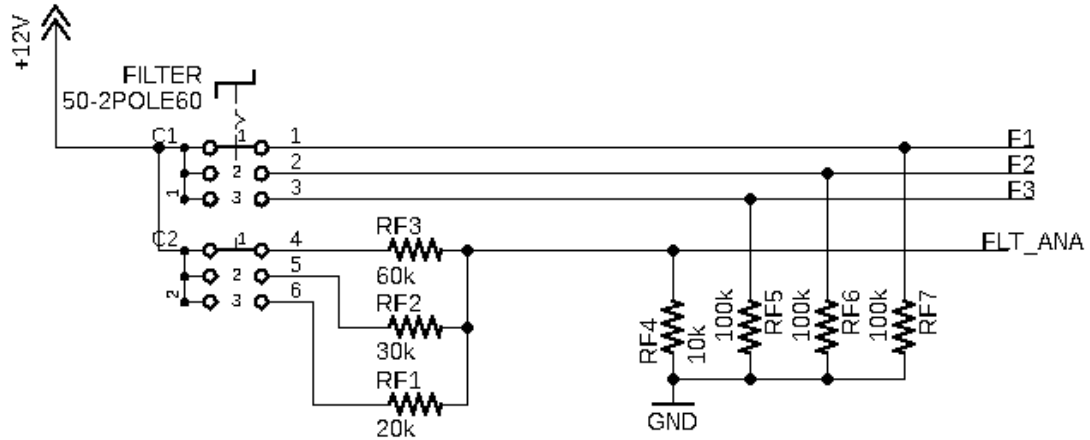
Figure 4.11: Logic Unit filter selection schematic

The maximum velocity range is selected using a second rotary switch with 9 positions. The controlling circuit schematic is given in Figure 4.12. The first and last positions of the switch are blocked. Position 2 initiates calibration mode by bringing the output line CAL_SELECTED to 12 V. The diodes in the circuit encode the position of the switch into the three digital output lines: A0, A1 and A2 according to Table 4.1. A2PRE is inverted using transistor T1 to produce A2, which needs to be active low (see Mixer amplifier/Additional Gain Stage section 4.3.3.5). The voltage divider that is formed by resistor RA9 and one of the resistors from RA10 to RA15 encodes the selected gain level with a specific voltage level on the output line AMP_ANA, which is recorded by the NI9205 ADC.

Table 4.1: Gain selection encoding. '1' represents a high logic level of +12V

Switch Position	Input Range	Gain	AMP_ANA [Volts]	Outputs			
				A0	A1	A2PRE	A2
2	CAL (100)	1	1.00	0	0	0	1
3	100	1	2.00	0	0	0	1
4	10	10	3.00	1	0	0	1
5	1	100	4.00	0	1	0	1
6	0.1	1000	5.00	1	1	0	1
7	0.01	10,000	6.00	1	1	1	0
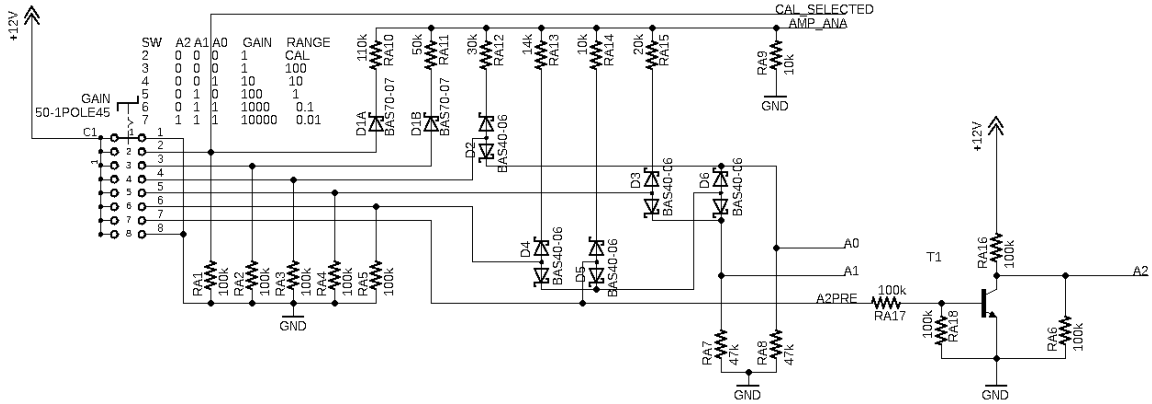
Figure 4.12: Logic Unit Gain selection schematic

The calibration pulse generator (Figure 4.13) utilizes a HD4093D Schmidt-Trigger NAND gate with RC feedback to generate a symmetric pulse train with a period from 1 to 8 seconds depending on the position of the adjustment potentiometer RC2. The remaining 3 gates of the HD4093D device are used as parallel inverting buffers and output the calibration signal on the CAL line.
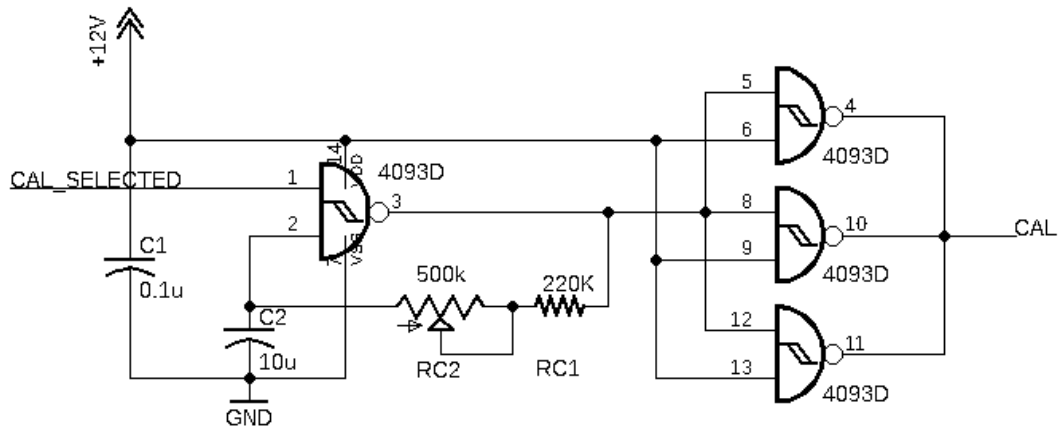
Figure 4.13: Logic Unit calibration pulse generator

The components of the logic unit are combined on one PCB board given in Figure 4.14. Power to the circuit, the 3 gain selection lines (A0, A1 and A2) and the 3 filter selection lines (F1, F2, F3) along with the calibration pulse, line is routed through a 12 pin 0.1" pitch male ribbon cable header.
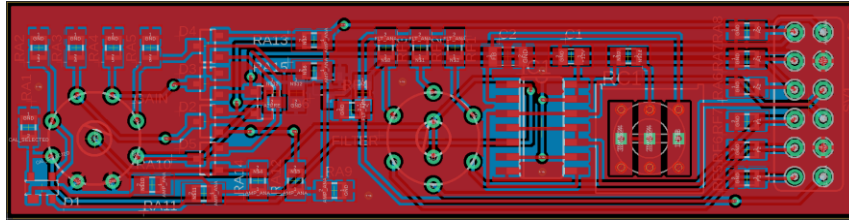
Figure 4.14: DYNAMate Logic unit PCB

4.3.3.3 Motherboard

The motherboard of the DYNAMate system (see PCB in Figure 4.17 and complete assembly in Figure 4.18) routes the control logic lines form the logic unit and power supply lines. Both logic and power supply lines connect using 3 position screw-terminal along the bottom edge of the PCB. Additionally, it handles input protection and the calibration of connected sensors.

The input protection for each differential input is up to 70 V as shown in Figure 4.16 using BAS70-04 diodes. The calibration pulse train generated by the logic unit is routed to two ADG1421 switches (Analog Devices, 2019a) as per Figure 4.16. The switches connect the +/-CAL_VOLTAGE to the input panel plug pins CAL+/-. The +/-CAL_VOLTAGE lines have a DC voltage, in this case +/-12 V and by using the Jumper shown in Figure 4.16 can be directly connected to the input plug to be used as a power supply for active sensors.
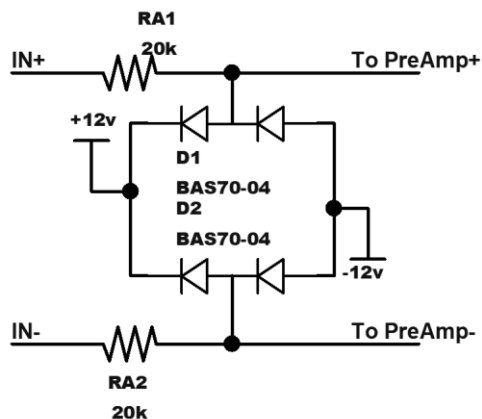
Figure 4.15: Input protection for one differential input
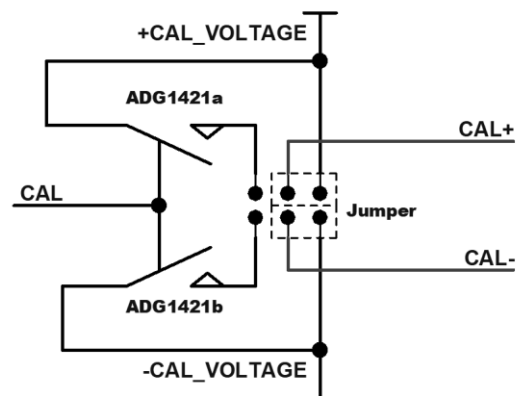
Figure 4.16: Calibration selector and switching

The motherboard PCB (Figure 4.17) is organized in 8 columns, one for each 3-component channel. Each column has 12 0.1" pitch 13 pin single row, low-profile female pin headers. They connect the signal chain modules in the following order from top to bottom:

1. Pre-amplifier.
2. Mixer/2nd pre-amplifier.
3. Filter PCBs grouped by filter frequency (32, 64, 128 Hz) and ordered by components X->Y->Z.
4. Post-amplifier.

The bottom row of the PBC contains the screw terminal for power, data and logic connections.
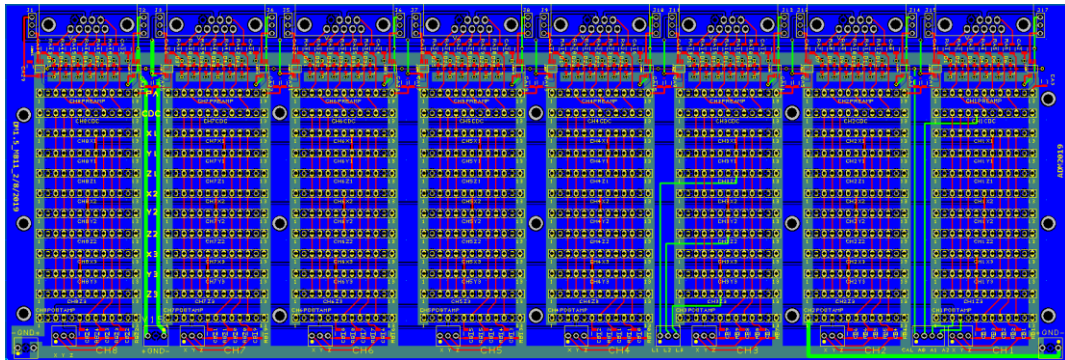
Figure 4.17: DYNAMate Motherboard PCB

Figure 4.18: DYNAMate motherboard and back panel plug complete assembly

4.3.3.4 Pre-Amplifier Stage

The preamplifier circuit given in Figure 4.19 is based on AD8226 Wide Supply Range, Rail-to-Rail Output Instrumentation Amplifier (Analog Devices, 2019b). This device was chosen for its superior noise performance compared to other devices on the market and the rail-to-rail output capability. The gain of the circuit is determined by the sum of the trimmer RP5 and fixed resistor RP6 and is given by equation (4.1). The range of gain based on the given resistor values given is from 4.8 to 7.1.

$$\mathbf{Gain} = \frac{\mathbf{49.5kOhm}}{\mathbf{RP5+RP6}} + \mathbf{1} \qquad\qquad \mathbf{(4.1)}$$

RA1, RA2 (Figure 4.15) together with CP1 form a 1st order low pass filter with a cut-off frequency of 400 Hz to remove high frequency noise before the amplification stage. Resistors RP1 and RP2 from Figure 1.19 balance the input to the AD8226 to circuit ground.
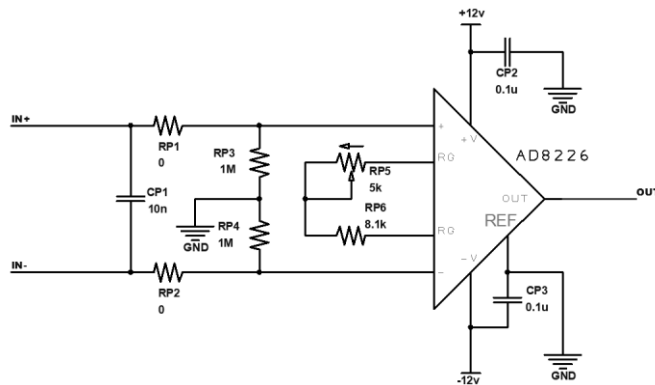
Figure 4.19: Preamplifier schematic
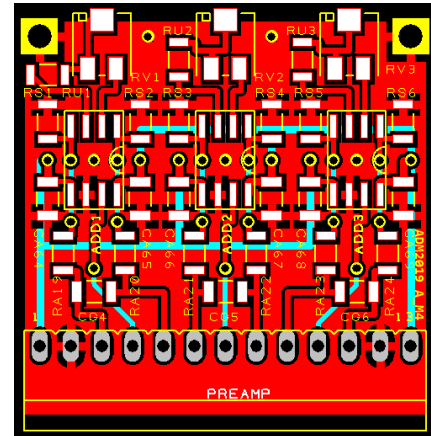
Figure 4.20: DYNAMate preamplifier PCB

4.3.3.5 Mixer amplifier/Additional Gain Stage

The mixer amplifier position was originally intended to be used to convert between the Galperin (UVW) coordinate system and standard XYZ coordinate system. In this configuration the slot is taken up by a secondary post-amplifier, based on the ADA4077

Low Offset and Drift, High Precision Dual Amplifier (Analog Devices, 2019c). The first amplifier is connected as a non-inverting amplifier with a gain of $10 \left(1 + \frac{RG2}{RG1}\right)$. The switch is an ADG1421 and it is controlled by logic line A2. A2 is pulled down by resistor RG3, and in this case the gain is 10, when A2 is 1 RG2 is shorted and the amplifier becomes a follower with a gain of 1. The second amplifier is configured as a buffer (follower after the first one). The PCB for this circuit is given in Figure 4.22
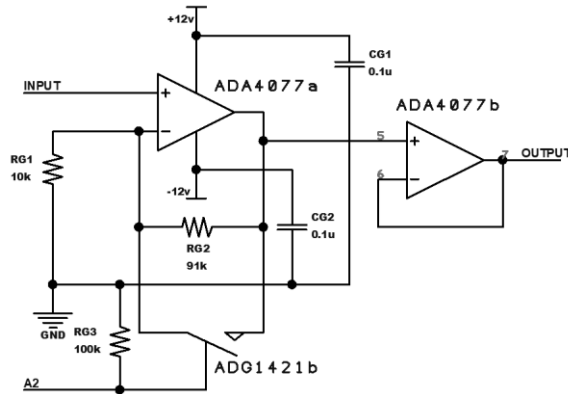
Figure 4.21: Secondary preamplifier schematic
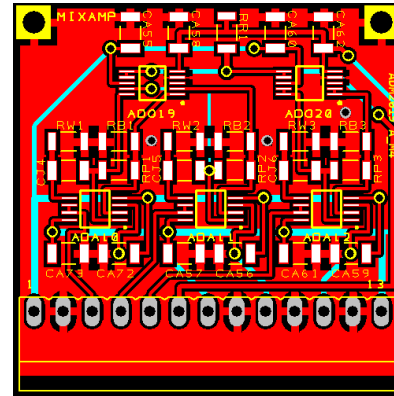
Figure 4.22: Secondary preamplifier PCB

4.3.3.6 Filter bank

The filter bank is constructed using 4th order Butterworth filters based on the Sallen-Key topology (see Figure 4.23) using an ADA4077 Dual amplifier. The bank consists of 32, 64 and 128 Hz filters, for each three component (XYZ) channel. There is a total of 9 filter PCBs, one for each frequency/component combination. The values of the filter's components required for achieve the cut-off frequencies are given in Table 4.2. Two ADG1421 switches enable each filter. The first ADG1421 switch pair turns on and off the power supply to the amplifiers to conserve power consumption. The second ADG1421 pair disconnects both the input and output from the signal chain. This allows for the 3 filters for each component to be connected in parallel. Figure 4.24 shows an example single component 128 Hz filter PCB. The filters' frequency response characteristics can be seen in Figure A.1 and Figure 4.31.
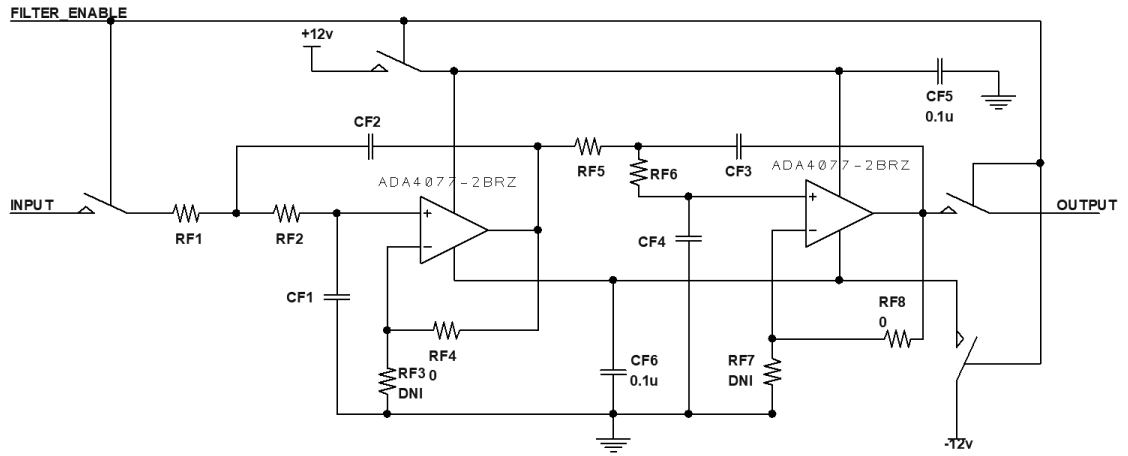
Figure 4.23: 4th order Butterworth Sallen-Key filter implementation schematic
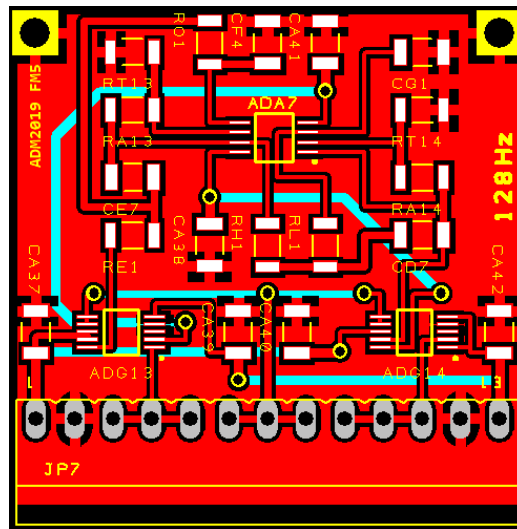
Figure 4.24: 4th order Butterworth Sallen-Key filter PCB

Table 4.2: Filter bank component values

Filter Cut-off	RF1 [kΩ]	RF2 [kΩ]	CF1 [nF]	CF2 [nF]	RF5 [kΩ]	RF6 [kΩ]	CF3 [nF]	CF4 [nF]
32Hz	14.3	76.8	100	220	17.8	63.4	470	47
64Hz	16.2	80.6	47	100	18.7	68.1	220	22
128Hz	16.9	86.6	22	47	20.5	75	100	10

4.3.3.7 Main-Amplifier Stage

The main amplifier stage is based on the AD8253 Programmable Gain Instrumentation Amplifier (Analog Devices, 2019d). The gain of this amplifier is determined by the logic levels on the A0 and A1 lines (see Table 4.3) that are generated by the logic unit and routed through the motherboard. Resistor R01 and capacitor C02 form a high-pass filter that removes any offset from the input to prevent the amplifier from saturating at high gain levels.

Table 4.3: AD8253 Gain selection

A1	A0	Gain
0	0	1
0	1	10
1	0	100
1	1	1000
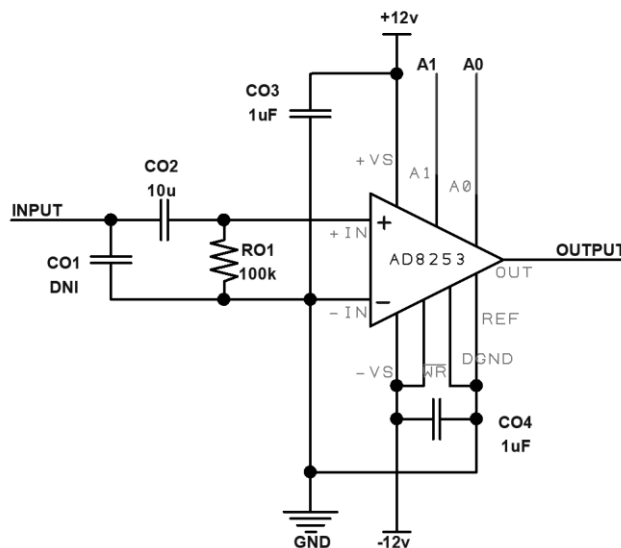
Figure 4.25: DYNAMate Post-amplifier schematic
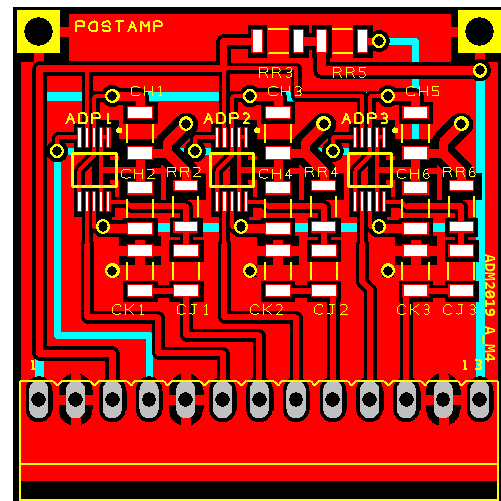
Figure 4.26: DYNAMate Post-amplifier PCB

4.3.3.8 ADC Buffer

The ADC buffer PCB (Figure 4.29 and Figure 4.27) provides a low impedance output connected to inputs of NI9205 ADC preventing large offsets from main amplifiers. Each of the 24 channels as well as the trigger line and the filter and amplification analog voltage level lines are connected using a custom-fitted ribbon cable to the buffer PCB. All channels on the buffer PCB use the same schematic (Figure 4.28) to interface to the ADC. Resistor RR19 and capacitor CC16 are located on the motherboard and form a high-pass filter to remove any remaining offset after the post amplifier stage. The outputs of all channels are combined into a standard DSUB37 connector that is mated with the NI9205 ADC module. The completed ADC buffer assembly can be seen in Figure 4.27.
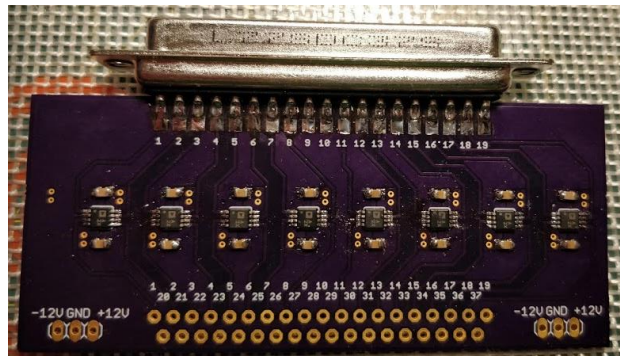
Figure 4.27: DYNAMate ADC buffer completed assembly
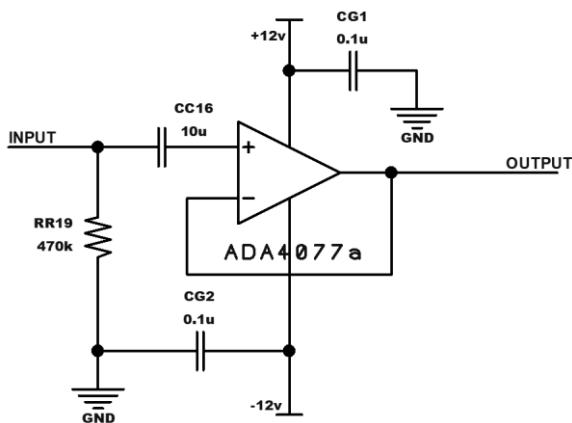
Figure 4.28: Single component ADC buffer amplifier
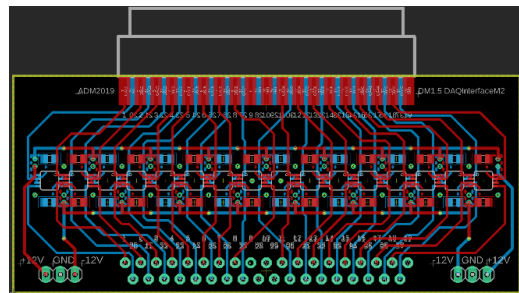
Figure 4.29: DYNAMate ADC buffer PCB

4.3.3.9 ADC module

The ADC module is based on the National Instruments NI9205 32 ±10 V, 250 kSamples/s, 16-Bit, 32-Channel C Series Voltage Input Module. Using a ready-made module, for optimization of development procedures as well as rely on already established data acquisition firmware. Simultaneous sampling for this number of channels is very expensive and using the more affordable and easier to configure system. Based on the 250 kSamples/s, the NI9205 allows for a maximum sample rate of 4 kHz when recording all 8, 3-component channels. The completed system assembly can be seen in Figure 4.30.

Two computer interface configurations of the DYNAMate DAQ system have been developed based on the interface chassis used with the NI9205 ADC:

- USB 2.0 Interface – using the National Instruments CDAQ-9171 Compact DAQ Chassis("cDAQ-9171 - National Instruments," n.d.).
- TCP/IP – using the National Instruments CDAQ-9191 Ethernet and 802.11 Wi-Fi CompactDAQ Chassis ("cDAQ-9191 - National Instruments," n.d.).
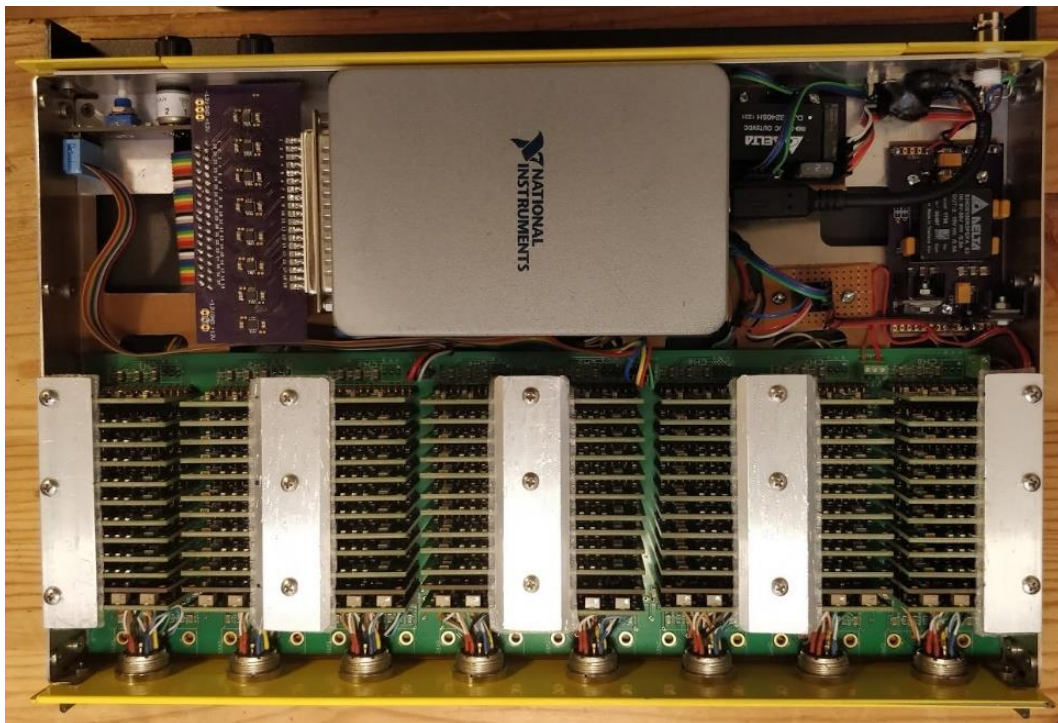
Figure 4.30: DYNAMate completed assembly with the top lid removed

4.4 DYNAMate Calibration and Validation

4.4.1 Calibration of System Gain

The DYNAMate system is designed to work with the accompanying 4.5 Hz DYNAMate sensors. Based on the design of these sensors a generator constant of 20 V/m/s is set for each individual sensor component. To measure and record data directly in velocity units (mm/s) the DYNAMate system provides a base (lowest) gain of 5, resulting in overall sensitivity of the system and sensor combination of 100 V/m/s. Measured values are further scaled to reflect the velocity ranges of interest. This scaling is achieved using precision programmable amplification in steps of 10, from 10 to 10000. Additionally, software scaling is applied to the sampled signals to convert the recorded voltage signal into velocity measurement, as described in section B.2.

Using precision programmable amplifiers allows for single calibration to be performed only for the base gain of the system within the passband. This calibration is done by introducing a sinusoidal signal with a known amplitude to the input of the DYNAMate system and recording the output of the signal chain for each component. For gain calibration a 5 Hz sine wave is used with a peak to peak amplitude of 1 V. With the gain of both the secondary pre-amplifier and the post amplifier set to 1, the amplitude of the output of the ADC buffer is measured and the pre-amplifier potentiometer is adjusted until the overall gain of the channel is 5 +/-1%. This combined with the DM 4.5 Hz 20 V/(m/s) gives a velocity conversion of 0.1 V/(mm/s) at system gain of 1, and 1 V/(μm/s) at the maximum gain of 10,000. The gain value is then confirmed at 3 and 10 Hz for each component.

4.4.2 DYNAMate frequency response estimation

The frequency response of the system is obtained by introducing a known sinusoidal signal to the input of the DYNAMate system using a function generator. Additionally, the input signal is recorded by one of the free channels of the NI DAQ ADC of the DYNAMate system and recorded along with the output of the component signal chains. The frequency of this signal is varied between 1 mHz and 500 Hz and the corresponding

voltage output of the signal chain for each component is recorded. All measurements are done on the lowest gain setting (5). The peak to peak amplitude of the input sinusoid is kept at 1 V for all frequencies.

To obtain the peak to peak amplitude of the output sinusoids, the recorded timeseries are fitted with a sine function using non-linear least mean squares. This allows accurate estimation of the frequency as well as the amplitude of the output sinusoids. The ratio between the input and output amplitudes are then calculated for all frequencies resulting in the system's gain-frequency response.

The measurements are repeated for all three available filter selections: 32 Hz, 64 Hz and 128 Hz. The mean response curve along with the spread, given by 3 times the standard deviation of the values, is given in Figure 4.31, which also gives the combined response of the 2 first order high-pass filters in the signal chain. . The three high-frequency drop-offs are the gain-frequency responses of the three low-pass selectable filters.

Due to the filter resistors values having an accuracy of 1% and the capacitors values having an accuracy of 5% there was a variation of the cut-off frequency of the filters.
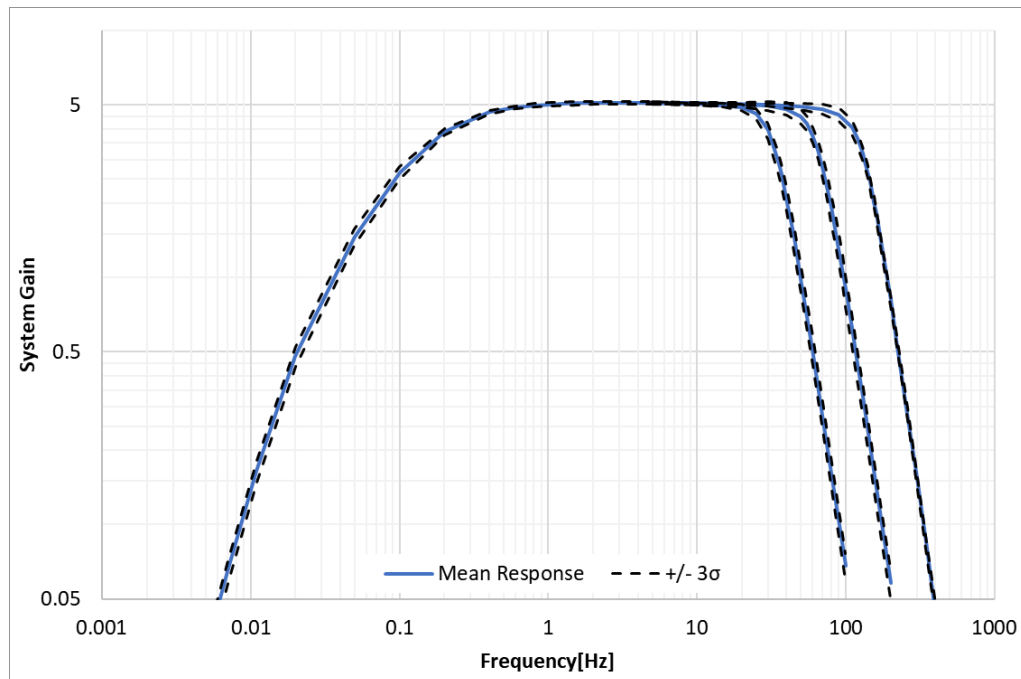
Figure 4.31: DYNAMate mean gain-frequency response for all selectable filters

4.4.3 DYNAMate hardware filters

4.4.3.1 High-pass filters

There are two high pass filters in each component's signal chain. They are first order RC (resistor-capacitor) filters with component values given in the table below. Due to inexact match between the design capacitor value and the installed capacitor value the corner frequencies do not match exactly.

The measured values given in Table 4.4 are obtained by first estimating the cutoff frequency of the higher frequency filter (#1) and then correcting for the roll-off slope. The second filter cutoff is obtained from the corrected response curve

The ADC buffer filter has a cut-off frequency of 0.016 Hz and the preamplifier high-pass filter has a cut-off frequency of 0.159 Hz. Combined, the -3 dB point at low frequencies is 0.17 Hz with a 40 dB/dec roll-off and at high frequencies it is based on the filter selection – 32, 64 or 128 Hz with an 80 dB/dec roll-off.

Table 4.4: DYNAMate high-pass filters

Filter	#1	#2
R[Ω]	100k	1Meg
C[Farad]	10u	10u
Theoretical -3dB Frequency [Hz]	0.16	0.016
Measured -3dB Frequency [Hz]	0.176	0.0185

4.4.3.2 Low-pass filters

The low-pass filters are 4th order Butterworth analog filters implemented using a standard Sallen-Key topology as given in Figure 4.23. The table below summarizes the cutoff frequencies as measured from the frequency response of each individual component of the prototype DYNAMate System.

Table 4.5: DYNAMate Low-pass filters

Channel Component		Filter Bank			Channel Component		Filter Bank		
		32Hz	64Hz	128Hz			32Hz	64Hz	128Hz
Ch1	X	30.9	62.5	123.9	**Ch5**	X	32.2	60.1	123.3
	Y	31.6	60.8	124.5		Y	32.5	61.5	124.4
	Z	31.0	62.1	123.0		Z	30.9	61.7	122.1
Ch2	X	31.8	61.1	124.0	**Ch6**	X	31.6	61.5	120.7
	Y	31.9	62.3	123.2		Y	31.8	61.2	121.9
	Z	31.5	60.6	122.8		Z	31.8	61.2	122.5
Ch3	X	32.1	61.4	123.5	**Ch7**	X	30.6	58.8	121.2
	Y	32.1	61.2	124.8		Y	32.7	61.8	122.7
	Z	31.3	60.0	123.8		Z	32.4	61.4	121.8
Ch4	X	31.6	61.1	120.9	**Ch8**	X	31.0	61.7	122.9
	Y	32.4	63.0	120.0		Y	32.1	61.3	123.5
	Z	31.8	61.8	119.5		Z	32.7	62.4	123.1

The largest variability in cutoff frequencies is observed for the 128 Hz filter bank. This can also be clearly seen in figure 1 by the standard deviation limits given for the 128 Hz filter response. This is due to the uncertainty in component values and further adjustment may be required to better tune the performance close to the cutoff frequency.

4.4.4 DYNAMate Validation using Geode Seismometer and L4C-3D sensor

To validate the performance of the DYNAMate system a comparison between it and the well-established Geode Seismograph is undertaken. Both systems are connected in parallel to a L4C-3D velocimeter with damping set to 0.6 and both systems are set to their lowest possible gain.

The calibration windings of the velocimeter are connected a function generator that outputs a sine function with frequency between 50 mHz and 50 Hz. The amplitude of the calibration signal is adjusted to ensure no clipping occurs in either system for all test frequencies.

Both systems record the sensor output, and sinusoidal functions are fitted, as discussed above, to the resulting waveforms to estimate the output amplitude and accurate frequency. These amplitudes are then plotted in Figure 4.32, with DYNAMate results shown in blue

and Geode in orange. It is evident that there is a significant difference between the results from the two systems.

The L4C-3D velocimeter with damping of 0.6 has a slight overshoot in its frequency response at its corner frequency (1 Hz), is well described by the DYNAMate system. The same cannot be observed from the Geode result, due to the drop-off in gain at 1 Hz that is characteristic to the Geode system. The DYNAMate system, in contrast has a normalized gain of ~1.0 at 1 Hz.

To correct that effect and allow for the validation of the DYNAMate system, and instrument response correction is utilized similar to the frequency domain approach described in section 3.4. Figure 4.33 gives the gain-frequency responses of both systems. These ratio of the two responses is used to establish a correction curve. Using this correction curve the L4C-3D test data from the geode is adjusted and is given by the dashed line in Figure 4.32. It is evident that the correction as accounted for the drop-off in gain of the geode and the two systems now show nearly identical results.
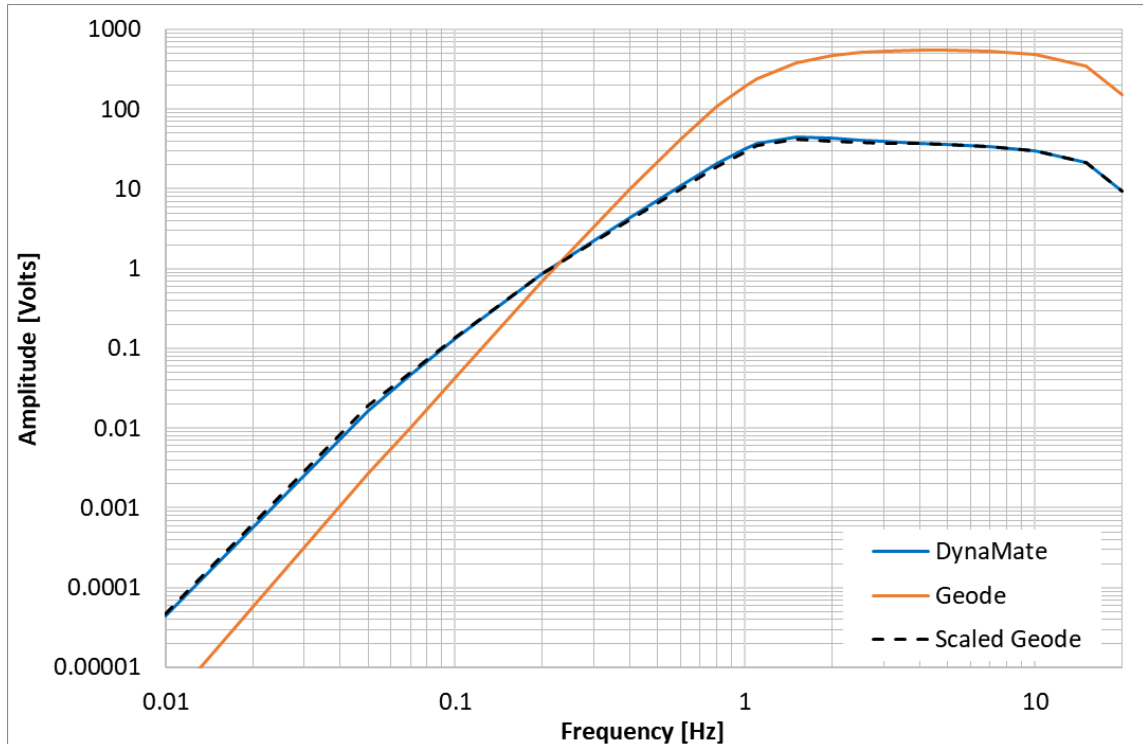
Figure 4.32: System Validation using L4C-3D velocimeter
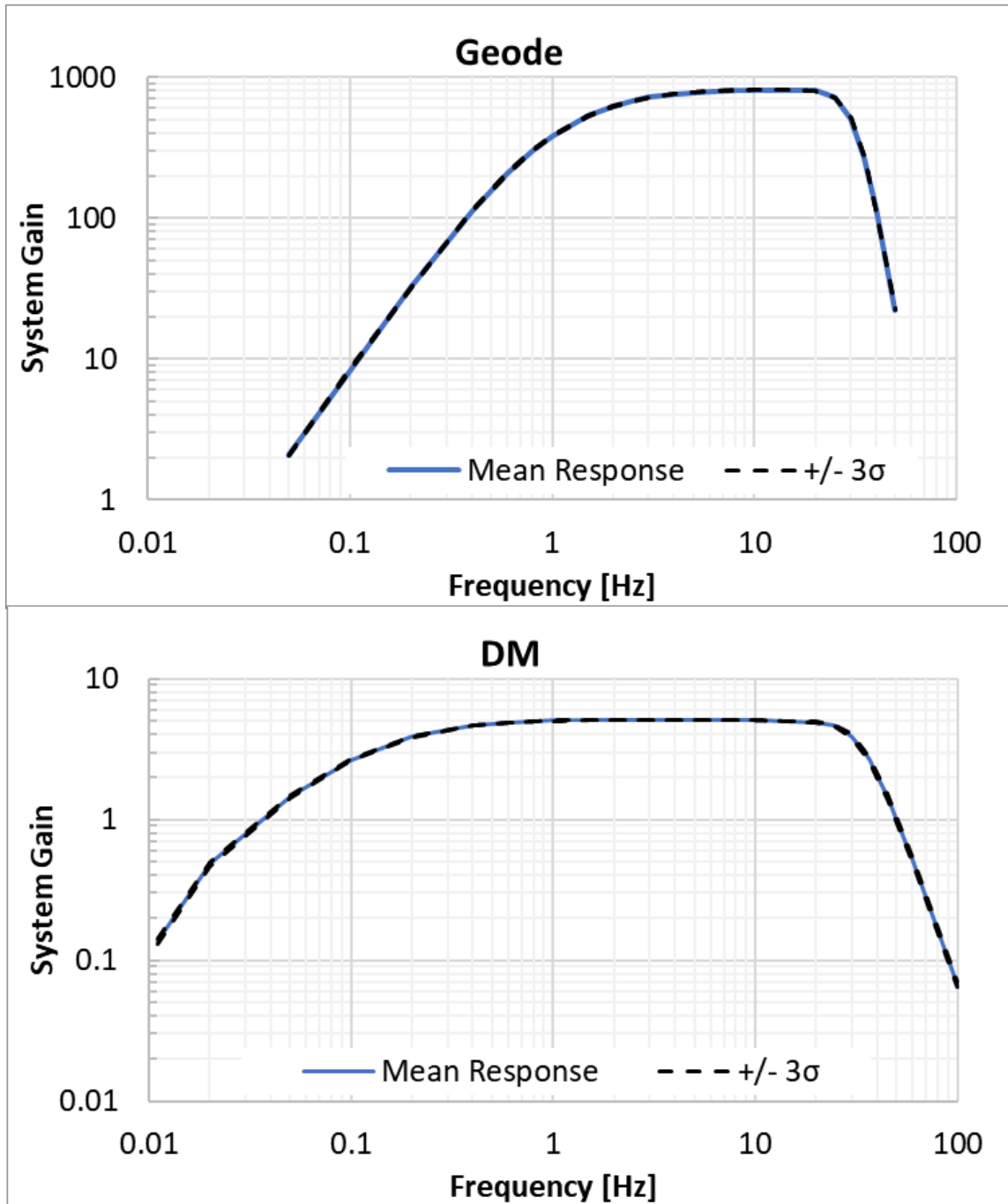
Figure 4.33: Geode and DYNAMate (DM) system responses

The close match between the corrected Geode data and DYNAMate data serves as a validation of the performance of the DYNAMate system. The output accuracy in terms of velocity, depends on accurate knowledge of the sensor's generator constant.

4.4.5 DYNAMate validation through field studies

Table 4.6 gives a few examples of field data collected with both the DYNAMate data acquisition system and the Geode seismograph. The recordings are taken using both the L4C-3D and DM 4.5Hz velocimeters during the Wilmont field study. Each test point is measured using 4 sensors. From top to bottom in each pane the HVSRs are from: L4C-3D North, DM 4.5 Hz North, L4C-3D South and DM 4.5 Hz South.

Recordings are done sequentially, first the sensors are connected to the Geode seismograph, then moved to the DYNAMate system without repositioning the sensors. Therefore, some differences between the two recording devices are due to temporal changes in the noise spectra at the recording site, as the two devices do not operate simultaneously. However, they are representative of the same soil structure as the sensor location and installation is not altered between recordings. The major difference in the recorded HVSR lies in the high frequency sections of the curves, where the geode has a significantly reduced response and therefore records mostly noise, whereas the DYNAMate can produce clear HVSR peaks at these higher frequencies. Additionally, the higher sensitivity at high frequencies of the DYNAMate system gives rise to HVSR peaks with higher amplitudes than the ones recorded at the same location with the Geode.

Table 4.6: Sample Field study verification using HVSR curves recorded with both the Geode(left) and DYNAMate(right) systems.
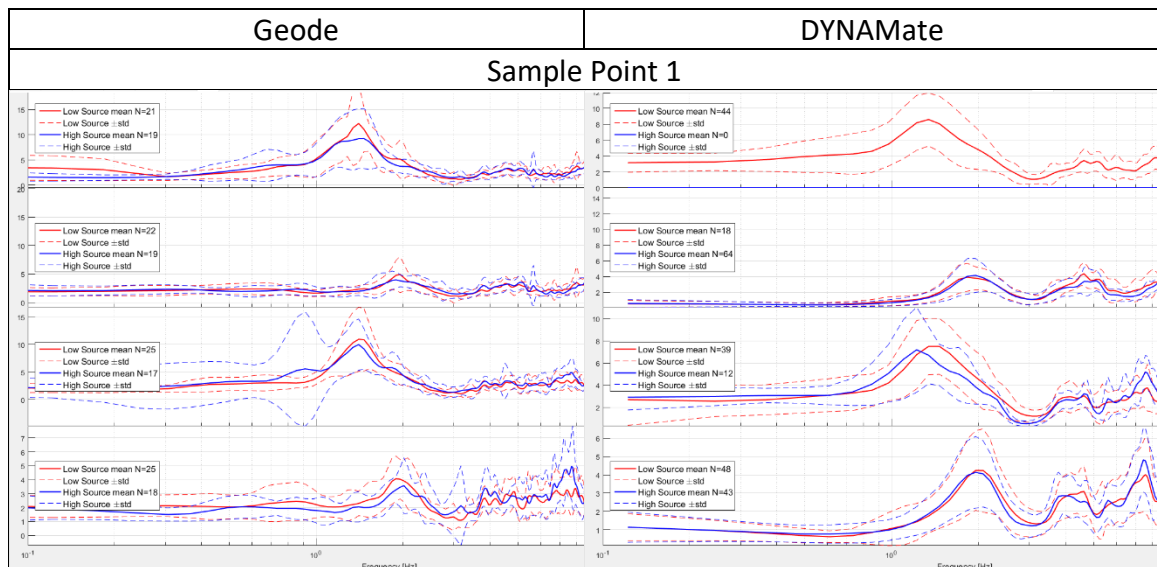
Sample Point 2
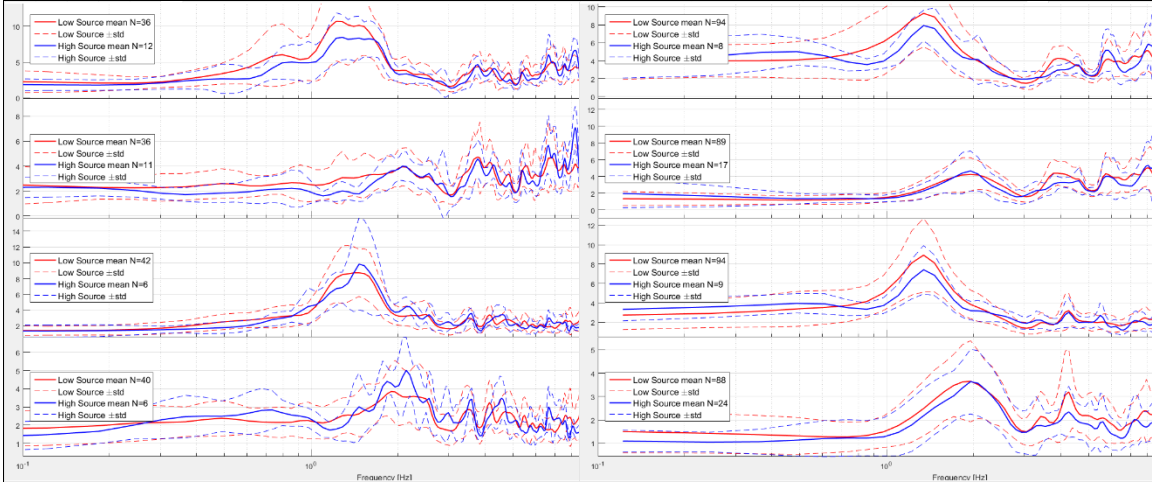
Sample Point 3
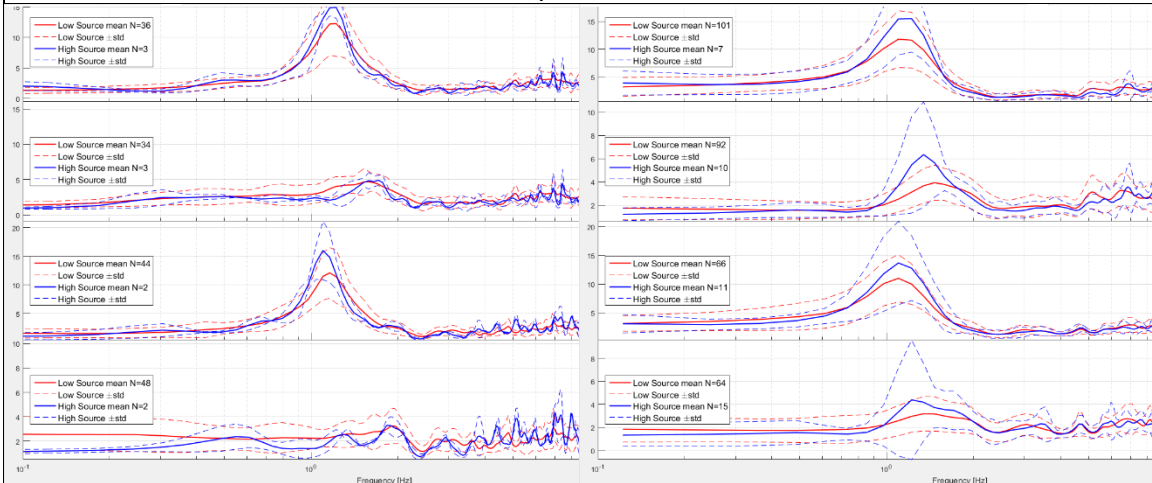
Sample Point 4
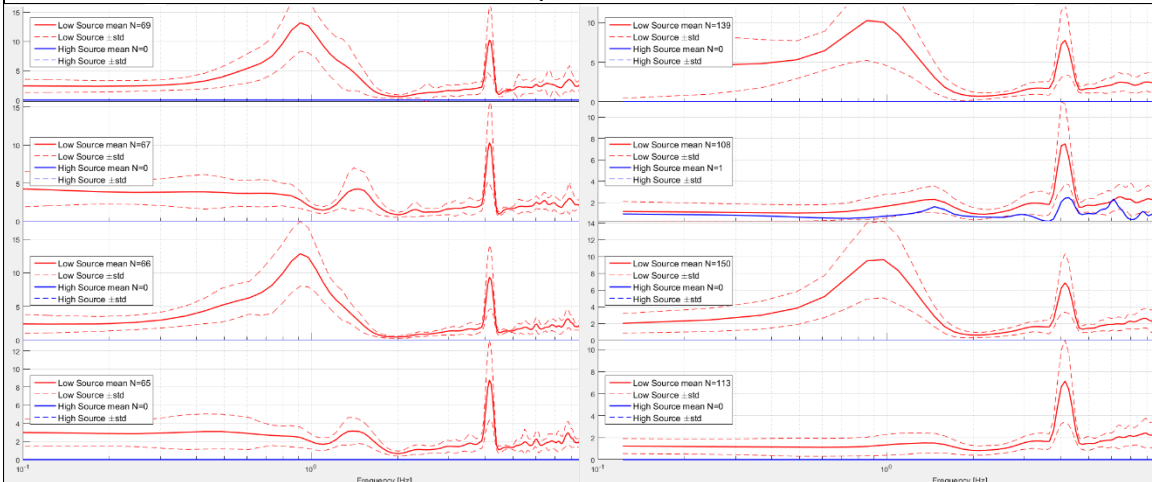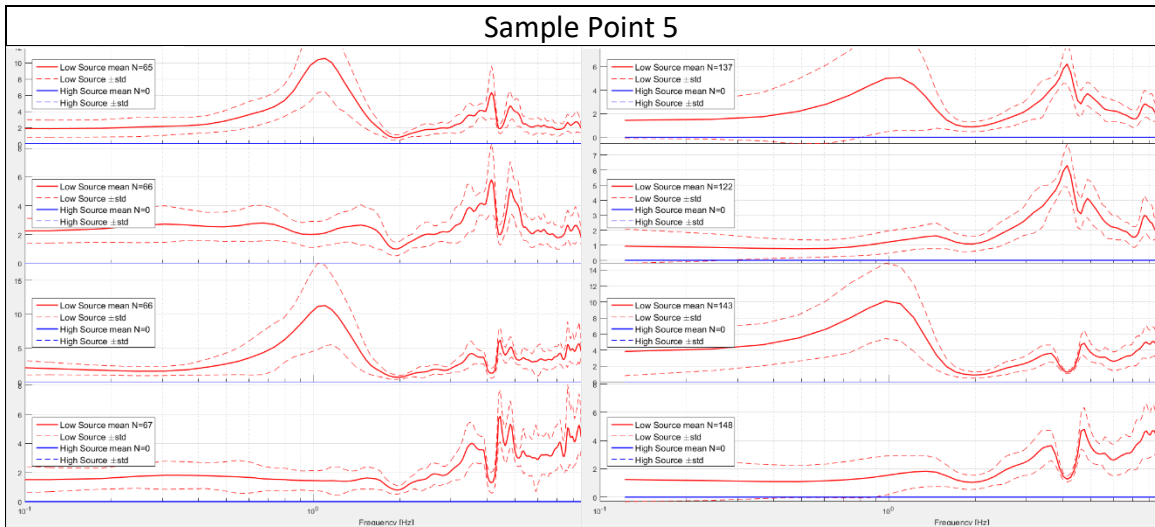
An additional verification was performed using the Tromino recorded. In this scenario the DYNAMate system was used with a Guralp 40T 40 sec seismograph and the results are compared to the output of the Tromino for two different test points as given in Figure 4.34.

Overall there is a very good agreement between the results from both systems and the major difference can be seen at low frequencies, below 1 Hz, where the Tromino, which uses 4.5 Hz geophones as a measurement device, exhibits a much larger standard deviation compared to the DYNAMate system using a Guralp 40T
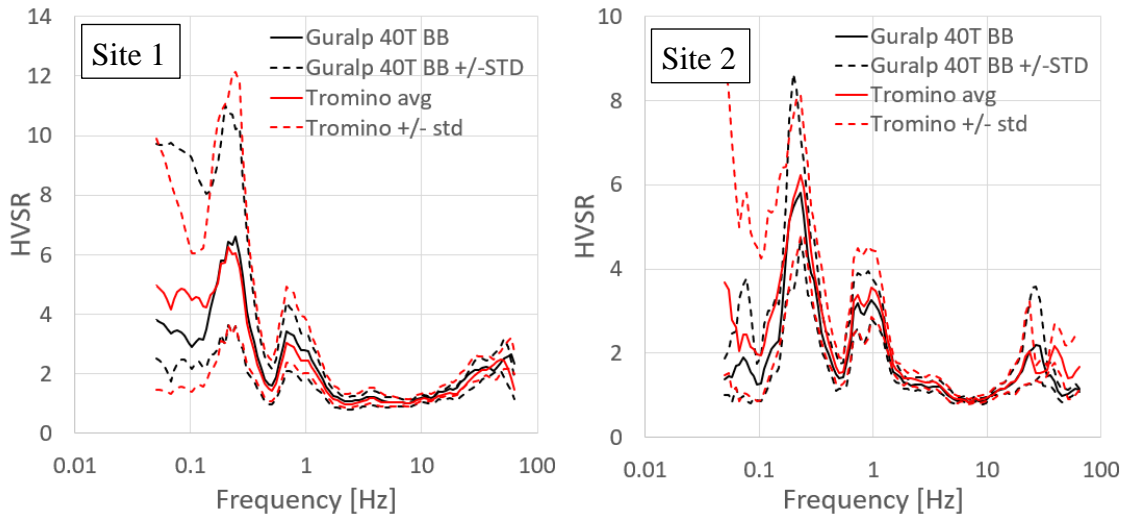
Figure 4.34: Field HVSR results from the DYNAMate system equipped with a Guralp 40T and compared with HVSRs from Tromino at two different sites

4.5 Conclusion

This chapter described the requirements and design choices made to produce the DYNAMate vibration data acquisition system. The technical solution was adapted to the general requirements for seismological and industrial equipment. The DYNAMate DAQ can handle different types and number of sensors using programmable configurations. The developed hardware system has been tested and verified and the third prototype iteration of the system has been successfully utilized in several HVSR field studies as well as several foundation vibration assessments and vibration attenuation studies. The design is based on existing hardware modules and software libraries and is suitable for mass-production.

Visualization, logging and data processing software was developed to accompany the DAQ system, described in Appendix B, and perform the following tasks in order to satisfy the rest of the initial requirements:

- Data Synchronization
- Dynamic channel allocation
- Real-time and post-processing-based Instrument Response correction
- Data Logging in an accessible format (TDMS, XLSX)
- Real-time data visualization
- Data Processing, including the conversion from the standard velocity input to acceleration and displacement and perform basic spectrum analysis.

Calibration of the DYNAMate DAQ is done using a function generator and the operation of the system is verified using parallel, simultaneous measurement of a L4C-3D velocimeter with a Geode seismograph. The instrument response of the Geode seismograph is corrected using IRC before comparison of the recorded data is made.

Additionally, field data is presented showing the comparable results between the DYNAMate system and Tromino and Geode measurement systems. In theses cases both L4C-3D and Guralp 40T sensors were used.

Chapter 5. Field Studies

5.1 Introduction

Seismic waves characteristics change as they propagate through the uppermost layers of soil and rock according to the specific shallow geological structure at a given site, and thus the transfer function of the site changes as well. The transfer function of a site relates ground motion characteristics at the surface to the incoming seismic waves, which can involve increases in the duration and amplitude of earthquake shaking within a narrow frequency band (Molnar et al., 2014). The transfer function is governed by the mechanical properties of the rock and soil layers as well as the rock topography. Soil layers may alter the amplitude or frequency composition of incoming seismic waves, and the particular shape of the bedrock at the site can introduce focusing, dispersion, reverberation and other effects (Davis et al., 2000; Gao et al., 1996; Hartzell et al., 2010).

Among all other elastic parameters of materials, shear-wave velocity (Vs) is the best indicator of the soil/rock stiffness. The soil structure is determined mainly by the vertical variation in V_S. To evaluate these velocity profiles, multi-channel analysis of surface waves MASW survey is used. In this chapter, case studies are presented for evaluating the dynamic soil properties using MASW and determining the site transfer function employing Horizontal-to-Vertical Spectral Ratio (HVSR).

The study areas for the HVSR and MASW surveys were north and west of Lake Ontario as shown in Figure 5.1. The selection of study site was informed by the bedrock topography and surficial drift thickness maps presented in MRD207 (Ontario Geological Survey, 2006) as well as the surficial geology map of Southern Ontario given in MRD128-Revised (Ontario Geological Survey, 2010). This area is part of seismically "stable" continental interior (Fenton et al., 2006). Geologically, it is situated in the Interior Platform, characterized by relatively thin (1.0 km), flat-lying calcareous Paleozoic strata (Williams, 1984; Williams et al., 1991). This region is underlain by a broad northeast-trending basement arch, comprising the Algonquin and Findlay Arches, separating the Appalachian (Allegheny) and Michigan sedimentary basins (Easton and Carter, 1995). The Precambrian

rocks that underlie the sedimentary platform are part of the Grenville Province of the Canadian Shield.
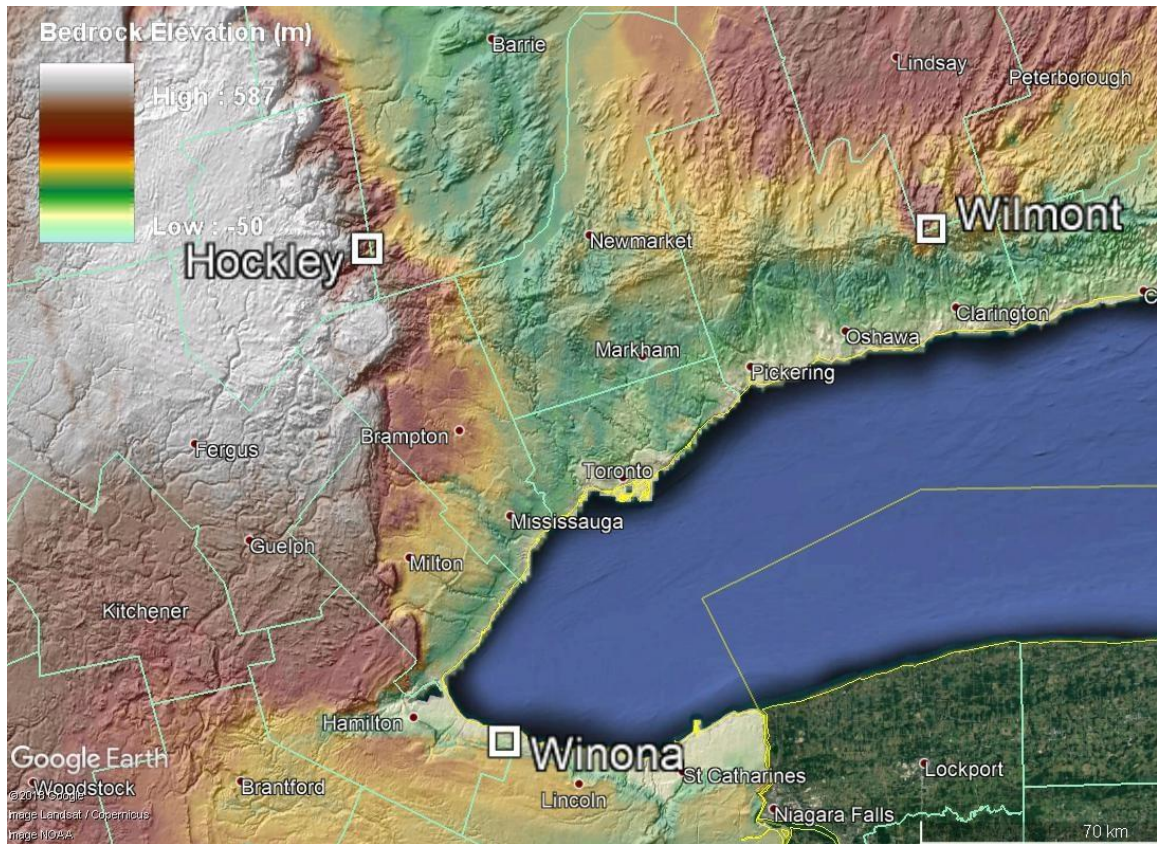
Figure 5.1: Bedrock elevation in the study area based on MRD128 (Ontario Geological Survey, 2010) and MRD207 (Ontario Geological Survey, 2006)

5.2 Methodology

Study sites were selected using MRD207 (Ontario Geological Survey, 2006) bedrock and drift thickness map for the area of Southern Ontario. Zones with large changes in bedrock topography, i.e. peaks and valleys in the bedrock were located. From the available locations with such features, further selection was based on avoidance of urban development to minimize cultural noise, existence of accessible roads spanning the features of interest and considering limitations related to the logistics of performing the studies. To investigate topography effects from both the ground surface and the bedrock interface, HVSR

measurements were conducted, and to obtain relevant velocity profiles MASW was utilized.

One of the main advantages of HVSR is the possibility to directly obtain at least some of the sites' dominant and secondary resonances. It is a suitable technique to evaluate the characteristics of the local site response through direct observation of seismic ground motion during local and regional earthquakes. Such studies are usually applicable to areas with high seismicity. In areas with low seismicity, like Central Ontario, ground vibration from small earthquakes and ambient seismic noise are convenient tools to estimate the effect of surface geology on seismic motion. Therefore, records of microtremors at the ground surface were used to find the quasi-transfer function of the site (QTS) in the frequency domain. The QTS is obtained by normalizing the site horizontal spectrum by its vertical spectrum. The HVSR usually provides a clear peak that is correlated with the fundamental S-wave resonant frequency for the uppermost layer, and the observed peaks correlate with the depths to the nearest high contrast boundary.

5.2.1 Field Work and Data Collection

MASW profiles were obtained using a Geode 24 channel seismograph. The locations for MASW studies were chosen on available flat areas within the study site, where the MASW data was considered helpful to future HVSR investigations. Twenty-four 4.5 Hz geophone receivers were spread 5m apart, resulting in a total spread length of 120 m. The strikes were performed on either side of the spread line at distances of 10, 20 and 30 m. Receiver spacing (dx = 5m) was chosen to avoid any possible spatial aliasing of the shortest wavelength recorded and to maximize the effectiveness of dispersion analysis. The source for the strike was a 10lb sledgehammer impacting an aluminum plate embedded in the ground. Using 10 consecutive impacts at each source point, the records were stacked and data processing was conducted using both SurfSeis (KGS, 2019) and Geopsy (SESAME Geopsy Team, 2019) software packages.

HVSR measurements were performed using L4-3D 3-component sensors, as well as DYNAMate 4.5 Hz velocimeters (DM 4.5 Hz, see section 3.3). Additionally, data was recorded using both DYNAMate 2.0 DAQ system and the Geode seismograph. The use of

multiple instruments was done as a form of verification of the performance of the prototyped DYNAMate DAQ system (see Chapter 3, Chapter 4 and Appendix B). HVSR results presented here represent the average of both DYNAMate and Geode measurements and exclude results from the DM 4.5 Hz as these sensors did not reveal the fundamental 1 Hz or lower peaks present in the three sites presented here. This was expected as the signal level at 1 Hz for the DM 4.5 Hz is too small and no longer distinguishable from usable signals in that range.

The HVSR measurements were taken along the preselected bedrock features. Data collection was limited to available straight roads in the area and the point spacing was governed by the condition of the third-class road shoulder and maximum spread of the available sensor cables. In most cases, each HVSR recording was done using two sensors: one referred to the as the north sensor (N), and one referred to as the south sensor (S). This was done to expedite data collection. In some cases, only one sensor was used, either due to inability to properly position a second sensor, or after the fact where single sensors were used to fill in gaps in the HVSR line. Table 5.1, Table 5.2 and Table 5.3 list the geographical locations for all test points along with the sensors used and number and duration of the recordings.

5.2.2 Data Analysis

Analysis of HVSR data was performed using a custom developed MATLAB GUI that incorporates the following tasks:

- Filtering: which involves data conditioning and noise removal.
- Windowing: this includes selection of window duration and removing end effects with a Hanning window.
- Spectral Smoothing: this is achieved by applying the band-pass filter based (BPF) spectral smoothing.
- Source Separation: this is conducted for low noise levels only.
- HVSR Analysis: this is achieved by performing statistical analysis of HVSR ensembles.

The collected HVSR curves were gridded and interpolated to produce maps for the Hockley Hills and Wilmont studies including distance, frequency and amplitude of the transfer function. Linear interpolation was used to increase the distance sampling to 100 m using the originally sparsely distributed measurement points

Analysis of MASW data was performed using Kansas City SurfSeis software and verified using Geopsy MASW plugin. Multiple profiles were produced using SurfSeis for all performed strike's offsets and the results were averaged to obtain the final profiles. In contrast, Geopsy processes the dispersion curves from all strike location for a given MASW spread were analyzed simultaneously.

5.3 Field Study Sites

5.3.1 Winona – HVSR for surface slope using escarpment

To investigate the effects of surface topography, a part of the Niagara Escarpment near Winona, ON was studied (see Figure 5.2). Data was obtained using DYNAMate DAQ 2.0 (with lowered low-frequency cutoff of 0.017 Hz) and a combination of L4-3D and Guralp 40T (40 sec period seismograph). The study demonstrated the applicability of low frequency sensors for HVSR studies. However, the analysis of the results revealed the susceptibility of these sensors to wind noise. The method of installation of such sensors is particularly important to ensure protection for the environmental effects, especially strong wind, to facilitate appropriate measurements. However, in some cases transfer of excitation from nearby power-line poles or the escarpment itself are unavoidable. Long period sensors should be used as per manufacturer recommendations, i.e. in seismic station vaults or boreholes to be protected from wind disturbances on the sensor itself. Wind effects on surrounding vegetation, infrastructure and topography will still affect the recordings and needs to be accounted for in post-processing of the results. Test point locations and experimental setup (sensor type and duration of recordings) are given in Table 5.1

The area is characterized by MRD128 (Ontario Geological Survey, 2010) as primarily very shallow bedrock overlain by a thin layer of till and sections of glaciolacustrine deposits and is part of the Niagara escarpment formation. The L4-3D and the Guralp 40T were connected simultaneously to the DYNAMate DAQ system. The sensors were installed on

concrete pavers partially buried in the topsoil at each site. Leveling of the sensors was done using sand under the pavers and the adjustment of the leveling feet on both devices. Data was collected at a sampling frequency of 200 Hz with the 128 Hz hardware filter selected. HVSR was calculated for 45 windows for each of the measurement points. The duration of the windows is 81.92 sec windows (16384 samples with Fs=200 Hz). The windows are chosen with 75% overlap and subjected to Hanning windowing after being separated into high and low level bins using the total velocity vector and a threshold (Mihaylov et al., 2016). Smoothing of the resulting spectra is based on the BPF approach with n = 32.

Table 5.1: Winona field study test point locations, number of measurements and sensors used

Test Point	Latitude	Longitude	Elevation	Number of Tests	Duration	Sensors Used
Winona 1	43.20198	-79.6753	193.64	2	600sec	L4-3D; Guralp 40T
Winona 2	43.20147	-79.6757	193.82	3	600sec	L4-3D; Guralp 40T
Winona 3	43.19992	-79.6762	195.09	4	600sec	L4-3D; Guralp 40T
Winona 4	43.19672	-79.6773	198.41	2	600sec	L4-3D; Guralp 40T
Winona 5	43.20567	-79.6712	103.32	2	600sec	L4-3D; Guralp 40T

The collected HVSR data are presented in Figure 5.3. Wind induced motions of the Niagara escarpment introduced significant uncertainties in the evaluation of the HVSR results, especially for test point Winona1. Low frequency peaks produced by wind action at close distance had considerable effect on the higher sensitivity Guralp 40T. In such conditions, the Guralp 40T does not seem to be well suited for HVSR measurements. Using the two farthest points from the slope, Winona4 and Winona5, the site can be characterized based on 2 major peak groups in the HVSR: one large amplitude peak around0.1Hz and smaller, lower amplitude peak in the range 0.4 to 0.5 Hz. HVSR peaks at frequencies higher (7-15 Hz) than the two main groups, which are likely associated with shallow boundaries of soil improvement and roadway embankment construction. All the lower frequency peak group have change dramatically or disappeared for the points closer to the slope surface, and in the case of Winona2 (75 m from the crest of the slope) no reliable HVSR peaks could be observed. For Winona3 (280 m from the crest of the slope), significant increase of the 0.1 Hz peak group was observed, with a slightly amplified 0.5 Hz peak group as compared to Winona4 and Winona5.

These results demonstrated that for such steep and high slopes, multiple peaks could be expected on the flat surface behind the crest of the slope. These peaks either merged or disappeared with increasing distance away from the crest. Similar peaks could not be observed at the bottom of the slope. This confirms numerical modelling results presented by (Messaoudi et al., 2012), as well as (Zhang et al., 2018).
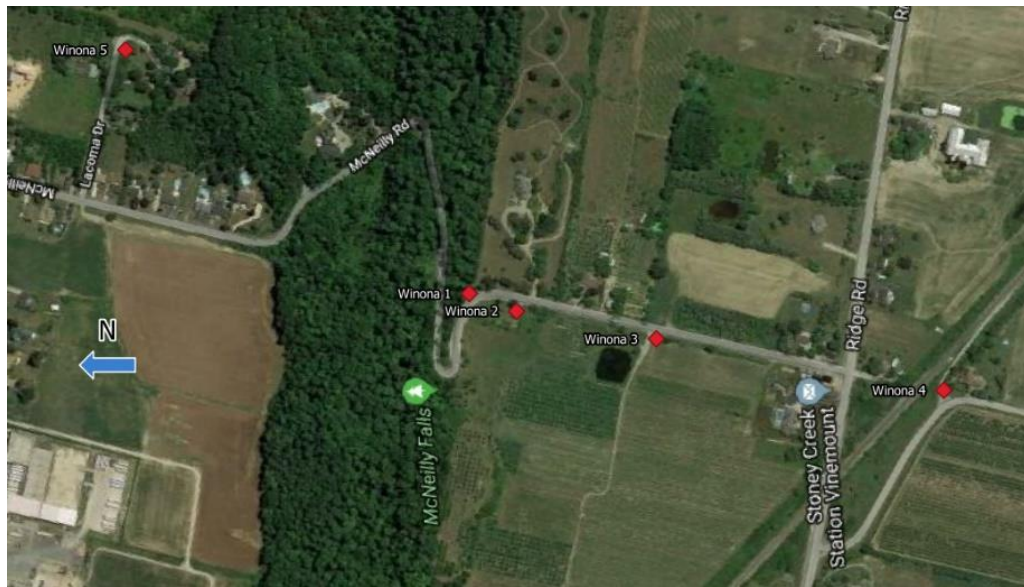
Figure 5.2: Winona HVSR study map based on the Google Map Satellite view raster
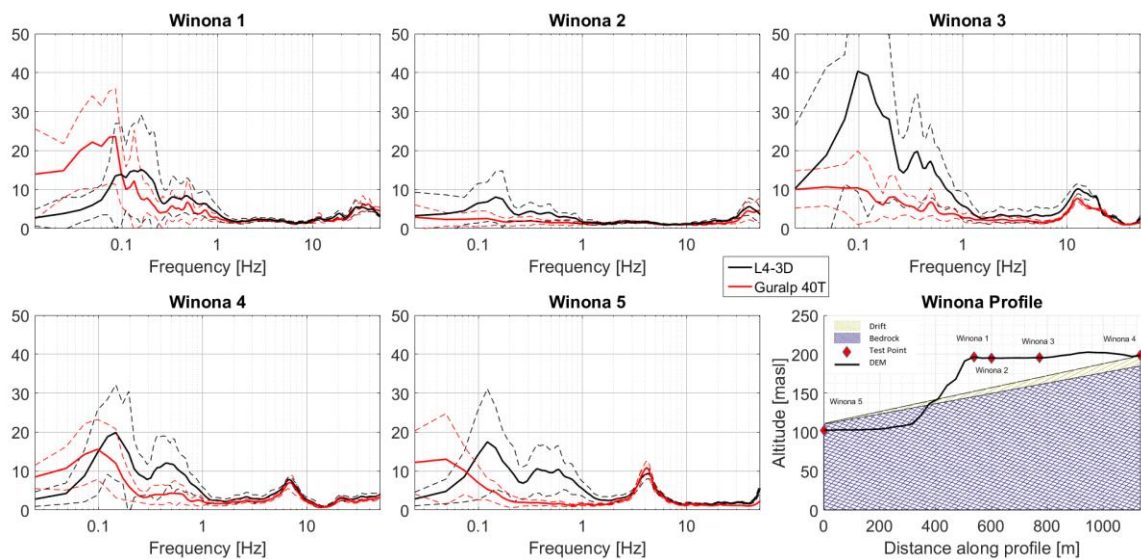
Figure 5.3:Winona HVSR study results. The black line is the DEM and the polygons are the thicknesses of: Blue – bedrock; Yellow - surficial drift. Based on MRD207

5.3.2 Wilmont

This study investigated the effect of the bedrock shape and surficial topology on HVSR results. The investigation site is characterized by one of the steeper bedrock slopes in Southern Ontario according to the MRD207 (Ontario Geological Survey, 2006) map. It is overlaid by deep and stratified glacifluvial and glaciolacustrine deposits with dispersed till and sand lenses. The test sites are located near Wilmont, ON. The map of the study area is shown in Figure 5.4, and the geological profile using bedrock boundary and drift thickness data from MRD207 are shown in Figure 5.5. The bedrock and drift thickness maps are presented in Figure 5.6 and Figure 5.7, respectively.

Figure 5.4: Wilmont site study map based on the Google Map Satellite view raster. Shading represents drift thickness
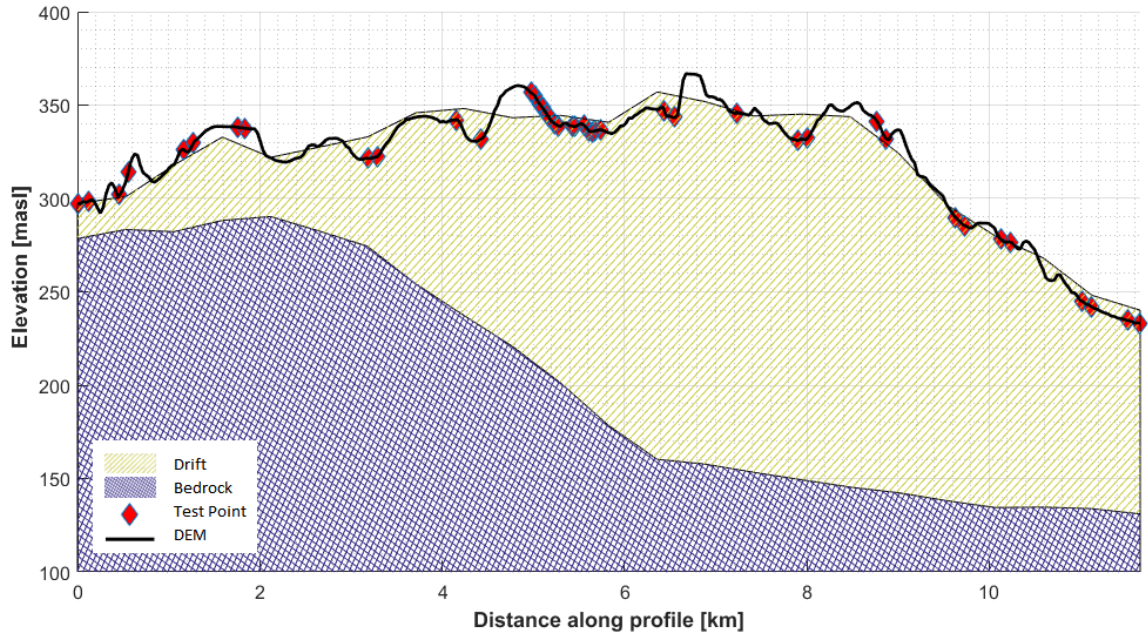
Figure 5.5: Wilmont site study profile using MRD207. The blue polygon defines the bedrock elevation and the yellow defines the overlying drift. The black solid line is the DEM model for the profile line (Ontario Geological Survey, 2006)

Microtremors were recorded at 42 test points in a line along third-class (dirt and gravel) roads in the area (Wilmont Rd. and Best Rd.). A combination of GEODE and DYNAMate DAQ along with L4-3D 1 Hz and DM 4.5 Hz sensors were used at all locations to verify the operation of the DYNAMate DAQ and establish sensor requirements for HVSR measurements in similar conditions. Table 5.2 provides the details of the test points and the tests conducted at each point.

HVSR data was analyzed for 35 windows at each of the measurement points. The duration of the window was 81.92 sec windows (16384 samples with Fs=200 Hz). The windows were selected with 75% overlap and subjected to the high/low source separation using the total velocity vector and a threshold (Mihaylov et al., 2016)). Smoothing of the resulting spectra is based on the BPF approach with n = 32. Additionally, 3 MASW profiles were carried out to establish the soil profile for the line. MASW data was collected using geophone spread at 5 m and strikes were applied at 10, 20 and 30 m on either side of each MASW spread line.

Table 5.2: Wilmont field study test point locations, number of measurements and sensors used

Test Point	Latitude	Longitude	Elevation	DYNAMate 2.0		Geode		Sensors Used
				Number of tests	Duration	Number of tests	Duration	
W1N	44.08	-78.664	360.934	4	312.5sec	5	131sec	L4-3D; DM 4.5
W1S	44.08	-78.6638	360.3392	4	312.5sec	5	131sec	L4-3D; DM 4.5
W2N	44.08	-78.6636	357.0064	4	312.5sec	5	131sec	L4-3D; DM 4.5
W2S	44.079	-78.6635	354.6744	4	312.5sec	5	131sec	L4-3D; DM 4.5
W3N	44.079	-78.6633	353.568	4	312.5sec	5	131sec	L4-3D; DM 4.5
W3S	44.079	-78.6632	350.7452	4	312.5sec	5	131sec	L4-3D; DM 4.5
W4N	44.078	-78.663	346.2185	3	312.5sec	5	131sec	L4-3D; DM 4.5
W4S	44.078	-78.6628	346.6312	3	312.5sec	5	131sec	L4-3D; DM 4.5
W5N	44.075	-78.6612	339.3791	4	312.5sec	5	131sec	L4-3D; DM 4.5
W5S	44.074	-78.6611	341.08	4	312.5sec	5	131sec	L4-3D; DM 4.5
W6N	44.075	-78.6615	337.1212	4	312.5sec	5	131sec	L4-3D; DM 4.5
W6S	44.075	-78.6613	338.8152	4	312.5sec	5	131sec	L4-3D; DM 4.5
W7N	44.077	-78.6623	341.2416	4	312.5sec	5	131sec	L4-3D; DM 4.5
W7S	44.076	-78.6621	340.6348	4	312.5sec	5	131sec	L4-3D; DM 4.5
W8	44.076	-78.6617	339.3983	4	312.5sec	5	131sec	L4-3D; DM 4.5
W9N	44.027	-78.6372	234.5051	4	312.5sec	5	131sec	L4-3D; DM 4.5
W9S	44.026	-78.6367	233.3413	4	312.5sec	5	131sec	L4-3D; DM 4.5
W10N	44.032	-78.6392	244.9527	4	312.5sec	5	131sec	L4-3D; DM 4.5
W10S	44.031	-78.6388	241.3484	4	312.5sec	5	131sec	L4-3D; DM 4.5
W11N	44.039	-78.6422	278.6127	5	312.5sec	5	131sec	L4-3D; DM 4.5
W11S	44.038	-78.6418	276.7741	5	312.5sec	5	131sec	L4-3D; DM 4.5
W12N	44.043	-78.644	291.8329	4	312.5sec	5	131sec	L4-3D; DM 4.5
W12S	44.042	-78.6437	287.3845	4	312.5sec	5	131sec	L4-3D; DM 4.5
W13N	44.05	-78.6471	337.655	4	312.5sec	5	131sec	L4-3D; DM 4.5
W13S	44.049	-78.6467	328.3866	4	312.5sec	5	131sec	L4-3D; DM 4.5
W14N	44.057	-78.6501	331.9804	4	312.5sec	5	131sec	L4-3D; DM 4.5
W14S	44.056	-78.6497	329.2204	4	312.5sec	5	131sec	L4-3D; DM 4.5
W15	44.063	-78.6527	347.092	4	312.5sec	5	131sec	L4-3D; DM 4.5
W16N	44.069	-78.6583	363.7577	4	312.5sec	5	131sec	L4-3D; DM 4.5
W16S	44.068	-78.6579	368.1128	4	312.5sec	5	131sec	L4-3D; DM 4.5
W17N	44.121	-78.6828	297.1814	4	312.5sec	5	131sec	L4-3D; DM 4.5
W17S	44.12	-78.6823	295.3795	4	312.5sec	5	131sec	L4-3D; DM 4.5
W18N	44.117	-78.6829	294.0863	4	312.5sec	5	131sec	L4-3D; DM 4.5
W18S	44.116	-78.6827	300.6304	4	312.5sec	5	131sec	L4-3D; DM 4.5
W19N	44.111	-78.6784	333.3068	4	312.5sec	5	131sec	L4-3D; DM 4.5
W19S	44.111	-78.678	329.7179	4	312.5sec	5	131sec	L4-3D; DM 4.5
W20N	44.107	-78.6762	338.0208	4	312.5sec	5	131sec	L4-3D; DM 4.5
W20S	44.106	-78.6759	337.5893	4	312.5sec	5	131sec	L4-3D; DM 4.5
W21	44.085	-78.6663	333.7688	4	312.5sec	5	131sec	L4-3D; DM 4.5
W22	44.087	-78.6673	334.8292	4	312.5sec	5	131sec	L4-3D; DM 4.5
W23N	44.095	-78.6709	318.5335	4	312.5sec	5	131sec	L4-3D; DM 4.5
W23S	44.094	-78.6706	320.5462	4	312.5sec	5	131sec	L4-3D; DM 4.5

128
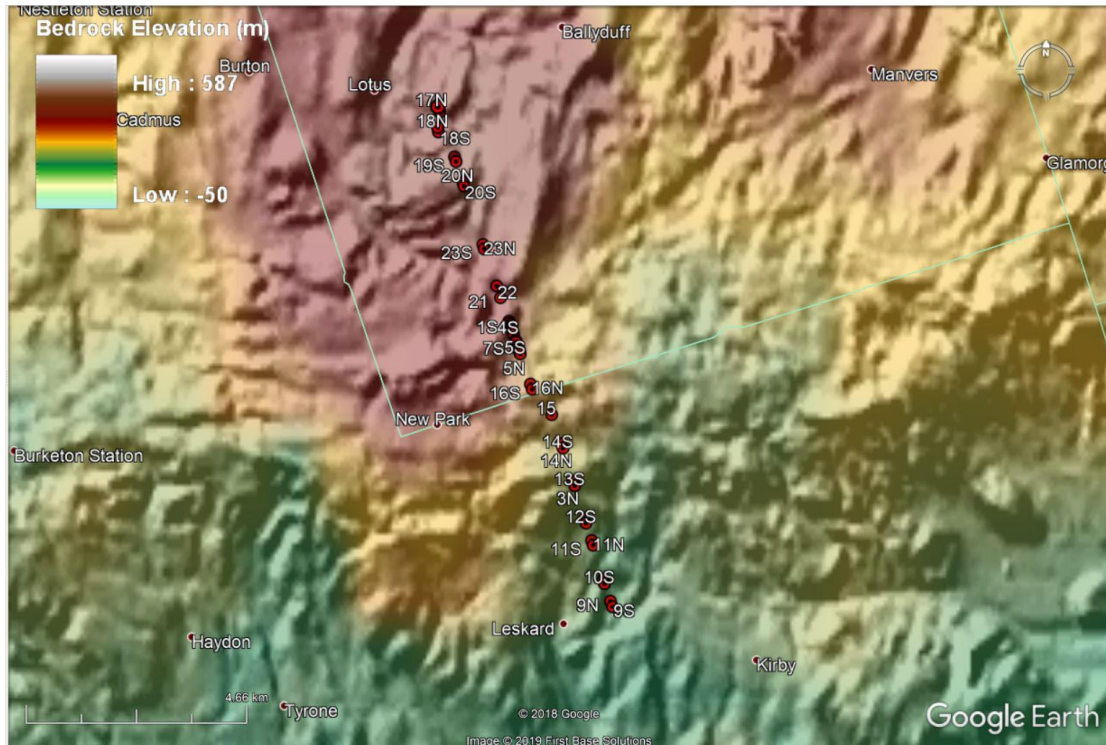
Figure 5.6: Wilmont study area bedrock elevation from MRD207(Ontario Geological Survey, 2006)
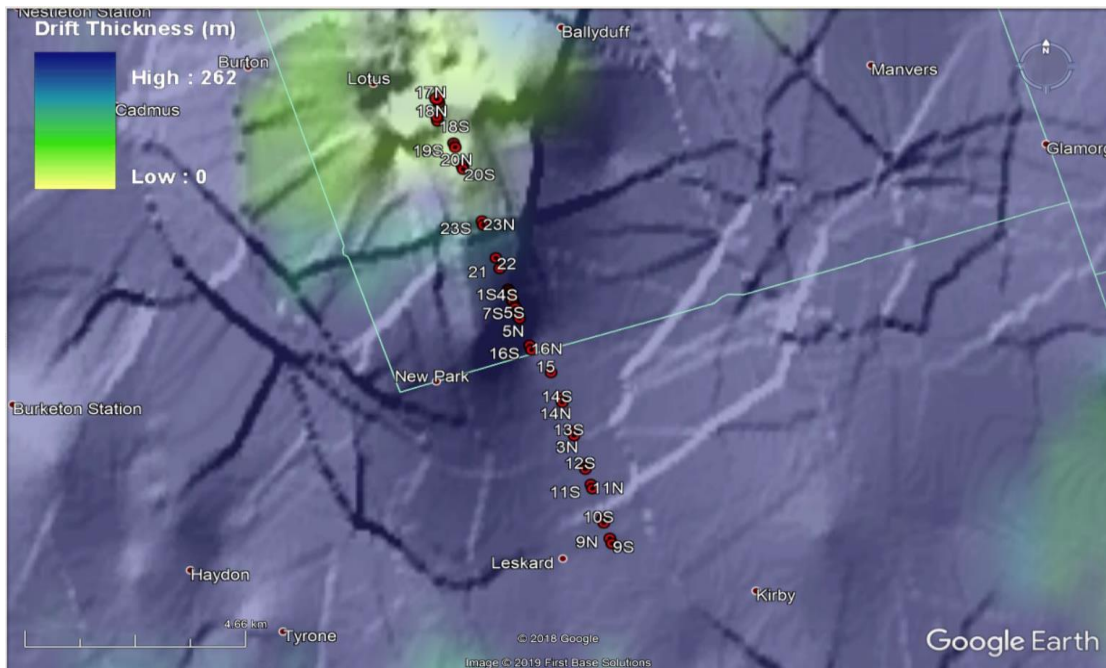
Figure 5.7: Wilmont study area drift thickness from MRD207(Ontario Geological Survey, 2006)

5.3.2.1 MASW Investigation

The receivers were spaced 5m apart and strikes were performed on either side of the spreads at distances of 10, 20 and 30 m to account for the presumed sloping bedrock but no significant difference in stratification was observed in the profiles obtained from either side of the spreads. The initial model for the interpretation of shear wave velocity profile assumed linear increase of shear wave velocity with depth, and the layer thickness was selected based on the expected wavelength for each layer. To calculate the average shear wave velocity using the thickness (d_i) and corresponding velocity (V_{S_i}) of each layer, the following equation is used (For V_{s30} calculations, layers up to depth of 30m are considered):

$$\overline{V_S} = \frac{\Sigma d_i}{\Sigma t_i} = \frac{\Sigma d_i}{\Sigma\left(\frac{d_i}{V_{S_i}}\right)}$$

(5.1)

The performed MASW investigations did not reach the depth of contrast but showed a gradient increase in shear wave velocity for all 3 measurement profiles as shown in Figure 5.8. In the case of MASW2, the expected depth to bedrock was ~25m and the MASW profile did not exhibit a small change near that depth. However, a similar increase in V_s at 25m could be observed in the other two MASW profiles. Overall, all three profiles represent approximately the same soil velocity profile, within the bounds of the investigations' standard deviations as given by the dashed lines in Figure 5.8. Additionally, analysis with both SurfSeis and Geopsy resulted in equivalent soil profiles. In both cases the maximum depth of certainty was no larger than 24m.
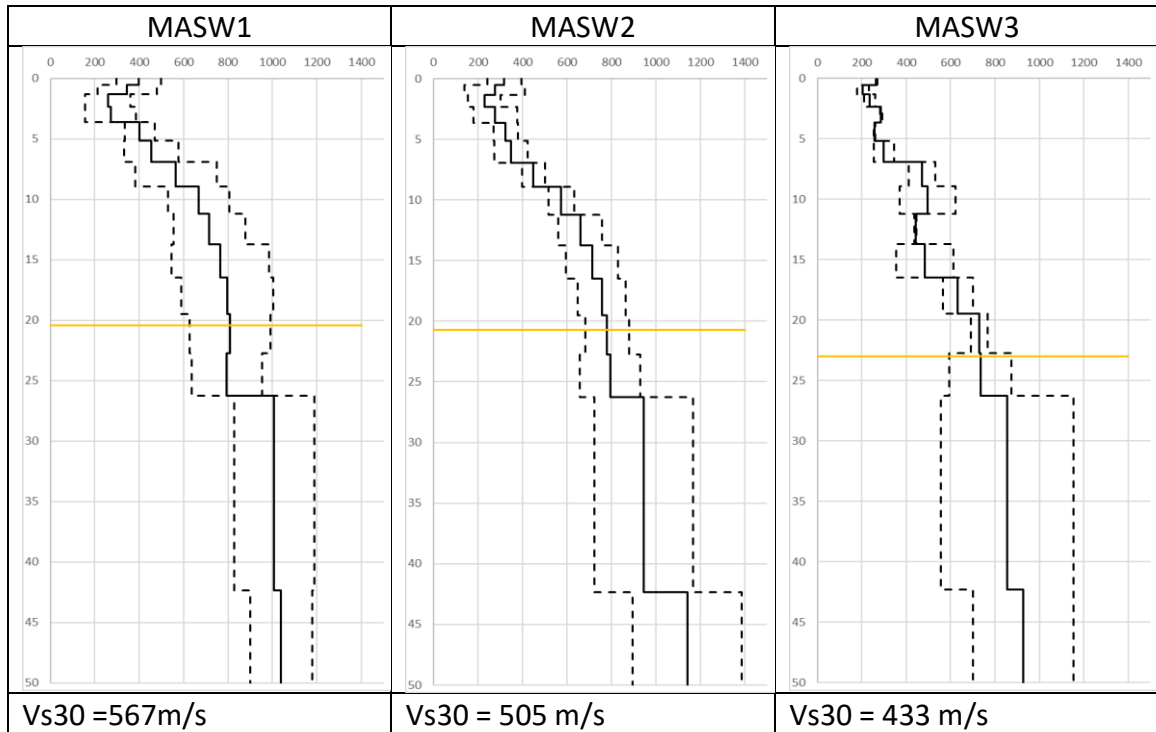
Figure 5.8: Shear Wave velocity profiles for Wilmont study area obtained using MASW. Dashed lines are one standard deviation range from all processed profiles. The yellow line represents the depth of certainty for the models.

5.3.2.2 HVSR Investigation

The results from the HVSR investigation for this field study have been separated into three sections: Northern, middle and Southern. This was done to improve readability of the results and differentiate between the different conditions encountered in each section.

5.3.2.2.1 North Section of Wilmont Field Study

HVSR curves for the northern section of the Wilmont investigation are presented in Figure 5.9 This section is characterized by a dip in the bedrock elevation and relatively flat surface topography. The first three test points in the profile W17N, W17S and W18N show a minor 1.3Hz peak, but due to the presence of both higher and lower frequency peaks at approximately the same amplitude, it cannot be considered reliable. With the increase in

drift thickness beyond test point W18N, a shift in the dominant peak from 1.3Hz to 1Hz was observed (based on V_{s30} that's a change of 28m depth).
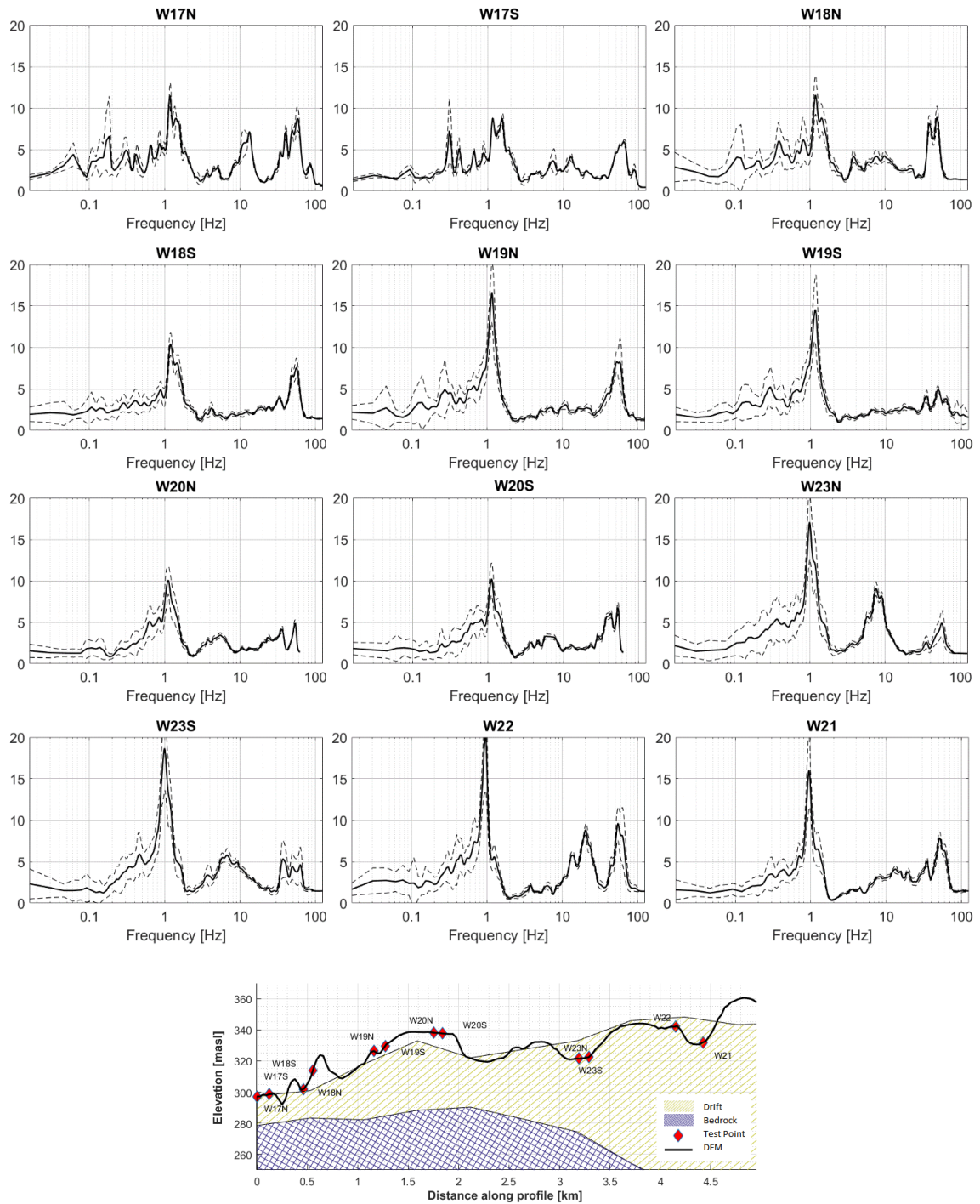
Figure 5.9: Northern Section of Wilmont HVSR profile

The 1 Hz peak was dominant for the rest of the points of this section. Higher frequency peaks in two groups 9-20 Hz and 40-80 Hz were also present at all test points most likely from shallower interfaces, as no correlation to topography can be made. At the crest of the surface slope, test points W20N and W20S exhibited significant broadening and reduction in amplitude of the main peak from 1 Hz to 0.2-1 Hz with half the amplitude of W19S. Test points W23N, W23S and W22 show an increase amplitude to levels comparable to W19S, followed by a small reduction at test point W21.

5.3.2.2.2 Middle Section of Wilmont Field Study

The middle section of the Wilmont investigation is characterized by the steepest surface slope encountered along the profile. A larger density of HVSR test points was utilized along this section to allow better characterization of the behavior of HVSR along this type of surficial topography. Additionally, for this section the bedrock depth was large (~200m) with a slope in the bedrock at that depth. The length and angle of dip of the bedrock slope was larger than the surfaces one, according to MRD207 (Ontario Geological Survey, 2006). No points were located at or beyond the crest of the hill north of test point W1N due to very saturated soil conditions, narrow crest and the fact that the section of the road on top of the crest was in a thickly forested section of the profile. In addition to the HVSR investigation, an MASW sounding was conducted at the middle of this section at the toe of the hill.

Figure 5.10: Middle section of the Wilmont profile

The 1Hz dominant peak present in the northern section of the Wilmont investigation was also dominant for the middle section of the investigation. The sloping surficial topography did not affect the frequency of this dominant peak, but it affected the amplitude. This trend holds for all test points until the toe of the slope at test point W4N, with test point W4S again showing a strong dominant 1 Hz peak. All test points have high frequencies grouping of peaks between 20 Hz and 60 Hz that could be due shallow interfaces such as the road embedment. Test points W3N and W3S show sharp peaks at 4 and 10 Hz, however those could not be correlated with any site-specific features. Test point W6S shows an additional dominant peak at 0.5 Hz with a comparable amplitude to the 1 Hz dominant peak. This is spit in the dominant peak is only observed at test point W6S.

Reducing the sharpness of the smoothing function (by setting n=16), picking the dominant peak amplitude for each point in the middle section of the profile and normalizing the values by the mean of the amplitudes the curve presented in Figure 5.11 is achieved. This result seems to agree with the model proposed by (Zhang et al., 2018) regarding the oscillation of the amplification factor with distance from crest, however the statistical uncertainty is too large to make a conclusive statement regarding the validity of the model for this particular case study.
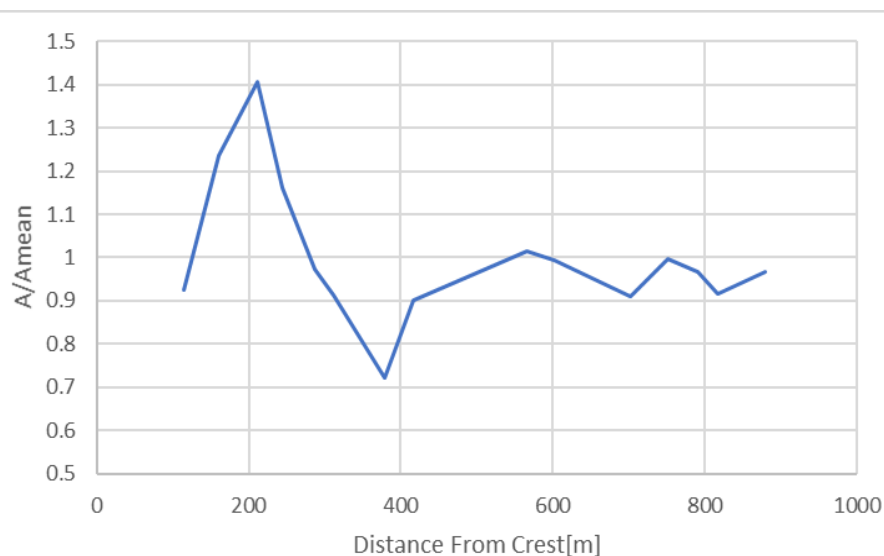
Figure 5.11: Variation of normalized amplification factor from HVSR data smoothed with a lower Q BPF, n=16.
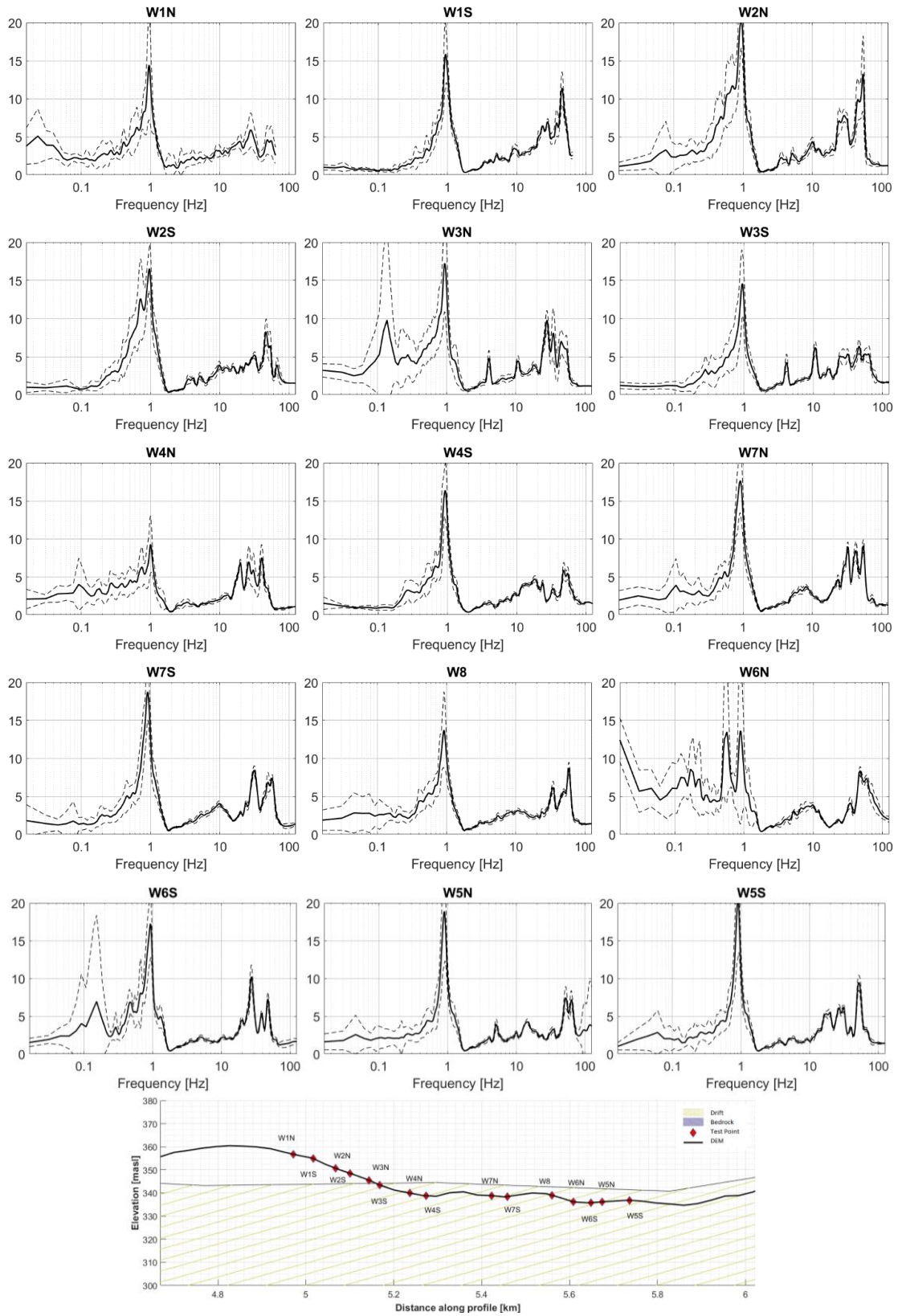
Figure 5.12: Middle Section of Wilmont HVSR profile

Figure 5.13 shows an interpolated colormap of the amplitudes of the HVSR results for the middle section of the Wilmont study. It presents the amplitude in color-scale against frequency and distance, with interpolation along the distance axis to achieve 100 m gridding. A stable 0.9 Hz peak, with intermittent higher frequency peaks can be observed. Frequency broadening of the peak from the crest of the hill to halfway down the slope is observed.
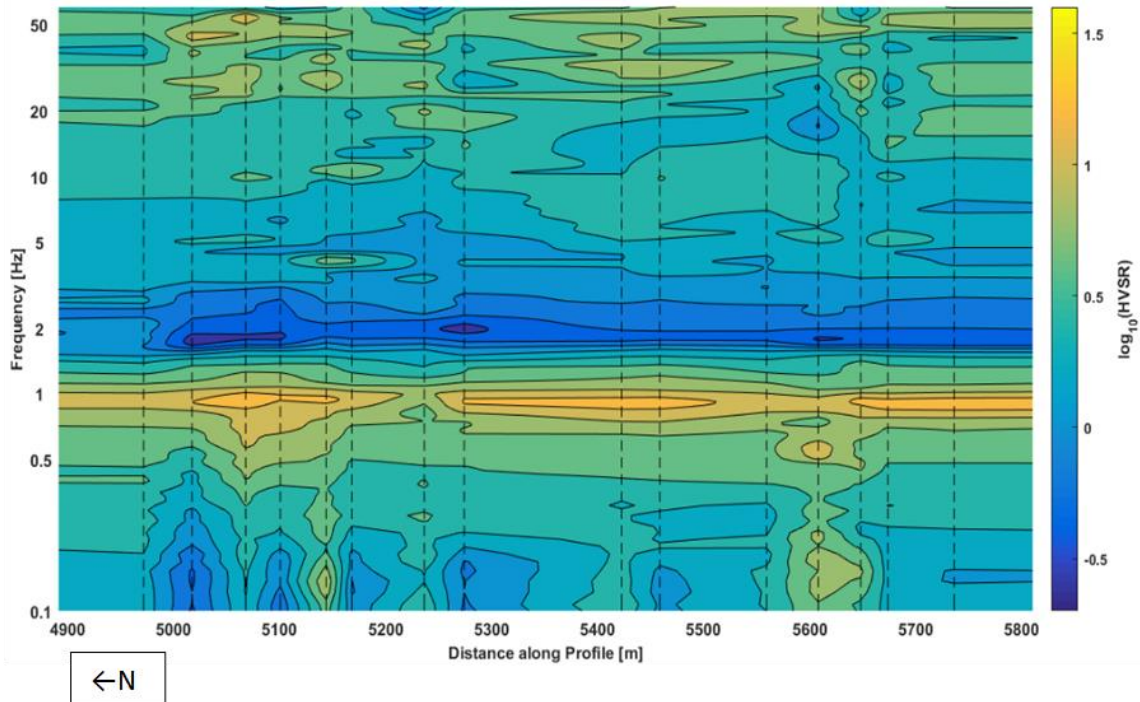
Figure 5.13: Interpolated HVSR frequency and amplitude distribution along the slope in the middle section of Wilmont study. Dashed lines represent test point locations.

The large drop in the ratio amplitude (~0.3) for frequencies higher than the fundamental peak indicates that the HVSR curves for this section are due to Rayleigh wave ellipticity as per (Fäh et al., 2001; Stephenson, 2003). These authors suggested that the trough in the HVSR indicates a predominance of Rayleigh waves in the noise records, and as is the case here is preceded by a peak at lower frequencies.

5.3.2.2.3 South Section of Wilmont Field Study

The south section of the Wilmont investigation is characterized by gently sloping surficial topography, with decreasing elevation north to south. According to MRD207, the bedrock elevation is also decreasing in the same direction, however at a slower rate. The depth to bedrock starts at 200 m at the north end, reducing to 100 m at the south end.

HVSR results are given in Figure 5.14, with the depth profile given at the bottom of the figure. The dominant resonance for this section, like the previous two, is at 1 Hz. In general, the peak's amplitude decreases with the decreasing of the thickness of the drift, the frequency of the 1 Hz peak to remain constant for the length of this section.

The 1Hz peak is dominant for the first two test points: W16N and W16S, followed by a large decrease, to a value of ~10, for the next 4 test points (W15, W14N, W14S and W13N). Some increase in the amplitude, to a value of ~15, is observed in the next 5 test points (W13S, W12N, W12S, W11N, W11S). Additionally, those 5 points are characterized by the appearance of a secondary peak at 8-10 Hz. Test point W10N exhibits a large reduction in 1Hz peak to values similar to W13N, and a reduction of the 10Hz peak as compared to the 4 points north of W13N.

Test points W10S and W9N have a double peak, at 1.2 Hz and 9.5 Hz with nearly equal amplitudes. The only other point that has a well-defined 9.5 Hz peak is W12S. Due to the distance between the W12S and W10S points and the relatively poor definition and low amplitude of the 9.5 Hz peak, it can be concluded that the 9.5 Hz peak is not a result of large geological feature, but more likely is a result of shallow intermittent interface. All test points have high frequencies grouping of peaks between 20 Hz and 60 Hz that could be due shallow interfaces such as the road embedment.
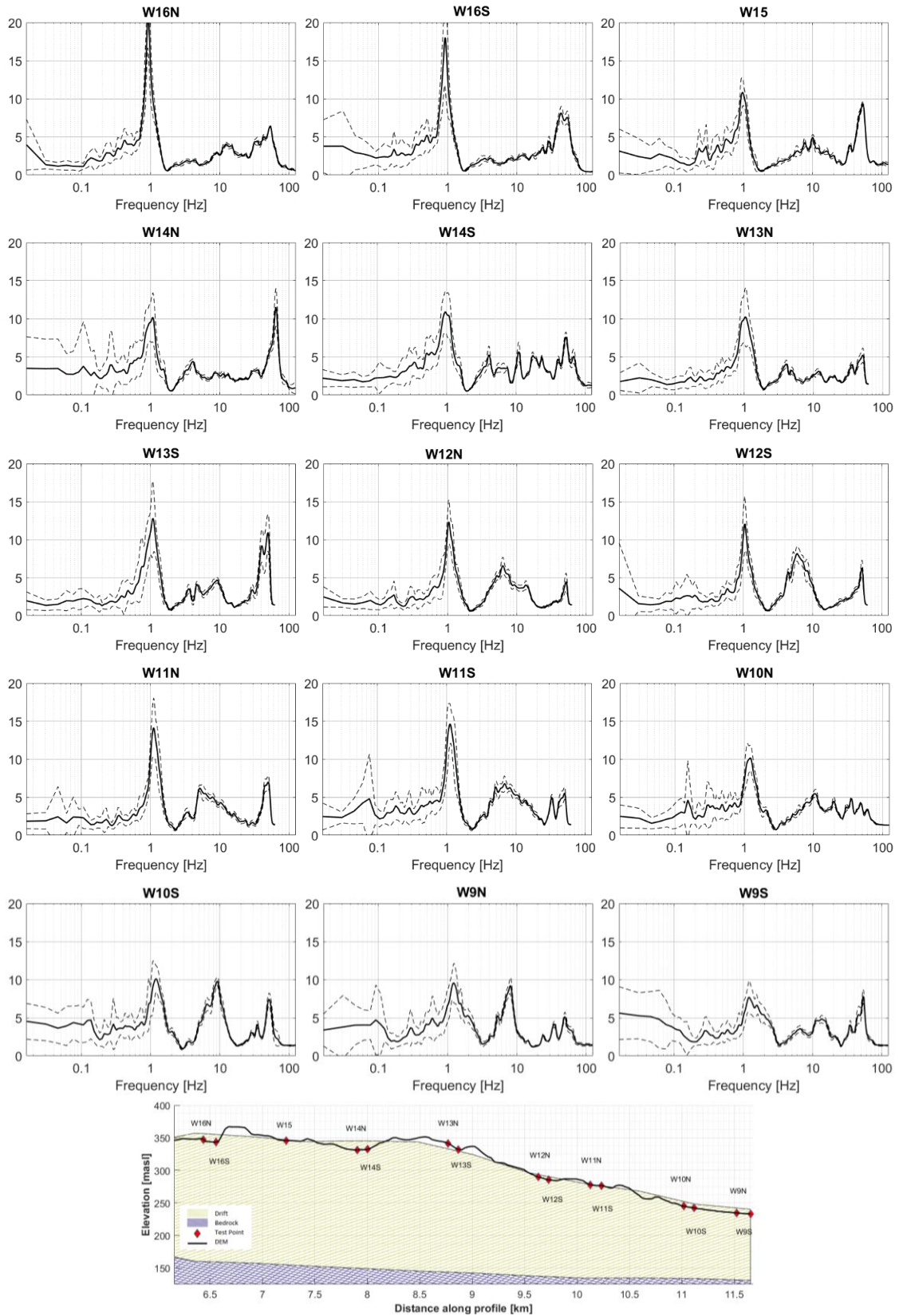
Figure 5.14:Southern Section of Wilmont HVSR profile

Based on the interpolated amplitude map given in Figure 5.15, the dominant frequency peak does not follow the depth to bedrock as predicted by MRD207. Based on the MRD profile, a high frequency peak is expected at the north end of the profile where the surficial deposit is thinnest, and the peak decreased in frequency further southward. At the south most section of the profile an increase of the fundamental frequency peak is to be expected. Instead, the dominant 1 Hz peak follows a near-parabolic curve changing from 1.4 Hz at the edges of the profile and having a minimum of 1 Hz at the lowest point in the bedrock surface. The rate of increase of the dominant frequency southward from the toe seems to be lower than northward. For the thin northern section, 1 Hz peaks are still present, albeit they have a much lower amplitudes than in the center of the profile and are masked by both higher and lower frequency peaks. The section of sloping bedrock beneath the middle of the investigation line can be characterized by relatively large HVSR ratios at the fundamental frequency. These ratios are exhibited at points south from the crest of the bedrock slope, and ratio values on or behind the crest are lower and comparable to the HVSR amplitudes at the toe of the bedrock slope.
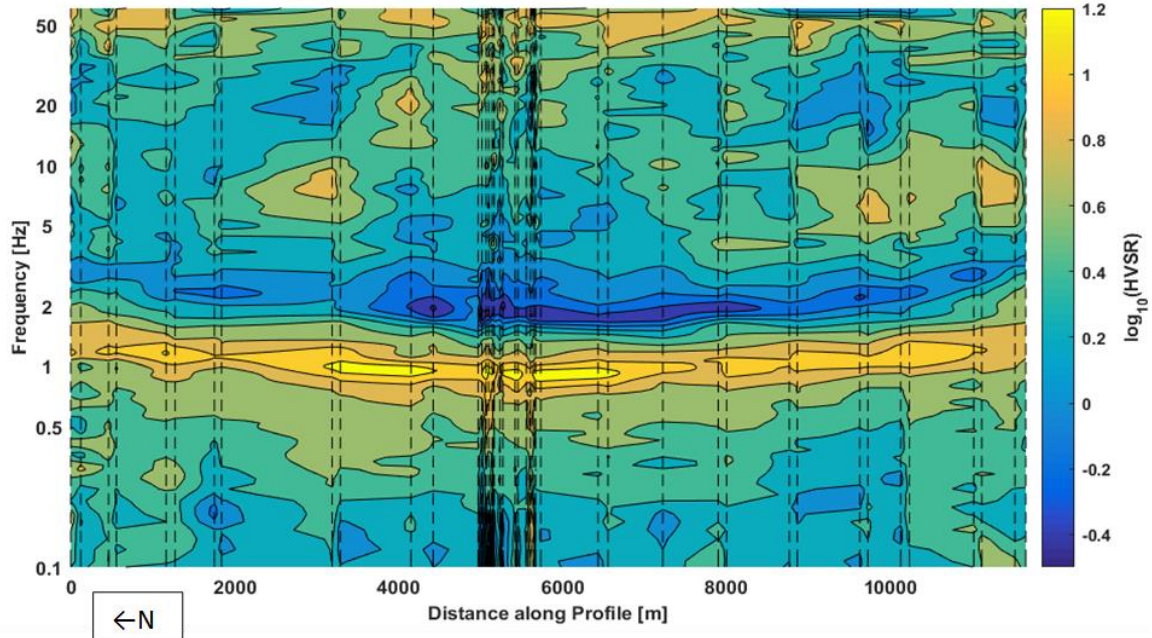
Figure 5.15: Interpolated distribution of HVSR dominant frequency and amplitudes along the profile, obtained from both the Geode and DYNAMate measurements. Dashed lines represent measurement point locations.

Knowing both the fundamental frequency (from HVSR) and the shear wave velocity profile (from MASW), the depth to boundary can be calculated using quarter wavelength approach (Kramer, 1996):

$$H = \frac{Vs}{4f_0} \tag{5.2}$$

With the average Vs from MASW2 (505 m/s) 1.4 Hz corresponds to 90 m depth, and the 1 Hz at MASW3 (433 m/s) gives 108 m, and at MASW1 (570 m/s) the depth is 142 m. This agrees with the trend of bedrock dip in MRD207, however suggests an average depth offset of ~75 m between the results of this study and the data in MRD207.

5.3.3 Hockley Hills Investigation

Another study was performed east of Orangeville, ON in the Hockley Hills area. In this case, the same equipment setup was used. 38 HVSR points (see Table 5.3 and Figure 5.16) were recorded, however no MASW profiles were taken. The overburden to bedrock boundary at this site is deeper (~250-300 m) than what was encountered in Wilmont, and the results are descriptive of deep sedimentary basin.

The site is located on the edge of the buried escarpment north of the city of Toronto. It is underlain by stratified glaciofluvial deposits mixed with till, and according to MRD207 test points H4S and H4N are located on a bedrock drift complex. The middle of the profile lies over a buried ravine-oriented east to west.

The study map is presented in Figure 5.16, and the bedrock and drift thickness maps are shown in Figure 5.17 and Figure 5.18, respectively. The geological profile using bedrock boundary and drift thickness data from MRD207 are presented in Figure 5.19.

Figure 5.16: Hockley hills site study map based on the Google Map Satellite view raster. Shading represents drift thickness
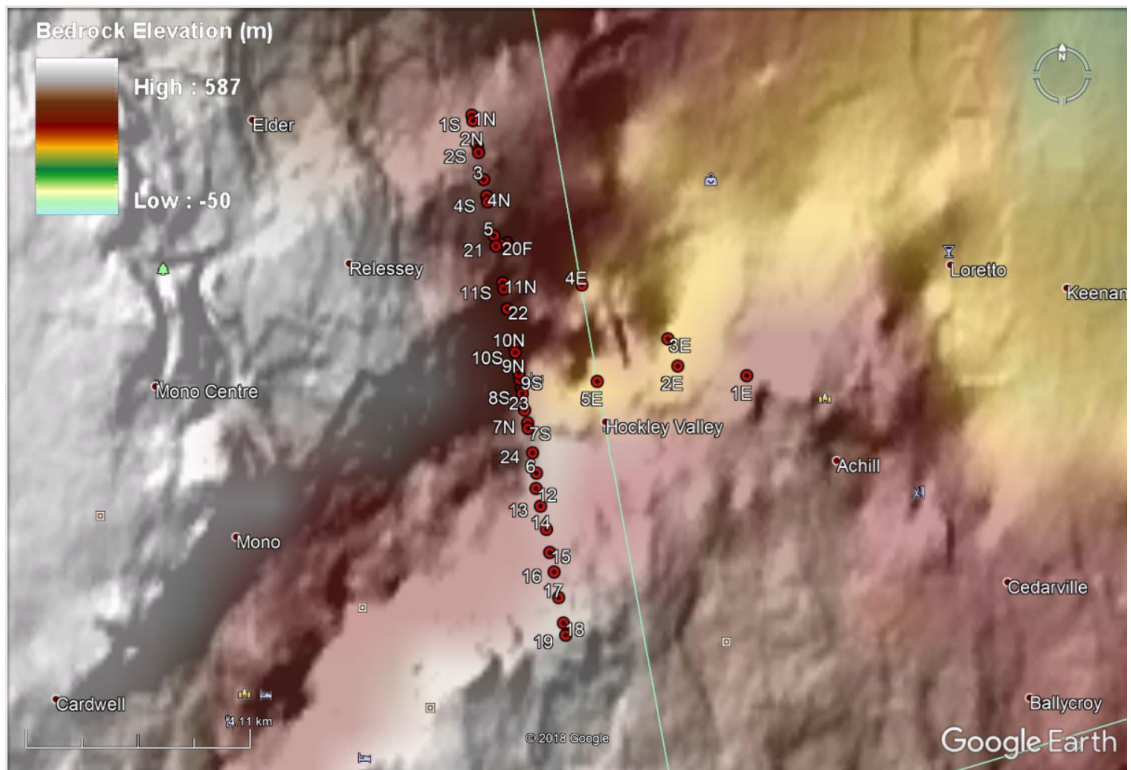
Figure 5.17: Hockley Hills study area bedrock elevation from MRD207(Ontario Geological Survey, 2006)
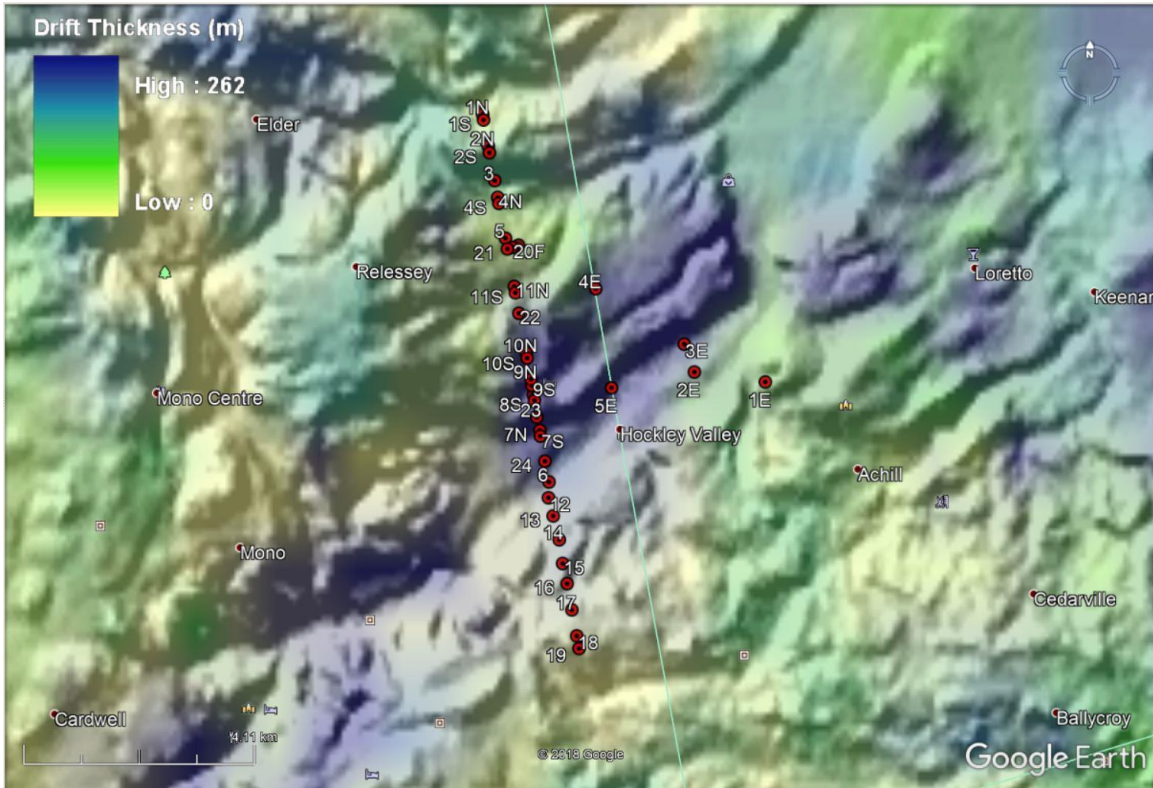
Figure 5.18: Hockley Hills study drift thickness from MRD207(Ontario Geological Survey, 2006)
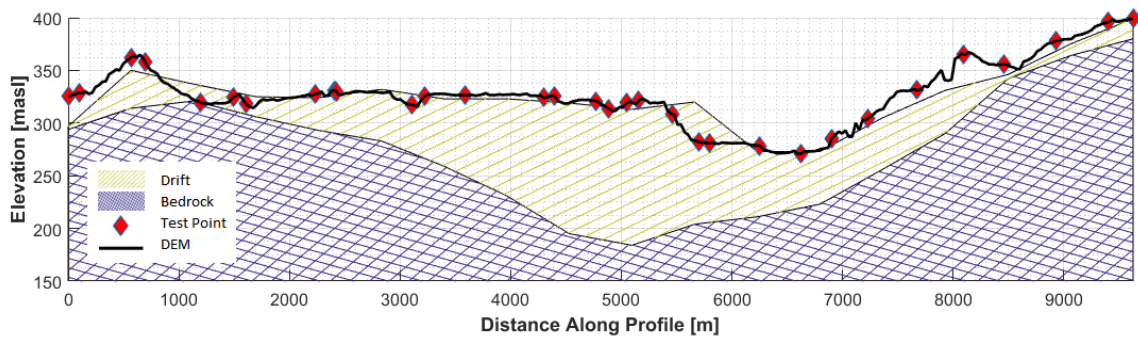
Figure 5.19: Hockley Hills site study profile using MRD207. The blue polygon defines the bedrock elevation and the yellow defines the overlying drift. The black solid line is the DEM model for the profile line (Ontario Geological Survey 2006)

Table 5.3:Hockley Hills field study test point locations, number of measurements and sensors used

Test Point	Latitude	Longitude	Elevation	DYNAMate 2.0		Geode		Sensors Used
				Number of Tests	Duration	Number of Tests	Duration	
HE1	44.02995	-79.9366	298.7886	1	600sec	5	131sec	L4-3D
HE2	44.03153	-79.9524	263.1304	2	600sec	5	131sec	L4-3D; DM4.5
HE3	44.03598	-79.9546	254.3474	2	600sec	5	131sec	L4-3D; DM4.5
HE4	44.04482	-79.9743	306.2806	1	600sec	5	131sec	L4-3D; DM4.5
HE5	44.02902	-79.9708	262.9703	1	600sec	5	131sec	L4-3D; DM4.5
H1N	44.07263	-79.9994	325.2107	2	600sec	5	131sec	L4-3D; DM4.5
H1S	44.07173	-79.9992	328.8625	2	600sec	5	131sec	L4-3D; DM4.5
H2N	44.06758	-79.9982	361.3861	2	600sec	5	131sec	L4-3D; DM4.5
H2S	44.0665	-79.9979	360.7396	2	600sec	5	131sec	L4-3D; DM4.5
H3	44.06207	-79.9967	318.9252	2	600sec	5	131sec	L4-3D; DM4.5
H4N	44.05938	-79.9961	324.0204	2	600sec	5	131sec	L4-3D; DM4.5
H4S	44.05843	-79.9958	317.8182	2	600sec	5	131sec	L4-3D; DM4.5
H5	44.05287	-79.9944	327.6833	2	600sec	5	131sec	L4-3D; DM4.5
H6	44.014	-79.9847	270.8984	2	600sec	5	131sec	L4-3D; DM4.5
H7N	44.02222	-79.9867	282.1563	2	600sec	5	131sec	L4-3D; DM4.5
H7S	44.02132	-79.9866	280.6487	2	600sec	5	131sec	L4-3D; DM4.5
H8N	44.02793	-79.9882	318.7566	2	600sec	5	131sec	L4-3D; DM4.5
H8S	44.027	-79.9879	322.8181	2	600sec	5	131sec	L4-3D; DM4.5
H9S	44.02938	-79.9885	313.599	2	600sec	5	131sec	L4-3D; DM4.5
H9N	44.0304	-79.9887	321.7809	2	600sec	5	131sec	L4-3D; DM4.5
H10N	44.03463	-79.9898	323.7321	2	600sec	5	131sec	L4-3D; DM4.5
H10S	44.03375	-79.9895	322.3455	2	600sec	5	131sec	L4-3D; DM4.5
H11S	44.04417	-79.9921	325.4251	2	600sec	5	131sec	L4-3D
H11N	44.04518	-79.9924	317.7418	2	600sec	5	131sec	L4-3D
H12	44.01148	-79.9848	277.3027	2	600sec	5	131sec	L4-3D
H13	44.00858	-79.9837	304.4904	2	600sec	5	131sec	L4-3D
H14	44.00478	-79.9824	331.0504	2	600sec	5	131sec	L4-3D
H15	44.001	-79.9816	364.8433	2	600sec	5	131sec	L4-3D
H16	43.9978	-79.9806	355.8479	2	600sec	5	131sec	L4-3D
H17	43.9936	-79.9796	378.3247	2	600sec	5	131sec	L4-3D
H18	43.98945	-79.9785	396.3452	2	600sec	5	131sec	L4-3D
H19	43.98745	-79.978	399.1295	2	600sec	5	131sec	L4-3D
H20B	44.05175	-79.9914	323.9916	2	600sec	5	131sec	L4-3D
H20F	44.05142	-79.9928	326.0485	2	600sec	5	131sec	L4-3D
H21	44.05117	-79.9939	327.6495	2	600sec	5	131sec	L4-3D
H22	44.0409	-79.9914	326.499	2	600sec	5	131sec	L4-3D
H23	44.02432	-79.9874	307.8316	2	600sec	5	131sec	L4-3D
H24	44.01732	-79.9856	278.4998	2	600sec	5	131sec	L4-3D

The HVSR investigation in Hockley hills is separated into 4 sections, 3 along the profile line: North, Middle and South and the fourth section complements the study by extending the investigation east with 5 test points. The points in the fourth section give additional data over the sloping bedrock as well as over the bedrock ravine.

5.3.3.1 Hockley Hills Eastern Section
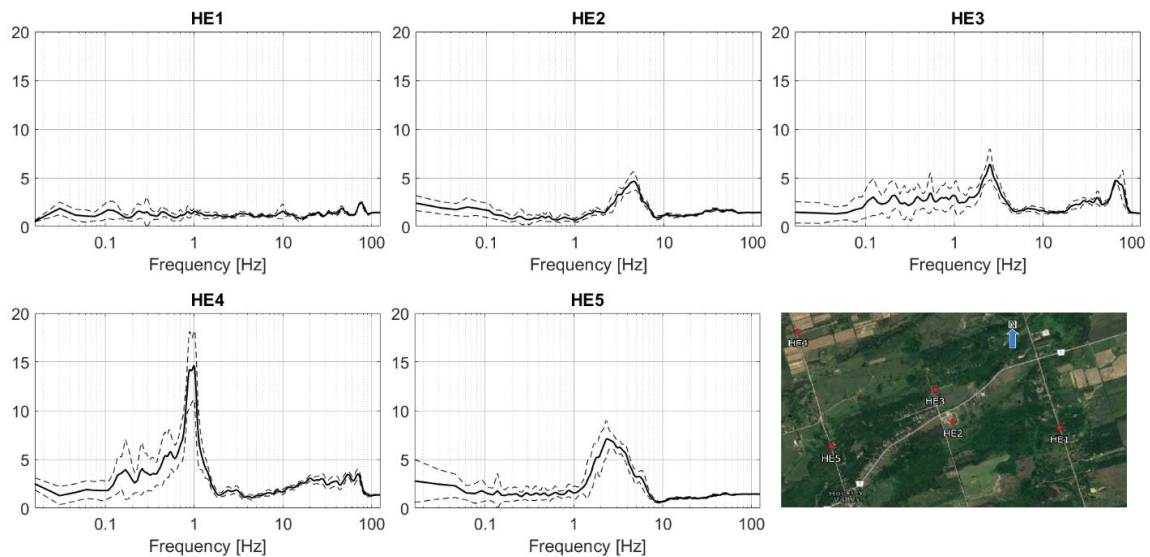
Figure 5.20: HVSR results for Eastern Section of Hockley Hills Investigation

Figure 5.20 shows the results of the HVSR investigation in the eastern section of Hockley Hills. The major peaks for the east section have a wide frequency range (between 2 Hz and 5 Hz) and low amplitude, however at the test point HE4 HVSR has a clear 1 Hz peak. Bedrock and drift data from MRD207 (Ontario Geological Survey, 2006) suggests that HE4 is sitting over a deep divot in the bedrock, and thus has thicker drift. The size of the divot though is very small compared to the distances between the points or the bedrock depth at the location. Test point HE5 is in similar conditions as HE4, however there is no clear 1 Hz peak at HE5 instead there is broad peak with a maximum at 2.3 Hz. Another difference is that HE5 lies on top of the buried valley that runs east to west, whereas HE4 is over the slope of the buried escarpment, albeit at approximately the same drift thickness. The HVSR at HE1 is flat, without any discernable peaks, suggesting no site effects or that the measurement was done on solid bedrock outcrop. However, as per MRD207 (Ontario Geological Survey, 2006) the depth to bedrock at this location is estimated at 23 m,

additionally observations on site did not suggest the existence of an outcrop. Test point HE2 has a shallower drift thickness of as per MRD207, however it exhibits a peak at 4.6 Hz

5.3.3.2 Hockley Hills Northern Section

HVSR results for the northern section are presented in Figure 5.21. As can be noted from Figure 5.21, the curves are relatively flat with a few high frequency peaks ~60-70 Hz most likely related to the effect of the road embankment thickness.
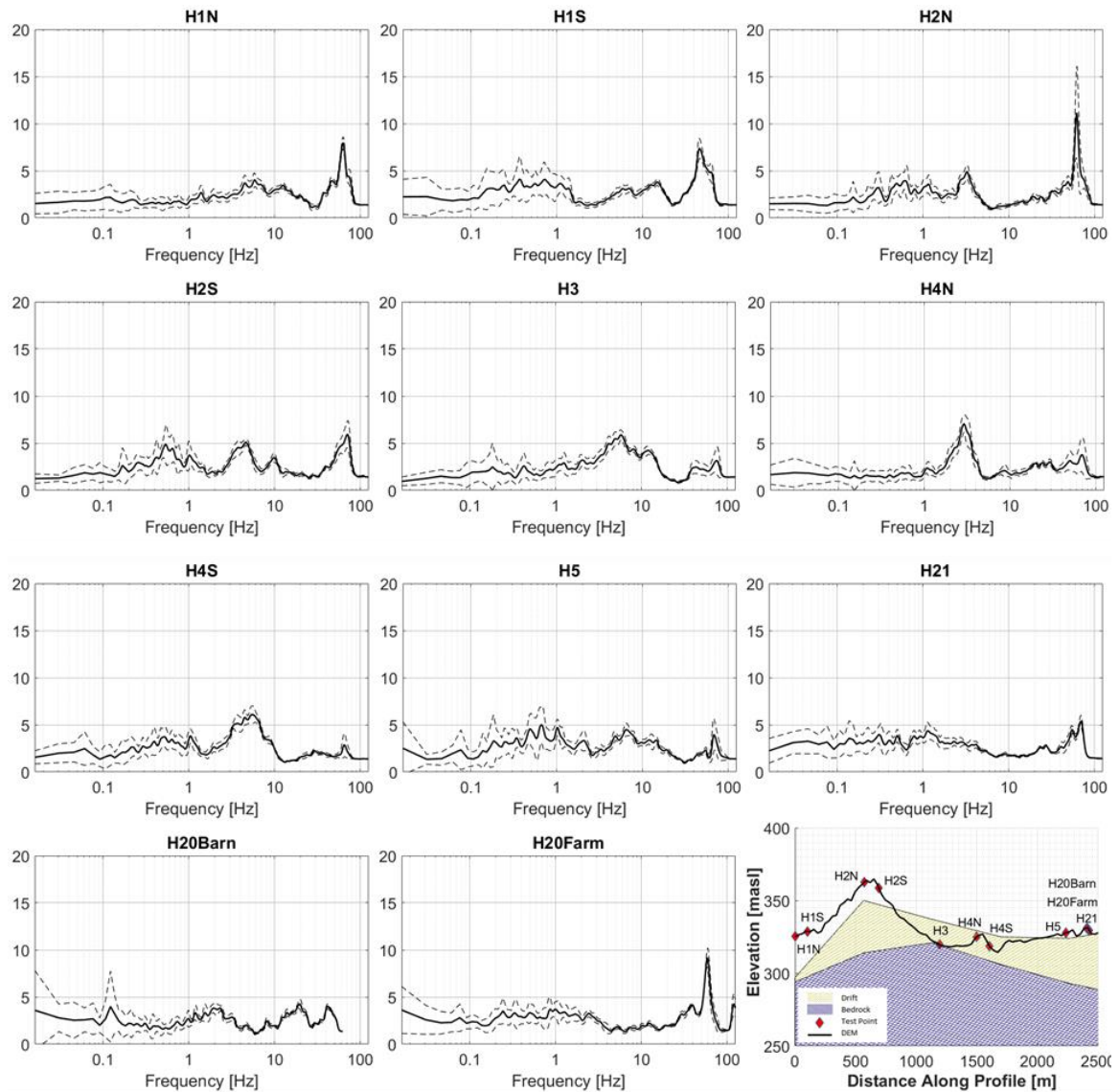
Figure 5.21: HVSR results for the northern section of Hockley Hills profile

Lower frequency peaks are present but do not satisfy SESAME's conditions for peak reliability (Acerra et al., 2004; Koller et al., 2004), with the exception of test points H4N and H4S that display peaks at 4 to 6 Hz. Test points from the grouping of H5, H21 and H20 through H4E, H3E and H1E form a profile along the buried escarpment section from west to east ending over the deeper drift thickness to the east of the line. Test points at the ends of this line exhibit near flat HVSR with no dominant peaks, with the midpoints: H4E and H3E exhibiting a dominant peak at 1 Hz and 2 Hz respectively, suggesting a reduction of thickness of overburden.

5.3.3.3 Hockley Hills Middle Section

Figure 5.22 shows the HVSR results for the middle section of the Hockley Hills investigation. The middle of the basin, from test point H9N to H6, is the only place that HVSR exhibits a clear 1 Hz peak. This peak first appears at H10S as it shifts from the higher frequency of 2 Hz at H10N, however its amplitude is too low for the peak to be considered reliable. This is the point where the bedrock becomes flatter according to the OGS model. As the depth is increasing from test point H10N toward the middle of the test line, the sharpness of the peak is maintained, but the amplitude increases, implying a stronger acoustic impedance contrast, or at least a larger effect on the horizontal spectrum for vertically propagating shear waves. Higher frequency peaks are also present, similar to the northern section.
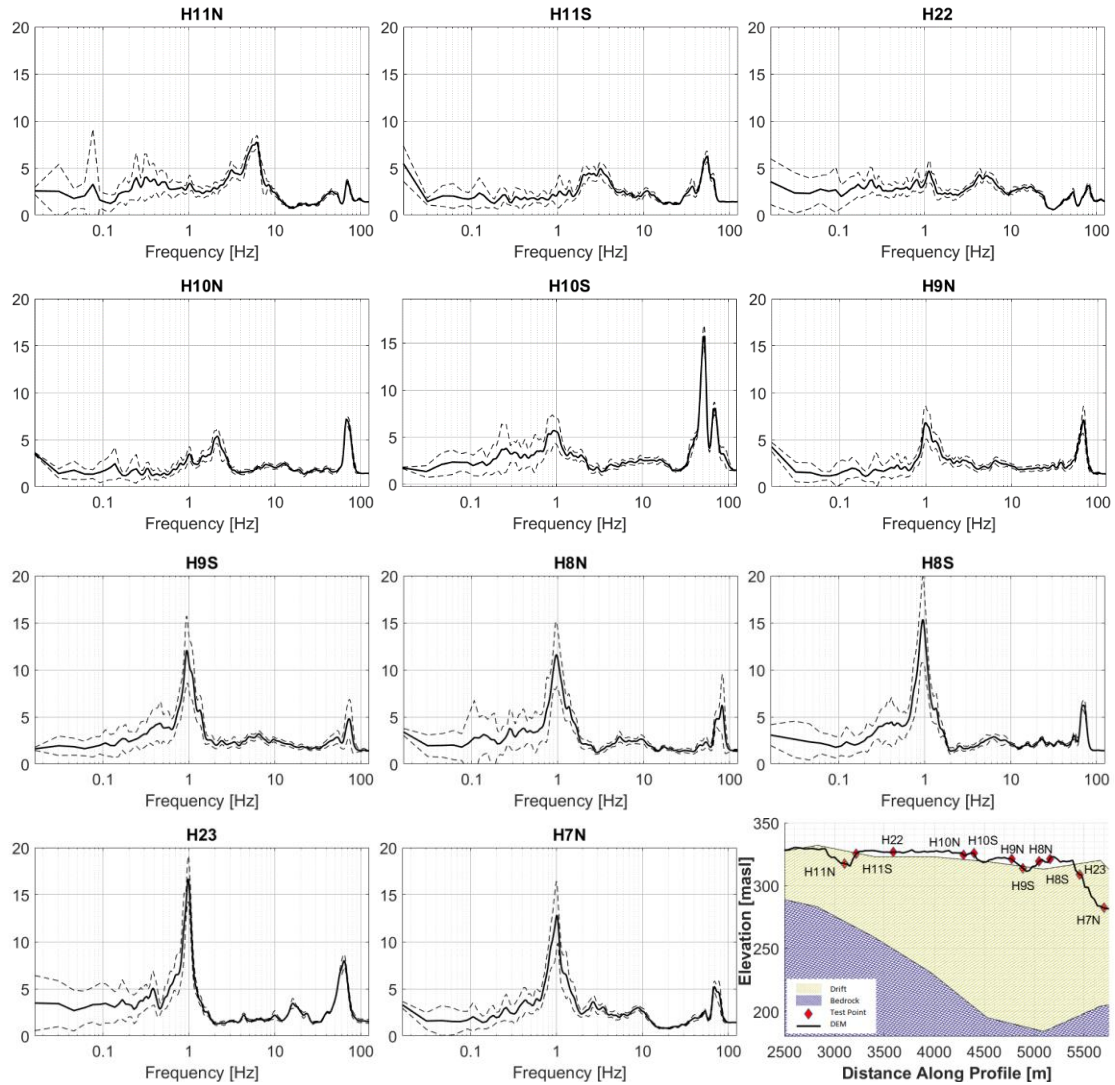
Figure 5.22: HVSR results for the middle section of Hockley Hills profile

5.3.3.4 Hockley Hills Southern Section

HVSR results for the southern section of the Hockley hills investigation are presented in Figure 5.23. Following the fundamental 1Hz peak from test point H7N southward, the peak first experiences broadening at points H7S and H24, followed by a gradual shift towards higher frequencies due to the shallowing of the drift. Before this peak's amplitude becomes unreliable at test point H14, there is a split at H13 showing two dominant frequencies: 1 Hz and 2.2 Hz.

The HVSR curve from test point H15 exhibits a multiple split low-frequency peaks, which could be a function of its position on top of a narrow hill. The lower frequency peaks are not present at the neighboring test points H14 and H16. The test points over the shallow drift section from H16 southward have clear higher frequency peaks between 9 Hz (at H16) and 11 Hz (at H17).
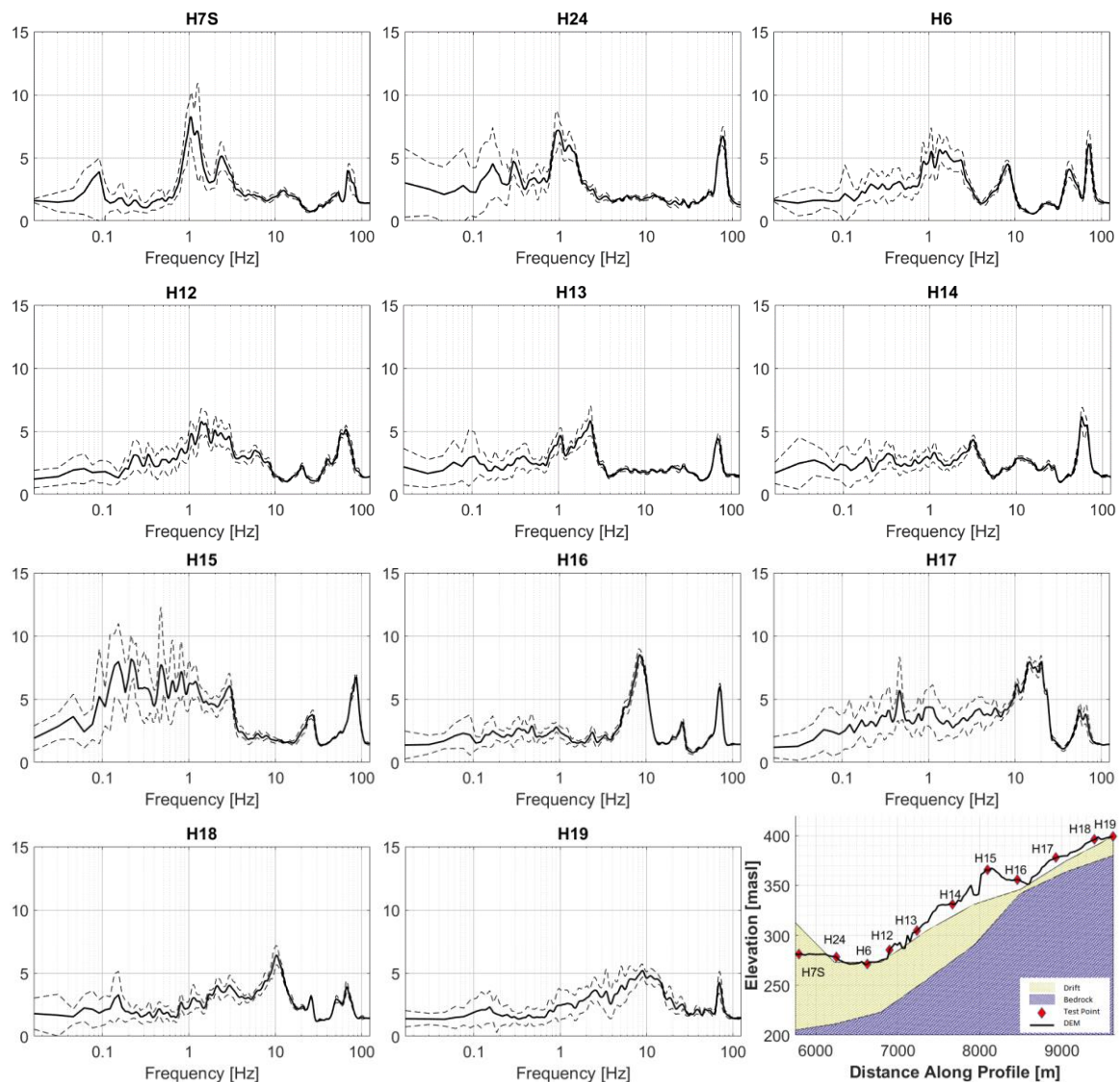
Figure 5.23:HVSR results for the southern section of Hockley Hills profile

Evaluating the interpolated map of the HVSR frequency and amplitude distribution (Figure 5.24), the focusing effect is observed, which is suggested by the clear maximum around the 1 Hz peak over the middle of the bedrock valley. Looking southward from the middle of the profile, the dominant peak shifts towards higher frequencies reaching 10 Hz at the edge of the profile (H19). This effect is much less pronounced in the northern section of the profile. High frequency peaks ~60-70 Hz, due to shallow interfaces, are intermittent along the profile which could be a result of soil conditions under the sensor.
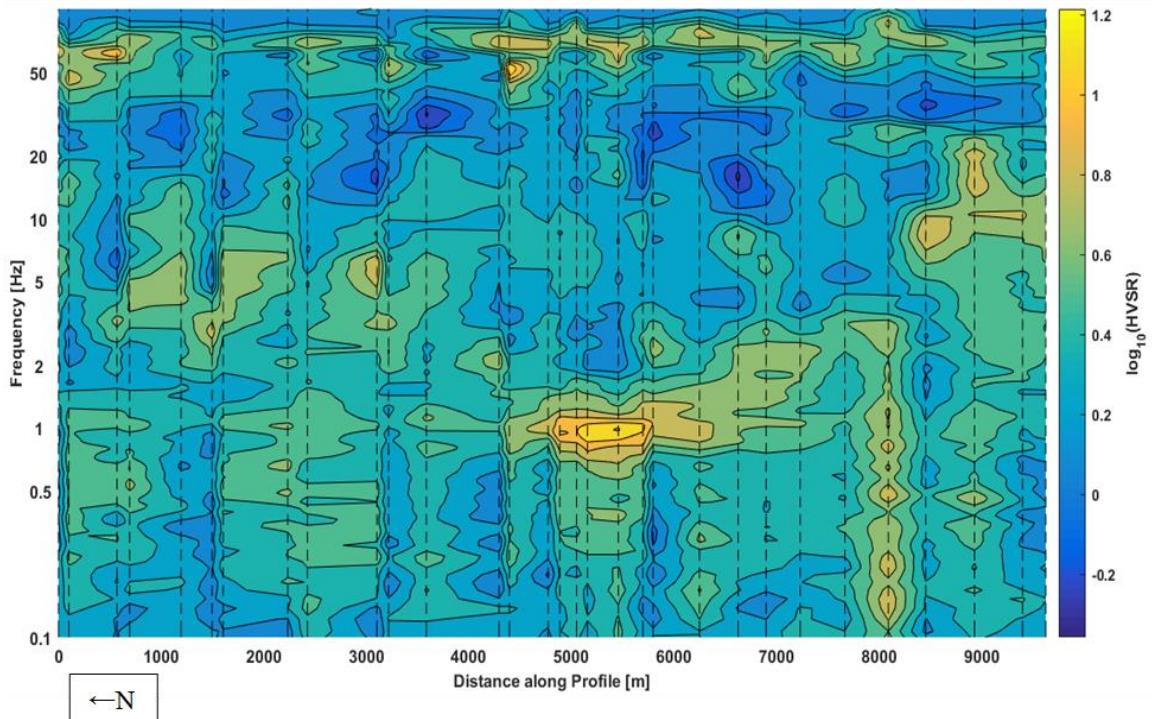
Figure 5.24: Interpolated distribution of HVSR dominant frequency and amplitudes along the profile, obtained from both the Geode and DYNAMate measurements. Dashed lines represent measurement point locations.

5.4 Conclusions

Based on the field studies presented herein, the following conclusions regarding the applicability of the methods and interpretation of the results can be drawn:

- OGS MRD207 does not provide accurate information regarding the bedrock elevation and drift thickness at the scale of these studies.
- Mass HVSR studies can be used to estimate changes in drift thickness under similar conditions.
- Mass HVSR investigation, when combined with MASW to obtain averaged soil shear velocities, can be used to amend existing bedrock and drift thickness models.
- Sloping surficial topography gives rise to amplification factors that vary along the flat surface behind the crest of the slope.
- When designing new construction situated over sloping surficial topography, the site amplification needs to be assessed at multiple points beyond the crest and toe of the slope to establish the maximum expected level of amplification.
- Site response amplification due to focusing of seismic wave arrivals can be observed in narrow valleys as well as over buried, deep and long slopes in the bedrock.
- When focusing is present due to bedrock topography, no significant fundamental peaks were observed away from the center of the valley.
- Wind has a strong effect on HVSR recording, especially in conditions where the sensor is directly affected by gusts, or nearby structures can induce earth motion due to the wind.
- Presenting the results from a HVSR profile as shown in Figure 5.13, Figure 5.15 and Figure 5.24 is useful in evaluation of drift thickness and topography effects.
- The results obtained from the Geode Seismograph and the DYNAMate 2.0 System were almost identical, which verified the accuracy of the developed system.

Chapter 6. HVSR parameterization

6.1 Introduction

Current methods of predicting ground motions for future earthquakes are based on an assumed seismological model of the source and the propagation effects. Ground Motion Prediction Equations (GMPEs) as defined for example by Boore and Atkinson (Boore and Atkinson, 2008) are used to establish expected peak ground velocities (PGV) and peak ground accelerations (PGA) at a site for a given earthquake size and epicentral distance. Commonly, GMPEs are empirically derived from the regression of recorded strong motions. A typical GMPE expression without the error term is given as:

$$lnY = F_M(M) + F_D(R_{JB}M) + F_S(V_{S30}R_{JB}M) \tag{6.1}$$

where Y is the response variable, M is moment magnitude, R_{JB} is the Joyner-Boore distance (the shortest distance from a site to the surface projection of the rupture surface), V_{S30} is the average shear-wave velocity to a depth of 30 m; F_M, F_D, and F_S are respectively: the magnitude scaling function, distance function, and site amplification function. Site characterization based on V_{S30} as the sole site parameter is in general an oversimplification of the site conditions. In practice, access to more site parameters is limited especially when producing a hazard map for a large area, and the use of V_{S30} may be justified. However, when available, additional site parameters should be obtained and incorporated in the GMPE generation. In general, V_{S30} is not closely related to the spectral amplification of soft soil sites. In some cases, V_{S30} can be complemented by the dynamic characteristics of the site, such as shear wave velocity profile or fundamental frequency f_0 (Bora et al., 2015; Pitilakis et al., 2013; Rubeis et al., 2011). Even with these two site parameters, the function F_S is still an oversimplification for real site response, especially in cases with layered soil profiles, fault zones, complicated surface or subsurface geometry. In practice, the site response curve can have more than one dominant response peak, in addition to the fundamental one. Flores et al. (Flores et al., 2013) showed that layered models can exhibit HVSR curves with more than one peak aside from the fundamental one and Tran (Tran Thanh Tuan, 2009) demonstrated that the secondary maximum may be associated with resonance frequencies of deeper layers. Additionally, Flores et al. (Flores et al., 2013)

reported that for certain values of the Poisson ratio, for the simple model of one or more layers over half-space, two peaks of the theoretical ellipticity may exist, as well as ellipticity inversion.

The simple site response models defined by Malischewsky (Malischewsky and Scherbaum, 2004) are commonly used to approximate site effect; however, this method does not fully describe real HVSR curves. Models incorporating multilayer soil profiles allow for better control of the shape of the resulting HVSR curves. Stafford (Stafford et al., 2017) showed, using SDOF model responses, that the site response is dependent on the magnitude and distance to the event, especially for short periods and small-magnitude scenarios.

Using GMPEs in engineering design requires knowledge of the seismic source parameters. In general, the far-field earthquake spectra is modelled by the simple Brune model (Brune, 1970), which relates the spectrum of the shear radiation to the stress released across an equivalent circular fault surface. The size of the rupture determines the corner frequency. The far-field velocity spectrum is given by:

$$\Omega(\omega) \; = \; \langle\mathfrak{R}\rangle \frac{\Delta\sigma\beta}{\mu} \frac{r}{R} F(\epsilon) \frac{\omega}{\omega^2+\alpha^2} \qquad (6.2)$$

where $\langle\mathfrak{R}\rangle$, is the average of the source radiation pattern, r is the equivalent circular fault radius, R is the distance, β is the average shear wave velocity at the fault, μ is the shear modulus, $\Delta\sigma$ is the effective stress drop, $F(\epsilon)$ is the stress drop term, and $\alpha = 2.21\ \beta/r = \omega_c = 2\pi f_c$, where f_c is the corner frequency (in Hz). In order to properly estimate the corner frequency of the source spectrum, it is important to remove the influence of the site response from the horizontal components of earthquake records measured at soil sites. Changes to the source model parameters are observed by adopting the simple Brune model given in Equation (6.2), replacing $\omega = 2\pi f$ and simplifying it as follows:

$$\Omega(f) = \frac{CM_0 2\pi f}{1+(f/f_c)^2} \qquad (6.3)$$

where $C = \langle\mathfrak{R}\rangle Ap/(4\pi\rho\beta^3 R)$, and $f_c = 4.9E6\ \beta(\Delta\sigma/M_0)^{1/3}$, $A=2.0$ is the free surface amplification, M_0 is the seismic moment and p is the proportion of the horizontal

components in the radiation pattern ($p \approx 0.71$) (Gail M Atkinson, 1993). This equation is fitted to the calculated velocity spectra using least-mean squared optimization algorithm.

Regardless of the utilized method, evaluation of the site effects and calculation of spectral amplification require information about geophysical properties such as soil stratigraphy, V_s profile, soil density, Poisson's ratio, etc. In addition, the method should allow defining the damping and natural frequency for each layer. This paper proposes a HVSR approximation model based on site measurements, and the Q factor/damping is determined by best fit approach. Therefore, the model curve cannot significantly exceed the source HVSR curve, which would underestimate the amplification factor in most cases as Attakan (Atakan et al., 2004) noted. The obtained model can be used to complement the site amplification function F_S in Equation (6.1), or to modify the horizontal ground motion component from an expected earthquake spectrum.

This model is applicable for elastic soil behavior. If a strong earthquake causes significant strain in soil layers, the reduction in shear strength and Q factor should be considered accordingly (Mihaylov, 2011). Additionally, by correcting for the site effect present in seismic records it would be possible to better approximate the Brune model to the earthquake spectra, and therefore obtain the source parameters more accurately. The simplification of the parameter space for the definition of GMPEs has strong effects on the epistemic variability of GMPEs, especially at long return periods. Additionally, the site's deeper velocity structure may not be identical, or even similar to the one (proxy) from which the strong motion data for the GMPEs was obtained. In most cases, especially when designing for longer period of return earthquakes, Los Angeles basin data is used. GMPE applications to sites in Southern Ontario need to consider the difference in the drift layer thickness and overall lower velocity profile. Having the HVSR models for both the site under investigation and the proxy site, the strong motion record can be adjusted by first dividing it by the proxy model and then multiplying it by the site model. This procedure may better reflect ground motion at the site under investigation.

6.2 Study Area and Data Selection for HVSR Modelling Verification

The Southern Ontario Seismic Network (SOSN/Polaris) is comprised of three-component broadband (Guralp CMG3ESP 60sec seismometers and KS-2000M 120sec seismometers) seismic stations, located mainly in the Greater Toronto Area and Niagara region of Ontario, Canada (Mereu et al., 2013). This is the area of Lake Ontario extending around the lake from east of Toronto to Hamilton to Niagara Falls. Due to the high population density, there are a lot of anthropogenic microtremor sources from major highways, railroads and manufacturing facilities. The surficial geology of Southern Ontario primarily consists of varying types and thicknesses of Quaternary deposits. The thickness of the drift layer varies between 0m and 200m across the region, and overlays a bedrock composed of Phanerozoic sedimentary rocks, which in turn overlie the older Precambrian rocks of the Canadian Shield. The bedrock elevation also varies from 0 masl up to ~500 masl and exhibits several irregular features such as the Niagara escarpment, as well as several ancient buried valleys (Eyles et al., 1997).

The events used in this study were the four largest recent earthquakes in Southern Ontario with available records by SOSN. The chosen events have magnitudes up to 4.3 m_N and hypocentral depths ranging from 4 to 18 km within the Precambrian Shield. (Mereu et al., 2002). Location, data, calculated depth, and magnitude for the events are given in Table 6.1. Analysis was performed using data from all SOSN stations that had records available for the time of the event. This paper shows results from several of the SOSN stations: Acton (ACTO), Bruce (BRCO), Pickering (PKRO), St. Catharines (STCO), Tyneside (TYNO) and Wesleyville (WLVO). All 6 stations are equipped with the Guralp CMG3ESP seismometer. The sample rate of the obtained seismograph records is 100Hz. Figure 6.1 shows the map of the study area, and Table 6.2 gives the distances and azimuthal direction between the stations and events. Waveform data was obtained from the GSC database (Earthquakes Canada, GSC, 2019).
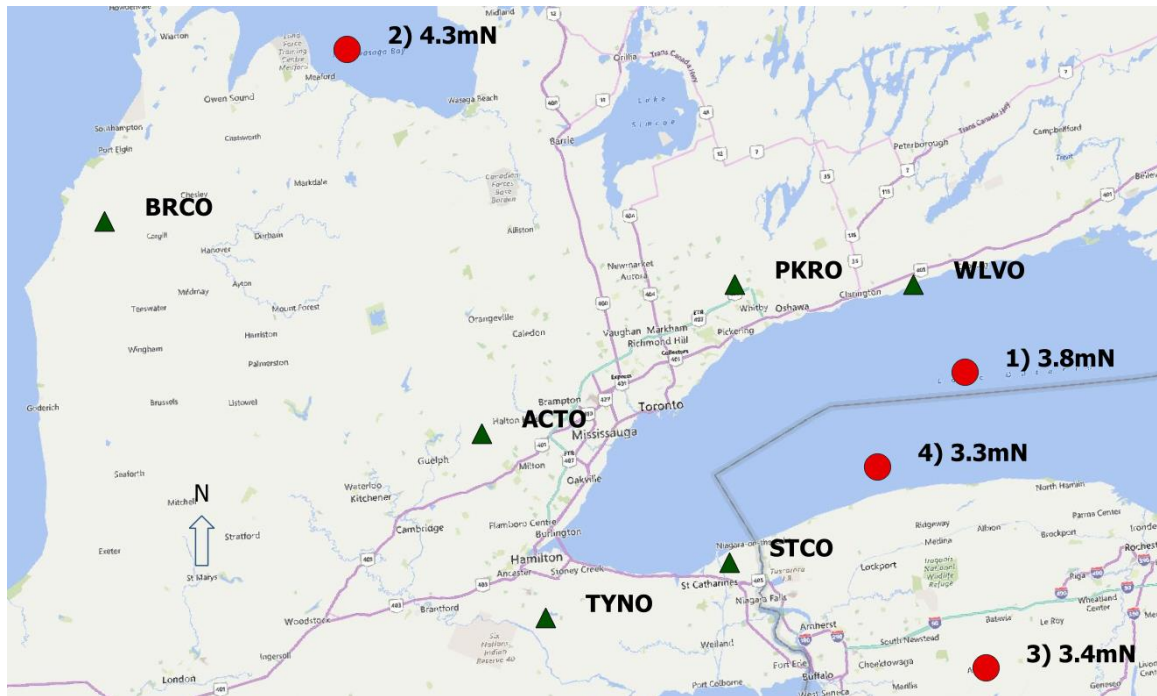
Figure 6.1: Selected Events and SOSN/Polaris stations in Southwestern Ontario used for HVSR calculation

Table 6.1: Earthquakes used in the analysis(Earthquakes Canada, GSC, 2019)

Event#	Date	Time (UT)	Latitude	Longitude	Depth	Magnitude
1	2004/08/04	23:55:26	43.677	-78.239	4.0g	3.8 m_N
2	2005/10/20	21:16:28	44.677	-80.482	11.0g	4.3 m_N
3	2009/06/05	15:07:52	42.864	-78.252	18.0g	3.4 m_N
4	2017/07/11	6:27:45	43.436	-78.589	7.5g	3.3 m_N

Table 6.2: Distances and direction from each station to the events used

Event#		Station					
		ACTO	BRCO	PKRO	STCO	TYNO	WLVO
1	Distance [km]	147	265	75	92	147	31
	Backazimuth [°]	87	103	115	56	64	155
2	Distance [km]	123	90	137	194	183	186
	Backazimuth [°]	344	57	306	328	345	298
3	Distance [km]	168	299	139	84	134	118
	Backazimuth [°]	119	120	151	117	100	174
4	Distance [km]	120	246	70	53	110	56
	Backazimuth [°]	99	110	146	62	69	196

6.3 Methodology

Noise recordings used to obtain a site HVSR are often affected by anthropogenic sources, wind noise, and instrument drift. To minimize the influence of the anthropogenic sources on the noise recording, data recorded during nighttime was used. Noise records of 30 min were selected for all stations starting at 2 am on June/2/2006. Wind effects as well as instrument drift were reduced by filtering the waveforms with 2nd order digital Butterworth high-pass filter with a cut-off frequency of 0.3 Hz.

6.3.1 HVSR Calculation

To further improve the HVSR accuracy, the signal was separated into low-level and high-level noise sections as per Mihaylov et al. (Mihaylov et al., 2016). The approach utilized the running average of the RMS of the total velocity vector, which in the case of microtremor contaminated with traffic or machinery noise must be smoothed before applying a threshold, to remove any spurious detection. Smoothing is duration dependent, where the duration of the smoothing window is chosen to be comparable to the disturbance duration, i.e. traffic passing by. Thresholding with hysteresis was then used to split the record into high- and low-level sections. The total velocity amplitude vector in discrete time is defined as:

$$|V_{total}(n)| = \sqrt{V_x(n)^2 + V_y(n)^2 + V_z(n)^2} \qquad (6.4)$$

The total velocity vector is then smoothed by using a Bartlett window, which is like the triangular window, however the first and last samples of the window are 0, additionally for odd lengths the window has a single sample at the peak, and for even samples there are two:

$$W_{Bartlett}(n) = \begin{cases} \dfrac{2n}{N} \; for \; n \in \left[0; \dfrac{N}{2}\right] \\ 2 - \dfrac{2n}{N} \; for \; n \in \left[\dfrac{N}{2}; N\right] \end{cases} \qquad (6.5)$$

The width of the smoothing window is determined experimentally to account for the encountered disturbances' duration and amplitudes. For example, in the case of vehicular traffic on a highway the window width is set to 10-13 sec. The resulting smoothed waveform is then compared to an adjustable threshold, splitting the signal into sections. The threshold location for each recorded signal is estimated manually based on the overall signal noise level as well as the amplitude and duration of the disturbance that is to be avoided in the HVSR calculation. The duration of the disturbance is used to establish the width of the smoothing window, and therefore the smoothness of the envelope that results from the application of the Bartlett window. Therefore, with a wide Bartlett window longer disturbance can be accounted for, however a longer portion of the signal before and after the disturbance are part of the disturbance it instead of background noise. The threshold level is then selected to allow for a maximum number of low-level, or noise windows without including any effects due to external disturbances.

Each section is further divided into processing windows of a specified duration, and overlap. The sections are then processed individually and the resulting HVSR are collected to form a statistical population. A Hann window is then applied to each section to eliminate sharp onsets and cut-offs. Each noise section is then filtered with a 6th order digital Butterworth high pass 0.1 Hz filter.

For the SOSN station data each section of the noise signal was separated into 80-sec windows with 50% overlap, for which the Fast Fourier Transform (FFT) was calculated. The large 80 sec windows were used since that the smallest sampled frequency is inversely proportional to the time window duration, and the overlap allows for the use of many windows per record, improving statistical quality. Thus, the produced HVSR curve covers the lower frequency range < 1 Hz. Only sections classified as having low noise signal are used to construct the HVSR model.

For the earthquake records, the window length was reduced to 20sec to accommodate for the duration of P- and S-wave. This increased the smallest sampled frequency by FFT but ensures that enough windows of only earthquake motion can be separated from the original signal.

The resulting spectra were then smoothed using Band-Pass Filters (BPFs) as will be defined later, resulting in three spectra for the three components (S_{NS}, S_{EW}, S_V). Using a smoothing operator inevitably brings the local minima (low points) of a spectrum curve (ones close to zero) up towards the mean of the spectral curve and does the opposite for peaks/maxima in the spectrum. This operation reduces the occurrences of very large values in the resulting HVSR curve due to the vertical component with spectral components close to zero. HVSR curves for each window were computed using Equation (6.6), as per Nakamura (Nakamura, 2009, 1989):

$$HVSR = \frac{\sqrt{S_{NS}^2 + S_{EW}^2}}{S_V} \tag{6.6}$$

Finally, the site HVSR curve was obtained as the average of the ensemble of all defined windows' spectra. The resulting HVSR curves can be seen in Figure 6.2 along with the HVSR curves obtained for each one of the four earthquakes recorded at the same stations. The earthquake HVSR was calculated over both the P and S waves. Figure 6.2 confirms the assumption that the HVSR curve does not exceed the site amplification due to strong motion. The results confirm the HVSR curves already presented by Murphy and Eaton (Murphy and Eaton, 2005) for the seismic stations installed here.

Complex surface wave generation due to randomly distributed and randomly acting external disturbances, results in a complex and unpredictable signal generation at the site that cannot be separated into sources without additional information, i.e. more sensors at the site or weather and wind monitoring (with sufficient resolution), neither of which were available for the chosen stations. The HVSR curves and corresponding models are therefore calculated based on the total horizontal vector.

6.3.2 Spectral Smoothing

In engineering practice, structural resonances are usually below 10 Hz, and design often relies on earthquake records from events with magnitude larger than 3, for which the Brune source spectra corner frequency (Equation 6.3), is less than 10Hz as is shown in Aki (Aki, 1972) and Sarkar and Duda (Duda and Sarkar, D, 1985). Therefore, strong motion HSVR

for frequencies larger than 10 Hz is related to the roll-off slope of the source spectrum and the energy contained in the higher frequency band is significantly smaller than in the band 1-10 Hz.

Discrete spectra obtained using the FFT operation have a finite frequency resolution determined by the length of the signal window and sample rate. This resolution is relatively large compared to the value of frequency at the low-frequency end of the spectrum (<1 Hz) and that leaves very few data points describing that range. At the high-frequency end, the spectral resolution is less than the value of frequency, resulting in spurious spectral noise, which often obscures dominant peaks. The averaging of individual horizontal and vertical components before the HVSR calculations here is proposed to be performed by BPFs, which produce smoothed HVSR at high frequency. It is more convenient to present HVSR in logarithmic frequency and linear H/V ratio scales. This approach eliminates the unstable evanescent extrema from individual spectra without skipping the stable and significant high-frequency components. These eliminated peaks have no particular significance in geological interpretation or in the design practice and obscure the H/V ratio behavior at frequencies above the corner frequencies of the expected earthquake. HVSR interpretation, for practical cases, can be very subjective and using the BPFs approximation avoids misinterpretation in the high-frequency range.
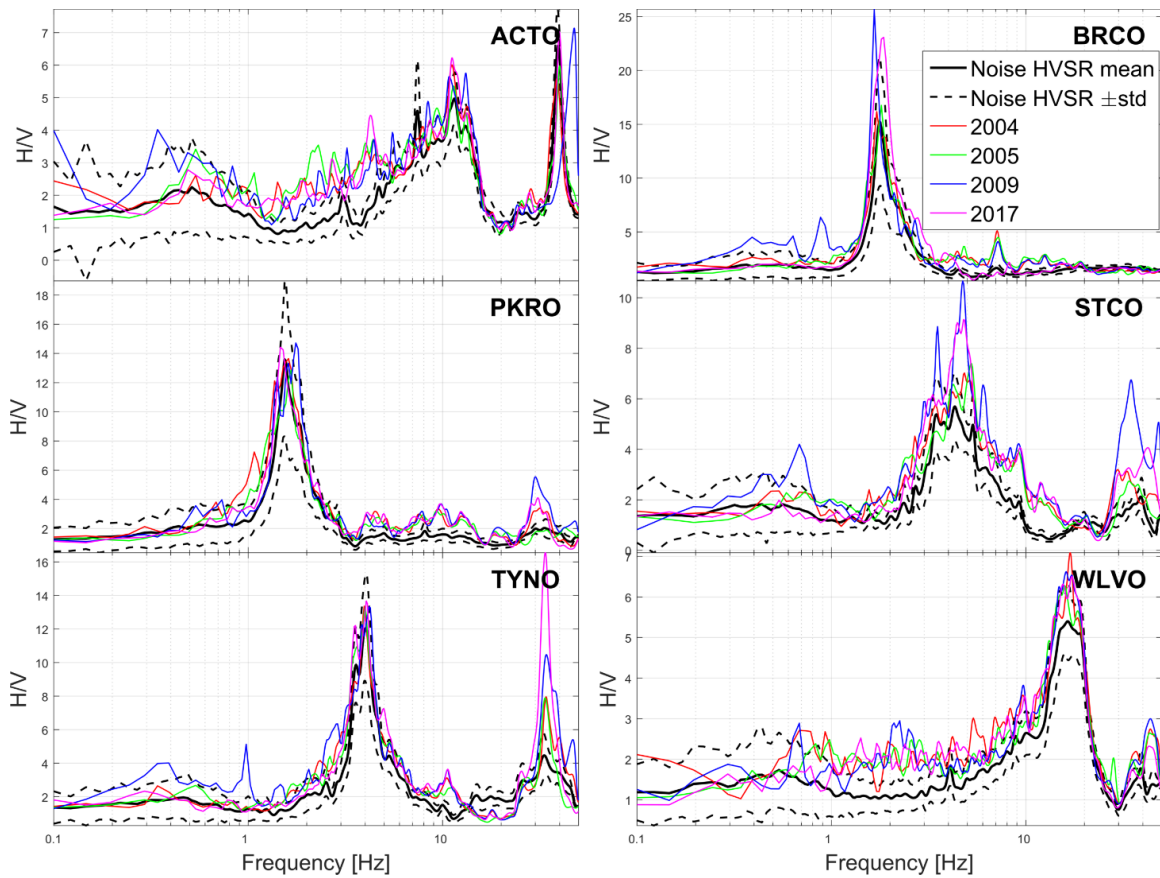
Figure 6.2: Comparison of HVSR from noise and earthquake data obtained for the stations given in Table 6.2

Spectral smoothing is a filtering operation performed on frequency data instead of a time signal. As with any filtering operation the result is determined by the function used to define the filter. The operation can be described using convolution by the following equation:

$$S_{out}(f = f_n) = S_{in}(f) * H(f) = \sum_{f=0}^{f=f_{Nyquist}} H(f_n - f)S_{in}(f) \qquad (6.7)$$

The purpose of the summation operator in the equation above is to show that both input (S_{in}) and output (S_{out}) spectra are discrete. $H(f)$ are the values of a symmetrical non-causal filter and f_n is the center frequency for the operation. Each element of the discrete output spectrum $S_{out}(f_n)$ is calculated using the input spectral values around f_n both behind and ahead in frequency, thus introducing the requirement for non-causality. A simplification is

added to the process here: the convolution operation is not required, since *H(f)* is defined as symmetric, in which case a running average operation, using *H(f)* as the weight vector is performed. Non-causality of the filter allows the function to look ahead and perform the averaging. Additionally, using a symmetrical function for smoothing also limits the peak shift in the HVSR after the operation.

Another common problem in spectral smoothing is the reduction of the amplitude with increasing frequency. This occurs when functions have a constant bandwidth regardless of the center frequency, and it is due to the linear distribution of frequencies in the discrete spectrum. To solve this problem, functions of constant quality factor (Q) should be used instead. This has the effect that regardless of frequency the function has a constant width in logarithmic frequency (see Figure 6.4, top). Most commonly used smoothing function for HVSR data processing is given by Konno and Ohmachi (Konno and Ohmachi, 1998). The authors introduced it to tackle the reduction in amplitude problem, and is defined as:

$$H(f, f_c, b) = \left[\frac{sin(log_{10}((f/f_c)^b))}{log_{10}((f/f_c)^b)}\right]^4 \tag{6.8}$$

The Konno & Ohmachi (KO) window function, however, has side lobes present around the center peak. This introduces a wider range of frequencies with higher weights into the calculation of the smoothed spectra. The side lobes can be reduced by increasing the steepness of the function (increasing b); however, this will also reduce its effective width and result in a rougher (less smooth) output spectrum. To avoid this problem, and with inspiration from the SDOF modelling by Malischewsky (Malischewsky and Scherbaum, 2004), the following band-pass filter is proposed here:

$$|BPF(A, f, f_c, n)| = A\left[\frac{(f/f_c)^2}{(1-(f/f_c)^2)^2+(f/f_c)^2}\right]^n \tag{6.9}$$

Where f_c is the corner frequency of the filter, and for $n=1$ the damping is 0.5. The resulting function (see Figure 6.3) has a quality factor (Q) that is constant regardless of the center frequency and determined only by the value of *n*. The function is asymptotic to 0 to both

the left and right of the center frequency, and therefore does not have side-lobes. The following equation is used to solve for the Q factor of the resulting function:

$$Q = \frac{\sqrt{f_1 f_2}}{f_1 - f_2} \tag{6.10}$$

Where f_1 and f_2 are -3dB intercept frequencies of filter characteristic, which are the solutions to equation 6.9 when it equals 0.7071 (-3dB)

Substituting $a = (f/f_0)^2$ into Equation (6.9) results in:

$$|BPF(A, f, f_0, n)| = A \left[\frac{a}{(1-a)^2 + a} \right]^n \tag{6.11}$$

Setting A=1 the -3dB intercept can then be found:

$$\left[\frac{a}{(1-a)^2 + a} \right]^n = \frac{1}{\sqrt{2}} \Rightarrow \frac{a}{(1-a)^2 + a} = 2^{-\frac{1}{2n}} \Rightarrow a^2 - a\left(1 + 2^{\frac{1}{2n}}\right) + 1 = 0$$

Letting $\vartheta = 1 + 2^{\frac{1}{2n}}$, then solving results in the two roots: $a_{1,2} = \frac{\vartheta \pm \sqrt{\vartheta^2 - 4}}{2}$

Based on substitution above $f = f_0 \sqrt{a}$, using Equation (6.10), and postulating that f2>f1:

$$f_1 f_2 = f_0^2 \sqrt{\left(\frac{\vartheta + \sqrt{\vartheta^2 - 4}}{2}\right)\left(\frac{\vartheta - \sqrt{\vartheta^2 - 4}}{2}\right)} = f_0^2 \sqrt{\left(\frac{\vartheta^2 - (\vartheta^2 - 4)}{4}\right)} = f_0^2 \tag{6.12}$$

$$f_2 - f_1 = f_0 \left[\sqrt{\frac{\vartheta + \sqrt{\vartheta^2 - 4}}{2}} - \sqrt{\frac{\vartheta - \sqrt{\vartheta^2 - 4}}{2}} \right] = \frac{f_0}{\sqrt{2}} \left[\sqrt{\vartheta + \sqrt{\vartheta^2 - 4}} - \sqrt{\vartheta + \sqrt{\vartheta^2 - 4}} \right] \tag{6.13}$$

$$Q = \frac{f_0}{\frac{f_0}{\sqrt{2}} \left[\sqrt{\vartheta + \sqrt{\vartheta^2 - 4}} - \sqrt{\vartheta + \sqrt{\vartheta^2 - 4}} \right]} = \frac{\sqrt{2}}{\sqrt{\vartheta + \sqrt{\vartheta^2 - 4}} - \sqrt{\vartheta + \sqrt{\vartheta^2 - 4}}} \tag{6.14}$$

$$Q^2 = \frac{2}{\left(\sqrt{\vartheta + \sqrt{\vartheta^2 - 4}} - \sqrt{\vartheta + \sqrt{\vartheta^2 - 4}} \right)^2} = \frac{1}{\vartheta - \sqrt{(\vartheta^2 - \vartheta^2 + 4)}} = \frac{1}{\vartheta - 2} \tag{6.15}$$

Substituting $\vartheta = 1 + 2^{\frac{1}{2n}}$ yields the final expression for the Q factor of the BPF function:

$$Q = \sqrt{1/\left(2^{\frac{1}{2n}} - 1\right)} \Leftrightarrow n = \frac{0.5 \log 2}{\log(1 + Q^{-2})} \tag{6.16}$$

$$dropoff\ slope = f_0 \frac{dBPF(f)}{df} = 24n\left(\frac{dB}{oct}\right) = 80n\left(\frac{db}{dec}\right) \qquad (6.17)$$
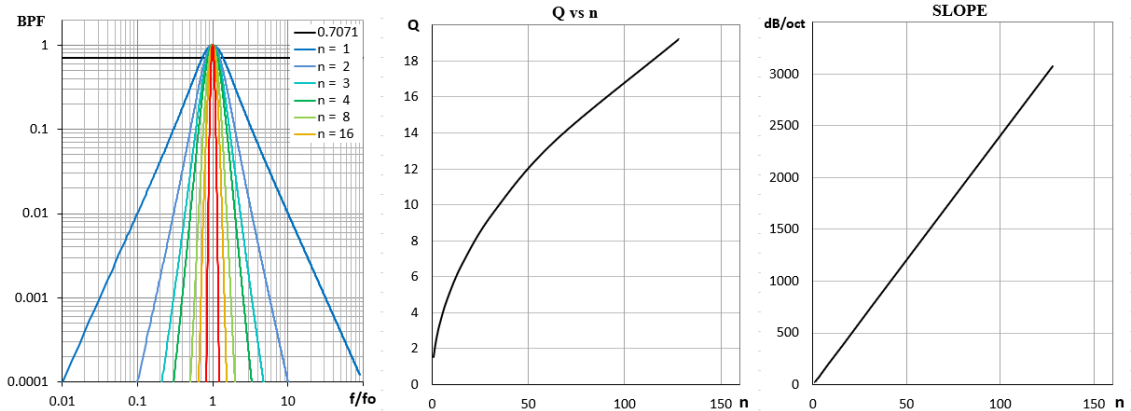
Figure 6.3: Filter response for normalized frequency (left), Quality factor (middle), and logarithmic slope in dB/oct (right) as a function of slope steepness(n) given in Equations (6.16) and (6.17)

Figure 6.4 compares the spectra obtained employing several logarithmic smoothing functions: KO function and BPF as well as a constant logarithmic slope triangle function. The *n, b* and triangle slope are chosen such that all 3 smoothing functions have the same bandwidth for a given center frequency. Additionally, two non-logarithmic windows are included: A Parzen window (Konno and Ohmachi, 1998) with bandwidth set to 0.5Hz and the Dolph-Chebyshev (DC) (Smith, 2011) window with $a = 5$. The latter two functions do not maintain their width in a logarithmic scale, and the effect on the smoothed spectra is more noise in the high frequency range as compared to the low frequency as can be noted from Figure 6.4. The overall width of the function (of either type) determines the final smoothness of the spectra. This can be seen with the triangle smoothing, where the triangle function is the one with the smallest roll-off slope, as well as with the Parzen and DC windows, of which the Parzen window is wider for any given center frequency, and correspondingly the overall amplitudes in the Parzen smoothed spectra are lower than the ones obtained with DC. The effect of the KO sidelobes can be best observed at the low frequency range of the sample spectrum where it adds some artifacts to the result. As stated before, increasing the order of the BPF filter (increasing n, and thus Q) results in closer and closer approximation of the original spectrum.
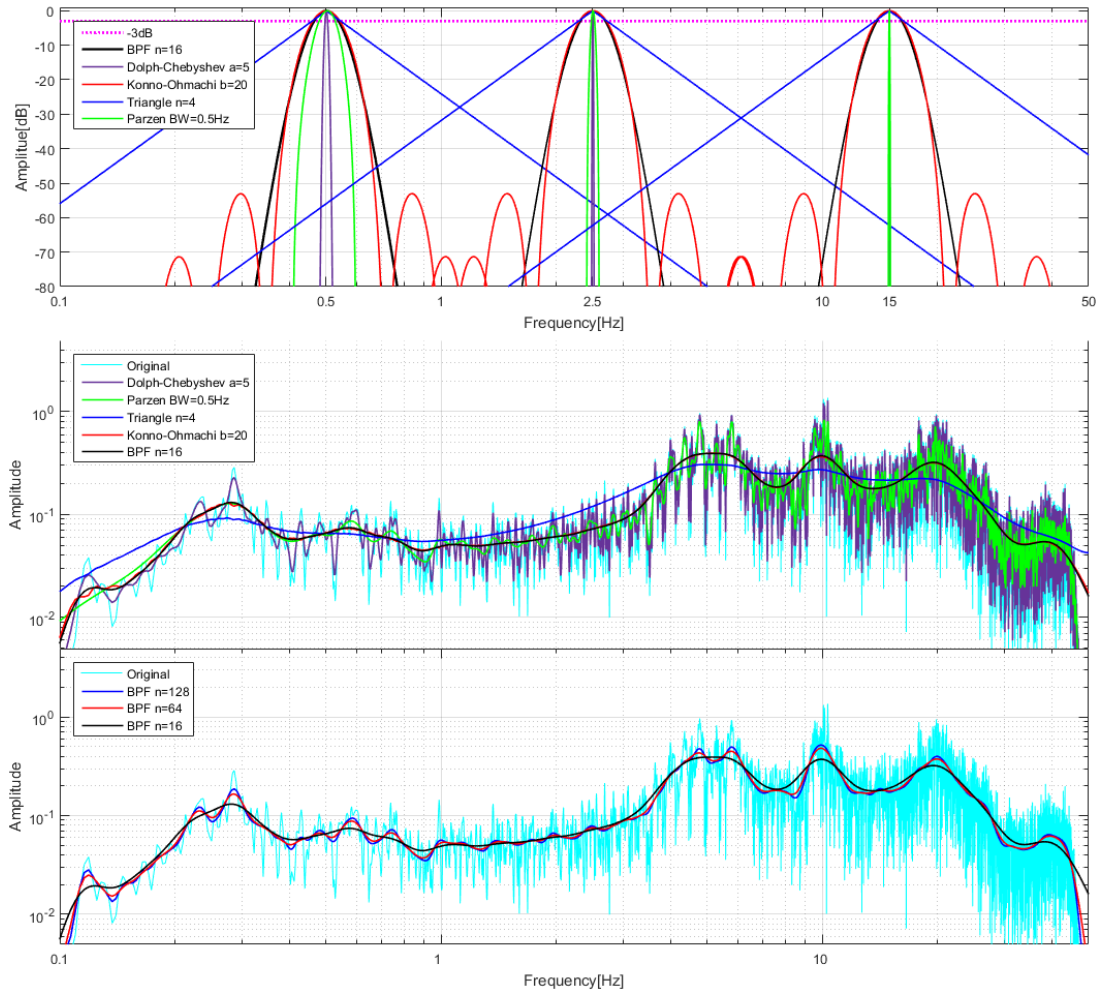
Figure 6.4: Comparison of smoothing functions for 0.5, 2.5 and 15 Hz (top), Effect on a sample spectrum (middle), and Effect of increasing Q for the BPF(bottom)

In the KO smoothing function, the *b* parameter controls the Q-factor; however, reducing the Q factor, which is required for a smoother spectrum, increases the normalized amplitudes of the side-lobes. Therefore, the BPF was selected as the smoothing function in the current study to avoid the artifacts introduced by the KO sidelobes, and at the same time, it is incorporated in the developed HVSR model as a basis function. Thus, smoothing of the spectra was performed using the proposed BPF function, which gives sharp roll-off slope without side-lobes, with n = 256 and equivalent Q = 13.6.

Due to smoothing the expected amplitude of each peak is reduced proportional to the width of the smoothing operation (Konno and Ohmachi, 1998).

6.3.3 HVSR Model

It is widely accepted to approximate the soil resonances obtained by HVSR as response of a Single Degree of Freedom Oscillator (SDOF), given in the following equation:

$$|H(f, f_n, \xi_n)| = \frac{1}{\sqrt{\left(1 - \left(\frac{f}{f_n}\right)^2\right)^2 + \left(\frac{2hf}{f_n}\right)^2}} \tag{6.18}$$

The same approach was used in the determination of the response spectrum by McGuire (McGuire, 1977; McGuire et al., 2002). This representation assumes that for higher frequencies the response is steeply decaying, and after convolution the high-frequency portion of the signal convolved with the SDOF response will be greatly diminished. In a layered soil model, multiple resonances are often observed in the HVSR curve, and thus multiple resonators should be used to approximate the HVSR curve. Therefore, to approximate a given HVSR curve, a set of parallel BPFs was used. This set includes one all-pass filter, BPF_0, which was used to establish a base level for the HV ratio of 1 as per Nakamura's assumption that the vertical motion is not affected by the soil response.

Each BPF's response spectrum was defined by the center frequency (f_0), gain (A) and slope steepness (n) as given by Equation (6.9). The responses of the BPFs are independent of each other. Combining the responses of the BPFs in order to approximate the HVSR can be achieved either through multiplication or addition. In the case of multiplication, neighboring BPFs attenuate each other, as the peak of one is multiplied by the tail of another. This results in higher A and Q parameters required for the BPFs and makes matching the low frequency roll-off of the HVSR curve much more difficult. Therefore, the final model is comprised of the sum of all BPFs, which is allowable as the BPF responses are independent. It is important to note here that each BPF filter does not describe a layer, but that the site response due to the combination of all layers and geometry is approximated by their combined sum in the HVSR model. Every BPF function is assumed to be independent of the other functions in the set. The final model, composed of N independent BPF functions is defined in by the following equation:

$$HVSR_{model}(f) = 1 + \sum_{k=1}^{N} BPF(A_k, f_{0,k}, n_k, f) \qquad \textbf{(6.19)}$$

6.3.4 Model Optimization

The sum of the BPF responses was subtracted from the original HVSR to produce an error difference, whose RMS can be used to tune the BPF parameter set. This sum of BPF responses has a non-linear relationship to the steepness parameter *n* of the BPF. Non-linear Least Squares (NLMS) and the Sequential quadratic programming (SQP) constrained optimization (Nocedal and Wright, 2006) were used to estimate the parameter set that minimizes the RMS of the error.

Either optimization method adjusts the gain and steepness parameters, while the center frequencies are pre-defined and kept constant. Constraints were placed that limit the parameter values to $n \geq 0, A < HVSR(f_i)$ BPF gain is limited to the HVSR value at each selected peak frequency. The HVSR model is obtained as the sum of the optimized BPFs as demonstrated in the flowchart presented in Figure 6.5 and discussed below.

From the original HVSR curve, the initial HVSR model was developed by automatically identifying and selecting the most prominent peaks, using common signal processing algorithms. The peak identification algorithm finds local maxima in the HVSR curve with requirements for minimum peak prominence (amplitude compared to neighboring maxima), peak width and distance between consecutive peaks.

The selection of the peaks, such that the approximation is true to the original HVSR is not trivial in practical cases. More than one BPF is often required to fully describe the shape of any given HVSR peak. In some cases, one large HVSR may obscure a neighboring smaller peak, if detectable this smaller peak has the effect of broadening the HVSR peak or introducing an inflection point on one of the slopes. Picking these inflection points as additional BPFs results in a better fit to the original HVSR curve. This set of peaks was used to set the frequency parameters for the BPFs, which was kept constant throughout the optimization For each selected center frequency, a BPF function was initialized with the corresponding value of the original HVSR curve as an initial estimate for the amplitude (A) BPF parameter. All slope (n) parameters are initialized to 128, equivalent Q = 9.6.

Depending on the original HVSR curve, and fit error requirements, more or less BPF functions can be used to either give a finer approximation of the original or produce a simpler model, respectively.
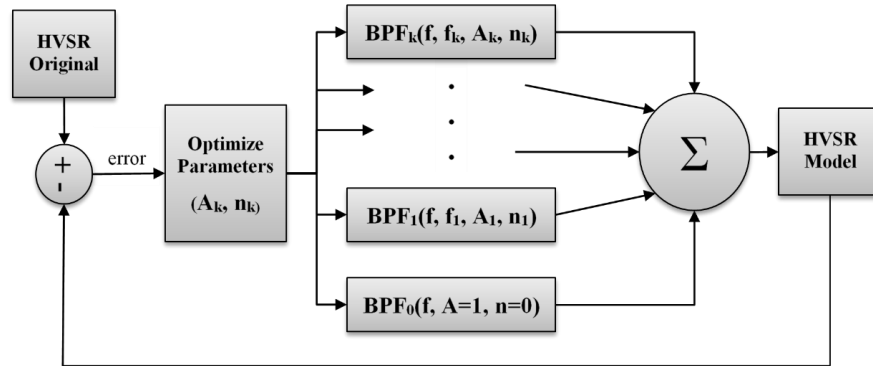
Figure 6.5: Simplified procedure for estimating a parametric HVSR spectral model

Solving constrained non-linear optimization problems often arise in engineering applications, and there are a variety of tools to address this challenge. SQP provides a sound theoretical foundation and convenient algorithm and is generally considered one of the best optimization techniques for these types of problems.

For the application considered here, the selection of filter parameters to best match a given HVSR curve can be thought of as a constrained non-linear optimization problem (NLP). Since the filters describing the HVSR curve are meant to incorporate some property or combination of properties of the underlying soil layers and structures, their parameters are limited to a viable parameter space within which these filters can represent the physical environment. For example, in the present model the slope of the filter roll-off should be limited to ensure that it remains a bandpass filter (i.e. convex not concave spectral shape), and to ensure that the amplitude can never be below 0 for the case of a ratio between two real spectra. A typical NLP problem can be generally stated as follows:

$$minimize\ f(x), for\ x \in \Psi^n\ subject\ to\ \begin{array}{c} h(x) = 0 \\ g(x) \leq 0 \end{array} \qquad (6.20)$$

In Equation (6.20), Ψ^n defines the parameter space of the problem, f(x) is the objective function that is defined on $\mathfrak{R}$ and takes a scalar value for any given set of parameters representing the optimality of the solution defined by these parameters. The functions h(x) $\in \mathfrak{R}^m$ and g(x) $\in \mathfrak{R}^p$ are the equality and inequality constraints, applied to any or to all of the parameters. In this case, there is no non-linear constraint; however, using this algorithm allows establishing relationships between different BPFs in terms of their parameters. The constraint functions g(x) can be used to limit the layer parameters such as Vs, density, etc.

SQP solves the optimization problem iteratively by modelling the NLP for a given iteration (x_k) by a Quadratic Programming Subproblem, solving the QP subproblems which are then used to calculate a new iterate (x_{k+1}). The construction for this new iterate is done such that the sequence of iterates converges to a local minimum. Additional minima can be found by using a varying set of starting parameter values. The SQP algorithm is suited for small scale problems, i.e. problems that have a limited number of parameters, or a large input set resolution. It does provide the ability to introduce functional, non-linear constraints on the parameter set. If such constraints are not required, or cannot be obtained from available data, the Non-Least squares Levenberg-Marquardt (Marquardt, 1963) algorithm can be much better suited to the problem, improving performance significantly over SQP, while producing similar results.

The full modeling procedure, starting from field data and resulting in HVSRs and corrected spectra was incorporated in a semi-automatic MATLAB program with convenient graphical user interface (GUI). The GUI allows pre-processing the data using the procedure mentioned above and enables the user to tune the signal separation into high and low sources in order to produce the site HVSR after applying smoothing to the input spectra. Once the HVSR is calculated, the output can be either an HVSR model, or an existing HVSR model can be imported, and the correction described above is applied. In the latter case, the output of the program is the corrected (modified) spectra and time series.

6.4 Application and Results

BPF models were developed to approximate the HVSR curves obtained using nighttime noise and the results are presented in Figure 6.6 for the SOSN stations given in Table 6.2 where dashed lines represent the individual BPF responses used in the model. Additionally, the HVSR of strong motion (S-wave and P-wave) for each of the earthquakes in Table 6.1 was calculated. Window size of 20sec overlapped by 50% was used to establish the mean values presented in Figure 6.2. The dominant frequencies (with HVSR value at the peak frequency greater than 2) present in the night-time noise HVSR are given in Table 6.3.

Table 6.3: Dominant frequencies detected in the nighttime noise HVSR model

Station	*ACTO*	*BRCO*	*PKRO*	*STCO*	*TYNO*	*WLVO*
Dominant frequencies	5-11 Hz 40 Hz	2 Hz	2 Hz	3-5 Hz 40 Hz	4 Hz 25-40 Hz	15-20 Hz

Comparison of the HVSR curves presented in Figure 6.2 shows that for almost all considered cases there is good agreement between the HVSRs from noise before the earthquake and from the earthquake. Both the fundamental frequency and amplitude of the strong motion HVSR are within two standard deviations of the noise HVSR mean curve, except for station STCO, where the strong motion HVSR amplitude exceeds the noise HVSR amplitude for frequencies >20 Hz. Despite the difference in amplitude between the noise and earthquake HVSRs, corrected STCO data show similar results to stations TYNO, ACTO and WLVO.

In some cases, the application of the HVSR model provides better results if the original NS-EW waveforms are rotated to radial and transversal components (local coordinate system). This can provide better separation between SH and P-SV seismic waves. Unfortunately, wave-separation depends not only on the back azimuth to the source but also on source orientation and existing vertical geological structures. For this application, all waveforms are rotated according to the backazimuth values given in Table 6.2.
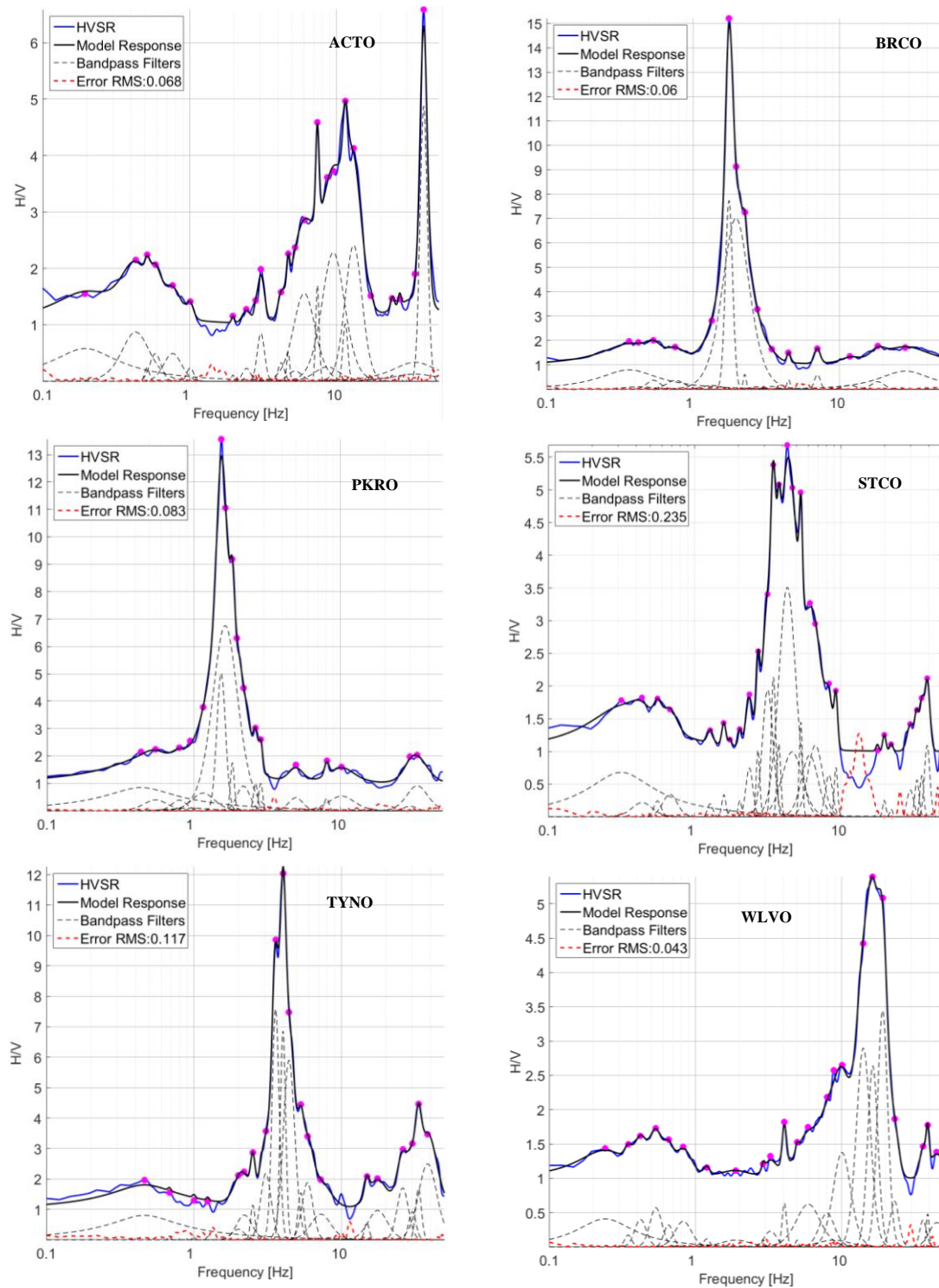
Figure 6.6: HVSR Models obtained from nighttime noise at the chosen SOSN/Polaris stations. The red points on the curves indicate the BPF center frequencies used for the approximation of the HVSR spectra. Dashed lines represent the individual BPF responses used in the model

The BPF models developed for the chosen stations (Figure 6.6) were used to reduce the site effects present in the earthquake records of the four events listed in Table 6.1. For this purpose, the rotated (from NS-EW to Transverse and Radial components) horizontal non-smoothed spectra of each component are divided by the modelled response. The modelled response is real-valued, and therefore the modified spectra retains the original signals' phase. After performing an inverse Fourier Transform, the resulting waveforms show reduced site effects. For all stations Figure 6.8 to Figure 6.11, show the rotated horizontal and vertical components of the waveforms and the waveforms corrected for the site response using their corresponding station models. If the Nakamura assumption is perfect, the corrected waveform would be as recorded over bedrock. The similarity between corrected horizontal and original vertical spectra for all considered stations agrees with the assumption that only the horizontal components of the motion are affected by the site effect.

The change in source corner frequency is particularly evident for stations ACTO and WLVO, which have a dominant HVSR peak at a frequency greater than 10Hz. For these stations, the corner frequency is reduced, which is particularly evident for events #1 (Figure 6.8) and #2 (Figure 6.9). For the other two events, the shift in frequency is smaller and thus less evident. For stations STCO and TYNO, the corner frequency increases slightly for Events # 1 (Figure 6.10) and #4 (Figure 6.11); however, for the other two events there is no significant change. For stations PKRO and BRCO there is no obvious change in the corner frequency for any of the events. The modification of the spectra after the correction for the site response shows variations in the corner frequency between the stations for the same event. Possibly these variations are related to the mechanism of the earthquakes. Further detailed study using the proposed methodology may be helpful in obtaining additional information about the seismic source. Examples of the calculated velocity spectra with the Brune model fit are given in Figure 6.7, for the two of the cases analyzed in this study. After the removing the site response for station ACTO the corner frequency moved form 5.55 Hz to 3.58 Hz, and for BRCO from 2.22 to 3.17 Hz, however the low-frequency portion of the spectra also experienced changes which would imply changes to the seismic moment (reduced seismic moment). The Brune spectra parameters are more consistent after correction.

In all cases, the PGV are reduced after correction. The reduction in PGV is generally greater when the HVSR has higher (>10Hz) dominant peaks. For all events, stations ACTO and WLVO exhibit the largest reduction in PGV due to the correction. The effect of the correction on the PGV of stations BRCO and PKRO is very small, especially for events #3 and #4 (Figure 6.10 and Figure 6.11) where the PGV value is nearly unchanged. Both events have magnitudes less than 3.5. Stations STCO and TYNO, after correction have reduced PGV for all events but the reduction is less than that observed for stations ACTO and WLVO.

Based on the behavior of the corrected waveform and spectra, the station results can be organized in three categories:

- BRCO/PKRO – dominant HVSR peak less than 2 Hz. Site response correction has minimal effect for all considered events
- STCO/TYNO – one dominant peak around 4Hz and one >30 Hz. For all considered events, exhibit a reduction in PGV, however corner frequency shift is only observed in data from events with magnitudes less than 3.5.
- ACTO/WLVO – one or more high frequency >10 Hz dominant peaks. Response correction has a large effect on both the PGV and corner frequency for all considered events
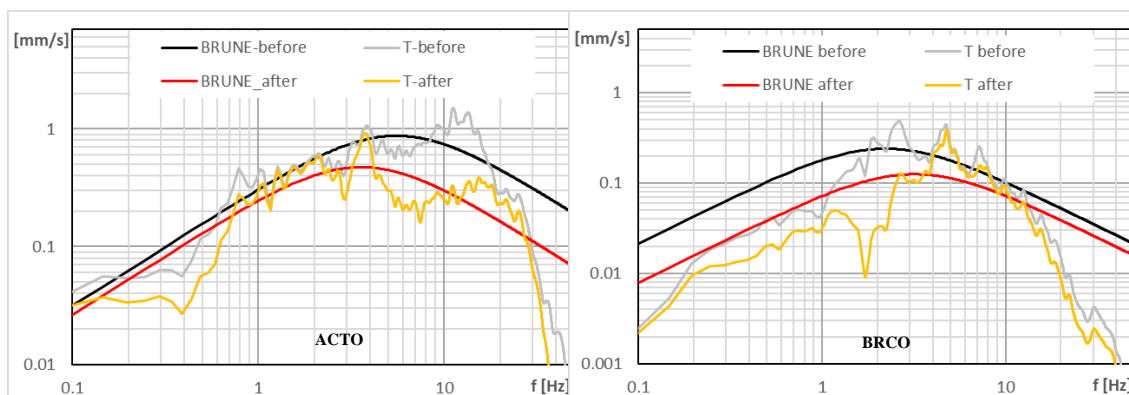
Figure 6.7: Brune spectra for stations ACTO and BRCO for the 2005/10/20 4.3 m$_N$ earthquake (#2)
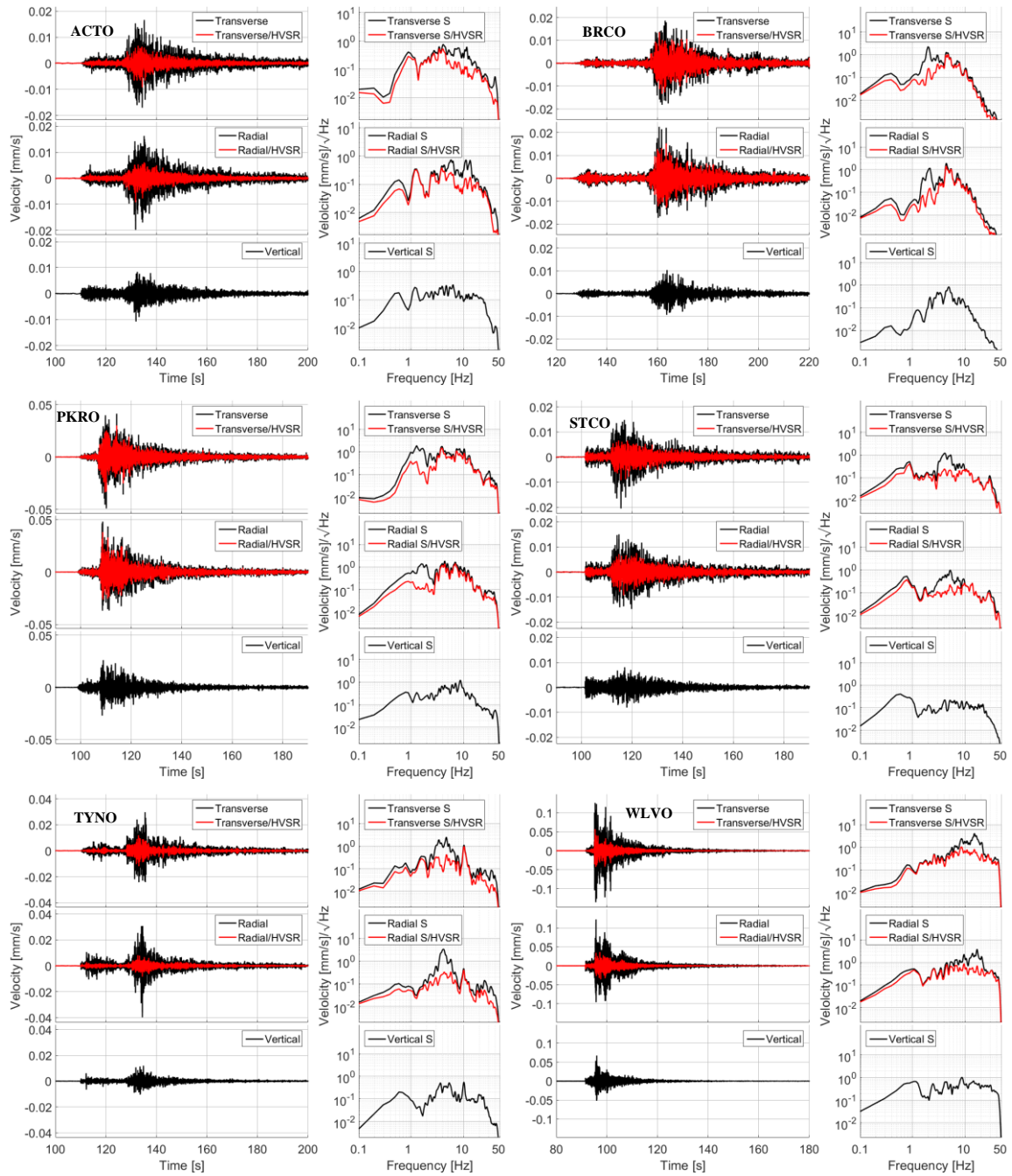
Figure 6.8: Earthquake records and S-wave velocity spectra of all 6 stations for the 2004/08/04 3.8 m_N event (#1)
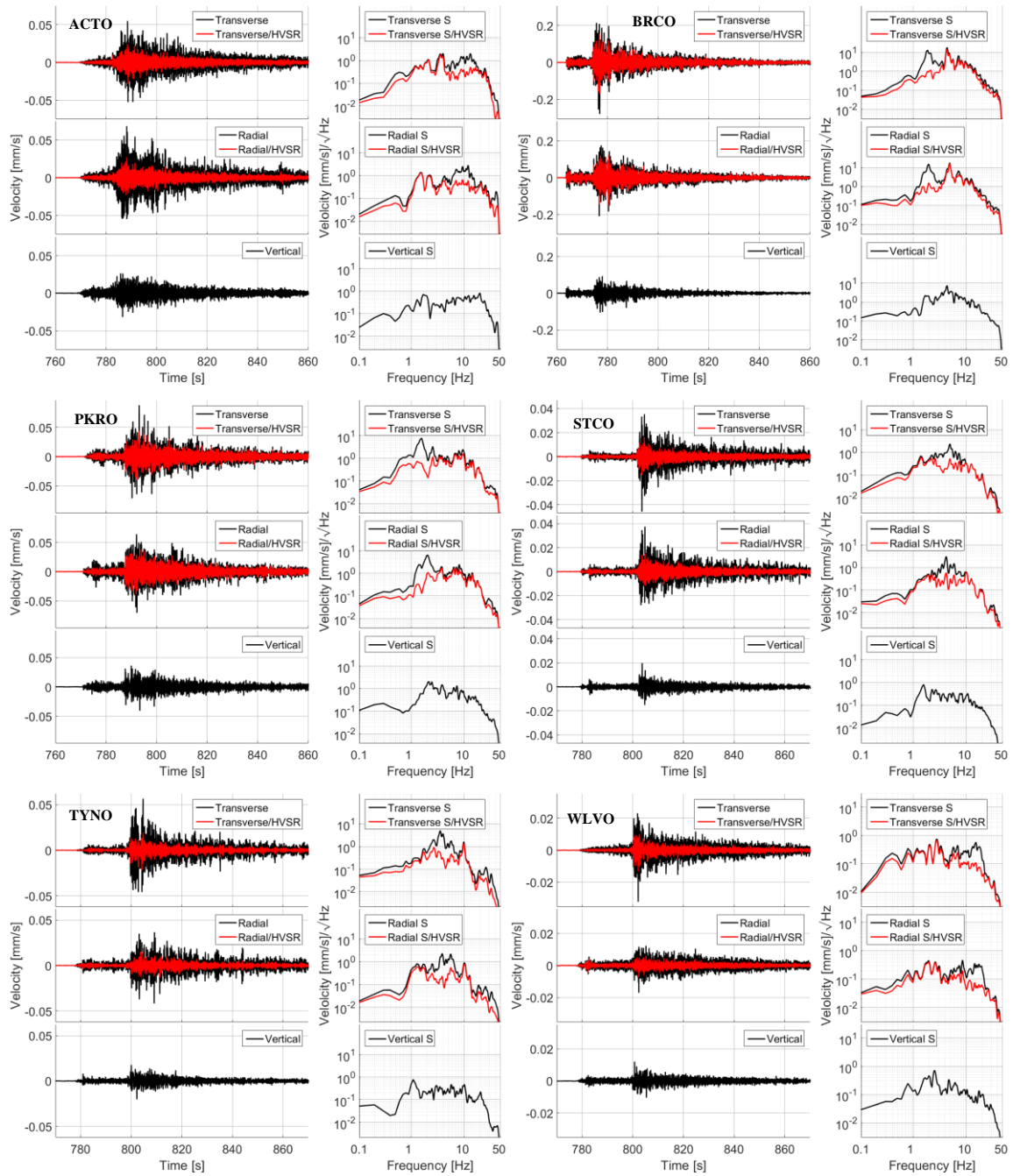
Figure 6.9: Earthquake records and S-wave velocity spectra of all 6 stations for the 2005/10/20 4.3 mN event (#2)
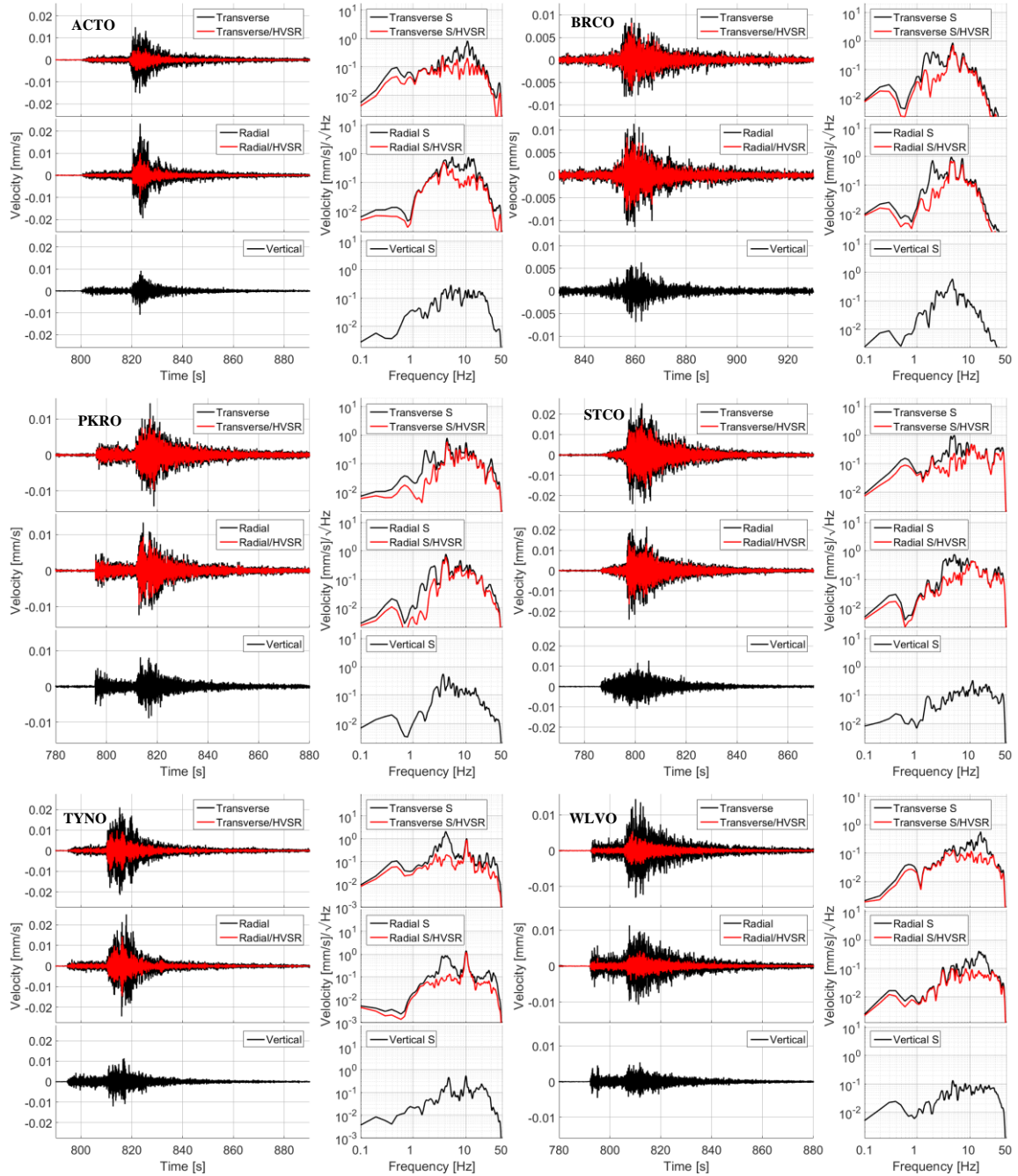
Figure 6.10: Earthquake records and S-wave velocity spectra of all 6 stations for the 2009/06/05 3.4 mN event (#3)

175
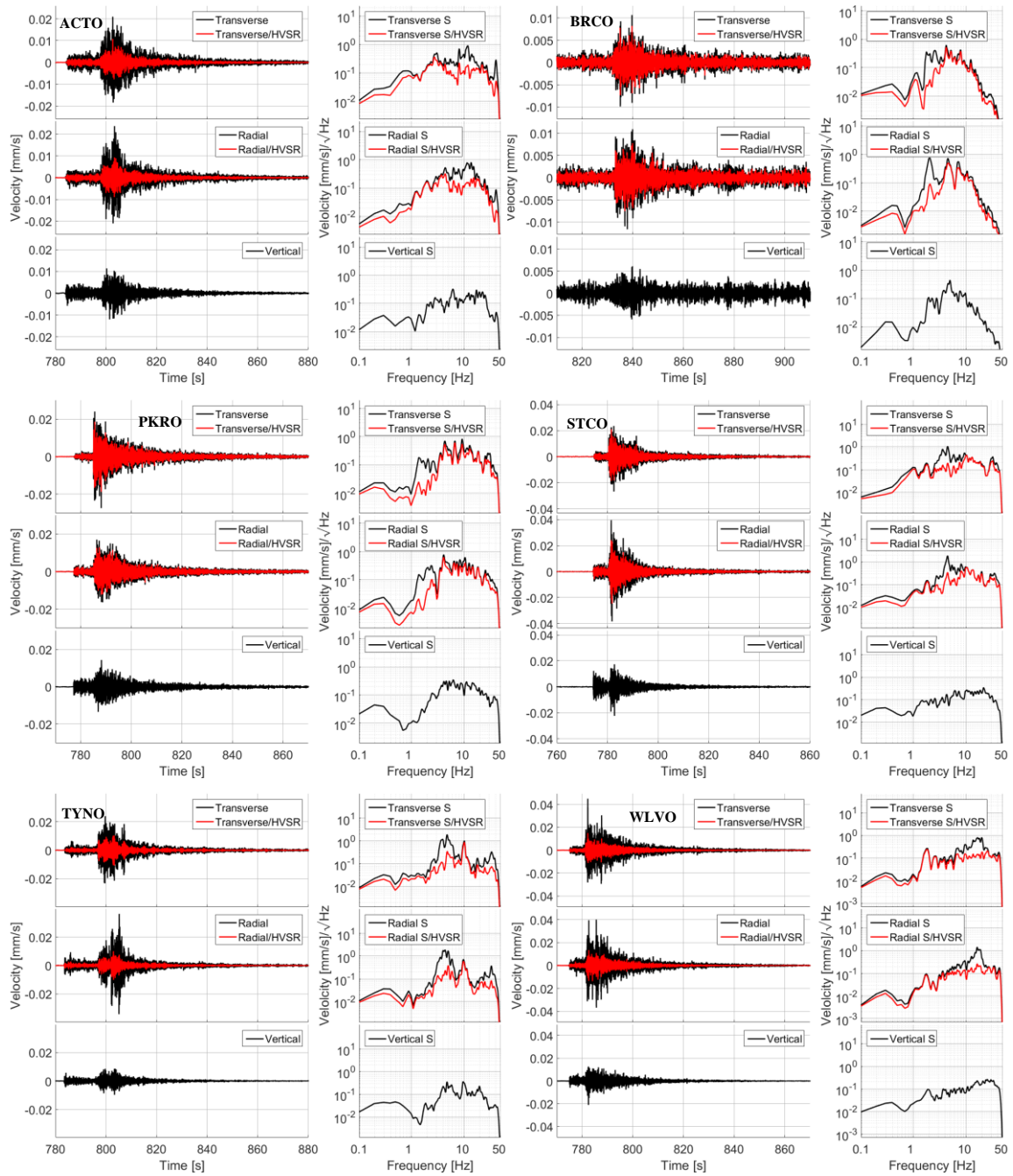
Figure 6.11: Earthquake records and S-wave velocity spectra of all 6 stations for the 2017/07/11 3.3 m$_N$ event (#4)

6.5 Conclusion

As the HVSR method has been gaining popularity in several applications, a proper consideration of the data processing required to generate a viable HVSR curve is important. The present paper describes the developed approach to approximate the HVSR curve from field data, including both microtremors and strong motion. The aim was to evaluate the feasibility of the parametrized HVSR model and to demonstrate some potential use cases. Practical considerations regarding the smoothing of the pre-HVSR spectra were presented, and the effect of different smoothing functions was demonstrated. It was concluded that pre-HVSR spectra need to be smoothed using constant slope (Q) symmetric functions with enough width to maintain peak differentiability but to remove spurious noise from the spectrum. Averaging of the spectra before calculation of HVSR and presenting the HVSR curve in logarithmic frequency/linear H/V ratio scales results in a smoother spectrum and eliminates the unstable peaks in high-frequency range, which are not used in the design practice or geological interpretation. To this end, the proposed BPF function is used instead of the commonly used KO function, in order to avoid artifacts introduced by the KO side-lobes. The HVSR represented as a sum of BPFs facilitates simulating the curve in an analytical form that can have increasing degrees of accuracy, depending on how many of the BPFs are chosen to describe it. This procedure was implemented as a MATLAB GUI, available on GitHub (Mihaylov, 2019b)

The design and application of a procedure for automatic HVSR parametrization using a parallel set of BPFs is demonstrated on data from the Southern Ontario Seismic Network (SOSN/Polaris). For the strong ground motion events and stations listed in Table 6.2 it is found that there is good agreement between the microtremor HVSR and the strong motion HVSR. This match is better for determination of the center frequencies of the dominant peaks in the spectra; however, the HVSR underestimates the amplitudes. The results agree with previous studies of the same SOSN stations. The model HVSR was used to remove the site response from the S-wave spectra for four medium size earthquakes in Southern Ontario (Table 6.1). For this purpose, the rotated (from NS-EW to Transverse and Radial components) horizontal non-smoothed spectra of each component are divided by the

modelled response. The spectra of the horizontal components show very good similarity to the spectra of the vertical component.

The visual comparison of the corrected and non-corrected spectra of the horizontal components show some shift of the corner frequency in the spectra towards the lower frequency for the stations with dominant frequency in the HVSR above 10 Hz (ACTO and WLVO). In some cases, there is a shift in the corner frequency towards the higher frequency.

The parametrization of the HVSR as BFSs can be used for study of the temporal variations at different noise conditions (e.g. night, day, different wind speed etc.). This will allow quantitative estimation of the variations in terms of dominant frequencies and corresponding amplitudes.

The proposed modeling tool may be applied to estimate the influence of the site response on earthquake waveforms and spectra. Estimation of the expected Brune source model, especially the corner frequency, for each site can be performed after removing the site response influences on the earthquake spectra using the proposed model. Changes in the corner frequency could significantly alter the expected source parameters. Based on Equation (6.3), a change in the corner frequency of the assumed Brune spectra will lead to a change in both the stress drop and the rupture radius of the seismic source. Further development of the methodology for correction of the earthquake spectra for local site conditions can be obtained by averaging the HVSR models for different noise conditions. Potentially, using the noise recorded just before the event to obtain the HVSR model could be more adequate as it better represents the conditions at the time of the event.

The HVSR model proposed here can be used to evaluate the effect of the site specifics on the potential ground motion from future earthquakes. This can be done by amplifying the amplitude spectra of the expected ground motion with the model HVSR and performing the inverse FFT to obtain the modified waveforms with the site effect. The phase spectra remain the same and it does not need to be modified. The result will be a better representation of the expected ground motion than the estimated single response parameter (e.g. PGV) in the GMPE (e.g. Equation 6.1) based on the V_{S30}, as a sole site parameter.

The full HVSR curve modelled as BPFs can be used instead of only the main peak and its approximation as SDOF oscillator (as by (McGuire, 1977; McGuire et al., 2002)). In this way more resonant frequencies will be considered which potentially can coincide with some of the resonant frequencies of the designed structure at the site.

It is necessary to note that the used approximation of HVSR as a sum of BPFs is not related to any physical characteristics of the soil strata. This representation aims to describe as best as possible the HVSR curve only. At the interpretation stage of analysis, the sum of the BPFs should be considered as a whole.

Chapter 7. Summary and conclusions

This thesis investigated some problems related to the collection and processing of field data for site response investigations. The three main issues related to site investigations that were identified and investigated in order:

- Usability and applicability of standard geophysical equipment and data acquisition systems to the tasks and challenges of site investigations.
- Data processing techniques for geophysical data analysis, as well as the effects of sloping topography, bedrock inclination and amplitude of motion on the results.
- Application of results obtained using geophysical methods to improve site assessment understanding and seismic hazard analysis

The first part of this thesis was focused on the development of an innovative data acquisition system and sensors that are easy to use in a wide range of field applications. This involved the prototyping of a DAQ system paired with sensors suitable for industrial, structural as well as geophysical applications. The applicability of the developed system in difficult site conditions was evaluated. Software and hardware solutions were proposed to solve the problem of limited frequency response of geophone elements.

The second part of this thesis involved conducting field studies with MASW and HVSR techniques to evaluate the influence of challenging site conditions such as sloping surface topography, complicated soil stratigraphy and inclined bedrock boundaries on the results of the applied methods. The results were compared to theoretical and numerical models for the evaluation of site amplification in such conditions.

In the third part of the thesis, an analytical model was developed to allow for the removal of site-effects from strong motion records. To better utilize the results of HVSR investigations a method for HVSR curve parameterization is proposed. Currently only the dominant frequency of the HVSR curve is utilized in further analysis, however the parametrized curve provides analytical expression that includes more information about the site amplification factor.

7.1 Future work

To build on the work done about the parameterization of empirical HVSR curves, the use of the model development methodology will be applied to data from seismic networks where data from coincident measurements on both the surface and in borehole is available. Such data can be obtained from Japan Meteorological Agency (JMA) for several sites in Japan.

Additionally, the application of the modelling technique should be utilized in complex surface and bedrock topographies by evaluating the changes to the model parameters over different features. Such studies will require large scale HVSR investigation to establish both a site for the reference HVSR model, and sufficient number of topographical features where the model can be applied and adjusted to correspond to the empirical field data. The differences between model parameters can then be used to give a better evaluation of the changes that the HVSR site specific curve will experience as a function of topography. Features where this approach is expected to yield information, additional to the site specific HVSR, include inclined bedrock boundaries and sloped surface topography.

Extend the work done in section 3.5.2 by completing the full three component sensor. The current prototype is based on one vertical geophone element, where the complete sensor requires an additional two horizontal components. Additionally, the temperature compensation approach used in the prototype needs to be tested in a suitable temperature-controlled environment.

All the improvements and modification that the DYNAMate vibrational data acquisition system has undergone as part of this thesis need to be combined into a finalized version of the design. This final version then needs to be prepared for out-of-house production by a third party so manufacture and distribution of the system can be enabled. This preparation will include detailed technical drawings and documentation required for the manufacture and assembly of system's integral components.

Bibliography

Acerra, C., Aguacil, G., Anastasiadis, A., Atakan, K., Azzara, R., Bard, P.-Y., Basili, R., Bertrand, E., Bettig, B., Blarel, F., others, 2004. Guidelines for the implementation of the H/V spectral ratio technique on ambient vibrations measurements, processing and interpretation. European Commission–EVG1-CT-2000-00026 SESAME.

Aki, K., 1972. Scaling Law of Earthquake Source Time-Function. Geophysical Journal International 31, 3–25. https://doi.org/10.1111/j.1365-246X.1972.tb02356.x

Al-Hunaidi, M., 1993. Insights on the SASW nondestructive testing method. Canadian Journal of Civil Engineering 20, 940–950.

Al-Husseini, M.I., Glover, J.B., Barley, B.J., 1981. Dispersion patterns of the ground roll in eastern Saudi Arabia. GEOPHYSICS 46, 121–137. https://doi.org/10.1190/1.1441183

Analog Devices, 2019a. ADG1421 Datasheet and Product Info | Analog Devices [WWW Document]. URL https://www.analog.com/en/products/adg1421.html (accessed 12.18.19).

Analog Devices, 2019b. AD8226 datasheet [WWW Document]. URL https://www.analog.com/media/en/technical-documentation/data-sheets/AD8226.pdf (accessed 12.18.19).

Analog Devices, 2019c. ADA4077-2 Datasheet and Product Info | Analog Devices [WWW Document]. URL https://www.analog.com/en/products/ada4077-2.html (accessed 12.18.19).

Analog Devices, 2019d. AD8253 Datasheet and Product Info | Analog Devices [WWW Document]. URL https://www.analog.com/en/products/ad8253.html#product-overview (accessed 12.18.19).

Angel, Y., Achenbach, J.D., 1984. Reflection and transmission of obliquely incident Rayleigh waves by a surface-breaking crack. The Journal of the Acoustical Society of America 75, 313–319.

Arai, H., Tokimatsu, K., 2004. S-wave velocity profiling by inversion of microtremor H/V spectrum. Bulletin of the Seismological Society of America 94, 53–63.

Arai, H., Tokimatsu, Kohji, 2005. S-Wave Velocity Profiling by Joint Inversion of Microtremor Dispersion Curve and Horizontal-to-Vertical (H/V) Spectrum. Bulletin of the Seismological Society of America 95, 1766–1778. https://doi.org/10.1785/0120040243

Arai, H., Tokimatsu, Kohji, 2000. Effects of Rayleigh and Love waves on microtremor H/V spectra, in: Proceedings of the 12th World Conference on Earthquake Engineering. Presented at the 12th world conference on earthquake engineering, pp. 1–8.

Atakan, K., Duval, A., Theodulidis, N., Guillier, B., Chatelain, J., Bard, P., 2004. SESAME-Team. 2004. The H/V spectral ratio technique: experimental

conditions, data processing and empirical reliability assessment, in: 13th World Conference in Earthquake Engineering, Vancouver, Paper.

Atkinson, G.M., 2008. Ground-Motion Prediction Equations for Eastern North America from a Referenced Empirical Approach: Implications for Epistemic Uncertainty. Bulletin of the Seismological Society of America 98, 1304–1318. https://doi.org/10.1785/0120070199

Atkinson, G.M., Adams, J., 2013. Ground motion prediction equations for application to the 2015 Canadian national seismic hazard maps. Canadian Journal of Civil Engineering 40, 988–998. https://doi.org/10.1139/cjce-2012-0544

Atkinson, G.M., Boore, D.M., 2006. Earthquake Ground-Motion Prediction Equations for Eastern North America. Bulletin of the Seismological Society of America 96, 2181–2205. https://doi.org/10.1785/0120050245

Atkinson, G.M., Boore, D.M., 1995. Ground-Motion Relations for Eastern North America. Bulletin of the Seismological Society of America 85, 17–30.

Bard, P., 2004. The SESAME project: an overview and main results, in: Proc. of 13th World Conf. on Earthquake Engineering, Vancouver, BC, Canada, August. pp. 1–6.

Bard, P., Riepl-Thomas, J., 2000. Wave propagation in complex geological structures and their effects on strong ground motion. Wave motion in earthquake engineering 37–95.

Bard, P.-Y., 1998. Microtremor measurements: a tool for site effect estimation, in: Proceeding of the Second International Symposium on the Effects of Surface Geology on Seismic Motion. Yokohama Japan, pp. 1251–1279.

Barzilai, A., VanZandt, T., Kenny, T., 1998. Improving the Performance of a Geophone Through Capacitive Position Sensing and Feedback. Presented at the merican Society of Mechanical Engineers International Congress, p. 8.

Beker, M.G., 2013. Low-frequency sensitivity of next generation gravitational wave detectors. s.n.], S.l.

Ben-Zion, Y., Sammis, C.G., 2003. Characterization of Fault Zones. Pure appl. geophys. 160, 39.

Bettig, B., Bard, P.Y., Scherbaum, F., Riepl, J., Cotton, F., Cornou, C., Hatzfeld, D., 2001. Analysis of dense array noise measurements using the modified spatial auto-correlation method (SPAC): application to the Grenoble area. Bollettino di Geofisica Teorica ed Applicata 42, 281–304.

Binder USA, 2019. Female panel mount connector, solder, 12 - 19 contacts, UL approval [WWW Document]. URL https://www.binder-usa.com/products/miniature-circular-connectors/m16-ip67/female-panel-mount-connector-solder-12-19-contacts-with-ul-approval-1.html (accessed 12.18.19).

Bonilla, L.F., 2002. Borehole Response Studies at the Garner Valley Downhole Array, Southern California. Bulletin of the Seismological Society of America 92, 3165–3179. https://doi.org/10.1785/0120010235

Bonnefoy-Claudet, S., Cornou, C., Bard, P.-Y., Cotton, F., Moczo, P., Kristek, J., Fäh, D., 2006a. H/V ratio: a tool for site effects evaluation. Results from 1-D noise simulations. Geophysical Journal International 167, 827–837. https://doi.org/10.1111/j.1365-246X.2006.03154.x

Bonnefoy-Claudet, S., Cotton, F., Bard, P.-Y., 2006b. The nature of noise wavefield and its applications for site effects studies. Earth-Science Reviews 79, 205–227. https://doi.org/10.1016/j.earscirev.2006.07.004

Boore, D.M., Atkinson, G.M., 2008. Ground-Motion Prediction Equations for the Average Horizontal Component of PGA, PGV, and 5%-Damped PSA at Spectral Periods between 0.01 s and 10.0 s. Earthquake Spectra 24, 99–138. https://doi.org/10.1193/1.2830434

Bora, S.S., Scherbaum, F., Kuehn, N., Stafford, P., Edwards, B., 2015. Development of a Response Spectral Ground-Motion Prediction Equation (GMPE) for Seismic-Hazard Analysis from Empirical Fourier Spectral and Duration Models. Bulletin of the Seismological Society of America 105, 2192–2218. https://doi.org/10.1785/0120140297

Borcherdt, R.D., 1970. Effects of local geology on ground motion near San Francisco Bay. Bulletin of the Seismological Society of America 60, 29–61.

Bowden, G., 2005. Calibration of Geophone Micro-seismic Sensors (No. SLAC-TN-05-023, 839683). https://doi.org/10.2172/839683

Bozorgnia, Y., Abrahamson, N.A., Atik, L.A., Ancheta, T.D., Atkinson, G.M., Baker, J.W., Baltay, A., Boore, D.M., Campbell, K.W., Chiou, B.S.-J., Darragh, R., Day, S., Donahue, J., Graves, R.W., Gregor, N., Hanks, T., Idriss, I.M., Kamai, R., Kishida, T., Kottke, A., Mahin, S.A., Rezaeian, S., Rowshandel, B., Seyhan, E., Shahi, S., Shantz, T., Silva, W., Spudich, P., Stewart, J.P., Watson-Lamprey, J., Wooddell, K., Youngs, R., 2014. NGA-West2 Research Project. Earthquake Spectra 30, 973–987. https://doi.org/10.1193/072113EQS209M

Brincker, R., Bolton, B., Brandt, A., 2011. Calibration and Processing of Geophone Signals for Structural Vibration Measurements, in: Proulx, T. (Ed.), Structural Dynamics, Volume 3. Springer New York, New York, NY, pp. 1375–1379. https://doi.org/10.1007/978-1-4419-9834-7_121

Brincker, R., Lagö, T.L., Andersen, P., Ventura, C., 2005. Improving the Classical Geophone Sensor Element by Digital Correction, in: Roceedings of IMAC-XXIII: A Conference & Exposition on Structural Dynamics. Presented at the IMAC-XXIII: A Conference & Exposition on Structural Dynamics, Orlando, FL, USA, p. 10.

Brown, L.T., 2002. Comparison of Shear-Wave Slowness Profiles at 10 Strong-Motion Sites from Noninvasive SASW Measurements and Measurements Made in Boreholes. Bulletin of the Seismological Society of America 92, 3116–3133. https://doi.org/10.1785/0120020030

Brune, J.N., 1970. Tectonic stress and the spectra of seismic shear waves from earthquakes. Journal of Geophysical Research 75, 4997–5009. https://doi.org/10.1029/JB075i026p04997

Capon, J., 1969. High-resolution frequency-wavenumber spectrum analysis. Proceedings of the IEEE 57, 1408–1418. https://doi.org/10.1109/PROC.1969.7278

cDAQ-9171 - National Instruments [WWW Document], n.d. URL https://www.ni.com/en-ca/support/model.cdaq-9171.html (accessed 12.19.19).

cDAQ-9191 - National Instruments [WWW Document], n.d. URL https://www.ni.com/en-ca/support/model.cdaq-9191.html (accessed 12.19.19).

Chatelain, J.-L., Guillier, B., Cara, F., Duval, A.-M., Atakan, K., Bard, P.-Y., The WP02 SESAME team, 2008. Evaluation of the influence of experimental conditions on H/V results from ambient noise recordings. Bull Earthquake Eng 6, 33–74. https://doi.org/10.1007/s10518-007-9040-7

Chávez-García, F.J., Raptakis, D., 2017. Local amplification and subsoil structure at a difficult site: Understanding site effects from different measurements. Soil Dynamics and Earthquake Engineering 92, 334–344. https://doi.org/10.1016/j.soildyn.2016.10.008

Chávez-García, F.J., Tejeda-Jácome, J., 2010. Site response in Tecoman, Colima, Mexico—I: Comparison of results from different instruments and analysis techniques. Soil Dynamics and Earthquake Engineering 30, 711–716.

Chen, L., Zhu, J., Yan, X., Song, C., 2004. On arrangement of source and receivers in SASW testing. Soil Dynamics and Earthquake Engineering 24, 389–396. https://doi.org/10.1016/j.soildyn.2003.12.004

Claprood, M., 2012. Spatially Averaged Coherency Spectrum (SPAC) Ambient Noise Array Method. Shear Wave Velocity Measurement Guidelines for Canadian Seismic Site Characterization in Soil and Rock 94.

Collette, C., Carmona-Fernandez, P., Janssens, S., Artoos, K., Guinchard, M., 2011. Review of sensors for low frequency seismic vibration measurement (No. ATS/Note/2011/001 (TECH)). CERN.

Cornou, C., Kristek, J., Ohrnberger, M., Giulio, G.D., 2004. Simulation of Seismic Ambient Vibrations - II H/V and Array Techniques for real sites 13.

Davis, P.M., Rubinstein, J.L., Liu, K.H., Gao, S.S., Knopoff, L., 2000. Northridge earthquake damage caused by geologic focusing of seismic waves. Science 289, 1746–1750.

Delta Electronics, 2019a. DH06S1212A Delta Electronics | Power Supplies - Board Mount | DigiKey [WWW Document]. URL https://www.digikey.com/product-detail/en/delta-electronics/DH06S1212A/941-1533-ND/3464818 (accessed 12.18.19).

Delta Electronics, 2019b. S24DE/S24SE Series - Delta Electronics - 26W to 30W | Online Catalog | DigiKey Electronics [WWW Document]. URL

https://www.digikey.com/catalog/en/partgroup/s24de-s24se-series/28169 (accessed 12.18.19).

Dergach, P.A., Tubanov, Ts.A., Yushin, V.I., Duchkov, A.A., 2019. Features of Software Implementation of Low-Frequency Deconvolution Algorithms. Seism. Instr. 55, 345–352. https://doi.org/10.3103/S0747923919030046

Drouet, S., Triantafyllidis, P., Savvaidis, A., Theodulidis, N., 2008. Comparison of Site-Effects Estimation Methods Using the Lefkas, Greece, 2003 Earthquake Aftershocks. Bulletin of the Seismological Society of America 98, 2349–2363. https://doi.org/10.1785/0120080004

Duda, J., Sarkar, D, 1985. Spectral P-wave Magnitudes, Aki's w-squared Model and Source Parameters of Earthquakes. Tecronophysics 175–193.

Earthquakes Canada, GSC, 2019. Continuous Waveform Archive [WWW Document]. Nat. Res. Can. URL http://earthquakescanada.nrcan.gc.ca/stndon/AutoDRM/index-eng.php (accessed 1.12.19).

Easton, R., Carter, T., 1995. Geology of the Precambrian basement beneath the Paleozoic of southwestern Ontario, in: Basement Tectonics 10. Springer, pp. 221–264.

Evangelista, L., Santucci de Magistris, F., 2015. Some Limits in the Use of the MASW Technique in Soils with Inclined Layers. Geotechnical and Geological Engineering 33, 701–711. https://doi.org/10.1007/s10706-015-9852-1

Eyles, N., Arnaud, E., Scheidegger, A.E., Eyles, C.H., 1997. Bedrock jointing and geomorphology in southwestern Ontario, Canada: an example of tectonic predesign. Geomorphology 19, 17–34. https://doi.org/10.1016/S0169-555X(96)00050-5

Fäh, D., Kind, F., Giardini, D., 2003. Inversion of local S-wave velocity structures from average H/V ratios, and their use for the estimation of site-effects. Journal of Seismology 7, 449–467. https://doi.org/10.1023/B:JOSE.0000005712.86058.42

Fäh, D., Kind, F., Giardini, D., 2001. A theoretical investigation of average H/V ratios. Geophysical Journal International 145, 535–549.

Fenton, C.H., Adams, J., Halchuk, S., 2006. Seismic Hazards Assessment for Radioactive Waste Disposal Sites in Regions of Low Seismic Activity. Geotech Geol Eng 24, 579–592. https://doi.org/10.1007/s10706-005-1148-4

Field, E.H., Jacob, K.H., 1995. A Comparison and Test of Various Site-Response Estimation Techniques, Including Three That Are Not Reference-Site Dependent. Bulletin of the Seismological Society of America 85, 17.

Flores, H., Malischewsky, P., Jentzsch, G., 2013. H/V spectral ratio analysis and Rayleigh modelization in Eastern Thuringia, Germany. Geofísica Internacional 52, 355–364. https://doi.org/10.1016/S0016-7169(13)71482-X

Foti, S., 2000. Multistation Methods for Geotechnical Characterization using Surface Waves. Politecnico di Torino.

Frankel, A.D., Carver, D.L., Williams, R.A., 2002. Nonlinear and linear site response and basin effects in Seattle for the M 6.8 Nisqually, Washington, earthquake. Bulletin of the Seismological Society of America 92, 2090–2109.

Franklin, G.F., Powell, J.D., Workman, M.L., 1990. Digital control of dynamic systems, 2nd ed. ed. Addison-Wesley, Reading, Mass.

Gail M Atkinson, 1993. EARTHQUAKE SOURCE SPECTRA IN EASTERN NORTH AMERICA. Bulletin of the Seismological Society of America 83, 1778–1798.

Gal, M., Reading, A.M., Ellingsen, S.P., Koper, K.D., Gibbons, S.J., Näsholm, S.P., 2014. Improved implementation of the fk and Capon methods for array analysis of seismic noise. Geophysical Journal International 198, 1045–1054. https://doi.org/10.1093/gji/ggu183

Gao, S., Liu, H., Davis, P.M., Knopoff, L., 1996. Localized amplification of seismic waves and correlation with damage due to the Northridge earthquake: evidence for focusing in Santa Monica. Bulletin of the Seismological Society of America 86, S209–S230.

Ghofrani, H., Atkinson, G.M., 2014. Site condition evaluation using horizontal-to-vertical response spectral ratios of earthquakes in the NGA-West 2 and Japanese databases. Soil Dynamics and Earthquake Engineering 67, 30–43. https://doi.org/10.1016/j.soildyn.2014.08.015

Gribler, G., Liberty, L.M., Mikesell, T.D., Michaels, P., 2016. Isolating retrograde and prograde Rayleigh-wave modes using a polarity mute. GEOPHYSICS 81, V379–V385. https://doi.org/10.1190/geo2015-0683.1

Gucunski, N., 1992. Numerical simulation of the SASW test. Soil Dynamics and Earthquake Engineering 11, 213–217.

Gucunski, N., Woods, R.D., 1992. Numerical simulation of the SASW test. Soil Dynamics and Earthquake Engineering 11, 213–227.

Guéguen, P., Cornou, C., Garambois, S., Banton, J., 2007. On the Limitation of the H/V Spectral Ratio Using Seismic Noise as an Exploration Tool: Application to the Grenoble Valley (France), a Small Apex Ratio Basin. Pure appl. geophys. 164, 115–134. https://doi.org/10.1007/s00024-006-0151-x

Haghshenas, E., Bard, P.-Y., Theodulidis, N., SESAME WP04 Team, 2008. Empirical evaluation of microtremor H/V spectral ratio. Bulletin of Earthquake Engineering 6, 75–108. https://doi.org/10.1007/s10518-007-9058-x

Harkrider, D.G., 1970. Surface waves in multilayered elastic media. Part II. Higher mode spectra and spectral ratios from point sources in plane layered earth models. Bulletin of the Seismological Society of America 60, 1937–1987.

Harkrider, D.G., 1964. Surface waves in multilayered elastic media I. Rayleigh and Love waves from buried sources in a multilayered elastic half-space. Bulletin of the Seismological Society of America 54, 627–679.

Hartzell, S., Ramirez-Guzman, L., Carver, D., Liu, P., 2010. Short Baseline Variations in Site Response and Wave-Propagation Effects and Their Structural Causes: Four

Examples in and around the Santa Clara Valley, California. Bulletin of the Seismological Society of America 100, 2264–2286. https://doi.org/10.1785/0120090278

Havskov, J., Alguacil, G., 2004. Instrumentation in earthquake seismology. Springer.

Havskov, J., Ottemoller, L., 2010. Routine Data Processing in Earthquake Seismology. Springer Netherlands, Dordrecht. https://doi.org/10.1007/978-90-481-8697-6

Heisey, J.S., Ii, K.H.S., Meyer, A.H., 1982. Moduli of Pavement Systems from Spectral Analysis of Surface Waves. Transportation Research Record 852, 22–31.

Hiltunen, D.R., Woods, R.D., 1990. Variables Affecting the Testing of Pavements by the Surface Waves Method. TRANSPORTATION RESEARCH RECORD 1260, 42–52.

Horike, M., 2001. Comparison of Site Response Characteristics Inferred from Microtremors and Earthquake Shear Waves. Bulletin of the Seismological Society of America 91, 1526–1536. https://doi.org/10.1785/0120000065

Huang, N.E., Wu, Z., 2008. A review on Hilbert-Huang transform: Method and its applications to geophysical studies. Reviews of Geophysics 46. https://doi.org/10.1029/2007RG000228

Hunt, R.E., 2005. Geotechnical engineering investigation handbook. Crc Press.

Iwasaki, T., Tatsuoka, F., 1977. Effects of grain size and grading on dynamic shear moduli of sands. Soils and foundations 17, 19–35.

Jafari, M.K., Shafiee, A., Razmkhah, A., 2002. Dynamic properties of fine grained soils in south of Tehran. Journal of Seismology and Earthquake Engineering 4, 25.

Jafarzadeh, F., Sadeghi, H., 2012. Experimental study on dynamic properties of sand with emphasis on the degree of saturation. Soil Dynamics and Earthquake Engineering 32, 26–41. https://doi.org/10.1016/j.soildyn.2011.08.003

Jamroni, R., Imran, A.M., Azikin, B., 2017. Analysis of Microtremor Data Using Horizontal to Vertical Spectral Ratio (HVSR) Method of Makassar, South Sulawesi. International Journal of Engineering and Science Applications 4, 63–68.

Kawase, H., Mori, Y., Nagashima, F., 2018. Difference of horizontal-to-vertical spectral ratios of observed earthquakes and microtremors and its application to S-wave velocity inversion based on the diffuse field concept. Earth, Planets and Space 70. https://doi.org/10.1186/s40623-017-0766-4

Kawase, H., Sanchez-Sesma, F.J., Matsushima, S., 2011. The Optimal Use of Horizontal-to-Vertical Spectral Ratios of Earthquake Motions for Velocity Inversions Based on Diffuse-Field Theory for Plane Waves. Bulletin of the Seismological Society of America 101, 2001–2014. https://doi.org/10.1785/0120100263

Kester, W., 2004. Analog-digital conversion. Analog Devices, Analog Devices.

KGS, 2019. KGS--SurfSeis MASW Software [WWW Document]. URL http://www.kgs.ku.edu/software/surfseis/index.html (accessed 11.28.19).

Khaheshi Banab, K., Motazedian, D., 2010. On the Efficiency of the Multi-Channel Analysis of Surface Wave Method for Shallow and Semi-Deep Loose Soil Layers. International Journal of Geophysics 2010, 1–13. https://doi.org/10.1155/2010/403016

Kim, D.-S., Lee, J.-S., 2000. Propagation and attenuation characteristics of various ground vibrations. Soil Dynamics and Earthquake Engineering 19, 115–126. https://doi.org/10.1016/S0267-7261(00)00002-6

Kinemetrics, 2019. SS-1 Ranger Seismometer from Kinemetrics Inc. : Quote, RFQ, Price and Buy [WWW Document]. AZoSensors.com. URL https://www.azosensors.com/equipment-details.aspx?EquipID=17 (accessed 10.28.19).

Kishida, T., 2017. Comparison and Correction of Modulus Reduction Models for Clays and Silts. J. Geotech. Geoenviron. Eng. 143, 04016110. https://doi.org/10.1061/(ASCE)GT.1943-5606.0001627

Köhler, A., Ohrnberger, M., Scherbaum, F., Wathelet, M., Cornou, C., 2007. Assessing the reliability of the modified three-component spatial autocorrelation technique. Geophysical Journal International 168, 779–796. https://doi.org/10.1111/j.1365-246X.2006.03253.x

Koller, M.G., Chatelein, J.-L., Guillier, B., Duval, A.-M., Atakan, K., Lacave, C., Bard, P.-Y., 2004. Practical User Guidelines and Software for the Implementation of the H/V Ratio Technique : Measuring Conditions, Processing Method and Results Interpretation 10.

Konno, K., Ohmachi, T., 1998. Ground-motion characteristics estimated from spectral ratio between horizontal and vertical components of microtremor. Bulletin of the Seismological Society of America 88, 228–241.

Kramer, S.L., 1996. Geotechnical earthquake engineering. In prentice–Hall international series in civil engineering and engineering mechanics. Prentice-Hall, New Jersey.

Lachetl, C., Bard, P.-Y., 1994. Numerical and theoretical investigations on the possibilities and limitations of Nakamura's technique. Journal of Physics of the Earth 42, 377–397.

Lacoss, R.T., Kelly, E.J., Toksöz, M.N., 1969. Estimation of Seismic Noise Structure Using Arrays. GEOPHYSICS 34, 21–38. https://doi.org/10.1190/1.1439995

Lermo, J., Chávez-García, F.J., 1994. Are microtremors useful in site response evaluation? Bulletin of the seismological society of America 84, 1350–1364.

Lermo, J., Chávez-García, F.J., 1993. Site effect evaluation using spectral ratios with only one station. Bulletin of the seismological society of America 83, 1574–1594.

Lontsi, A.M., Sánchez-Sesma, F.J., Molina-Villegas, J.C., Ohrnberger, M., Krüger, F., 2015. Full microtremor H/V(z, f) inversion for shallow subsurface characterization. Geophysical Journal International 202, 298–312. https://doi.org/10.1093/gji/ggv132

López Casado, C., Garrido, J., Delgado, J., Peláez, J.A., Henares, J., 2017. HVSR estimation of site effects in Melilla (Spain) and the damage pattern from the 01/25/2016 Mw 6.3 Alborán Sea earthquake. Natural Hazards. https://doi.org/10.1007/s11069-017-3132-8

Malischewsky, P.G., Scherbaum, F., 2004. Love's formula and H/V-ratio (ellipticity) of Rayleigh waves. Wave Motion 40, 57–67. https://doi.org/10.1016/j.wavemoti.2003.12.015

Mancuso, C., Vassallo, R., 2002. Small strain behavior of a silty sand in controlled-suction resonant column – torsional shear tests 11.

Maranò, S., Reller, C., Loeliger, H.-A., Fäh, D., 2012. Seismic waves estimation and wavefield decomposition: application to ambient vibrations: Seismic waves estimation. Geophysical Journal International 191, 175–188. https://doi.org/10.1111/j.1365-246X.2012.05593.x

Marquardt, D.W., 1963. An algorithm for least-squares estimation of nonlinear parameters. Journal of the society for Industrial and Applied Mathematics 11, 431–441.

Martin, A., Yong, A., Stephenson, W., Boatwright, J., Diehl, J., 2017. Geophysical Characterization of Seismic Station Sites in the United States–the Importance of a Flexible, Multi-Method approach.

MATLAB Runtime - MATLAB Compiler [WWW Document], n.d. URL https://www.mathworks.com/products/compiler/matlab-runtime.html (accessed 12.19.19).

McGuire, R.K., 1977. Seismic design spectra and mapping procedures using hazard analysis based directly on oscillator response. Earthquake Engineering & Structural Dynamics 5, 211–234.

McGuire, R.K., Silva, W.J., Costantino, C.J., 2002. Technical basis for revision of regulatory guidance on design ground motions: development of hazard-and risk-consistent seismic spectra for two sites (Technical Report No. NUREG/CR-6769). Division of Engineering Technology, Office of Nuclear Regulatory Research ….

Mereu, R.F., Asmis, H.W., Dunn, B., Brunet, J., Eaton, D., Dineva, S., Yapp, A., 2002. The Seismicity of the Western Lake Ontario Area: Results from the Southern Ontario Seismic Network (SOSN), 1992-2001. Seismological Research Letters 73, 534–551. https://doi.org/10.1785/gssrl.73.4.534

Mereu, R.F., Dineva, S., Atkinson, G.M., 2013. The Application of Velocity Spectral Stacking to Extract Information on Source and Path Effects for Small-to-Moderate Earthquakes in Southern Ontario with Evidence for Constant-Width faulting. Seismological Research Letters 84, 899–916. https://doi.org/10.1785/0220130009

Meroi, E.A., Schrefler, B.A., Zienkiewicz, O.C., 1995. Large strain static and dynamic semisaturated soil behaviour. International Journal for Numerical and Analytical Methods in Geomechanics 19, 81–106.

Messaoudi, A., Laouami, N., Mezouer, N., 2012. Topographic effects on the seismic responses of slopes. Presented at the 15th World Conference on Earthquake Engineering, p. 8.

Mihaylov, A., 2019a. sashkosnail/SensorCalibrate.

Mihaylov, A., 2019b. sashkosnail/HVSR_code.

Mihaylov, A., 2019c. sashkosnail/DynaMATE.

Mihaylov, A., 2019d. sashkosnail/MatlabScripts.

Mihaylov, D., El Naggar, M.H., Dineva, S., 2016. Separation of High- and Low-Level Ambient Noise for HVSR: Application in City Conditions for Greater Toronto Area. Bulletin of the Seismological Society of America 106, 2177–2184. https://doi.org/10.1785/0120150389

Mihaylov, D.G., 2011. Seismic microzonation of Great Toronto Area and influence of building resonances on measured soil responses (Thesis submitted as part of the requirements for PhD degree in Civil Engineering,). The University of Western Ontario, Canada.

Miller, G.F., Pursey, H., 1955. On the Partition of Energy between Elastic Waves in a Semi-Infinite Solid. Proceedings of the Royal Society A: Mathematical, Physical and Engineering Sciences 233, 55–69. https://doi.org/10.1098/rspa.1955.0245

Miller, R.D., Xia, J., Park, C.B., Ivanov, J.M., 1999. Multichannel analysis of surface waves to map bedrock. The Leading Edge 18, 1392–1396. https://doi.org/10.1190/1.1438226

Molnar, S., Cassidy, J.F., Olsen, K.B., Dosso, S.E., He, J., 2014. Earthquake Ground Motion and 3D Georgia Basin Amplification in Southwest British Columbia: Deep Juan de Fuca Plate Scenario Earthquakes. Bulletin of the Seismological Society of America 104, 301–320. https://doi.org/10.1785/0120110277

Motazedian, D., Khaheshi Banab, K., Hunter, J.A., Sivathayalan, S., Crow, H., Brooks, G., 2011. Comparison of Site Periods Derived from Different Evaluation Methods. Bulletin of the Seismological Society of America 101, 2942–2954. https://doi.org/10.1785/0120100344

Mucciarelli, M., Gallipoli, M.R., 2001. A critical review of 10 years of microtremor HVSR technique. Boll Geof Teor Appl 42, 255–266.

Mucciarelli, M., Gallipoli, M.R., Arcieri, M., 2003. The stability of the horizontal-to-vertical spectral ratio of triggered noise and earthquake recordings. Bulletin of the Seismological Society of America 93, 1407–1412.

Murphy, C., Eaton, D., 2005. Empirical site response for POLARIS stations in southern Ontario, Canada. Seismological Research Letters 76, 99–109.

Nakamura, Y., 2009. Basic Structure of QTS (HVSR) and Examples of Applications, in: Mucciarelli, M., Herak, M., Cassidy, J. (Eds.), Increasing Seismic Safety by Combining Engineering Technologies and Seismological Data. Springer Netherlands, Dordrecht, pp. 33–51. https://doi.org/10.1007/978-1-4020-9196-4_4

Nakamura, Y., 2000. Clear identification of fundamental idea of Nakamura's technique and its applications, in: Proceedings of the 12th World Conference on Earthquake Engineering. Auckland New Zealand.

Nakamura, Y., 1989. A method for dynamic characteristics estimation of subsurface using microtremor on the ground surface. QR Railway Tech. Res. Inst. 30, 25–33.

Nakamura, Y., Samizo, M., 1989. Site effect evaluation of surface ground using strong motion records, in: Proc. 20th JSCE Earthquake Eng. Symposium. pp. 133–136.

National Instruments, 2019. NI-9205 [WWW Document]. URL https://www.ni.com/en-ca/support/model.ni-9205.html (accessed 12.18.19).

National Instruments, n.d. LabVIEW Runtime Download - National Instruments [WWW Document]. URL https://www.ni.com/en-ca/support/downloads/software-products/download.labview-runtime.html#329458 (accessed 12.19.19a).

National Instruments, n.d. NI-DAQmx Download - National Instruments [WWW Document]. URL https://www.ni.com/en-ca/support/downloads/drivers/download.ni-daqmx.html#333268 (accessed 12.19.19b).

National Instruments, n.d. TDM Excel Add-In for Microsoft Excel Download - National Instruments [WWW Document]. URL http://www.ni.com/example/27944/en/ (accessed 12.19.19c).

National Research Council of Canada. Canadian Commission on Building and Fire Codes, 2015. National Building Code of Canada 2015, National Building Code of Canada; no. 14th edition. National Research Council of Canada. https://doi.org/10.4224/40001268

Nazarian, S., Ii, K.H.S., Hudson, W.R., 1983. Use of Spectral Analysis of Surface Waves Method for Determination of Moduli and Thicknesses of Pavement Systems. Transportation Research Record 930, 38–45.

Nazarian, S., Stokoe, K.H., 1983. Evaluation of moduli and thicknesses of pavement systems by spectral-analysis-of-surface-waves method. The Center.

Nazri, F.M., Tan, C.G., Ramli, M.Z., 2016. Investigation of Site-Specific Shear Wave Velocity for Geotechnical Engineering Applications Using Microtremor Array Measurement. Soil Mechanics and Foundation Engineering 53, 332–335. https://doi.org/10.1007/s11204-016-9407-3

Nocedal, J., Wright, S.J., 2006. Numerical optimization 2nd. Springer.

Ohori, M., 2002. A Comparison of ESAC and FK Methods of Estimating Phase Velocity Using Arbitrarily Shaped Microtremor Arrays. Bulletin of the Seismological Society of America 92, 2323–2332. https://doi.org/10.1785/0119980109

Ohtsuki, A., Harumi, K., 1983. Effect of topography and subsurface inhomogeneities on seismic SV waves. Earthquake Engineering & Structural Dynamics 11, 441–462.

Ontario Geological Survey, 2010. Surficial geology of southern Ontario. Ontario Geological Survey, Toronto.

Ontario Geological Survey, 2006. Bedrock topography and overburden thickness mapping, southern Ontario. Ontario Geological Survey, Sudbury, Ont.

Park, C., Miller, R.D., Xia, J., 1997. Multi-channel analysis of surface waves (MASW)—a summary report of technical aspects, experimental results, and perspective. Kansas Geological Survey 97–10.

Park, C.B., Miller, R.D., Xia, J., 1999. Multichannel analysis of surface waves. Geophysics 64, 800–808.

Park, C.B., Miller, R.D., Xia, J., Ivanov, J., 2007. Multichannel analysis of surface waves (MASW)—active and passive methods. The Leading Edge 26, 60–64.

Peng, Z., Ben-Zion, Y., 2006. Temporal Changes of Shallow Seismic Velocity Around the Karadere-Düzce Branch of the North Anatolian Fault and Strong Ground Motion. Pure appl. geophys. 163, 567–600. https://doi.org/10.1007/s00024-005-0034-6

Picozzi, M., 2005. Statistical Analysis of Noise Horizontal-to-Vertical Spectral Ratios (HVSR). Bulletin of the Seismological Society of America 95, 1779–1786. https://doi.org/10.1785/0120040152

Pilz, M., Parolai, S., Leyton, F., Campos, J., Zschau, J., 2009. A comparison of site response techniques using earthquake data and ambient seismic noise analysis in the large urban areas of Santiago de Chile. Geophysical Journal International 178, 713–728. https://doi.org/10.1111/j.1365-246X.2009.04195.x

Pitilakis, K., Riga, E., Anastasiadis, A., 2013. New code site classification, amplification factors and normalized response spectra based on a worldwide ground-motion database. Bulletin of Earthquake Engineering 11, 925–966. https://doi.org/10.1007/s10518-013-9429-4

Proakis, J.G., 2001. Digital signal processing: principles algorithms and applications. Pearson Education India.

Rayleigh, Lord, 1885. On Waves Propagated along the Plane Surface of an Elastic Solid. Proceedings of the London Mathematical Society s1-17, 4–11. https://doi.org/10.1112/plms/s1-17.1.4

Rix, G., Leipski, E., 1991. Accuracy and resolution of surface wave inversion: in Blaney, GW and Bhatia, SK (eds.), Recent advances in instrumentation, data acquisition and testing in soil dynamics: American Society of Civil Engineers. Geotechnical Special Publication 17–32.

Roesset, J., Chang, D., Stokoe, K.H., 1991. Comparison of 2-D and 3-D models for analysis of surface wave tests. Unknown Journal 111–126.

Rong, M., Li, H., Yu, Y., 2019. The difference between horizontal-to-vertical spectra ratio and empirical transfer function as revealed by vertical arrays. PLoS One 14. https://doi.org/10.1371/journal.pone.0210852

Rubeis, V.D., Cultrera, G., Cadet, H., 2011. Statistical Estimation of Earthquake Site Response from Noise Recordings. Presented at the 4thIASPEI / IAEEInternational Symposium, University of California Santa Barbara, p. 9.

Sánchez-Sesma, F.J., Rodríguez, M., Iturrarán-Viveros, U., Luzón, F., Campillo, M., Margerin, L., García-Jerez, A., Suarez, M., Santoyo, M.A., Rodríguez-Castellanos, A., 2011. A theory for microtremor H/V spectral ratio: application for a layered medium: Theory for microtremor H/V spectral ratio. Geophysical Journal International 186, 221–225. https://doi.org/10.1111/j.1365-246X.2011.05064.x

Satoh, T., Kawase, H., Matsushima, S., 2001. Differences Between Site Characteristics Obtained From Microtremors, S-waves, P-waves, and Codas. Bulletin of the Seismological Society of America 91, 313–334. https://doi.org/10.1785/0119990149

Scherbaum, F., 2013. Of poles and zeros: Fundamentals of digital seismology. Springer Science & Business Media.

Sercel, 2019. Seismometers, Analog Seismic Sensors - Sercel [WWW Document]. URL https://www.sercel.com/products/Lists/ProductSpecification/Geophones_specifications_Sercel_EN.pdf (accessed 10.28.19).

SESAME Geopsy Team, 2019. Geopsy home: software applications for ambient vibration techniques [WWW Document]. URL http://www.geopsy.org/ (accessed 11.28.19).

Seyhan, E., Stewart, J.P., 2014. Semi-Empirical Nonlinear Site Amplification from NGA-West2 Data and Simulations. Earthquake Spectra 30, 1241–1256. https://doi.org/10.1193/063013EQS181M

Smith, J.O., 2011. Spectral Audio Signal Processing. W3K Publishing, http://books.w3k.org/.

Song, K., Tong, S., Ding, Z., Dong, L., 2016. An electromagnetic feedback method to improve low-frequency response performance of geophone, in: 2016 IEEE SENSORS. Presented at the 2016 IEEE SENSORS, IEEE, Orlando, FL, USA, pp. 1–3. https://doi.org/10.1109/ICSENS.2016.7808704

Stafford, P.J., Rodriguez-Marek, A., Edwards, B., Kruiver, P.P., Bommer, J.J., 2017. Scenario Dependence of Linear Site-Effect Factors for Short-Period Response Spectral Ordinates. Bulletin of the Seismological Society of America 107, 2859–2872. https://doi.org/10.1785/0120170084

Stephenson, W., 2003. Factors bounding prograde Rayleigh-wave particle motion in a soft-soil layer, in: Proceedings of the 2003 Pacific Conference on Earthquake Engineering. New Zealand Soc. of Earthquake Engineering, p. 15.

Stewart, J., Boore, D., Campbell, K., Erdik, M., Silva, W., 2012. Site effects in parametric ground motion models. PEER Center UC, BerkeleyReport to GEM.

Stokoe, K.H., Wright, S., Bay, J., Roesset, J., 1994. Characterization of geotechnical sites by SASW method. Unknown Journal 15–25.

Teledyne Geotech, 2019. Teledyne Geotech S-13 Short Period Sensor | PASSCAL Instrument Center [WWW Document]. URL

https://www.passcal.nmt.edu/content/instrumentation/sensors/short-period-sensors/s-13 (accessed 10.28.19).

Toshiba, 2019. TLP291 | Photocouplers | Toshiba Electronic Devices & Storage Corporation | Americas – United States [WWW Document]. URL https://toshiba.semicon-storage.com/us/product/opto/photocoupler/detail.TLP291.html (accessed 12.18.19).

Tran Thanh Tuan, D.F., 2009. The ellipticity (H/V -ratio) of Rayleigh surface waves. Geowissenschaftlichen Fakultat der Friedrich-Schiller-Universit, Jena.

Tremblay, R., Atkinson, G.M., Bouaanani, N., Daneshvar, P., Léger, P., Koboevic, S., 2015. Selection and scaling of ground motion time histories for seismic analysis using NBCC 2015, in: Proceeding 11th Canadian Conference on Earthquake Engineering, Victoria, BC, Canada, Paper No.

Tsuboi, S., 2001. Verification of Horizontal-to-Vertical Spectral-Ratio Technique for Estimation of Site Response Using Borehole Seismographs. Bulletin of the Seismological Society of America 91, 499–510. https://doi.org/10.1785/0120000239

Uebayashi, H., 2003. Extrapolation of irregular subsurface structures using the horizontal-to-vertical spectral ratio of long-period microtremors. Bulletin of the Seismological Society of America 93, 570–582.

Vidal, F., Alguacil, G., Navarro, M., González-Herrera, R., Aguirre, J., 2016. Characteristics of the earthquake ground motion in Tapachula (Mexico) from acceleration and ambient noise data.

Vucetic, M., Dobry, R., 1991. Effect of soil plasticity on cyclic response. Journal of geotechnical engineering 117, 89–107.

Wichtmann, Triantafyllidis, 2004a. Influence of a cyclic and dynamic loading history on dynamic properties of dry sand, part I: cyclic and dynamic torsional prestraining. Soil Dynamics and Earthquake Engineering 24, 127–147. https://doi.org/10.1016/j.soildyn.2003.10.004

Wichtmann, Triantafyllidis, 2004b. Influence of a cyclic and dynamic loading history on dynamic properties of dry sand, part II: cyclic axial preloading. Soil Dynamics and Earthquake Engineering 24, 789–803. https://doi.org/10.1016/j.soildyn.2004.05.002

Williams, H., 1984. Miogeoclines and suspect terranes of the Caledonian–Appalachian Orogen: tectonic patterns in the North Atlantic region. Canadian Journal of Earth Sciences 21, 887–901.

Williams, H., Hoffman, P.F., Lewry, J.F., Monger, J.W., Rivers, T., 1991. Anatomy of North America: thematic geologic portrayals of the continent. Tectonophysics 187, 117–134.

Xenaki, V.C., Athanasopoulos, G.A., 2008. Dynamic properties and liquefaction resistance of two soil materials in an earthfill dam—Laboratory test results. Soil

Dynamics and Earthquake Engineering 28, 605–620. https://doi.org/10.1016/j.soildyn.2007.10.001

Yoon, S., 2005. Array-based measurements of surface wave dispersion and attenuation using frequency-wavenumber analysis (PhD Thesis). Georgia Institute of Technology.

Yuliyanto, G., Harmoko, U., Widada, S., 2017. Identify the slip surface of land slide in Wirogomo Banyubiru Semarang Regency using HVSR method. International Journal of Applied Environmental Sciences 12, 2069–2078.

Zhang, J., Andrus, R.D., Juang, C.H., 2005. Normalized shear modulus and material damping ratio relationships. Journal of Geotechnical and Geoenvironmental Engineering 131, 453–464.

Zhang, S.X., Chan, L.S., Chen, C.Y., Dai, F.C., Shen, X.K., Zhong, H., 2003. Apparent phase velocities and fundamental-mode phase velocities of Rayleigh waves. Soil Dynamics and Earthquake Engineering 23, 563–569. https://doi.org/10.1016/S0267-7261(03)00069-1

Zhang, Z., Fleurisson, J.-A., Pellet, F., 2018. The effects of slope topography on acceleration amplification and interaction between slope topography and seismic input motion. Soil Dynamics and Earthquake Engineering 113, 420–431. https://doi.org/10.1016/j.soildyn.2018.06.019

Zywicki, D.J., 1999. Advanced signal processing methods applied to engineering analysis of seismic surface waves (PhD Thesis). Georgia Institute of Technology.

Appendix A: DYNAMate Specifications

Operation Limits

Parameter	Value	Units
Maximum Voltage		
Trigger	5000	
Sensor Input	70	Volts
DC Power Input	36	
USB	10	
Temperature Range	-10 to +70	°C

Power Requirements

Parameter	Value	Units
DC Input Voltage	9-36	Volts
Current Consumption	450	mA

Input Parameters

Parameter	Value	Units
Sensor Input Impedance	40	kΩ
Trigger Input Impedance	10	

Data Acquisition

Parameter	Value	Units
Resolution	16	bit
Sample Rate	4000 downsampled to 1000	Hz
Conversion Time	4	µs
Analog Bandwidth	250	Hz
CMRR, DC to 60 Hz	100	dB
Gain Error	115	ppm
SNR	75	dB
Crosstalk	-65	dB
Noise floor	G = 1, 10, 100, 1000 0.5	µV peak
	G = 10,000 10.0	

Filters and Amplification

Filter Bank – low-pass	32, 64, 128	Hz
Roll-off	80	dB/dec
High-pass	0.17	Hz
Roll-off	40	dB/dec
Input Amplifier		
Gain	x5, x50	
Output Amplifier		
Gain	x1, x10, x100, x1,000, x10,000	
Calibrated Sensitivity Scales	100, 10, 1, 0.1, 0.01, 0.001	mm/s
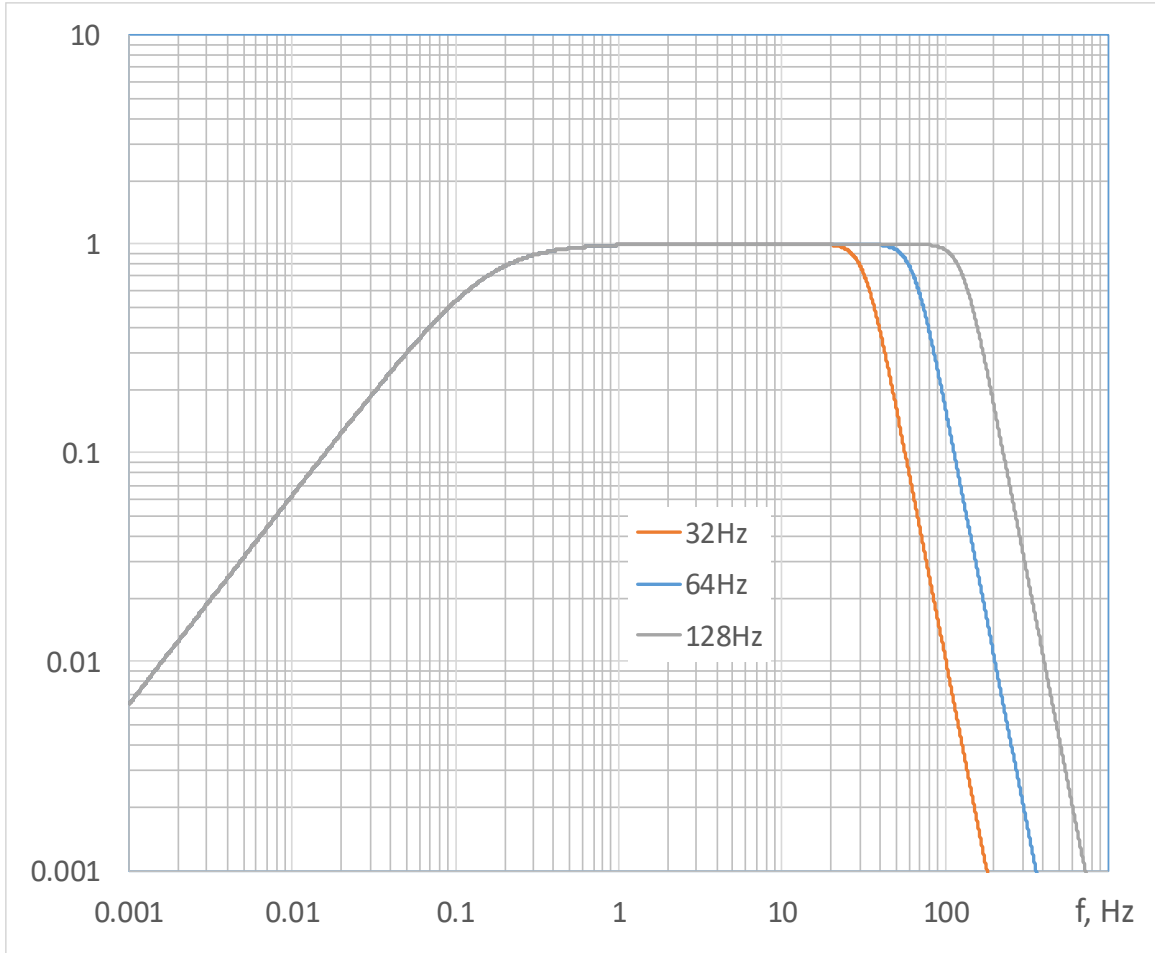
Figure A.1: DYNAMate single component normalized frequency response for the different filter selections

Appendix B: DYNAMate Software Suite

B.1 Introduction and Requirements

The main goal of the DYNAMate control and logging software is to establish a minimalistic, simple to use and understand graphical user environment for the collection of vibration measurement data using DYNAMate. The application supports all 8 channels of the DYNAMate DAQ system simultaneously and allows for the selection and configuration of all or a subset of channels depending on the application.

The source code for the application can be found on GitHub: (Mihaylov, 2019c). To execute the application 32bit LabVIEW Runtime LVRTE2017_f2 (National Instruments, n.d.) or newer is required. NI DAQ-mx(National Instruments, n.d.) drivers are required to connect to the DYNAMate DAQ over either USB or TCP/IP.

All logged data is saved in TDMS format. It can be opened in Microsoft Excel, using the TDM Excel Add-In for Microsoft Excel(National Instruments, n.d.). Alternatively, DYNAMate Process can be used to open, analyze and export the data in Excel format.

B.2 Operational Description

The main graphical user interface (GUI) of the application is shown in Figure B.2. For the given example, only two channels are selected, and the waveforms can be seen stacked vertically in the right-hand side of the GUI. The waveforms have units of mm/s regardless of the currently selected range. The left-hand side of the GUI contains the controls and indicators, for detail see Figure B.1.

The settings dialog (Figure B.3) allows the configuration of acquisition, triggering and logging parameters. It is divided using tabs into 3 panes: Logging, Channels and Description.

The Description pane of the Setting dialog can be used to title the measurement for later reference as well as to keep notes regarding experimental/measurement conditions.

Control	Description
Start/Stop button	All controls are disabled until the Start button is pressed, once the system is running the start button will toggle to the stop button, which terminates the current acquisition task and disables other controls.
Force Trigger	
Settings button	The trigger can be forced, which will toggle a data recording based on the last setting configured in the settings menu.
Currently selected amplification scale in mm/s	Logging configuration can be modified through the Settings window
	The current hardware configuration is displayed in the two bar controls, which are read only, as those settings can only be changed using the knobs provided on the DAQ unit.
	The displayed chart amplitude will scale according to the currently selected amplification, and it will always be displayed in mm/s.
Currently selected filter	Any change to the max/min amplitude controls will affect all chart displays at the same time and disable autoscaling for all charts. If it is required scales can be set individually for each chart by clicking the number displayed on the corresponding axis and entering the required values. Autoscaling can be either set individually for each chart by right clicking the chart or the amplitude scale, and then selecting the auto scale option, or at the same time for all charts by clicking the autoscale control.
Max amplitude	
Min amplitude Toggle Auto scale For all charts	The length of data displayed at a time can be adjusted for all charts at the same time by using the chart Length control.
Chart duration	The status display will show the current state of the unit, as well as potential error messages relevant to the operation of the unit.
Status Display	
Close the application	The application can be closed by clicking the exit button, which will be terminating the current acquisition session, and close any open logging files.
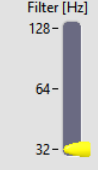
Figure B.1: DYNAMate Logging user interface controls and indicators

The Logging pane is used to configure the sampling frequency (max 1000 Hz), record duration, pre-trigger buffer duration. The pre-trigger buffer will store up to the specified number of seconds of data and store it in the output file at offset time stamp, i.e. for a 10 seconds record with a 2 second pre-trigger the final file will begin at time -2 seconds and be 12 seconds long (ending at 10 seconds). This pane also allows the user to set logging parameters such as data logging path and file name, triggering condition.
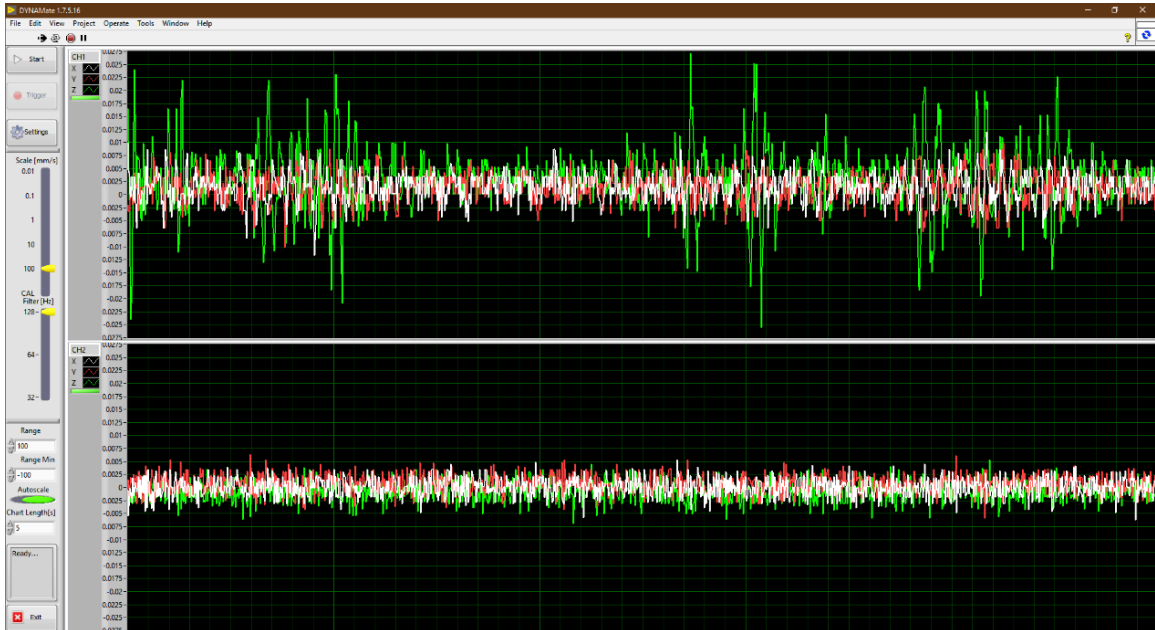
Figure B.2: DYNAMate v1.75 Graphical user interface. Channel 1(CH1) is recording microtremmor using DM 4.5 Hz; Channel 2(CH2) is recording the DAQ noise under short-circuit input conditions.
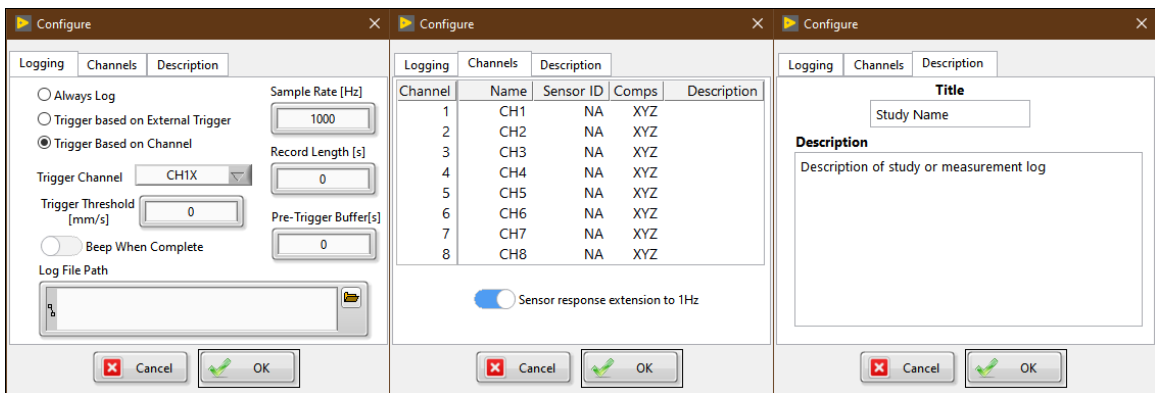
Figure B.3: DYNAMate settings dialog

Four different triggering options are supported:

- Always Log –As soon as the start button is pressed all data will be recorded to the specified file.
- External Trigger –Logging will start based on the external trigger.
- Based on channel -By specifying a channel number and a threshold, logging will begin as soon as the given channel crosses the specified threshold. Channels available for triggering must be selected as active channels in the Channels pane.
- Forced Trigger –When in either External Trigger or Channel trigger, pressing the Trigger button on the Main UI will start the logging process, bypassing any trigger requirements.

Each time a trigger condition occurs, a new filename is created using the provided filename, by concatenating the filename with the timestamp of file creation. Each file will contain a maximum number of samples determined by the specified Record length. If the Beep when complete switch is set, then at the end of each record DYNAMate will play the system notification sound to alert the operator to the end of recording event.

The channel configuration pane of the Settings dialog configures which channels are considered active and if available which DM 4.5 Hz sensor is connected to each channel. It also allows for each channel to be named, given a brief description and sensor orientation. This metadata is stored along with the recorded data in the output TDMS files. Sensor IDs should be specified correctly for response expansion to work accurately. The Sensor IDs are matched to individual IRC curves generated for each manufactured DM 4.5 Hz from a look-up table. The IRC curves will expand the frequency range down to 1 Hz. If no ID is specified a generic $f_n = 4.5$ Hz, $h=0.707$ IRC will be used. If the sensor response extension is enabled, then DYNAMate will both visualize and log corrected data.

B.2.1 Core messaging and data acquisition

The main functional core of the DYNAMate application is based on the National Instruments Continuous Measurement and Logging (NI-DAQmx) template. This template utilizes five loops that handle the different aspects of the application. The loops are

executed concurrently and exchange data and control signals using data queues and data notifiers. The data notifier allows new data block sampled to overwrite the old one and triggers a new notification, even if the old one has not been processed yet. Therefore, the notifier is only used to provide blocks of sampled data to the data visualization loop where missing blocks will not affect the measurement results. The general data and control flow can be seen in Figure B.4.
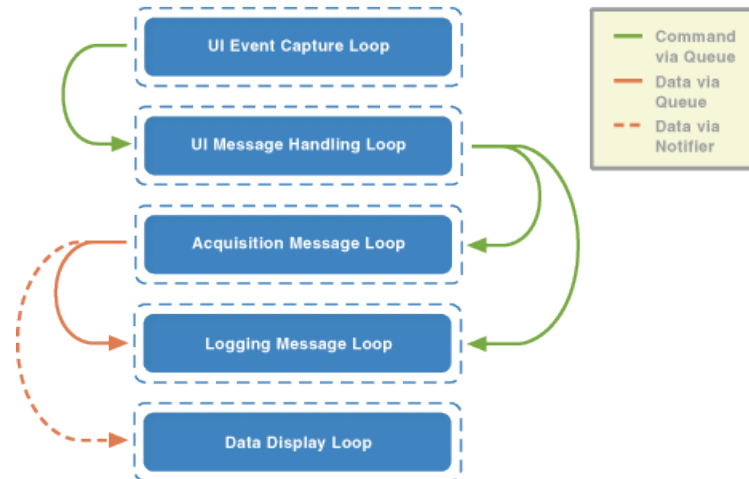
Figure B.4: Main operational loops and data flow of the DYNAMate application

Significant modifications were made to the template project, leaving only the signaling mechanisms intact. Large portions of the main user interface were redone to accommodate indicators and controls needed for operating the DYNAMate DAQ, along with corresponding logic. The main loops were also modified and are described as follows:

- Event handling - The Event Handling Loop produces messages based on front panel events, such as the user interacting with the available controls. Additional events were added to handle updates of the selected trigger and selected filter voltage input and corresponding user interface controls, as well as events that handle the scaling and synchronization of the data visualization panels.
- User interface messaging - A Message Handling Loop that receives messages from the Event Handling Loop and responds by routing appropriate messages to the other Message Handling Loops.

- Acquiring data - A Message Handling Loop that is idle until the Start condition is given after which it continuously acquires data regardless of whether a trigger condition has occurred. This is done to allow real-time visualization of the data stream. Instrument response correction (IRC), a circular buffer and oversampling were added to this loop to accommodate the needs of DYNAMate measurements.

- Logging data - A Message Handling Loop that logs acquired data once a trigger condition occurs. Metadata export, such as the details entered in the Settings dialog is also logged.

- Displaying data - A While Loop that updates the waveform chart with acquired data by using the data notifier as a trigger. Originally the template was implemented using Waveform charts, that contain an internal buffer, however this did not allow for dynamic channel assignment. Therefore, this loop was modified to operate using a circular buffer and an array of waveform graphs. This allowed for the dynamic creation and operation of data displays which to the author's knowledge had not been successfully done in publicly available LabVIEW applications.

B.2.1.1 Data Processing

Real-time should not be confused with immediate data processing and visualization, rather it's a term that defines systems which can process and visualize/log data segments within the time required to acquire the next data segment, thus they do not introduce an ever increasing lag between the input and output of the system. In systems that perform more than simple data acquisition, there will always be some delay between data acquisition and visualization/logging, this is the processing delay. The requirements for the duration of this delay are application dependent. To limit processing delay, limited data processing is done on the recorded data, and more intensive operations, for example spectrum analysis are provided as a separate post-processing tool.

The NI DAQ-mx driver collects data in blocks before releasing it to the processing software. As opposed to processing of individual samples, where signal routing and overhead function calls will significantly increase the processing time per sample,

processing blocks of data can be much more efficient. Data is collected in blocks with duration equal to 10 sampling periods.

Each data block contains 3-component signals for each selected channel (i.e. 12 signals for 4 channels) as well as the Trigger, Gain and Filter selected voltage level encoded signals. The latter two are used to adjust the state of the main user-interface indicators using thresholding, and the trigger is passed to the trigger handling logic shown in Figure B.7.

Most of the tasks performed by the DYNAMate logging software are related to GUI management, data and configuration routing as well as data visualization. They can be freely explored in the available source-code. This section focuses on the signal chain path and vibration data processing done by the logging software.

B.2.1.2 Data Acquisition

DYNAMate DAQ uses the method of oversampling (Havskov and Alguacil, 2004) to improve the dynamic range of the digital signals. The quantization errors due to the ADC of the individual samples in the oversampled waveform are shaped by a low pass filter and the averaged samples therefore have more accuracy and consequently a higher dynamic range within the downsampled bandwidth.

The oversampling process implemented for the DYNAMate logging software consists configuring the ADC module to sample channels at 4 times higher sampling frequency than what is specified in the settings dialog of the application. followed by a low pass anti-alias filter and down sampling to the specified rate (see Figure B.5).

The NI9205 module samples the input channels sequentially, which introduces a lag of 32/Fs (Fs is the oversampling frequency) between two adjacent channels. This is compensated using a linear interpolator before the signals are downsampled. This synchronizes the channel waveforms and updates each block's timestamp. Doing this before down sampling reduces the inter-sample error that the linear interpolator introduces to the signal.
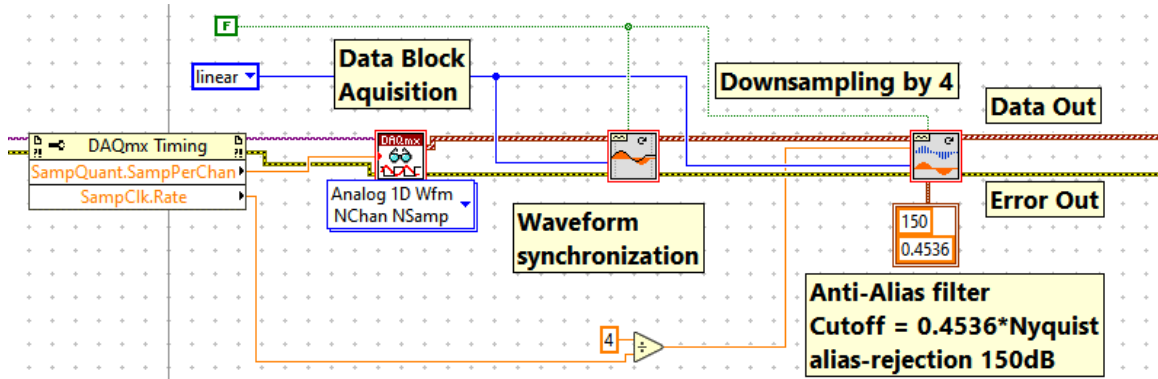
Figure B.5: Data Acquisition Section of the DYNAMate logging software

B.2.1.3 Instrument Response Correction

Instrument response correction is done using the IIR based real-time approach. A look-up table is generated of the 1 Hz IRCs for all manufactured DM 4.5 Hz sensors. This table is indexed using the Sensor IDs listed in the channel configuration of the Settings dialog. Additional sensors can be added to the ASCII format table using the numerator and denominator for the new IRC.

The process is implemented in DYNAMate using an IIR filter block nested in an in-place structure. The in-place operation structure prevents data copying performing operations on it. Data copy can lead to significantly increased execution time and memory usage. Response correction is not performed when the device is in calibration mode or when it is not specified in the Settings Dialog, this is done by introducing an all-pass zero phase set of dummy IIR coefficients. The IIR functional block processes one acquired block of data at a time, and since it requires both initial conditions for both inputs and outputs a buffer is used to store those between data acquisition events.
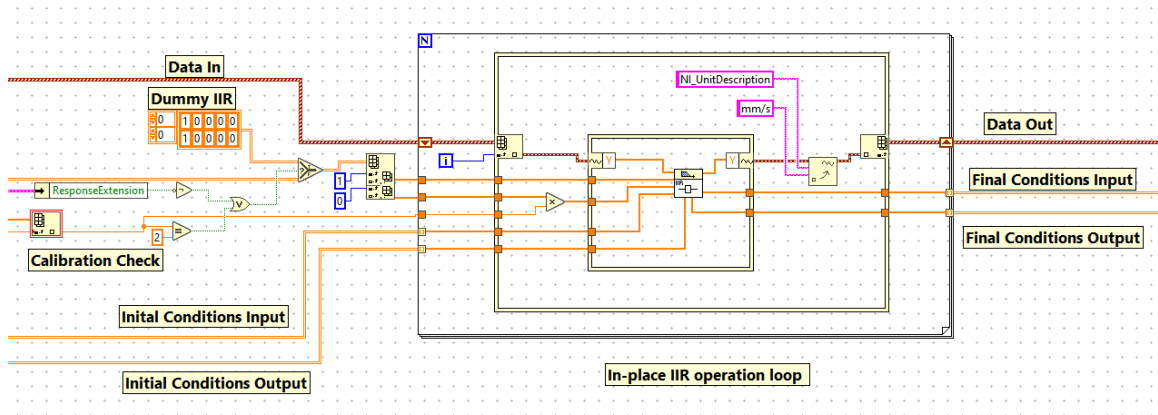
Figure B.6: Instrument response correction implemented in LabVIEW

B.2.1.4 Ring buffer operation and triggering

Trigger condition processing and circular buffer maintenance are shown in Figure B.7. The internal trigger (button on main UI, see Figure B.2) acts immediately on activation. The always logging condition uses the same logic as the internal trigger, with the difference that the trigger command is sent by the UI using the data notifier queue immediately at acquisition start. The external trigger is using an armed/disarmed logic that prevents false trigger inputs. For each data block the average level of the Trigger voltage is checked, and if it is above 5 V the external trigger is armed. When the external trigger fires, the Trigger line's voltage is dropped to 0 V and a trigger condition occurs. The trigger condition will not repeat until the voltage is raised to 5 V for a full blocks duration and the logic is re-armed. The channel trigger is based on a simple thresholding technique, where as soon as the specified channel component value exceeds the threshold a trigger condition occurs.

A ring buffer is introduced to the signal chain to store enough samples to cover the pre-trigger record duration specified in the Settings Dialog. This buffer stores blocks of sampled data for all channels during acquisition operation. When there is no pre-trigger record required the length of the buffer is one sample block. When a trigger condition occurs the sample of the current data block that corresponds to the time of the trigger firing is used to set a reference timestamp, this timestamp is used as time '0' for measurement. The trigger fire condition is forwarded to the data logging loop using the command queue

notifier to initiate the data logging process. The current data block is appended to the data in the ring buffer and the contents of it are released to the logging loop.
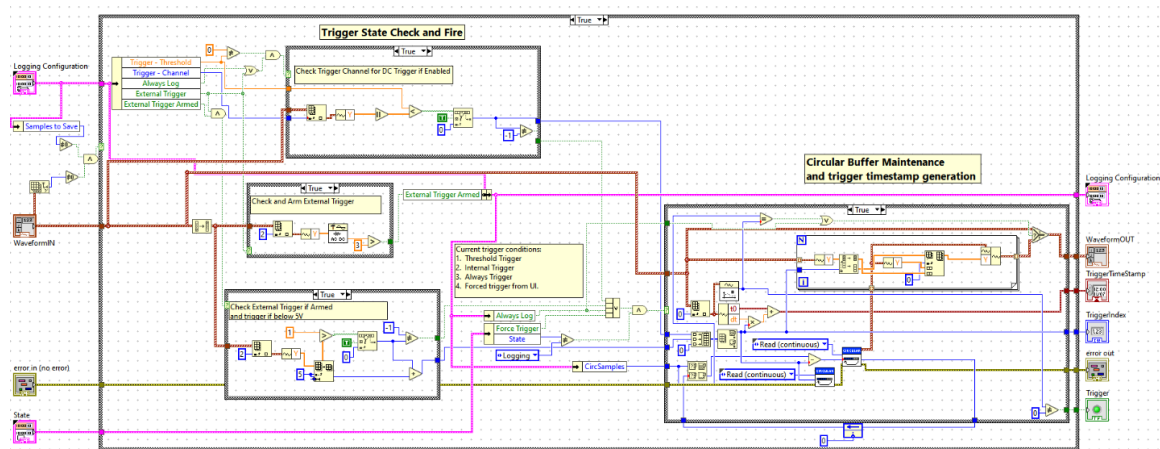
Figure B.7: DYNAMate trigger condition processing and circular buffer maintenance

B.2.2 MATLAB Based Post Processing Software - DYNAMate Process

B.2.2.1 Introduction

DYNAMate Process is a helper Graphical User Interface (see Figure B.8) used to process the data outputted from the DYNAMate DAQ System. It allows the user to process and investigate TDMS files and includes the following features:

- Visualize the recorded data.
- Extend the sensors' frequency range using a look-up table of input response correction curves.
- Produce a smoothed amplitude spectrum.
- Interactively investigate events in the data using the Zoom and Pan tools provided.
- Annotate the data and its spectrum using the Data Tips tool.
- Generate Displacement and Acceleration waveforms from the recorded Velocity data.

- Produce PNG images of the data including all annotations.

- Save All generated waveforms and spectra as an Excel XLSX file.

DYNAMate Process requires at least MATALB R2017b (9.3) Runtime ("MATLAB Runtime - MATLAB Compiler," n.d.) to be executed. Alternatively, if MATLAB R2017b is installed the runtime is not required. The source code and executable files can be obtained from GitHub (Mihaylov, 2019d).
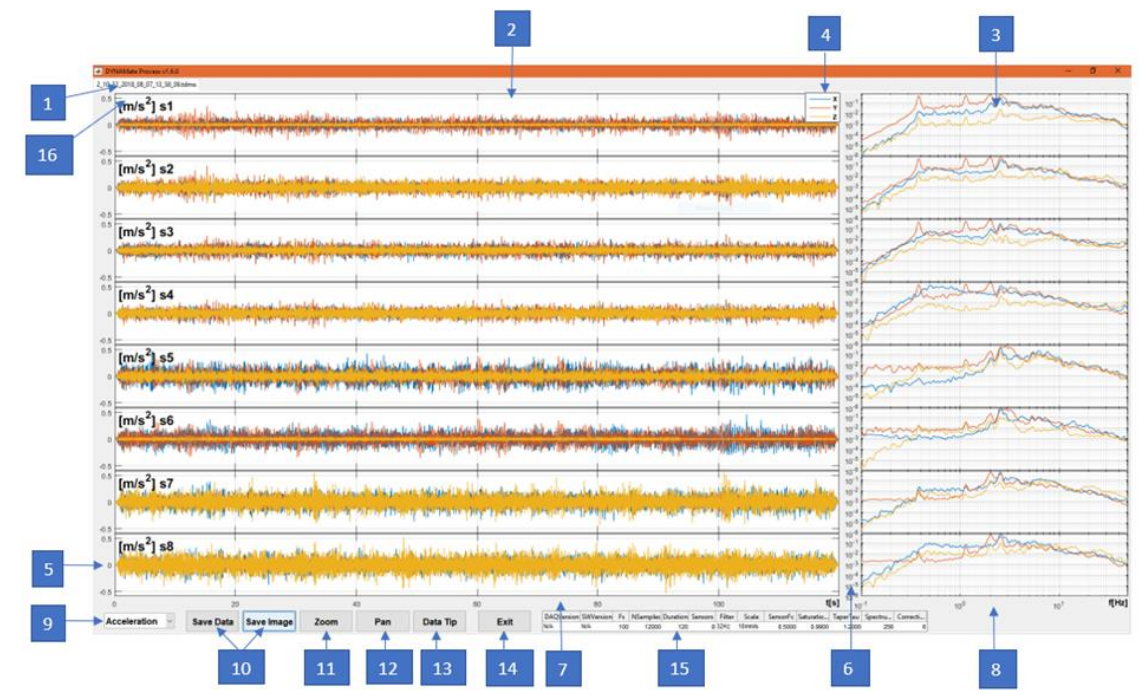
1	Tab control with open files	9	Acceleration/Velocity/Displacement selector
2	Time waveform graphs, one channel per row	10	Save Buttons
3	Frequency graphs, one channel per row	11	Zoom button (hold SHIFT to zoom out)
4	Legend	12	Pan button
5	First channel's amplitude scale	13	Data tip button (hold SHIFT to add more than one annotation)
6	First channels frequency amplitude scale	14	Exit button
7	Time axis for all channels' waveforms	15	Configuration Table (DAQ and Processing parameters) Read Only
8	Frequency scale for all channels' spectra	16	Channel Name and Units ([mm/s], [m/s^2] or [mm])

Figure B.8: DYNAMate Process Graphical User Interface Description

B.2.2.2 Startup and Operation

Upon Startup the software will display a splash screen while loading the MATLAB Runtime Environment in the background. This Runtime is used to facilitate program operation. Once the runtime loads, the user will be prompted with an Open File Dialog. In this dialog, the user can select one or multiple TDMS files for processing. Each file will be processed in turn and will generate one tab in the tabular environment of the Graphical User Interface (GUI), as shown in Figure B.2. Loading of DYNAMate TDMS data files considers the sensor configuration and uses the assigned sensor ID numbers and a look-up table to perform post-processing frequency range expansion as discussed in section 3.4.

During loading, the user will be prompted if sensor frequency response extension is required. If the correction is requested, a check for saturation on each channel is performed, as the correction procedure does not function correctly under saturation conditions. If saturation is detected, then a warning dialog will be presented. The warning dialog cannot be closed until loading is complete and shows to the operator the channels that are suspected of saturation, and to which file those channels belong. Correction will still be performed on the rest of the channels that satisfy saturation criteria. Saturated channels are displayed in the UI with dashed lines instead of the solid lines of non-saturated channels.

Once all the processing is complete, indicated by the loading bar present on screen during loading, the UI is generated and presented on the screen. At this point, all processing is complete and data analysis can begin. The displayed graphs can be changed between acceleration, velocity and displacement using the provided drop-down menu. For every channel all three components are shown along with their corresponding spectra for the currently visible time window.

The zooming, panning and data annotation functions are based on standard MATLAB figure operations with the following functionalities added specifically for this application:

- All time graphs have synchronized axis.
- All spectrum graphs also have synchronized axis.

- The graphs will follow the zoom and pan operations on one plot and adjust accordingly.

- Data annotation reflects the correct data units for the currently selected display mode: mm/s for velocity, m/s for acceleration and mm for displacement.

- Annotation will be removed when switching between Acceleration/Velocity/Displacement views.

B.2.2.3 Configuring processing parameters

To configure the processing parameters the a configuration file DYNAMate.cfg (Figure B.9) is located in the Startup directory of the software. The configurable parameters are:

- **taper_tau** – duration as a fraction (0-1) of the total signal length of the taper applied at the beginning and end of the signal. Specify 0 to disable.

- **specSmoothN** – sharpness of the window used to smooth the spectrum graphs. Band-pass filters as defined in section 6.3.2 are used for the smoothing operation. This field specifies the 'n' parameter for the BPF, and '0' can be specified to disable the smoothing operation.

- **EnableFc** – binary parameter that enables or disables the sensor frequency response extension.

- **targetFc** – specifies the target corner frequency for the sensor's response extension operation.

- **corrSteepnes** – drop off rate for the corrected response, equal to (value-2)*5 dB/dec.

- **SatThreshold** – Saturation detection threshold as a fraction of the scale used to record the data, i.e. at threshold 0.99, and scale selected of 10mm/s any signal with values greater than 9.9mm/s will be considered possibly saturated.

- **PathName** – last used folder path for data import.
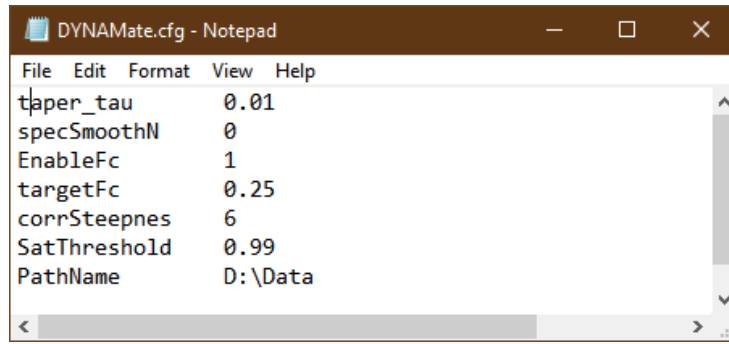
Figure B.9: Sample configuration file with default values for DYNAMate Process

B.2.2.4 Saving Data

The Save Data button exports the processed data of the currently selected tab and selected data tips to a XLSX Excel file and select an output filename. The exported Excel workbook contains 7 sheets: 'Configuration' (Configuration Information), 3 sheets for the Acceleration, Velocity and Displacement time waveforms and 3 sheets for the spectra of Acceleration, Velocity and Displacement (with a prefix 'FFT_'). The configuration sheet contains sensor and processing information as well as some signal statistics (see Figure B.10 for details). The data sheets display appropriate sensor names, components and units. The Save Image button will export a PNG graphics file of the currently configured view.

Figure B.10: Example exported data file from DYNAMate Process

Appendix C: Other Field Studies

C.1 Whitby

For a new residential development at the corner of Taunton Rd. and Country Ln. in Whitby, ON, the previous site of a golf course is being repurposed by grading and soil reclamation to achieve a level lot for construction of the residential development. The site is characterized by weak, relatively sensitive silty clay overlain by construction fill and silty sand.

The development is relatively large, and the study is limited to the accessible locations near boreholes, where available borehole logs can be correlated to the study results. These locations include BH309, BH310 and BH311. There is a notable difference in elevation across the site, due to the accumulation of reclaimed soil in the locations of BH309 and BH311, the accumulated soil is 3-4m higher than the rest of the site and is used to force settlement of the underlying saturated soil layers. Figure 1 illustrates the study site and locations of geophone spreads.

In all three locations the top 1-2m are comprised of compacted crust, cut by construction machinery tracks. The water level was at the top elevation of BH310, and within 3-5m of the elevation of BH309 and BH311

The purpose of the study was to establish a shear wave velocity profile for the area around the borehole locations. Additionally, the depth to bedrock, or the high contrast boundaries are to be determined using Nakamura's HVSR method.
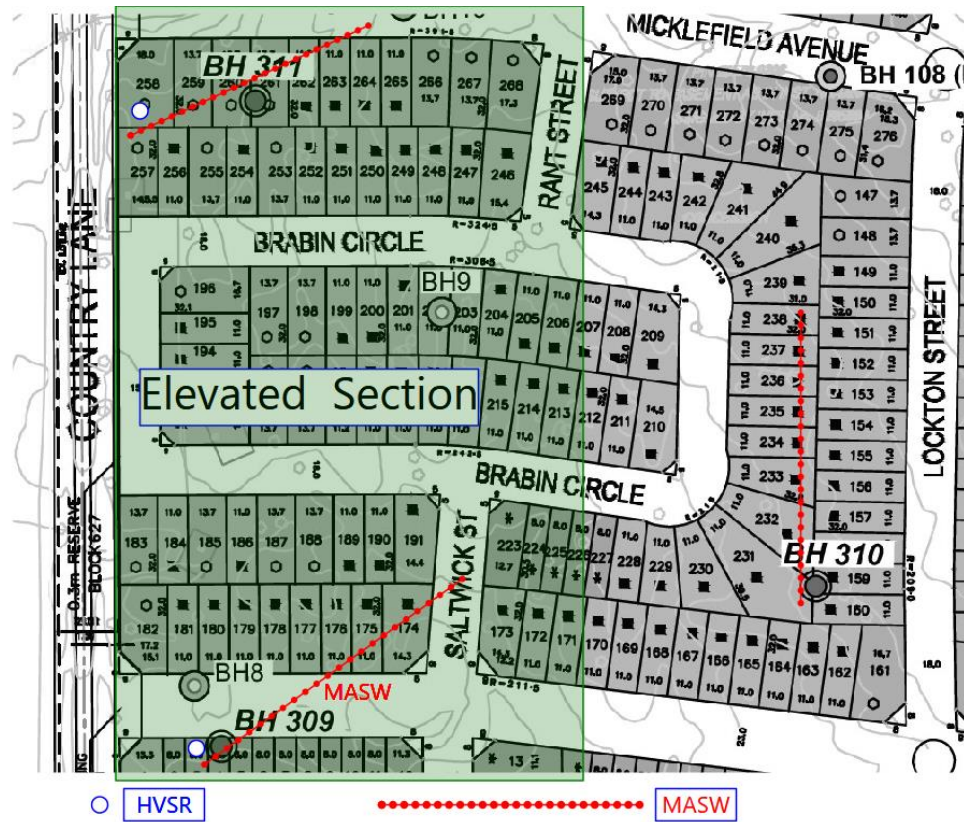
Figure C.1: Site map and MASW spreads

C.1.1 Investigation Methodology

Among all other elastic parameters of materials, shear-wave velocity (Vs) is the best indicator of the soil/rock stiffness. For this investigation shear-wave profiling was considered unreliable due to difficulties in generating shear waves and processing the acquired data at the very high ambient seismic noise (traffic vibrations and city noise) present on the site. Recently, surface wave methods have become the seismic techniques most often used to estimate the Vs structure of soil, because of their non-invasive nature and greater efficiency in data acquisition and processing Propagation velocity (called phase velocity) of surface waves is frequency/wavelength dependent. (This property is called dispersion. The soil structure is determined mainly by the vertical variation in Vs. By recording fundamental-mode Rayleigh waves propagating horizontally and directly from the seismic source to each receiver, the dispersive properties of the surface waves directly beneath the geophone spread can be measured and usually represented by a curve

(called dispersion curve) depicting variation of phase velocities with frequency. This curve is then used to estimate the vertical variation of Vs (1-D Vs profile) using a process called inversion.

Of the surface wave methods, MASW is the only geophysical (seismic) method which could give an acceptable approximation for Vs distribution with depth in noisy conditions.

A method to directly obtain at least some well-established resonances is the Horizontal to Vertical Spectral Ratio (HVSR) method proposed by Nakamura (1989). This is the easiest technique to evaluate characteristics of the local site response through direct observation of seismic ground motion during local and regional earthquakes. Such studies are generally applicable to areas with high seismicity. In areas with low seismicity, like Central Ontario, ground vibration from small earthquakes and ambient seismic noise are convenient tools to estimate the effect of surface geology on seismic motion. The method works on the assumption that the vertical spectrum of ground motion is unaffected by sedimentary layers and caries mainly information about the seismic source. The horizontal spectrum is changed due to sedimentary layers. The vertical vibrations could be used to deconvolve the source effects from the site effects affecting the horizontal motion.

Short records of microtremors of the ground surface are used to find QTS in the frequency domain. The QTS is result from normalizing the horizontal spectrum of each site by its vertical spectrum. The HVSR usually provides a clear peak that is correlated with the fundamental S-wave resonant frequency for the uppermost layer, and the observed peaks correlate with the depths to the nearest high acoustic contrast boundary.

C.1.2 Field Work

The fields work for the investigation was carried out on August 31, 2016. A total of three MASW profiles were made under the observation at the site, one at each borehole location.

The profile location was selected to provide coverage of an area along the building foundation. One-dimensional multi-spectral analysis of surface waves (MASW) was used to predict subsurface shear-wave interval velocities. The site location is very close to two county streets and recording were taken during construction operations on site, imposing strong limitations on the feasibility of other seismic methods because of the very high level of ambient ground vibration.

HVSR measurements of ambient noise were performed at the start location of each MASW spread and recorded using an L4-3D three component geophone for a duration of three minutes.

C.1.3 Data Collection

Considering the frequency-with-depth dependency of surface waves and the response characteristics of geophones, low-frequency (4.5 Hz) geophones were used as receivers and a heavy impact seismic source - 16-lb (5 kg) sledgehammer produced a broadband, relatively low-frequency signal. Distance ($x1$) between source and nearest receiver-station (called source offset) was chosen to minimize near-field effects caused by excessive stress-strain relationship from the impact source. This source offset is usually chosen to be about the same as the maximum depth of the investigation.

There are situations where source-to-receiver offsets that are less than the depth of interest could be appropriate. For our measurements we used source-to-receiver offset 3 m because of site imposed size limitations and very high ambient noise.

Receiver spacing ($dx = 2.5$m) was chosen to avoid any possible spatial aliasing of the shortest wavelength recorded and to maximize the effectiveness of dispersion analysis

Total length of receiver spread ($x_T = 60$ m) determines the farthest offset and receiver spacing. It was short enough, that strong body waves and higher-mode surface waves, usually dominating the record at far offsets, did not interfere with fundamental-mode dispersed waves used for dispersion analysis.

Specific source-receiver configurations are defined by source offset, receiver spacing, and receiver spread. A measurement consists of multichannel records (called a shot gathers) resulting from more than one seismic impact recorded at a single point by a fixed receiver spread. The vibration history and propagation of the source-generated seismic wave field is picked-up by each geophone along the spread and is represented by a time series referred to as a trace. A single 1-D shear wave velocity profile comes from all traces of MASW measurement and it depends on the earth materials directly beneath the spread.

C.1.4 Results

A 1-D Vs profile obtained using inversion, best represents the vertical Vs structure beneath the middle point of the geophone spread used for the analysis. Because of the enhanced effectiveness in data processing provided by multiple receivers recording, stacked measurements from several impacts and one source-receiver configuration were sufficient to produce 1-D Vs profiles.

No HVSR studies were done at the location of BH310, due to the high level of ambient noise from construction equipment. The velocity profiles are presented with one standard deviation measure, taken from a sample of inverted profiles.

The HVSR study demonstrates a clear contrast peak at 5Hz for BH309 and 5.2Hz for BH311. Additionally, the depth to the 5/5.2 Hz boundary is back figured using the derived mean shear wave velocity and the represented on the soil profile figures as a blue horizontal line. Moreover, the location of BH309 seems to exhibit double high-contrast boundary, one at approx. 9m and the second at approx. 18m, whereas the same boundary for BH311 is located at an approximate depth of 17.5m

Overall there is a good agreement between the measured HVSR peak and the soil profile contrasts. Using the lower frequency peak of the HVSR spectrum a rough measure of the depth to bedrock, depth to the 5/5.2 Hz boundary and effective MASW depth is obtained for each location as follows:

Table C.1: HVSR from Low- and High-level excitations in ambient noise

Test and Location	309_9L	309_13L	311_9L	311_13L
Depth to Bedrock[m]	249.75	240	199.2	217.5
Depth to 5Hz Boundary[m]	13.03	17.17	19.35	18.55
Effective Measurement Depth	23.5	24.23333	20	18.05
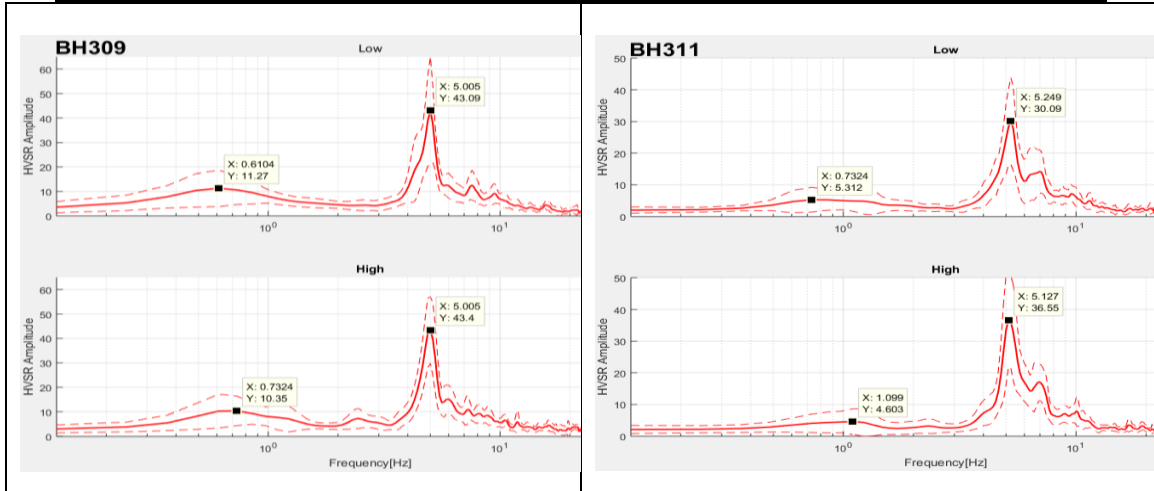
BH309
9 Layer Model
Elevation 116.2 m

Depth (m)	Vs (m/s)
0.000	171.504
1.125	152.287
3.500	187.123
5.625	249.430
9.000	639.036
13.125	630.707
18.000	650.029
23.625	734.209
71.400	734.209

BH310
12 Layer Model
Elevation 118.2 m
Dug out Approximately to 113.0m

Depth (m)	Vs (m/s)
0.00	272.99
0.65	76.63
1.61	396.15
2.88	149.99
4.45	294.39
6.33	323.67
8.51	448.74
11.00	604.86
13.79	683.74
16.89	661.85
20.29	981.62
40.15	981.62

BH311 9 Layer Model
Elevation 116.0 m

Depth (m)	Vs (m/s)
0.000	171.504
1.125	152.287
3.500	187.123
5.625	249.430
9.000	639.036
13.125	630.707
18.000	650.029
23.625	734.209
71.400	734.209
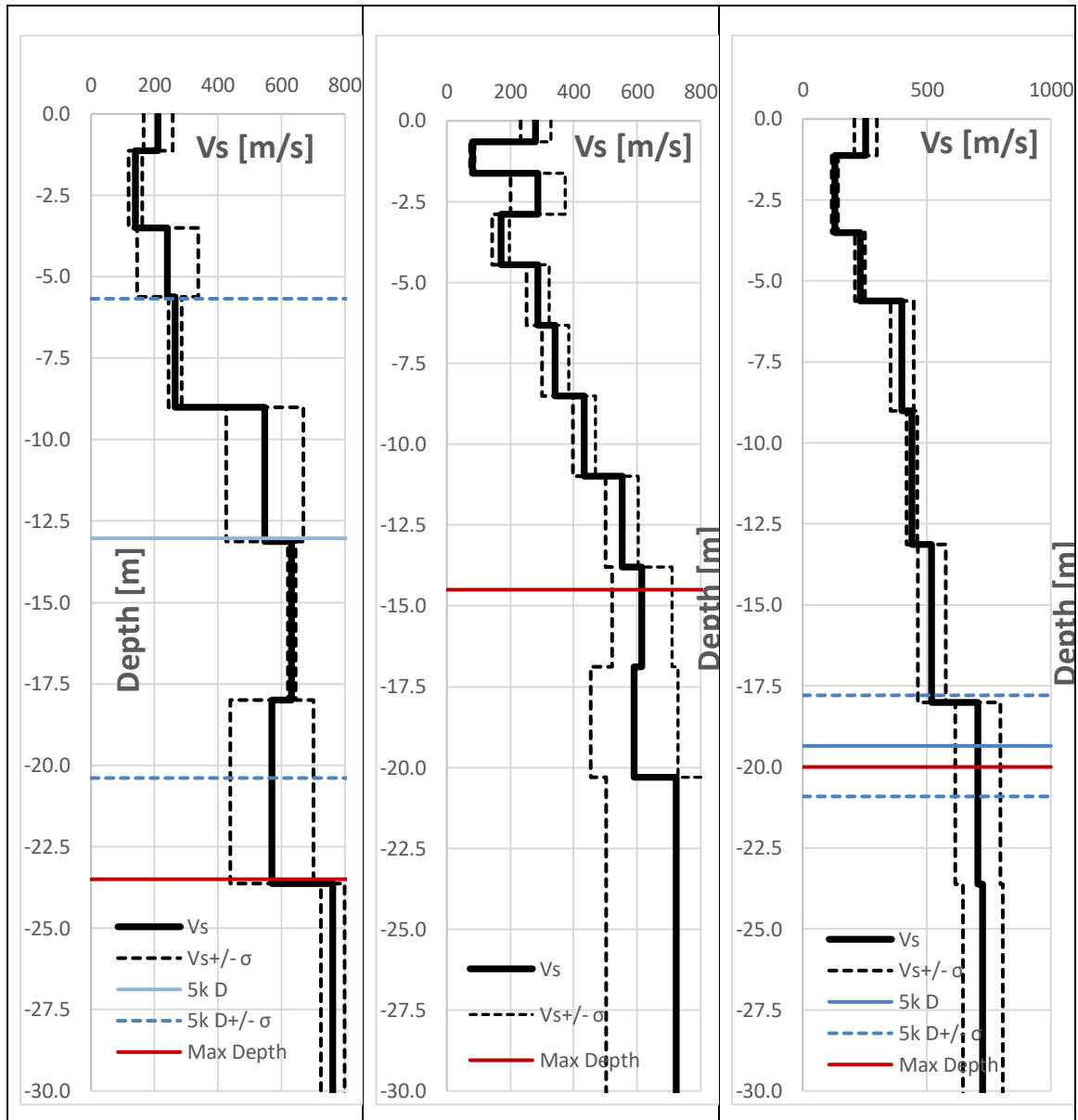
Figure C.2 Whitby MASW Results

C.2 Newmarket

The purpose of the study was to establish a shear wave velocity profile for the areas in the lower sections of glacial channels cut into the topography near Newmarket, Ontario. The map given in figure 1 illustrates the test points and their locations. Two studies were performed including HVSR contrast boundary estimation and MASW/SASW profiling at the lower sections of two of the channels.

Figure C.3: Newmarket Study map

Table C.2: Newmarket Test Point locations

Test Points	Location			Tests
	Landmark	Lat	Long	
NM1P1	scugog line 12	44.15027	-79.0869	top of hill HVSR
NM1P2	scugog line 10	44.14837	-78.9722	SASW MASW HVSR
NM1P3	scugog line 10	44.14582	-78.9832	top of hill HVSR
NM2P1	Blue Mountain Rd.	44.16331	-79.0885	top of hill HVSR
NM2P2	Blue Mountain Rd.	44.16441	-79.0834	SASW MASW HVSR
NM2P3	Blue Mountain Rd.	44.16535	-79.0788	rail trail HVSR

C.2.1 Investigation and Field Methodology

For this investigation, the 1-dimensional MASW measurement consists of a 24-channel array using 4.5-Hz geophones and Geometrics 24-channel (Geode) seismograph. Using 10 consecutive impacts of a 5-kg sledge on an alloy plate, records are collected, stacked and stored as digital files on a PC. Strike offset locations are chosen based on terrain and line excitation for the given conditions as well as targeted depth. Geophone were spread out at 2.2m and 5m intervals, resulting in spread length of 50.6//115m, and strike locations were at 10 and 20m from either side of the last element of the geophone spread.

C.2.2 Results

A 1-D Vs profile obtained using inversion, best represents the vertical Vs structure beneath the middle point of the geophone spread used for the analysis. Because of the

enhanced effectiveness in data processing provided by multiple receivers recording, stacked measurements from several impacts and one source-receiver configuration were sufficient to produce 1-D Vs profiles.

The following figures and tables illustrate the results of the HVSR and MASW for each borehole location. The velocity profiles are presented with one standard deviation measure, taken from a sample of inverted profiles. Overall there is a good agreement between the measured HVSR peaks and the soil profile contrasts.
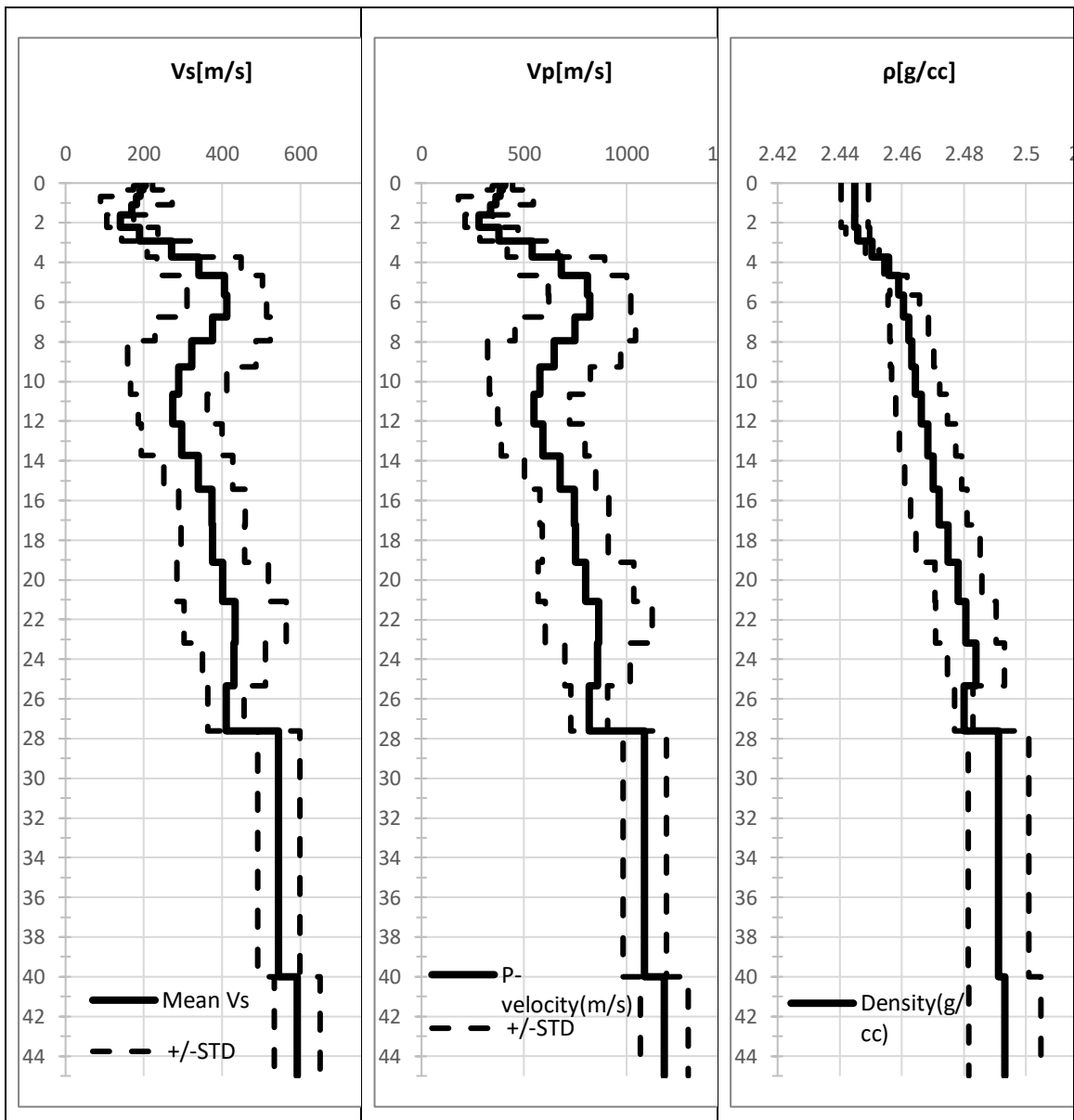
Figure C.4 Newmarket MASW Results Test 1

222

NM1P1		2.9Hz – 40-50m 11Hz – 5m 30Hz – 1m
NM1P2		2Hz – 55m(bedrock) 7.5Hz – 8.6m 21Hz -1.3m Top L4-3D Bottom 4.5Hz
NM1P3_hilltop		1.8Hz – 60m(bedrock) 9Hz – 6.5m 20Hz – 1.5m Top L4-3D Bottom 4.5Hz
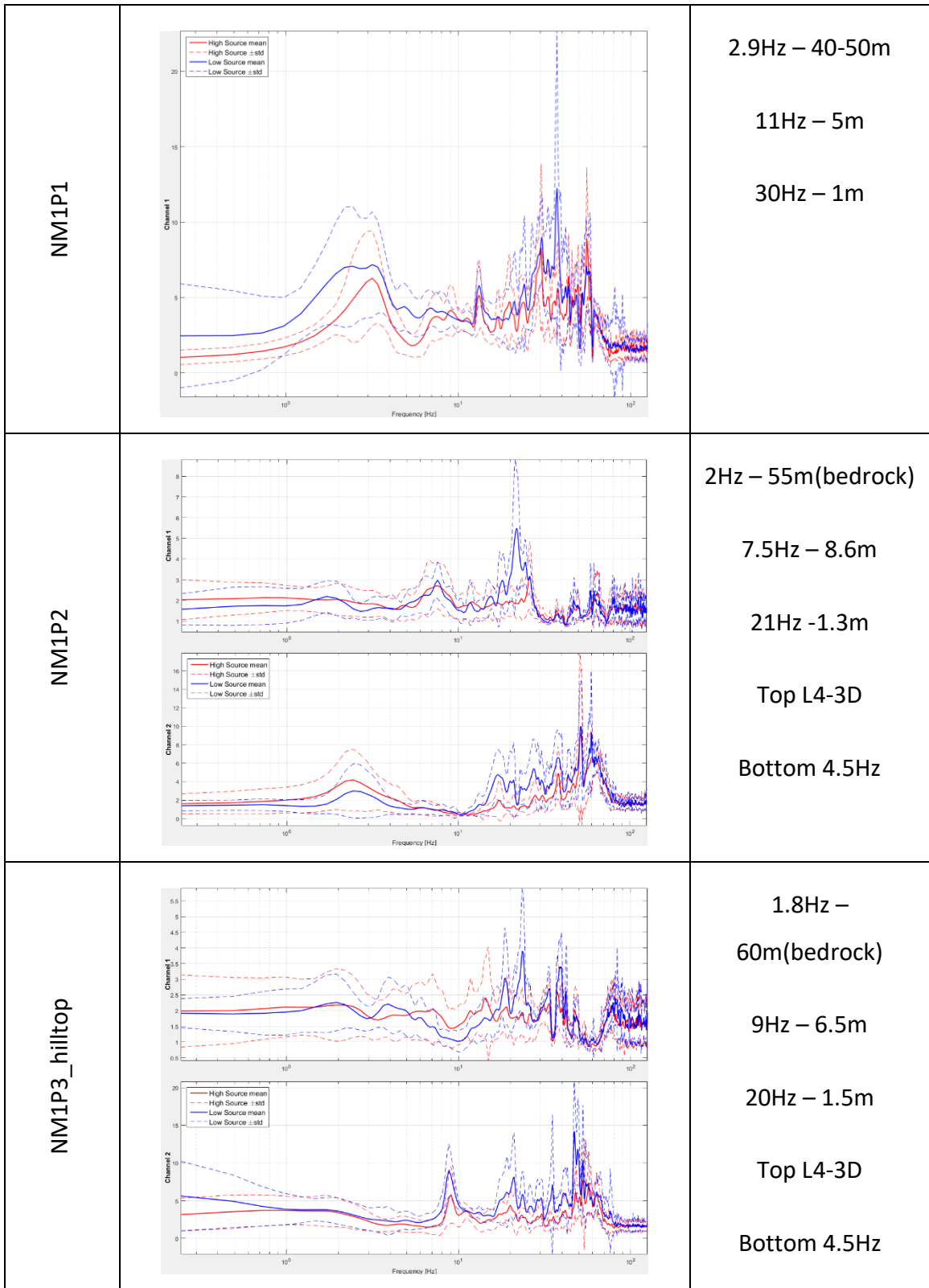
Figure C.5: Newmarket HVSR Results Test 1
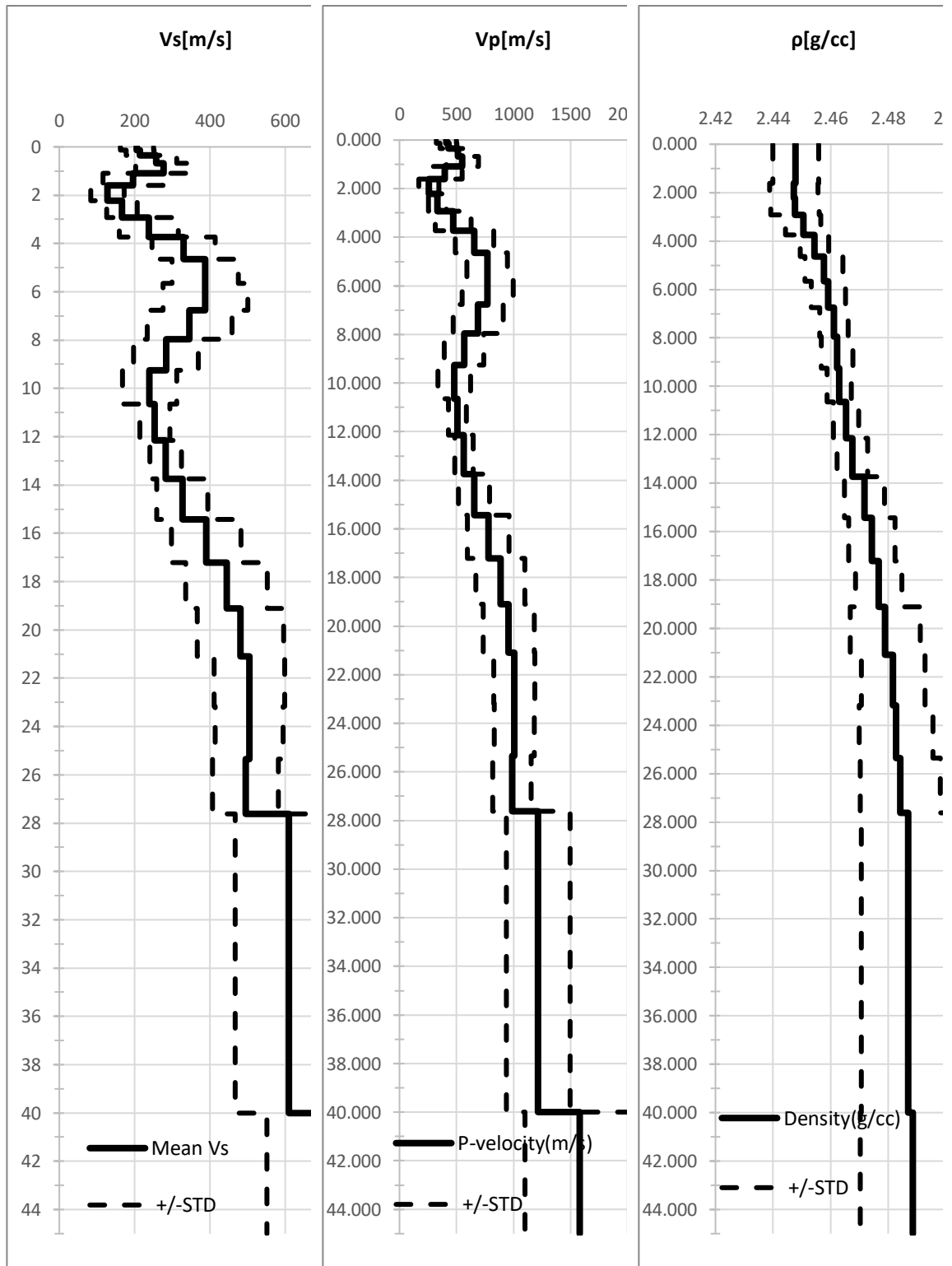
Figure C.6: Newmarket MASW results Test 2

NM2P1_hilltop		1.1Hz – (150m) 2.7Hz – 40m 3.1Hz – 25m 12Hz – 3.5m Top L4-3D Bottom 4.5Hz
NM2P2		0.8Hz – (200m) 1.2Hz – 100m 9.8Hz – 6m 16Hz – 2.5m 50Hz – 1m Top L4-3D Bottom 4.5Hz
NM2P3_rail trail		2Hz – 75m 6Hz – 10m 13Hz – 3. Top L4-3D Bottom 4.5Hz
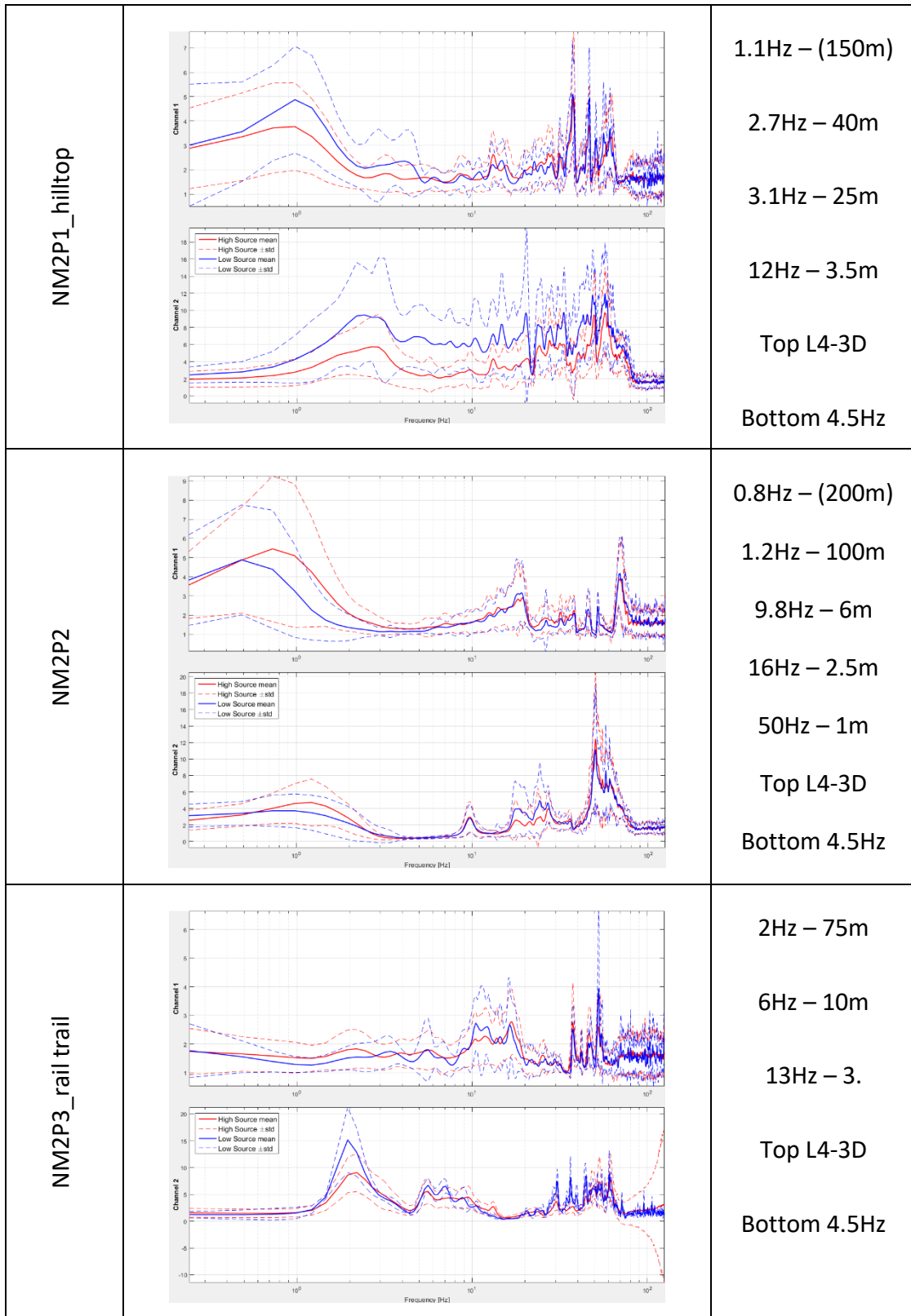
Figure C.7: Newmarket HVSR Results Test 2

C.3 Montmagny
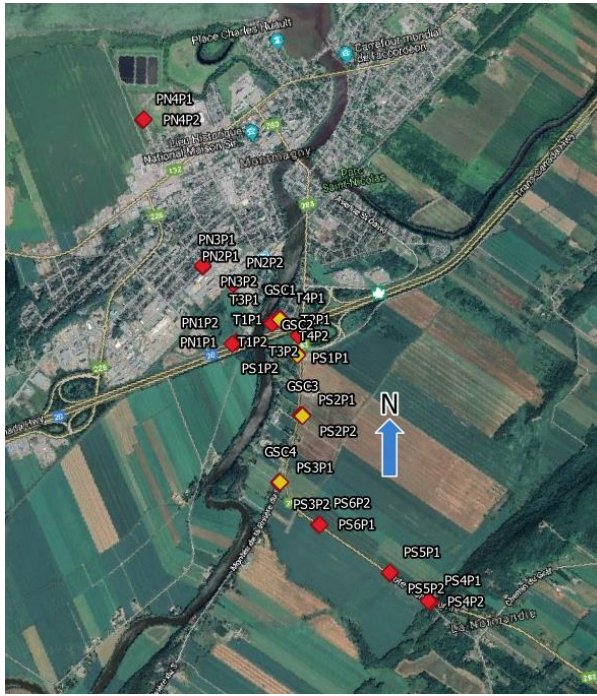
Figure C.8: Montmagny Field Study Map

The purpose of this study was to verify the methodology and protocol used to process HVSR microtremor data from both High and Low Sources. Data was collected using the L4-3D velocimeter and a GEODE NZ-2000 data acquisition system. The measurements points are given in figure 1. This study was performed with the aid of the GSC and parallel measurements were taken at some of the measurement points using Tromino™. Overall, a good agreement was found between Tromino data and the results of the proposed analysis protocol. This gives confidence to the rest of the measurements in the area and a preliminary bedrock map can be generated. No detailed soil profiling was performed at each point and the only geophysical information regarding the lithology at the site comes from the GLC-04 GSC borehole log. The average Vs for each point is then obtained by fitting a parabolic Vs profile with depth and extrapolating the required average Vs to the bedrock depth. HVSR data was collected from both low-level excitations (seismic noise) as well as high level excitations (i.e. traffic, wind sway of nearby transmission towers, etc.) These are label in the following figures by "High" and "Low". Additionally, each measurement was performed using 2 sensors, adding robustness and error checking, the first sensor is given in green and the second in red.

Comparing the results from the study to the data provided by the Tromino measurement system used by the GSC, there is a very close agreement between the recovered dominant frequencies and amplitude ranges, additionally the data processing method used in the field study gives additional information about the site, on top of what the Tromino

produces, in this case that's the fundamental resonance at some of the sites. Its only available at some of the sites due to noise contamination, and the relatively low frequency (correlating to depth to bedrock).

Table C.3: GSC Results Obtained using Tromino at the specified location in Montmagny, QC

Site	UTM E	UTM N	F$_o$[Hz] Tromino	F[Hz] Major Contrast	F[Hz] Bedrock
GLC-04 (BH)	381390	5202867	1.94	1.83	-
PS1	381465	5202570	2.66	2.7	0.77
PS2	381405	5202093	1.63	1.55	0.55
PS3	381127	5201626	1.41	1.35	0.55
PS4	382070	5200465	-	-	0.52
PS5	381817	5200750	-	3.3	0.61
PS6	381357	5201250	-	1.05	-
PN1	381085	5202765	-	1.5	0.65
PN2	381093	5203220	-	-	0.48
PN3	380886	5203405	-	3.5	0.49
PN4	380670	5204620	-	5.6	0.48
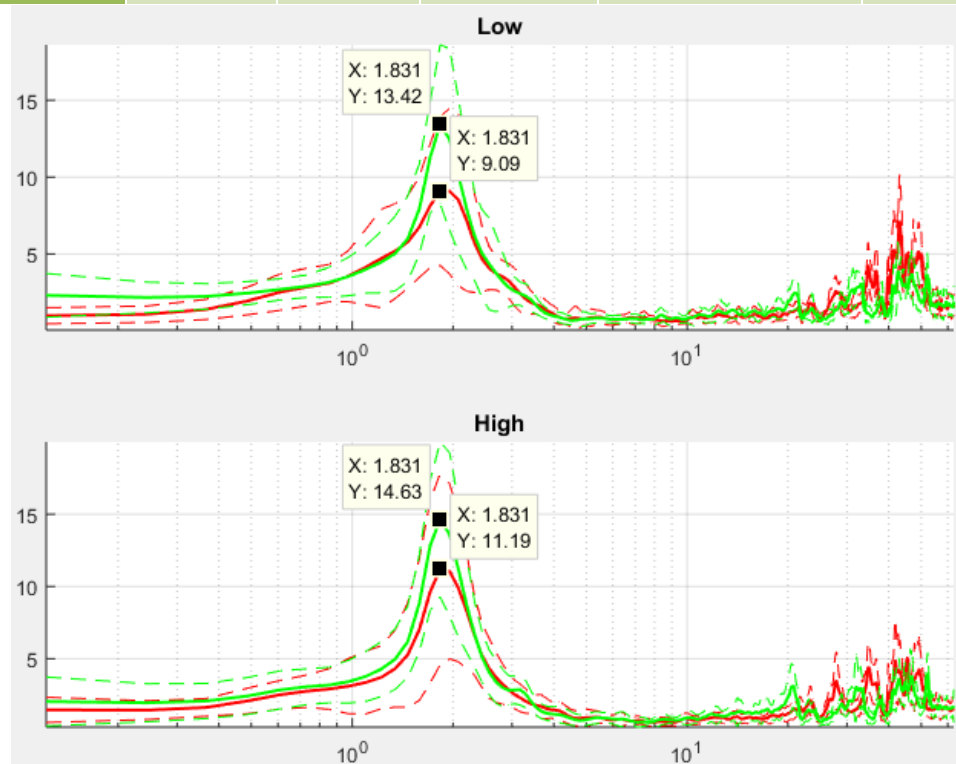
Figure C.9:Montmagny GLC-04 (Tromino)
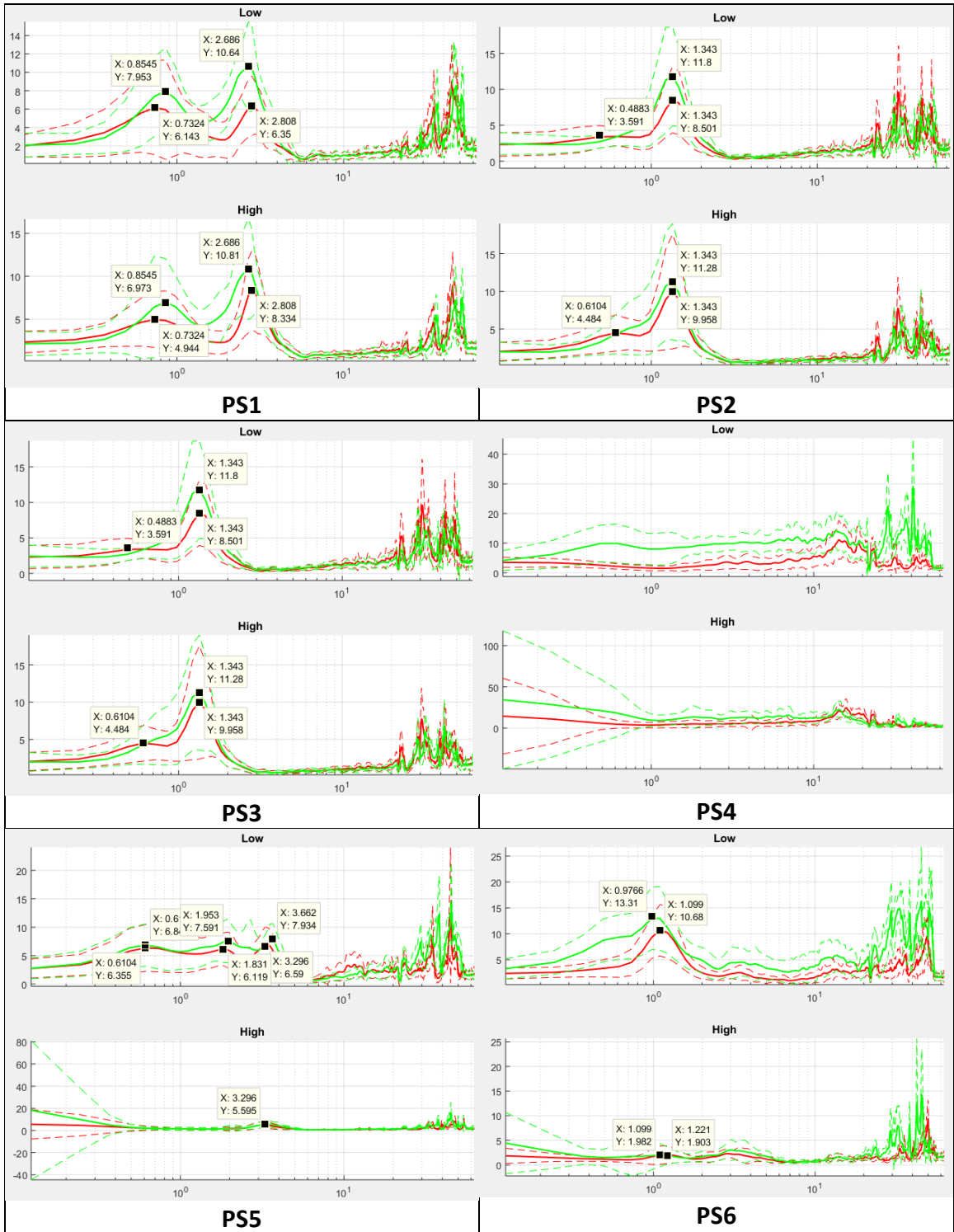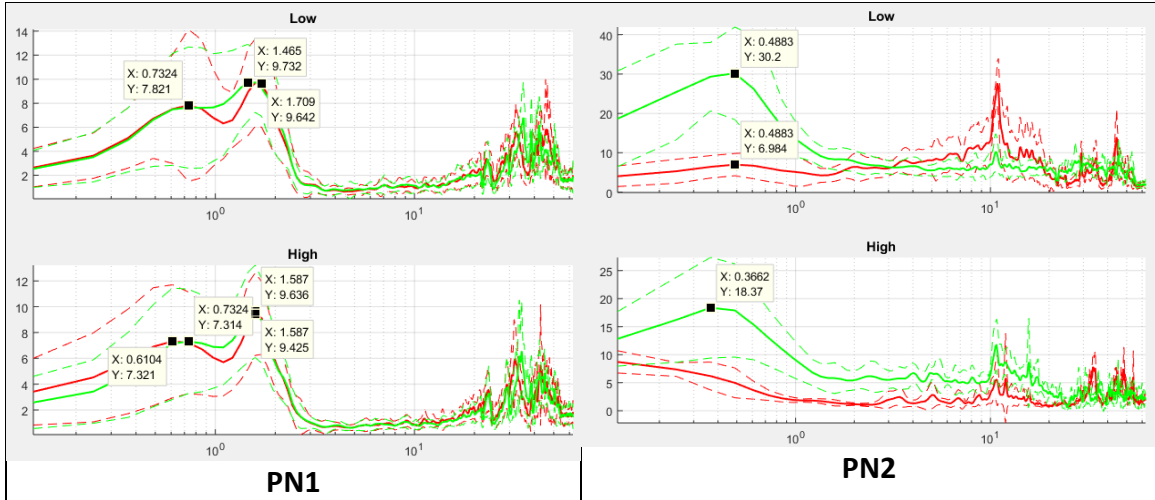
Figure C.10 Montmagny HVSR Results

Curriculum Vitae

Name: Aleksandar Mihaylov

Post-secondary Education and Degrees:

The University Of Western Ontario
London, Ontario, Canada
2005-2010 B.E.Sc., Electrical Engineering
B.E.Sc., Medical Biophysics

The University of Western Ontario
London, Ontario, Canada
2010-2012 M.E.Sc., Electrical Engineering

The University of Western Ontario
London, Ontario, Canada
2013-2019 Ph.D., Civil Engineering(ongoing)

Honors and Awards:

NSERC CGS M
2010-2012

Natural Science and Engineering Research Council (NSERC)
Doctoral Fellowship
Undergraduate Student Research Award (USRA)
2008-2010

Related Work Experience

Teaching and Research Assistant
The University of Western Ontario
2013-2018

Teaching Assistant
The University of Western Ontario
2010-2012

Research Assistant
Canadian Surgical Technologies and Advanced Robotics (CSTAR)
The University of Western Ontario
2008-2010

Publications:

1. Mihaylov, A., El Naggar, H., Mihaylov, D., Dineva, S., 2019. Approximate analytical HVSR curve using multiple band-pass filters and potential applications. Soil Dynamics and Earthquake Engineering 127, 105840.
2. Mihaylov, A., El Naggar, H., 2019. Extension of frequency range of geophone elements in post-processing and real-time vibration measurements. Acta Geophysica. Submitted